



HAL
open science

Study of the mechanism of fatigue crack initiation in 9Ni martensitic steel

Mahira Adna Cota Araújo

► **To cite this version:**

Mahira Adna Cota Araújo. Study of the mechanism of fatigue crack initiation in 9Ni martensitic steel. Structural mechanics [physics.class-ph]. Université de Lille, 2021. English. NNT : 2021LILUR032 . tel-03616547

HAL Id: tel-03616547

<https://theses.hal.science/tel-03616547>

Submitted on 22 Mar 2022

HAL is a multi-disciplinary open access archive for the deposit and dissemination of scientific research documents, whether they are published or not. The documents may come from teaching and research institutions in France or abroad, or from public or private research centers.

L'archive ouverte pluridisciplinaire **HAL**, est destinée au dépôt et à la diffusion de documents scientifiques de niveau recherche, publiés ou non, émanant des établissements d'enseignement et de recherche français ou étrangers, des laboratoires publics ou privés.

PhD Thesis

To obtain the grade of

DOCTOR

in Materials Science

by

Mahira Adna COTA ARAÚJO

Graduated Metallurgical Engineer from Universidade Federal de Minas Gerais - Brazil

Study of the mechanism of fatigue crack initiation in 9Ni martensitic steel

PhD defended on October 22, 2021 in front of the following dissertation committee:

Marion RISBET	Professor, Université de Technologie de Compiègne, France	President
Nathalie GEY	Research Fellow, LEM3-Université de Lorraine, France	Reviewer
Kim VERBEKEN	Professor, Gent University, Belgium	Reviewer
Nathalie LIMODIN	Director of Research, LAMCube Université de Lille, France	Examinator
Jean-Marc OLIVE	Research Fellow, I2M Université de Bordeaux, France	Examinator
Jérémie BOUQUEREL	Associate Professor, UMET, Centrale Lille Institut, France	Co-Supervisor
Jean-Bernard VOGT	Professor, UMET, Centrale Lille Institut, France	Supervisor

Lille
2021

Thèse de Doctorat

Pour obtenir le titre de

DOCTEUR

En Science des Matériaux

par

Mahira Adna COTA ARAÚJO

Ingénieure Métallurgiste diplômée de l'Universidade Federal de Minas Gerais (UFMG),
Brésil

Critère d'amorçage de micro fissures de fatigue dans l'acier martensitique 9Ni

Thèse défendue publiquement le 22 octobre 2021 devant la commission d'examen:

Marion RISBET	Professeure, Université de Technologie de Compiègne, France	Présidente
Nathalie GEY	Chargée de recherche, LEM3-Université de Lorraine, France	Rapporteuse
Kim VERBEKEN	Professeur, Université de Gand, Belgique	Rapporteur
Nathalie LIMODIN	Directrice de recherche, LAMCube Université de Lille, France	Examinatrice
Jean-Marc OLIVE	Chargé de recherche, I2M Université de Bordeaux, France	Examinateur
Jérémie BOUQUEREL	Maître de conférences, UMET, Centrale Lille Institut, France	Co-encadrant
Jean-Bernard VOGT	Professeur, UMET, Centrale Lille Institut, France	Directeur

Lille
2021

Mechanism of fatigue crack initiation in 9Ni martensitic steel

A dissertation submitted in partial fulfillment of the requirements for the degree of DOCTOR OF PHILOSOPHY.

Mahira Adna COTA ARAÚJO

Supervisor: Jean-Bernard Vogt
Co-Supervisor: Jérémie Bouquerel

Lille, 2021

Acknowledgements

Well, this is not only a Doctor title, but a proof of all trust and investment that my family did on me, thanks to my sister Maysa and my parents Rosimairé and Ernani. I would like to thank you all for believe in me, and thank myself also for not giving up from my dreams, this an accomplishment that I was dreaming for since I was a kid. This PhD was built up during a historical and very delicate moment for the society and yet we had to stay strong and productive... Those three years were very significant, meaning that all struggles that I had gave me capacity of dealing with many adversities.

I would like to thank my supervisors, specially to Jean-Bernard Vogt who guided me during this intense research. Thank you for believe in me, being so kind, supportive and welcoming. And for being exactly like me! Thanks to Ahmed, Alexandre Fadel and Jérémie for all the contributions about microscopy subject and techniques. Damien Creton, *"the best laboratory technician!"* who is always in a good mood and treating us like his daughters, this means a lot for someone who is far away from the family. Very kind thanks to my boyfriend, Thiago Ishikawa, for joining me on this adventure of being far away and still present (as far as possible), thank you very much for hearing me talking about the thesis all the time, giving me advice, for being patient and supportive as you always are. Thanks to the Geology guys, specially Jeff Gay, for the joy and the adventures of the first year! Bureau 227 partners, gratitude for being part of my everyday life and build a friendship, you have made my days better! Thanks for the big help during all the move in/move out days, Arthur!! The last but not less important, thanks to the 227-Brazilian girls: Isadora, for being so friendly and welcoming and for the wise words of support. Laís, who was literally 100% of the time by my side during those three years, thank you for you truly and special friendship, I will never forget the talks, the nice travels, the uncountable funny moments... You have made my days during the pandemic way lighter!

Thanks to all the people who made part of this and gave me support in some way staying by my side, my friends Wesley and Luiz França and mostly my psychologist, Andreia. Many thanks to Roberto Rocca Education Program for all the support and for having so much confidence in me.

"It Always Seems Impossible Until It Is Done" Nelson Mandela



Acronyms

PSB - Persistent Slip Bands

PSM - Persistent Slip Marks

γ - Austenite

α - Ferrite

α' - Martensite

fcc - face-centered cubic

bcc - body-centered cubic

XRD - X-ray diffraction

LCF - Low Cycle Fatigue

VHCF - Very-High Cycle Fatigue

FGA - Fine Granular Area

SEM - Scanning Electron Microscopy

BSE - backscattered electrons

SE -secondary electrons

EDS - Energy-dispersive X-ray spectroscopy

ECCI - Electron channelling contrast imaging

EBSD - Electron backscatter diffraction

EBSP - electron backscatter diffraction pattern

ECP - Electron channeling pattern

KAM - Kernel Average Misorientation

GROD - Grain Reference Orientation Deviation

GOS - Grain Orientation Spread

SSD - Statistically stored dislocations

GND - Geometrically necessary dislocations

LAB - Low Angle Boundary

HAB - High Angle Boundary

FIB - Focused Ion Beam

TEM - Transmission Electron Microscopy

SAEDP - Selected area electron diffraction pattern

HRTEM - High-Resolution Transmission Electron Microscopy

IFFT - Inverse Fast Fourier Transformation

AFM - Atomic Force Microscopy

MFM - Magnetic Force Microscopy

SWLI - Scanning White-light Interferometric

10T - Sample tempered for 10 hours

0.5T - Sample tempered for 30 minutes

WQ - Sample Quenched



Contents

1	Introduction	1
1.1	Goal	3
2	Literature Review	5
2.1	Martensitic Steels	5
2.1.1	Martensitic Transformation	5
2.1.2	Martensitic Microstructure	7
2.1.3	Crystallography	9
2.1.4	Tempered Martensite	11
2.1.5	Plastic Deformation in Martensitic Steels	11
2.2	Fatigue	12
2.2.1	Methods to Assess Fatigue Life	14
2.2.2	Low Cycle Fatigue Test	15
2.2.3	Low Energy Dislocation Structures Produced by Cyclic Deformation	18
2.2.4	Surface Relief	22
2.2.5	Shape of Extrusions	22
2.2.6	PSMs Visualization Techniques	23
2.2.7	Fatigue Surface Relief Models	26
2.2.8	Crack nucleation	29
2.3	9Ni steel	29

2.3.1	Heat Treatment	31
2.3.2	Microstructure of Quenched and Tempered 9Ni steel	33
2.3.3	Reversed Austenite	37
2.3.4	Mechanical Properties and Fatigue behavior of 9Ni steel	43
3	Materials and Methodology	49
3.1	Microstructure Characterization Techniques	49
3.1.1	X-ray Diffraction	50
3.1.2	Focused ion beam - FIB - Cross section visualization	51
3.1.3	Transmission Electron Microscopy- TEM	53
3.1.4	Scanning Electron Microscopy-based diffraction techniques	56
3.1.5	Scanning White Light Interferometry	67
3.2	Experimental Procedure and basic observations	69
3.2.1	Heat Treatment	70
3.2.2	Low cycle fatigue Testing	73
3.2.3	Post Fatigue Characterization	75
4	Results and Discussion	77
4.1	Water Quenched 9Ni steel - WQ sample	77
4.1.1	Non-deformed state	77
4.1.2	Cyclic stress-strain response and fatigue resistance	83
4.1.3	Topography Overview	86
4.1.4	Dislocation Structure and Microstructural Response	87
4.1.5	Cross-sectional view	97
4.1.6	Conclusions	103

4.2	30 Minutes Tempered 9Ni steel - 0.5T sample	106
4.2.1	Non-deformed state	106
4.2.2	Cyclic stress-strain response and fatigue resistance	111
4.2.3	Topography Overview	113
4.2.4	Dislocation Structure and Microstructural Response	113
4.2.5	Cross-sectional view	118
4.2.6	Conclusions	123
4.3	10 Hours Tempered 9Ni steel - 10T sample	126
4.3.1	Non-deformed state	126
4.3.2	Cyclic stress-strain response and fatigue resistance	131
4.3.3	Topography Overview	132
4.3.4	Dislocation Structure and Microstructural Response	133
4.3.5	Cross-sectional view	139
4.3.6	Conclusions	143
5	Outcome, Emerging Findings and Conclusions	147
5.1	Which microstructure is the most efficient?	148
5.1.1	Topography Overview	148
5.1.2	Light Interferometry	151
5.1.3	Fatigue response	152
5.1.4	Answer to the question	154
5.2	From intrusion to microcrack	155
5.2.1	Water Quenched Microstructure	155
5.2.2	10 Hours Tempered Microstructure	159

CONTENTS

5.2.3 Remarks 163

5.3 Selection criteria for technical analysis of austenite identification 163

5.3.1 Magnetic force microscopy (MFM) 164

5.4 Fatigue crack initiation in martensitic steels: role of greasy interface . . . 172

5.5 Concluding remarks 175

References **176**

A ANOVA - Roughness from SWLI **195**

B Fatigue data **201**

List of Tables

2.3.1	Chemical composition specifications according to ASTM A333 Gr.8 and EN 10028-4 standards	30
3.2.1	Chemical composition of the 9Ni steel given by the supplier	69
3.2.2	Vickers Hardness	71
4.1.1	Plastic strain at several stages for each applied strain	86
4.2.1	Plastic strain at the evaluated stages of fatigue life with $\Delta\epsilon_t=1.2\%$. . .	114
4.3.1	Plastic strain range of 10T sample at the evaluated stages of fatigue life with $\Delta\epsilon_t=1.2\%$	133

List of Figures

1.0.1	Examples of fatigue fracture surface and a pipeline leak. Font: NTSB 2010	1
2.1.1	Bain correspondence for martensitic transformation [11]	6
2.1.2	Formation of martensite in austenitic crystal [13]	6
2.1.3	Different martensite morphologies found in steels. a) lath α' (Fe-7%Ni-0.22%C), b) butterfly α' (Fe-20%Ni-0.73%C), c) plate type α' (Fe-8%Cr-0.9%C), d) lenticular α' (Fe-29%Ni-0.26%C), e) thin plate α' (Fe-31%Ni-0.23%C), f) ϵ martensite (Fe-24%Mn) [16]	7
2.1.4	Quenched lath martensite structure in low carbon alloys [17]	8
2.1.5	EBSD-Inverse Pole Figures of 0.2% low carbon (left) and 0.4% medium-carbon steel (right). Boundaries bigger than 8° are drawn as black lines [24]	8
2.1.6	The 24 variants in K-S relationship [15]	10
2.1.7	Representation of deformation mechanisms in lath martensite [17]	11
2.2.1	Fatigue stages [32]	13
2.2.2	S-N Curve	14
2.2.3	General Hysteresis Loops for three types of materials [33]	15
2.2.4	Hysteresis Loop	16
2.2.5	Typical Basquin and Manson-Coffin curves	17
2.2.6	Cyclic stress strain curve for bcc X10CrAl24 steel [37]	19
2.2.7	Planar and vein dislocation pattern in bcc X10CrAl24 steel at 5×10^{-5} strain amplitude (0.01% strain range) [37]	20
2.2.8	(left) Wall structure in bcc X10CrAl24 steel at 0.1% strain range (10-3 strain amplitude) and (right) labyrinth structure found at 0.4% strain range [37, 49]	20
2.2.9	Cell structure in bcc X10CrAl24 steel at 1% strain range (5×10^{-3} strain amplitude $g = [010]$) [49]	21
2.2.10	Ladder-like dislocation pattern in bcc X10CrAl24 steel cycled at 2×10^{-3} strain amplitude (0.4% strain range) [37]	21
2.2.11	Persistent slips marks morphologies in fcc metals [69]	23
2.2.12	Extrusion profiles detected by AFM tip in austenitic steel [84]	24
2.2.13	TEM-FIB cross sections of 12Cr steel [9]	25
2.2.14	TEM of FIB foil covered by Pt, the sample was cut from the surface of 316L steel [90]	25

LIST OF FIGURES

2.2.15	EGM-model of PSB surface profile formation [54]	26
2.2.16	Representation of dislocation arrangement of a Persistent Slip Mark [54] .	27
2.2.17	Polak's model of surface relief formation and surface profile of a PSM when point defects move back and forward from the PSB to the matrix [54] . . .	28
2.3.1	Effect of nickel content on impact toughness (adapted) [105]	30
2.3.2	Thermal heat treatments existent for 9Ni steel [109]	31
2.3.3	Iron-nickel phase diagram (adapted) [110]	32
2.3.4	Continuous Cooling Temperature diagram for 8.5Ni steel (adapted) [109] .	33
2.3.5	Optical and SEM microstructure of Quenched 9Ni steel [109]	34
2.3.6	Transmission electron microscopy image from Quenched 9Ni steel [115] . .	34
2.3.7	Microstructure of QIT 9Ni steel a) Optical micrograph d) Klemm's I etching showing the austenite as white bands. c) and f) EBSD phase map g) EBSD inverse pole figure [22]	35
2.3.8	Chemical composition analysis by EDS. Mn1 and Ni1 are the chemical composition referent to the white bands. Mn2 and Ni2 as the zones without microsegration [22]	35
2.3.9	EBSD map of 9Ni steel Quenched (800 °C/1 hour) + Tempered (600 °C/8 hours) a) phase map, austenite in red and cementite in yellow b) grain size image c) Kernel Map d) Kernel Average Misorientation map [109]	36
2.3.10	TEM micrograph of a structure obtained from quenching + tempering at 590 °C for 1h [99]	36
2.3.11	TEM micrographs of 9Ni steel tempered at 600°C for 1h indicating the presence of reversed austenite islands a) bright field image b) selected spot dark field image [115]	37
2.3.12	TEM image of Tempered 9Ni steel at 600 °C, the austenite phase was identified as the light phase between the martensite laths [109]	38
2.3.13	Schematic representation of microstructural development as a result of intercritical tempering of the as-quenched Fe-9Ni low carbon steel (adapted) [103]	39
2.3.14	Microstructure of a 9Ni steel bar QIT treated represented in 3 directions. b) Longitudinal to the rolling direction c) Normal to the rolling direction d) Transverse to the rolling direction [22]	40
2.3.15	STEM-EDS map of tempered 9Ni steel at 600 °C, considering iron, nickel, carbon and manganese [109]	40
2.3.16	EBSD grain boundary map and phase map showing the distribution of reversed austenite. The red dots are the austenite phase, red lines are 5° low angle boundaries and the blue lines are 10° low angle boundaries [96] .	41
2.3.17	Volume fraction of reversed austenite at different tempering temperatures [128]	41

LIST OF FIGURES

2.3.18	Evolution of reversed austenite fraction according to tempering times at 600 °C (adapted) [5]	42
2.3.19	XRD diffractogram of Quenched (800 °C/1 hour) + Tempered (600 °C/8 hours) 9Ni steel at different deformation levels from a tensile test performed at room temperature [109]	43
2.3.20	Evolution of austenite fraction in the stress-strain curve [109]	43
2.3.21	Engineering stress strain curve on 9Ni steel base metal [140]	44
2.3.22	The variation of mechanical properties and nickel content for normalized or quenched+tempered Ni steels [141]	45
2.3.23	Fracture surface from tensile test at room temperature (a,b) and at -196°C (c,d) [5]	45
2.3.24	Evolution of toughness as a function of austenite content in 9Ni steel (adapted) [103]	46
2.3.25	The cyclic stress response curves of welded 9Ni steel at a) room temperature, and b) cryogenic temperature (adapted) [137]	47
2.3.26	The relationship of the strain amplitude and the number of cycles to failure for welded 9Ni steel. a) room temperature b) cryogenic temperature (adapted) [137]	47
2.3.27	Crack propagation rate versus stress intensity factor for 9Ni steel tempered for 10 minutes, 1 hour and 12 hours [104]	48
3.1.1	Characterization Methods used in this study	49
3.1.2	Bragg's law conditions [143]	50
3.1.3	A working blunt-needle LMIS in ion generation mode [151]	51
3.1.4	FIB lift-out steps a) Deposition of a protective Pt coating across the PSMs. b) Ion bombarding around the selected area c) Trenching the thin lamella d) Extraction with the tungsten tip and transportation e) Ion 'welding' to the copper grid. f) Final thinning of lamella ready for TEM observation [87]	52
3.1.5	Different types of diffraction patterns obtained in a 100-kV TEM: A) amorphous carbon, B) an Al single crystal, C) polycrystalline Au (adapted) [157]	53
3.1.6	Two simplified basic modes of the TEM imaging A) diffraction mode: projecting the diffraction pattern and B) image mode: projecting the image [157]	54
3.1.7	a) HRTEM image of a monocrystalline Si and its twin structure b) IFFT image highlighting the twin [161]	55
3.1.8	EBSF pattern of Fe 36% Ni (fcc crystal structure), acquired with 15 kV [162]	56
3.1.9	Representation of the acquisition of EBSD patterns. Only one Kikuchi band is displayed in the image (adapted) [162]	57

LIST OF FIGURES

3.1.10	Steps of EBSD data acquisition [163]	57
3.1.11	Schematic of dislocations and subgrain boundaries and the effect on the EBSD pattern (adapted) [177]	60
3.1.12	EBSD pattern of Al 6061 alloy a) annealed b) 8.5% strain deformation, blurred pattern [178]	61
3.1.13	Schematic representation of KAM calculation [187]	62
3.1.14	Schematic representation of the defect contrast formation in ECCI [194] .	64
3.1.15	ECC image of the dislocation arrangement after fatigue test. The dislocation dense regions (walls, veins) appear as a bright contrast. The image on the side is in inverted contrast, being comparable to TEM studies [193]	65
3.1.16	Comparison between a) inverted c-ECCI and b) conventional TEM micrograph of the dislocation arrangement in a globular γ -TiAl grain [193]	67
3.1.17	2D Surface profile according to ISO 4287:1997	68
3.1.18	3D acquisition according to ISO 25178-2:2012 (adapted) [206]	68
3.2.1	Heat treatments routes adopted for this work	70
3.2.2	Austenite fraction measured by XRD as a function of the tempering time. WQ: water-quenched, 0.5T: tempered for 30 minutes and 10T: tempered for 10 hours.	71
3.2.3	Nital 3% and Klemm's II solution: sample WQ (a and d), sample 0.5T (b and e) and sample 10T (c and f). The yellow/brown zones indicates the martensitic constituent, blue zones corresponds to the bainitic constituent and the lighter dots or bands are the austenitic phase	72
3.2.4	SEM micrographs of 9Ni steel. WQ sample (left), 0.5T (middle), 10T (right)	73
3.2.5	EDS point analysis indicating element segregation into the white zones, identified as reversed austenite	73
3.2.6	Low cycle fatigue specimen geometry according to ASTM E606	74
3.2.7	Broad cross-section cut on fatigued specimens	76
4.1.1	TEM micrograph of the WQ sample	78
4.1.2	Inverse Pole Figure of a representative zone showing absence of any preferential texture in the WQ material	78
4.1.3	Phase map showing very few indexed pixels as austenite pointed by red arrows in the WQ material	79
4.1.4	a) Bright field image TEM of WQ 9Ni steel, b) Selected Area Diffraction Spot (SAED) of $(220)\gamma$, c) dark field image of the same area highlighting the austenitic phase	80
4.1.5	ECCI image showing the WQ structure of 9Ni steel	81
4.1.6	ECCI image showing the WQ structure of 9Ni steel, the austenite is indicated by the white arrows	81

LIST OF FIGURES

4.1.7	Twins identified by ECCI technique in WQ sample as indicated by the red arrows	81
4.1.8	Kernel Average Misorientation maps showing an initial microstructure composed of highly misoriented zones	82
4.1.9	Line Segment Misorientation + Image Quality - Misorientation distribution EBSD maps for WQ sample at the initial state	83
4.1.10	Evolution of the stress amplitude versus the number of cycles (left) and versus the fatigue life fraction (right) for the different total strain tests for WQ sample	84
4.1.11	Cyclic and monotonic stress-strain curves	85
4.1.12	Manson-Coffin curves showing a point of changing in slope at $\Delta\epsilon_t=1\%$ ($\Delta\epsilon_p=0.2\%$)	86
4.1.13	Surface roughness at life end of different LCF tests	87
4.1.14	c-ECCI images showing the dislocation and topography of the WQ 9Ni at each stage of cycling ($\Delta\epsilon_t=0.9\%$)	88
4.1.15	Planar dislocation structure localized within the laths next to the persistent slip marks at 50% of the fatigue life for the test at $\Delta\epsilon_t=0.9\%$	89
4.1.16	KAM maps evolution of WQ 9Ni steel at $\Delta\epsilon_t=0.9\%$. The white arrows and the dashed lines indicate the extrusions. c-ECCI and IPF images shows the scanned zone at 5% of life	90
4.1.17	Image Quality + LSM EBSD maps at $\Delta\epsilon_t=0.9\%$. The darker zones indicate the regions with the presence of extrusions. Blue arrows indicate the changing of misorientation level	91
4.1.18	Martensite parent grain reconstruction based on the Kurdjumov-Sachs orientation relation for the WQ 9Ni steel deformed at $\Delta\epsilon_t=0.9\%$. (b) Corresponding IPF map. The white dashed lines indicate the extrusions	92
4.1.19	c-ECCI images showing the dislocation and topography of the WQ 9Ni steel at several stages of fatigue life ($\Delta\epsilon_t=1.2\%$)	93
4.1.20	Highly dense dislocation walls (HDDW) aligned to a persistent slip mark that crosses a block boundary. One intrusion in the process of forming at the interface ($\Delta\epsilon_t=1.2\%$)	94
4.1.21	KAM maps evolution of WQ 9Ni steel at $\Delta\epsilon_t=1.2\%$. The white arrows and the dashed lines indicate the extrusions. c-ECCI and IPF images indicating the scanned zone at 5% of life	95
4.1.22	Image Quality + LSM EBSD maps of WQ 9Ni steel at $\Delta\epsilon_t=1.2\%$. The darker zones indicate the regions with the presence of extrusions. Blue arrows indicate the changing of misorientation level	96

LIST OF FIGURES

4.1.23	a) Martensite parent grain reconstruction based on the Kurdjumov-Sachs orientation relation for the WQ sample deformed at $\Delta\varepsilon_t=1.2\%$. b) Corresponding IPF map. The white dashed lines indicate the extrusions .	97
4.1.24	Selected zone comprising PSMs for FIB lamella extraction of the WQ sample fatigued at $\Delta\varepsilon_t=1.2\%$ at the end of fatigue life, the dots correspond to the Pt deposition mark the exact position of extraction	98
4.1.25	HRTEM image of WQ sample thin lamella showing accurately the sites of extrusions and intrusions at 5% of the fatigue life ($\Delta\varepsilon_t=1.2\%$). The yellow lines highlight the laths boundaries	99
4.1.26	HRTEM image of an extrusion formed at 5% of the fatigue life ($\Delta\varepsilon_t=1.2\%$). Enlarged view of the yellow dashed zone showing nanograins the yellow dashed line indicates the lath boundary)	100
4.1.27	HRTEM image of two extrusions formed at 5% of the fatigue life ($\Delta\varepsilon_t=1.2\%$). HAADF-STEM and EDX map of the yellow dashed zone. Yellow dashed lines indicate the lath boundary with small increase of carbon next to it .	101
4.1.28	HRTEM images of thin lamellae accurately indicate the sites of extrusions and intrusions at the end of the fatigue life ($\Delta\varepsilon_t=1.2\%$). Yellow dashed lines indicate the lath boundary and the blue dashed lines indicate the cell walls	102
4.1.29	HRTEM images of thin lamellae showing the microcracks ($\Delta\varepsilon_t=1.2\%$), cells identified next to the cracks highlighted by the blue dashed lines and nanograins were also identified at the intrusion tip	102
4.1.30	Representation of extrusions and intrusions nucleation sites for the WQ sample during fatigue at low and high strain	105
4.2.1	Inverse Pole Figure of a representative zone from the 0.5T sample	107
4.2.2	Phase map of the 0.5T sample, the reversed austenite is represented by the red color	107
4.2.3	a) Bright field image TEM of 0.5T sample, b) Selected Area Diffraction Spot (SAED) of $(220)\gamma$ plane, c) dark field image of the same area highlighting the austenitic phase	108
4.2.4	TEM micrograph of the 0.5T microstructure of 9Ni steel	108
4.2.5	c-ECCI image of the 0.5T microstructure of 9Ni steel, the red arrows point to the reversed austenite	109
4.2.6	c-ECCI image of the 0.5T microstructure of 9Ni steel	109
4.2.7	Kernel Average Misorientation map of the 0.5T sample at the initial state	110
4.2.8	Line Segment Misorientation + Image Quality - Misorientation distribution EBSD map for 0.5T sample at the initial state	110
4.2.9	Evolution of the stress amplitude versus the number of cycles (left) and versus the fatigue life fraction (right) for the different total strain tests for 0.5T sample	111

LIST OF FIGURES

4.2.10	Cyclic and monotonic stress-strain curves for the 0.5T sample	112
4.2.11	Manson-Coffin curves of the 0.5T sample	112
4.2.12	Evolution of surface damage accumulation resulted from LCF tests for the 0.5T sample, as a function of the total applied strain	113
4.2.13	c-ECCI images showing the dislocation and topography of the 0.5T sample at 5% and 50% of fatigue life	114
4.2.14	Highly dense dislocation walls (HDDW), cells and dislocation bands next to a persistent slip mark (extrusion) of the 0.5T sample at 5% of fatigue life	115
4.2.15	A closer look of c-ECCI images showing the dislocation and topography of the 0.5T sample at 5% and 50% of fatigue life. The red arrows point to the dislocations	115
4.2.16	Highly dense dislocation walls (HDDW), cells and dislocation lines next to an intrusion of the 0.5T sample ($\Delta\epsilon_t=1.2\%$)	116
4.2.17	Image Quality + LSM EBSD maps of 0.5T sample at $\Delta\epsilon_t=1.2\%$. The blue arrows indicate the regions with the presence of extrusions	117
4.2.18	a) KAM maps evolution of 0.5T sample at $\Delta\epsilon_t=1.2\%$. The white arrows and the dashed lines indicate the extrusions. b) c-ECCI and IPF images indicating the scanned zone at 50% of life	117
4.2.19	a) Martensite parent grain reconstruction based on the Kurdjumov-Sachs orientation relation for the 0.5T sample deformed at $\Delta\epsilon_t=1.2\%$. b) Corresponding IPF map. The white dashed lines indicate the extrusions .	118
4.2.20	Selected zone comprising PSMs for FIB lamella extraction of the 0.5T sample with $\Delta\epsilon_t=1.2\%$ at the end of fatigue life. The dots correspond to the exact position of lamella extraction	119
4.2.21	HRTEM images of two thin lamellae indicating the sites of extrusions and intrusions for the 0.5T sample at $\Delta\epsilon_t=1.2\%$ at the end of fatigue life . . .	120
4.2.22	FIB lamellae showing a zone containing a microcrack and pair of extrusion-intrusion next to an austenitic island for the 0.5T microstructure at the end of fatigue life ($\Delta\epsilon_t=1.2\%$)	120
4.2.23	a) HRTEM image the interface between martensite and austenite of the 0.5T sample, b) HAADF and EDX mapping of the chemical elements of the selected zone, c), d) and e) Austenite planes enhanced by IFFT	122
4.2.24	Phase Map, IPF and Band contrast images of the TKD scan conducted on a FIB lamellae of the 0.5T sample ($\Delta\epsilon_t=1.2\%$)	123
4.2.25	Representation of extrusions and intrusions nucleation sites for the 0.5T sample during fatigue	125
4.3.1	a) IPF, b) KAM, c) IQ +LSM and d) Phase Map of the 10T sample . . .	127

LIST OF FIGURES

4.3.2	a) Bright field image TEM of 10T sample, b) Selected Area Diffraction Spot (SAED) of (220) γ plane, c) dark field image of the same area highlighting the austenitic phase	128
4.3.3	TEM micrograph of the 10T sample	129
4.3.4	c-ECCI image of the 10T microstructure, the red arrows point to the reversed austenite	130
4.3.5	c-ECCI image of the 10T microstructure, the red arrows point to the reversed austenite	130
4.3.6	Evolution of the stress amplitude versus the number of cycles (left) and versus the fatigue life fraction (right) at different total strains for the 10T sample	131
4.3.7	Cyclic and monotonic stress-strain curves for the 10T sample	132
4.3.8	Manson-Coffin and Basquin curves of the 10 T sample	132
4.3.9	Surface damage accumulation resulted from LCF tests for the 10T sample	133
4.3.10	c-ECCI images showing the dislocation and topography of the 10T sample at each stage of cycling	134
4.3.11	c-ECCI images showing the dislocation evolution of the 10T sample at each stage of cycling	135
4.3.12	a) KAM maps evolution of 10T sample at $\Delta\epsilon_t=1.2\%$ b) c-ECCI and IPF images indicating the scanned zone at 50% of fatigue life. The white arrows and the dashed lines indicate the extrusions	136
4.3.13	Image Quality + LSM EBSD maps of 10T sample at $\Delta\epsilon_t=1.2\%$. The blue arrows indicate the regions with the presence of extrusions	137
4.3.14	a) Martensite parent grain reconstruction based on the Kurdjumov-Sachs orientation relation for 10T sample deformed at $\Delta\epsilon_t=1.2\%$. b) Corresponding IPF map. The white dashed lines indicate the extrusions .	138
4.3.15	EBSD phase maps evolution of 10T sample at $\Delta\epsilon_t=1.2\%$	139
4.3.16	Selected zone comprising PSMs for FIB lamella extraction of the 10T sample with $\Delta\epsilon_t=1.2\%$ at the end of fatigue life. The dots correspond to the Pt deposition marking the exact position of extraction	140
4.3.17	HRTEM images of two thin lamellae indicating the sites of extrusions and intrusions at $\Delta\epsilon_t=1.2\%$ at the end of fatigue life for the 10T sample	140
4.3.18	a) Diffraction pattern b) SAED and TEM images superposed indicating the austenite and the sites of extrusions marked by the black arrows at $\Delta\epsilon_t=1.2\%$ at the end of fatigue life for the 10T sample	141

LIST OF FIGURES

4.3.19	a) Diffraction pattern; b), c) and d) dark field-TEM images obtained with the (311) γ spot indicating the austenite and the sites of extrusions marked by the black arrows at $\Delta\epsilon_t=1.2\%$ at the end of fatigue life for the 10T sample. Blue and yellow dashed lines indicate the cells boundaries and lath boundaries, respectively	142
4.3.20	Representation of extrusions and intrusions nucleation sites for the 10T sample during fatigue	145
5.1.1	Surface topography after LCF tests for all microstructures analyzed at three different strain levels	148
5.1.2	Types of extrusions found on 9Ni steel. a) Band-like b) Coarse c) Cord-like d) Protrusion e) Ribbon-like f) Tongue-like	150
5.1.3	Distribution of extrusions for the 0.5T and 10T samples	150
5.1.4	Surface profile of the LCF tested specimens	151
5.1.5	Box-plot charts of the 2D measured parameters	151
5.1.6	Box-plot charts of the 3D measured parameters	152
5.1.7	Evolution of the stress amplitude versus the number of cycles of the 9Ni steel submitted to different heat treatments	153
5.1.8	Manson-Coffin curves of 9Ni steel submitted to different heat treatments	153
5.1.9	Hysteresis loops of the 9Ni steel submitted to different heat treatments	154
5.2.1	Cross-section view of a sample deformed at 50% of fatigue life ($\Delta\epsilon_t=1.6\%$)	155
5.2.2	Cross-section view of a sample deformed until the end of fatigue life ($\Delta\epsilon_t=0.8\%$). The dashed lines indicate the intrusions location	157
5.2.3	Cross-section view of a WQ sample deformed until the end of fatigue life ($\Delta\epsilon_t=1.6\%$)	158
5.2.4	Cross-section view of a 10T sample deformed at the end of fatigue life ($\Delta\epsilon_t=1.6\%$)	159
5.2.5	Cross-section view of the 10T sample deformed until the end of fatigue life ($\Delta\epsilon_t=0.8\%$). The dashed lines indicate the intrusions location	160
5.2.6	Cross-section view of the 10T sample deformed until the end of fatigue life ($\Delta\epsilon_t=1.6\%$). The dashed lines indicate the intrusions location	162
5.3.1	MFM principle of work [249]	165
5.3.2	a) MFM image of the duplex stainless steel with austenite (uniform) and ferrite (labyrinth pattern) b) Corresponding AFM topography with austenite (lighter) and ferrite (darker) [251]	165
5.3.3	MFM topographical (left) and magnetic force (right) and corresponding SEM image (bottom) image of the WQ sample, without deformation	166

5.3.4 Closer view of a MFM topographical (left) and magnetic force (right) of the WQ sample, without deformation. The dashed lines in the topographical image indicates a lath boundary, the blue arrows in the corresponding magnetic force image points to the bright spots aligned in the same location of the indicated boundary 167

5.3.5 MFM topographical (left) and magnetic force (right) of the WQ sample, after LCF test ($\Delta\varepsilon_t=1.2\%$). 167

5.3.6 MFM topographical (left) and magnetic force (right) of the WQ sample after LCF test ($\Delta\varepsilon_t=1.2\%$). The blue arrow points to the austenitic phase placed next to the extrusion. 168

5.3.7 MFM topographical images as a function of the lift height 169

5.3.8 MFM topographical (left) a magnetic force (right) of the 10T sample, without deformation 170

5.3.9 Closer MFM topographical (left) and magnetic force (right) of the 10T sample, without deformation 170

5.3.10 SEM image (left), MFM topographical (middle) and magnetic force (right) of the 10T sample after LCF test ($\Delta\varepsilon_t=1.2\%$) 171

5.3.11 Detailed view of a MFM topographical (left) and magnetic force (right) of the 10T sample after LCF test ($\Delta\varepsilon_t=1.2\%$) 171

5.4.1 Proposed mechanism of fatigue crack initiation in martensitic steels 173

Chapter 1

Introduction

Metal fatigue refers to the progressive deterioration and eventual failure of components subjected to cyclic stress that varies in time, being caused by mechanical forces or successive temperature changes. Fatigue failure of a component occurs through an irreversible energy dissipating process where surface damage activity will absorb some energy that was put into the materials during their operation. This type of failure is a big concern and is frequently present among all the various sorts of failures that a material might face. Figure 1.0.1 shows some examples of fatigue failures that a component can undergo, and may cause several accidents.



Figure 1.0.1: Examples of fatigue fracture surface and a pipeline leak. Font: NTSB 2010

There are two approaches to describe and investigate fatigue damage: metallurgical aspect and mechanical aspect [1]. Metallurgical approaches are concerned with the condition of the metal at all steps of the cyclic load, they are commonly interpreted to encompass the study of metal fatigue mechanisms. This will be the main focus of this study. Mechanical descriptions concentrate on the mechanical response to a certain range of loading circumstances, such as the number of load cycles required to induce failure. It is very important to take deep investigations of what leads to the fatigue failure because this type of damage impedes the component to work properly and by predicting failures,

efficiency can be improved concerning corrective maintenance.

The increased demand for clean energy sources has risen the interest in the use of Liquefied Natural Gas (LNG). The components fabricated by 9Ni steels often comprise oil and gas pipelines or part of the structure of containers due to their excellent cryogenic resistance. The mechanical properties of this steel grade have been extensively studied and it has been shown that the 9Ni steel and their welded joints attend very well the requirements for LNG applications [2–5]. The components that are part of the LNG storage and transport are frequently submitted to thermal contractions, often undergoing fatigue loading, which can cause low cycle fatigue (LCF) failure. Hence, it is very important to identify the LCF behavior for this material including cyclic plasticity and fatigue resistance. This implies understanding how the microstructure controls the response of the material against cyclic loading and how the fatigue damage starts in this material. Fatigue damage involves metallurgical evolution of the microstructure, crack initiation and its propagation. For the material of the present study, a martensitic steel, the metallurgical investigation is a tough task because of its very complex microstructure. Whereas former models of fatigue crack initiation are already proposed for simple microstructures.

By taking a deep look into the metallurgical approach of fatigue analysis, some studies have been making an effort to propose a mechanism that explores the very first stage of the damage accommodation [6–8]. In the case of less complex microstructures such as monocrystals, ferritic, and austenitic steels, a mechanism of fatigue crack initiation has been proposed by Pólak [7]. It is thought to be known that the initial surface damage results from the persistent slip bands, which are the irreversible dislocation structure formed under the cyclic straining. Those persistent bands will emerge at the surface, being classified as persistent slip marks, composed of the pair of extrusions and intrusions. The latter is related to be the very early stage of a microcrack initiation.

Concerning the complex microstructures, no former mechanism has been proposed yet, once the microstructure differs considerably from the ones investigated for the former mechanisms of crack initiation. It has been suggested that the finer martensitic structure behaves itself as the persistent slip bands, that will slide between each other and further developing a microcrack due to stress gradients. The martensitic interfaces play an important role in the appearance of microcracks, as reported by studies done with the 12Cr martensitic steel [9]. Based on the observations done in the literature, it is very interesting to observe if interfaces modifications can impact in some way the mechanism of plasticity of complex structures such as martensite.

A critical understanding of the mechanism of fatigue crack initiation, based on the influence of microstructural modifications induced by heat treatment promoting

precipitation of a new phase is strictly important for comprehending what drives the failure process of the material. Investigating the interface modifications is also interesting to observe what can be done to improve the fatigue life. With the approaches and extensive investigations carried out in this study, a new mechanism of fatigue crack initiation is proposed sustained from the ones already present in the literature. It is worth mentioning that the suggested fatigue crack initiation process for 9Ni steel can be extended to other alloys with a similar complex microstructure that allows gentle interface modifications.

1.1 Goal

The challenging points concerning this study on a 9Ni steel are summarized below:

1. Identify the mechanical response under cyclic loading and understand the cyclic plasticity mechanism in regards to the metallurgical microstructures;
2. Modify the interface by generating a new phase to observe its effects as well on the macroscopic response as on fatigue micro cracks nucleation;
3. Determine the first signs of surface damage in fatigue crack initiation stage on the different microstructures obtained
4. Propose a mechanism of fatigue crack initiation for the 9Ni complex martensitic microstructure.

Chapter 2

Literature Review

In this chapter, a detailed description of the background of the degree project is presented together with related work.

2.1 Martensitic Steels

Martensitic steels are one of the most important structural materials, they are known to have the highest hardness in the class of steels, possessing also high strength and wear resistance. There are multiple types and grades of martensitic steels, they can be classified into families according to their second major element and their application such as Fe-C, Fe-Cr, Fe-Ni alloys, or stainless steels depending on the proportion of elements. Other alloying elements in martensitic steels include manganese and molybdenum, for example.

The hard meta-stable phase is obtained by rapid cooling (quenching) of the austenite avoiding the formation of diffusion-dependent structures such as pearlite, ferrite, and cementite. The final microstructure after the quenching heat treatment is brittle in that way that the tempering treatment is necessary to ameliorate the mechanical properties.

2.1.1 Martensitic Transformation

The martensitic reaction starts at a temperature usually named M_s and ends at a temperature designated as M_f . M_s and M_f depend on the chemical composition of the material. If M_s is inferior to room temperature, no martensitic structure is obtained by simple heat treatment. A complete martensitic structure is formed if M_f is higher than room temperature.

The martensitic transformation is triggered from a given cooling rate which also depends on the chemical composition of the material. Sometimes cooling from the austenitic domain in water is necessary to transform the austenite into martensite, while in other cases air cooling is sufficient. It is a diffusionless transformation due to rapid

cooling, the carbon atoms are trapped in octahedral sites of a bcc structure. Then, the martensite assumes the bct structure, since there is a distortion in the lattice. This rapid transformation from fcc to bcc structure involves a substantial strain which is accommodated by the introduction of high-density defects. The martensitic reaction is formed by a shear mechanism, it happens when the surface is tilted into a new orientation.

A lattice deformation in the austenite structure is essential to generate the martensite. The combined deformations along the c axis and the expansion along the a_x axes is known as Bain Strain, which turns the structure of the parent phase into a new microstructure (Figure 2.1.1) [10].

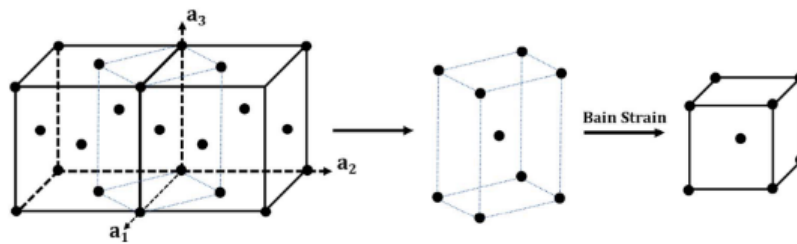


Figure 2.1.1: Bain correspondence for martensitic transformation [11]

The strain model conceived by Bain does not sufficiently describe the whole martensitic transformation. In order to minimize the energy during the martensitic transformation, the martensite will form in the shape of thin plates, conserving at least one plane from the parent austenite phase, combined with an appropriate rigid body rotation [12]. The plane that is maintained invariant is also denominated as habit plane. The habit plane is the preferred crystal plane in the parent austenite where the martensite is formed, and it will remain undistorted and unrotated to accommodate the deformation, being completely coherent with the parent austenite (Figure 2.1.2).

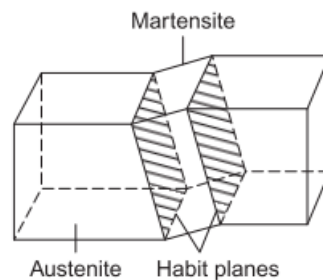


Figure 2.1.2: Formation of martensite in austenitic crystal [13]

The martensite is known as a hard phase due to the shear mechanism and the lattice distortion caused by the trapped carbon atoms. When the martensite is heated up again, the carbon atoms trapped in octahedral sites become mobile and form carbides, alleviating

the tension; this process is known as tempering heat treatment [14]. The hierarchical structure composed of packets, blocks, and laths act as barriers to dislocation movement, giving its hard characteristic. The martensitic transformation results in very thin lath shapes exhibiting a locally anisotropic microstructure [15].

2.1.2 Martensitic Microstructure

There are three types of martensite with different crystal structures: α' bcc/bct martensite (found in Fe-C-Ni alloys), ϵ hcp martensite, and fct martensite (vary rare). Figure 2.1.3 shows the ϵ and the diverse α' morphologies. The martensitic structures can have different morphologies: lath, lenticular, and plate, for example. The formation of each shape is determined by the M_s temperature and the chemical composition.

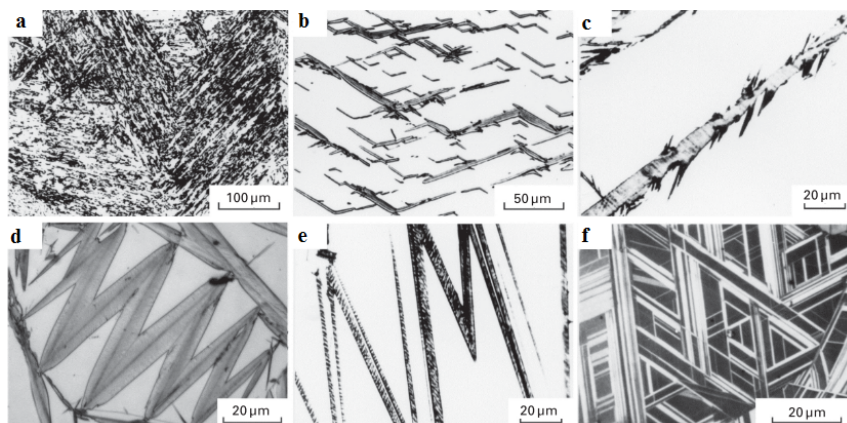


Figure 2.1.3: Different martensite morphologies found in steels. a) lath α' (Fe-7%Ni-0.22%C), b) butterfly α' (Fe-20%Ni-0.73%C), c) plate type α' (Fe-8%Cr-0.9%C), d) lenticular α' (Fe-29%Ni-0.26%C), e) thin plate α' (Fe-31%Ni-0.23%C), f) ϵ martensite (Fe-24%Mn) [16]

The morphology of martensite in low carbon steels is typically the lath structure. Lath martensite is present in Fe-C (<0.6% C), Fe-Ni (<28% Ni), Fe-Mn (<10% Mn) alloys, and in the majority of heat-treatable commercial steels. Lath martensitic steels have big industrial importance because it is usually a basic structure of high strength steels [16]. The lath martensite shows a very specific hierarchical structure, comprising packets, blocks, and laths. An austenitic grain is divided into packets (a group of well-developed parallel blocks that contains laths with the same habit plane). Each packet is then subdivided into blocks (group of laths of the same orientation-variant and misoriented by less than 10°), as demonstrated in Figure 2.1.4. The possible variations in local yield strength originated by the martensitic transformation linked to the lath size are represented by a color gradient. In addition, dislocation density is revealed by electron channeling contrast

imaging, and atom probe tomography (APT) highlights the interstitial carbon content [17]. The finer structure present in martensite can involve dislocations and twins. The substructure of water quenched lath martensite consists of tangled dislocations in high concentration, created by athermal transformation from high temperatures [18]. The terms cells and subgrains have been used to describe the morphologies of certain types of low-energy dislocation substructures, resulted in their uniform distribution.

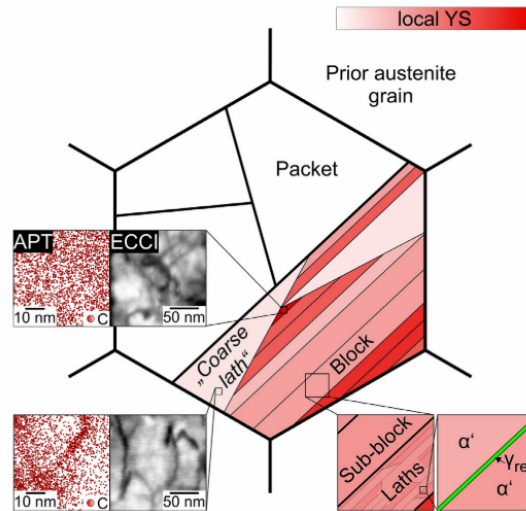


Figure 2.1.4: Quenched lath martensite structure in low carbon alloys [17]

Recent studies using the EBSD technique have helped to provide some advances in the comprehension of the complex martensitic structure [9, 15, 19–23]. The EBSD technique helps to visualize the relation between the parent austenite and the transformed martensite; make the distinction between the substructures; indicate the presence of misorientation induced by the geometric necessary dislocations and finally combine the morphology and crystallography. The different morphology and crystallography of low (0.2 wt%) and medium carbon (0.4 wt%) martensitic steels analyzed by EBSD is represented in Figure 2.1.5.

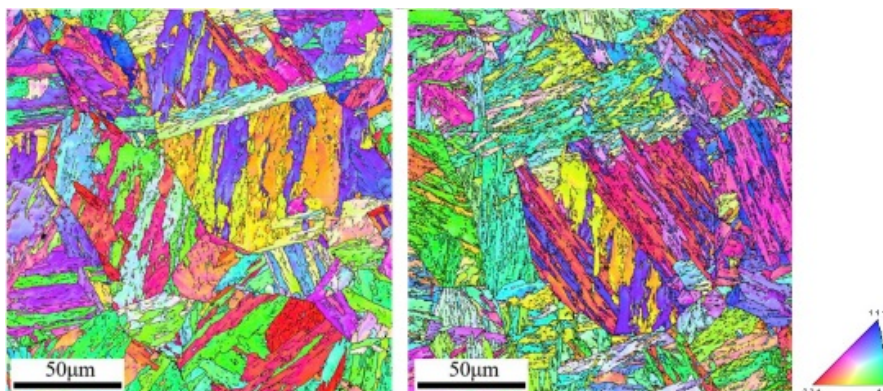


Figure 2.1.5: EBSD-Inverse Pole Figures of 0.2% low carbon (left) and 0.4% medium-carbon steel (right). Boundaries bigger than 8° are drawn as black lines [24]

2.1.3 Crystallography

A good crystallographic pairing between the parent and resulted phase in martensitic transformation is needed. During the martensitic transformation, the crystal lattice of the fcc austenite will suffer a shearing mechanism parallel to certain crystallographic planes with its vector parallel to particular crystallographic directions. The martensitic variants are those probable directions where the shearing mechanism will happen [12]. The orientation relationship states what planes and directions from the parent austenite and the transformed martensite are parallel. For a given orientation relationship, there are multiple equivalent orientations of the inherited phase, which are referred to as variants. In an idealized scenario, throughout the transformation, all variants have an equal chance of appearing in austenite grain. It has been observed, however, that some variations occurred more frequently during the transformation (known as variant selection) [25]. There are essentially three orientation relationships (ORs) that link the parent austenite and the transformed martensite:

- Kurdjumov-Sachs (K-S)
- Nishiyama–Wassermann (N-W)
- Greninger and Troiano (G-T)

Each of them fits well for a given material.

The G-T and N-W ORs are observed in alloys where the martensite plates have $\{259\}$ habit planes:

$$\{111\}\gamma \parallel \{011\}\alpha' \text{ and } \langle 112 \rangle\gamma \parallel \langle 011 \rangle\alpha'$$

The G-T ORs are suitable and accurate for 9Cr ferritic/martensitic steels:

$$\{110\}\gamma \parallel \{111\}\alpha \text{ and } \langle 17\ 17\ 7 \rangle\gamma \parallel \langle 12\ 17\ 5 \rangle\alpha'$$

The K-S ORs is valid for high-carbon steels with $\{225\}$ habit planes [14]:

$$\{111\}\gamma \parallel \{101\}\alpha' \text{ and } \langle 110 \rangle\gamma \parallel \langle 111 \rangle\alpha'$$

However, low carbon lath martensite also practically obeys the K-S relationship and its habit plane is close to $\{111\}\gamma$ or $\{557\}\gamma$ [16]. Since the 9Ni presents low carbon

content, attention will be paid to the K-S orientation relationship. The 24 K-S possible variants present in Figure 2.1.6 are grouped into four packets, which includes six variants sharing the same $\{110\}\alpha'$ habit plane (i.e. V1 to V6, V7 to V12, V13 to V18, and V19 to V24). The packets are further subdivided into blocks separated by high-angle boundaries that limit the dislocations slip [15]. The microstructure is yet divided into finer structures such as sub-blocks and low angle misoriented laths [17]. It was observed that in low-carbon steels, the sub-blocks have two K-S variants with a misorientation around 10 degrees [15]. The different misorientation characteristics of various boundaries in the lath martensite are expected to affect differently the strength of the lath martensite [26].

Twenty-four variants in K-S relationship

Variant No.	Plane parallel	Direction parallel				Rotation from Variant 1	
		[γ]	\parallel [α']	\parallel [α']	\parallel [α']	Axis (indexed by martensite)	Angle [deg.]
V1		[-1 0 1]	\parallel [-1 -1 1]	\parallel [-1 -1 1]	\parallel [-1 -1 1]	—	—
V2		[-1 0 1]	\parallel [-1 1 -1]	\parallel [-1 1 -1]	\parallel [-1 1 -1]	[0.5774-0.57740.5774]	60.00
V3	(111) γ	[0 1 -1]	\parallel [-1 -1 1]	\parallel [-1 -1 1]	\parallel [-1 -1 1]	[0.0000-0.7071-0.7071]	60.00
V4	\parallel (011) α'	[0 1 -1]	\parallel [-1 1 -1]	\parallel [-1 1 -1]	\parallel [-1 1 -1]	[0.00000.70710.7071]	10.53
V5		[1 -1 0]	\parallel [-1 -1 1]	\parallel [-1 -1 1]	\parallel [-1 -1 1]	[0.00000.70710.7071]	60.00
V6		[1 -1 0]	\parallel [-1 1 -1]	\parallel [-1 1 -1]	\parallel [-1 1 -1]	[0.0000-0.7071-0.7071]	49.47
V7		[1 0 -1]	\parallel [-1 -1 1]	\parallel [-1 -1 1]	\parallel [-1 -1 1]	[-0.5774-0.57740.5774]	49.47
V8		[1 0 -1]	\parallel [-1 1 -1]	\parallel [-1 1 -1]	\parallel [-1 1 -1]	[0.5774-0.57740.5774]	10.53
V9	(1-11) γ	[-1 -1 0]	\parallel [-1 -1 1]	\parallel [-1 -1 1]	\parallel [-1 -1 1]	[-0.18620.76660.6145]	50.51
V10	\parallel (011) α'	[-1 -1 0]	\parallel [-1 1 -1]	\parallel [-1 1 -1]	\parallel [-1 1 -1]	[-0.4904-0.46250.7387]	50.51
V11		[0 1 1]	\parallel [-1 -1 1]	\parallel [-1 -1 1]	\parallel [-1 -1 1]	[0.3543-0.9329-0.0650]	14.88
V12		[0 1 1]	\parallel [-1 1 -1]	\parallel [-1 1 -1]	\parallel [-1 1 -1]	[0.3568-0.71360.6029]	57.21
V13		[0 -1 1]	\parallel [-1 -1 1]	\parallel [-1 -1 1]	\parallel [-1 -1 1]	[0.93290.35430.0650]	14.88
V14		[0 -1 1]	\parallel [-1 1 -1]	\parallel [-1 1 -1]	\parallel [-1 1 -1]	[-0.73870.4625-0.4904]	50.51
V15	(-111) γ	[-1 0 -1]	\parallel [-1 -1 1]	\parallel [-1 -1 1]	\parallel [-1 -1 1]	[-0.2461-0.6278-0.7384]	57.21
V16	\parallel (011) α'	[-1 0 -1]	\parallel [-1 1 -1]	\parallel [-1 1 -1]	\parallel [-1 1 -1]	[0.65890.65890.3628]	20.61
V17		[1 1 0]	\parallel [-1 -1 1]	\parallel [-1 -1 1]	\parallel [-1 -1 1]	[-0.65890.3628-0.6589]	51.73
V18		[1 1 0]	\parallel [-1 1 -1]	\parallel [-1 1 -1]	\parallel [-1 1 -1]	[-0.3022-0.6255-0.7193]	47.11
V19		[-1 1 0]	\parallel [-1 -1 1]	\parallel [-1 -1 1]	\parallel [-1 -1 1]	[-0.61450.1862-0.7666]	50.51
V20		[-1 1 0]	\parallel [-1 1 -1]	\parallel [-1 1 -1]	\parallel [-1 1 -1]	[-0.3568-0.6029-0.7136]	57.21
V21	(11-1) γ	[0 -1 -1]	\parallel [-1 -1 1]	\parallel [-1 -1 1]	\parallel [-1 -1 1]	[0.95510.0000-0.2962]	20.61
V22	\parallel (011) α'	[0 -1 -1]	\parallel [-1 1 -1]	\parallel [-1 1 -1]	\parallel [-1 1 -1]	[-0.71930.3022-0.6255]	47.11
V23		[1 0 1]	\parallel [-1 -1 1]	\parallel [-1 -1 1]	\parallel [-1 -1 1]	[-0.7384-0.24610.6278]	57.21
V24		[1 0 1]	\parallel [-1 1 -1]	\parallel [-1 1 -1]	\parallel [-1 1 -1]	[0.91210.41000.0000]	21.06

Figure 2.1.6: The 24 variants in K-S relationship [15]

Based on the OR approaches, some computer-based statistical attempts from the EBSD data have been done with the purpose of reconstructing the parent austenite grain to better understand the plastic deformation and damage mechanisms for hierarchical structures. Several developments regarding the Parent Phase Reconstruction have led to devoted software, directly integrated in the latest versions of the EBSD data analysis suites from EDAX (TSL OIM) and Oxford Instruments (Aztec Crystal), but also to stand-alone applications such as, ARPGE [27], Merengue2 [28] and the MTEX analysis toolbox in MATLAB [29].

2.1.4 Tempered Martensite

The low toughness of quenched martensitic microstructures is a consequence of several factors that may include the lattice distortion caused by the shearing mechanism with the consequent creation of geometrically necessary dislocations (GNDs) and the high number of interfaces. In the quenched state, the carbon stays dissolved into the martensitic matrix in a supersaturated solid solution, showing high levels of tension. In that case, the tempering process is extremely needed to accommodate the tension, consisted of reheating the sample at temperatures below the A_{c1} , and cooled by air at moderate rates. This heat treatment allows the diffusion of elements and increases the ductility and toughness by coalescing the previous sharp structure due to the migration of dislocations, forming a particular microstructure of tempered martensitic laths. The laths are assembled in parallel inside a block, and those laths are composed of subgrains or recovered cells, with an average size of less than a micron. The laths have low angle boundaries weakly misoriented (less than 3°), the blocks, packets, and prior-austenitic grains have high-angle boundaries (greater than 15°).

2.1.5 Plastic Deformation in Martensitic Steels

Differently from the other family of steels which shows very simple structures, the martensitic steels show a hierarchical and complex structure. In that way, it is very important to understand how this microstructure reacts to the application of stresses.

Morsdorf et al [17] observed that the martensite plasticity is influenced by three combined mechanisms: the topological inclination, the slip system orientation, and microstructure. Those mechanisms are organized in Figure 2.1.7.

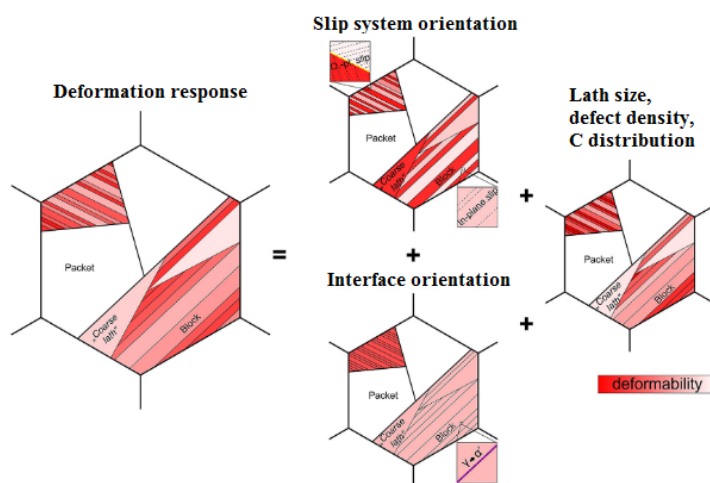


Figure 2.1.7: Representation of deformation mechanisms in lath martensite [17]

According to Du et al [30], the interface plasticity has a bigger contribution than the crystallographic slip during the initial deformation. It means that the initial deformation is governed by two mechanisms, the interfaces of laths oriented to a quasi-perpendicular direction to the load axis with interfacial plane oriented at $\sim 45^\circ$ induces local plasticity and also the strain localized horizontally within the laths oriented at 45° from load axis [17]. In his studies, local strain peak was identified mainly at the high angle block and packet boundaries where there is the existence of dislocation pile-ups. However, strain peaks were also seen in the middle of the blocks, when the best-oriented direction is at 45° from the load axis, having the highest shear stress, thus being able to be activated. It was also observed that the crystallographic orientation of a coarse lath is parallel to shear stress. Inside the best-oriented lath, the dislocations have a free wide path to move along the longitudinal direction. Ohmura et al [31] observed a dislocation absorption at a block boundary by an in-situ indentation in TEM and suggested a boundary sliding mechanism related to the $\{110\}$ nature of martensite interfaces, which naturally corresponds to the dominant slip plane.

The explored mechanisms were described mostly for monotonic tests. The focus of this research, however, is in regards to the fatigue response. The above-described mechanisms of plastic deformation in martensitic steels will provide support for the following investigations that will take place in this study.

2.2 Fatigue

Many equipment and materials are submitted by stresses that vary along the time, i.e. fatigue. Fatigue of materials has been receiving so much attention from researchers and engineers for a long time since this phenomenon is responsible for several failures in equipment. Each cycle of loading introduces damage in the crystal lattice which results in modification in the microstructure and in their mechanical properties. At the very first beginning, the damage seems to be negligible, but its accumulation after each cycle will lead to an inevitable failure of the material. So, in a few words, fatigue is a mechanical failure resulted from cyclic charging at low amplitude stress which is lower than the ultimate tensile strength σ_u but lower or higher than the yield strength σ_y . The applied stress may be axial (tension-compression), flexural (bending), or torsional (twisting).

The fatigue damage is composed of the following stages:

- Stage I-a: Microstructural changes and surface relief
- Stage I-b: Microcrack (or short crack) formation
- Stage I-c: Microcrack coalescence and macrocrack (or long crack) formation
- Stage II: Macrocracks Propagation
- Stage III: Final failure

Except for very high cycle fatigue (VHCF) where crack initiation is subsurface, the initiation stage (Stage I) happens at the surface of the material and provokes irreversible microstructural changes due to repetitive shear stress. It is the most complex stage and needs attention because cumulative damage can be prevented. Plenty of studies are concerned about the stage I-c and II. Even though, it is very useful to study how a crack initiates to better understand the material's life. Stage II occurs when the macrocrack changes its direction and is visible in a perpendicular direction to the tensile stress. The long crack propagates gradually and the crack growth rate depends on the stress intensity factor. Along the fatigue zone, the crack growth creates striations reflecting the blunting of the crack. Stage III or final failure is when the macrocrack reaches a given length, reducing the cross-sectional area of the component, causing the remaining surface to fracture in one tensile loading. It is similar to a fracture in the tensile test. The final fracture zone shows in general a ductile aspect and occasionally brittle, or a mixture of them.

Figure 2.2.1 represents all the fatigue stages.

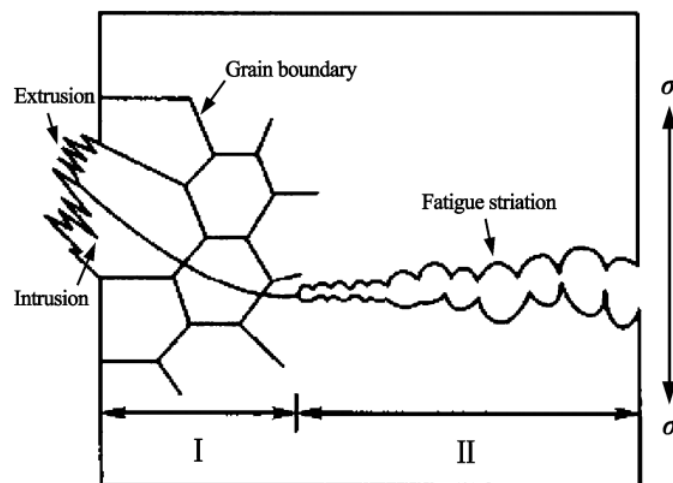


Figure 2.2.1: Fatigue stages [32]

2.2.1 Methods to Assess Fatigue Life

The fatigue analysis is necessary to estimate the material durability, hence is necessary to choose the method for testing the material depending on the solicitations that the component will be submitted. The fatigue life of the material will depend on the environment, the distribution of stresses, and the component geometry. It can be extended by modifying the internal structure, in a way that the cyclic stress response increases. Wöhler has performed experiments in steel specimens and has noticed that the fatigue resistance of the material depends on the stress amplitude (σ_a or S) and the number of cycles to failure (N), creating the S-N curve (Figure 2.2.2). This curve includes three domains:

- Low Cycle Fatigue domain (LCF) - Region I,
- High Cycle Fatigue domain - Region II,
- Very or ultra-high Cycle Fatigue domain (VHCF or UHCF) -Region III

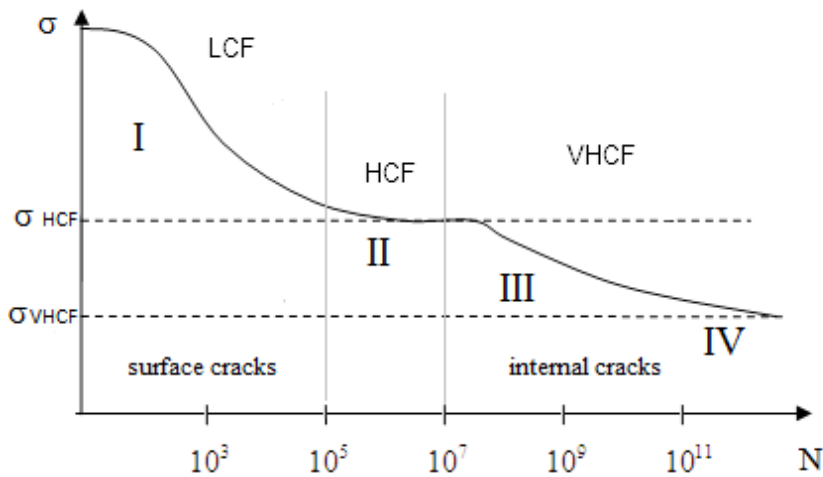


Figure 2.2.2: S-N Curve

In Region I or Coffin–Manson range, the material is stressed over the yield stress σ_y , and the plastic strain controls the fatigue life (Low Cycle Fatigue) [33]. Region II corresponds to the HCF regime, the material is submitted to alternating stress of amplitude σ_a lower than the yield stress σ_y . The material is deformed macroscopically in the elastic domain. The curve presents an asymptotic shape which made believe for a long time that a fatigue limit existed under which the material should exhibit an indefinite fatigue resistance. Thanks to the development of ultra-high frequency loading fatigue machines, it has been shown that this was not the case. It is now admitted that a material

can fail even if the applied stress is lower than the HCF fatigue limit, as depicted by Region III. A second fatigue limit characterizes the performance of the material in the VHCF regime (Region IV). As mentioned above, crack initiation takes place under the surface in VHCF often caused by internal defects or inclusions in the majority of cases while for the other cases, cracks initiate at the surface of the material. [34]. Furthermore, the generally admitted limit for LCF is $N_f = 10^4$ - 10^5 cycles, $10^5 < N_f < 10^7$ for HCF, and above 10^7 for VHCF [35].

2.2.2 Low Cycle Fatigue Test

Because the material is plastically deformed at each cycle in LCF, it is necessary to control the plastic deformation of the specimen and therefore to perform strain-controlled tests. As mentioned previously, the LCF test aims, in addition to the fatigue life measurement, to evaluate the cyclic stress-strain response. The strain control can be done by coupling a strain gauge extensometer on the specimen and by adjusting a predefined waveform. In LCF tests, it is usual to apply a triangular waveform with a mean strain value equal to zero (i.e. a strain ratio $R = \epsilon_{\min} / \epsilon_{\max} = -1$), to fix the strain rate and to change the amplitude from one test to another one. In parallel, the stress necessary to obtain the targeted strain is recorded in the form of stress-strain hysteresis loops as shown in Figure 2.2.3. As may be seen, the shape of the hysteresis loop (σ - ϵ) depends on the material.

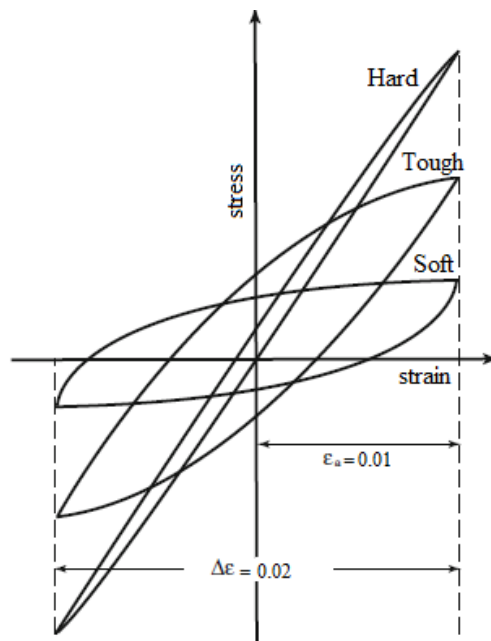


Figure 2.2.3: General Hysteresis Loops for three types of materials [33]

Figure 2.2.4 shows all the data that can be obtained from the hysteresis loop which represents the stress-strain evolution along each cycle, the line O-A-B refers to the first cycle, line C is the discharging part (compression).

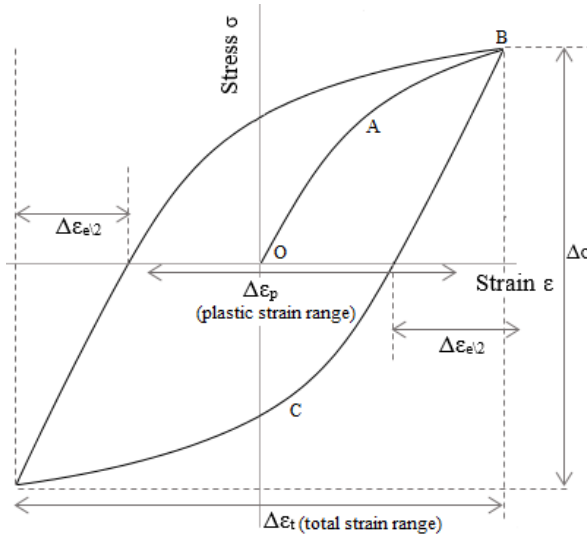


Figure 2.2.4: Hysteresis Loop

2.2.2.1 Fatigue resistance

The LCF resistance is mostly presented in a log-log scale of Strain range ($\Delta\epsilon$) or Strain amplitude ($\Delta\epsilon/2$) versus Number of Cycles to Failure (N_f) or the number of load reversal to failure ($2N_f$). The total strain range ($\Delta\epsilon_t$) is decomposed into the plastic strain range ($\Delta\epsilon_p$) and the elastic strain range ($\Delta\epsilon_e$) and their variation with the number of cycles to failure fit with a linear relationship. The elastic and plastic components of the total strain are measured on the hysteresis loop recorded at fatigue mid-life. According to Basquin, Manson, and Coffin, they can be fitted to a power law as follows:

$$\frac{\Delta\epsilon_t}{2} = \frac{\Delta\epsilon_p}{2} + \frac{\Delta\epsilon_e}{2} = \frac{\sigma_f}{E}(2N_f)^b + \epsilon_f(2N_f)^c \quad (2.1)$$

Where $\Delta\epsilon_t/2$, $\Delta\epsilon_p/2$, and $\Delta\epsilon_e/2$ are the total, plastic and elastic strain amplitudes, respectively. $2N_f$ is the Number of load reversals to failure, σ_f the fatigue strength coefficient, E the Young's modulus, ϵ_f the fatigue ductility coefficient, b the fatigue strength exponent, and c the fatigue ductility exponent [36]. Figure 2.2.5 displays a typical Basquin and Manson-Coffin curve.

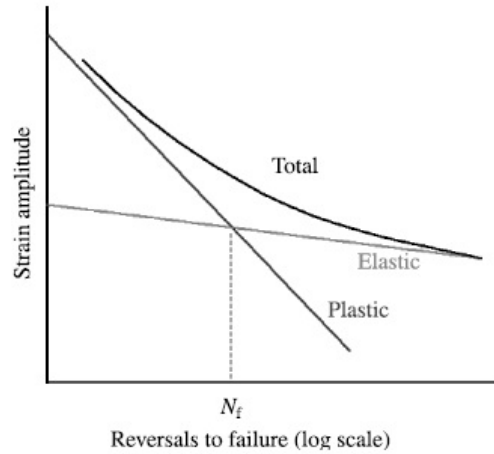


Figure 2.2.5: Typical Basquin and Manson-Coffin curves

2.2.2.2 Cyclic accommodation

During the fatigue test, materials can have different stress-strain responses. One of these is cyclic softening, where the stress needed to deform the material decreases with subsequent cycles. This response is typical for hard materials rich in dislocations. During the very first cycles, the available dislocations move more or less easily, annihilating or rearranging, and stress levels drop as the material is cycled. The opposite behavior is seen for materials that initially have low dislocation density. In this case, during the plastic straining, an augmentation in dislocation density will occur, showing stress strengthening, known as hardening. In general, cyclic softening and cyclic hardening tend to settle, leading to a period of stress stabilization. Besides, other responses are possible, such as cyclic hardening followed by cyclic softening and stabilization; cyclic hardening with subsequent stabilization period followed by secondary cyclic hardening; cyclic hardening followed by cyclic softening and then secondary cyclic hardening.

The interaction between dislocations leads to annihilation or their multiplication. Regarding martensitic steels, the annihilation rate is higher than multiplication, generating a cyclic softening [9]. The annihilation or production of dislocations followed by migration and production of point defects leads to the formation of low-energy dislocation configurations. The volume expansion of the low energy dislocation arrangement is responsible for cyclic softening [37]. The softening stage in 9–12%Cr steels and reduced-activation ferritic/martensitic steels is visibly related to the volume increase of the subgrains, due to the disappearance of low angle boundaries dislocations [38]. The presence of cyclic softening in martensitic steels has been related to the removal of laths and subgrain boundaries, the annihilation of dislocations inside the subgrains, and can be also linked to the localization of the cyclic strain into softer Persistent Slip Bands (PSBs) [9, 39–41].

2.2.3 Low Energy Dislocation Structures Produced by Cyclic Deformation

The deformation in the material brings two forms of dislocations: Geometrically Necessary Dislocations (GND) and Statistically Stored Dislocations (SSD). The GND regions show a crystallographic orientation, while in the SSD regions the overall Burger's vector is near zero [9]. Dislocation rearrangements occur during cyclic loading. Screw dislocations cross slip and annihilate each other while the edge dislocations set up themselves in clusters of vacancy or interstitial dipole loops. During the cyclic deformation, the positive and negative edge dislocations attract each other and annihilate, creating numerous vacancies [42].

Continuing the cyclic loading, the dislocation arrangement can no longer accommodate the imposed plastic strain, transforming the dislocation substructure into a softer lamella of a PSB, usually composed of a ladder-like structure. Ladder structures can support substantial plastic strain in the adjacent elastic matrix generating surface relief and crack initiation [37]. At higher values of plastic strain, the dislocations arrange themselves into a cell structure [43]. The term fatigue cell and subgrain occasionally lead to some confusion, because sometimes they are hard to be differentiated. The fatigue cells are created by the dislocation activity from several crystallographic planes during the cyclic plastic deformation, resulting in small almost equiaxed volumes separated by dislocation walls having a small angle of misorientation [38, 44]. The subgrains have misorientation angles with less than 5° , their origin is from thermal treatment or intense deformation during the fatigue test, being a subsequent step of the deformation process, where the dislocations are annihilated within the cells.

In the case of LCF, plasticity is induced in each cycle. On the course of the cycling, the defects are generated due to dislocation multiplication. The increase in dislocation density forces them to organize in a way that they can minimize the total energy of the system, creating an easy slip path for the mobile dislocations [45]. For bcc materials, the screw dislocation mobility is temperature dependent and the transition temperature of the regime depends on strain rate. In the regime called high temperature, sufficient thermal activation is available, so the screw dislocations can glide easily, reducing the yield stress. In this regime, the bcc material has similar behavior to the fcc materials [37, 43].

The dislocation response is very dependent on the temperature, slip character, and applied strain amplitude [8]. Diverse dislocation patterns would form at different fatigue cycles or in different materials, the major common point is that they assemble spatially

as alternate dislocation dense regions and dislocation-poor regions. The existence of each structure represents a transition from one stage to the next in the cyclic stress vs. strain curve (CSS), the CSS curve of a bcc steel is shown in Figure 2.2.6.

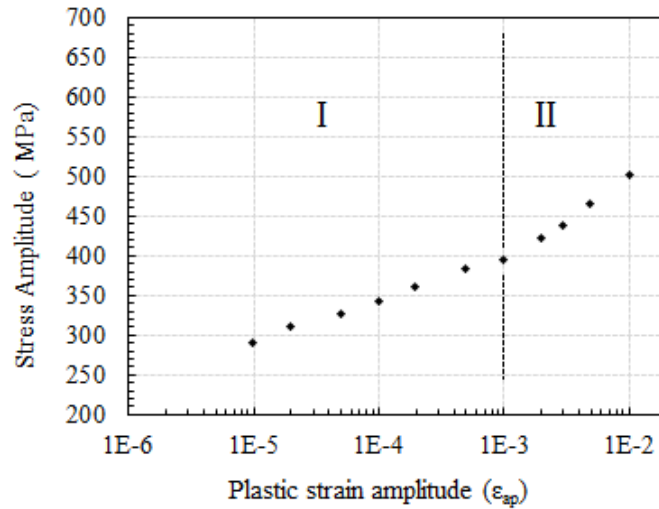


Figure 2.2.6: Cyclic stress strain curve for bcc X10CrAl24 steel [37]

Some structures obey a hierarchy of dislocation arrangement [46], the following dislocation patterns are mostly found on easy cross slip materials (fcc structure) such as copper and nickel but also have been observed in bcc metals and low-carbon steels [37, 47, 48]. In this case, the CSS curve was divided into two regions due to different slopes of the plotted curve, the dislocation patterns found will be adopted as the most probable to exist in martensitic steels.

At the lowest plastic strain in Regime I (5×10^{-5} strain amplitude or 0.01% strain range), planar arrays of edge dislocations on the primary slip plane are mostly present, the dislocations are arranged as thin sheets separated by dislocation-free layers (Figure 2.2.7). The vein structure was also found present in the matrix even though less frequent, this arrangement is consisted of bundles of edge dislocation loops and channels with low-density mobile screw dislocations [43].

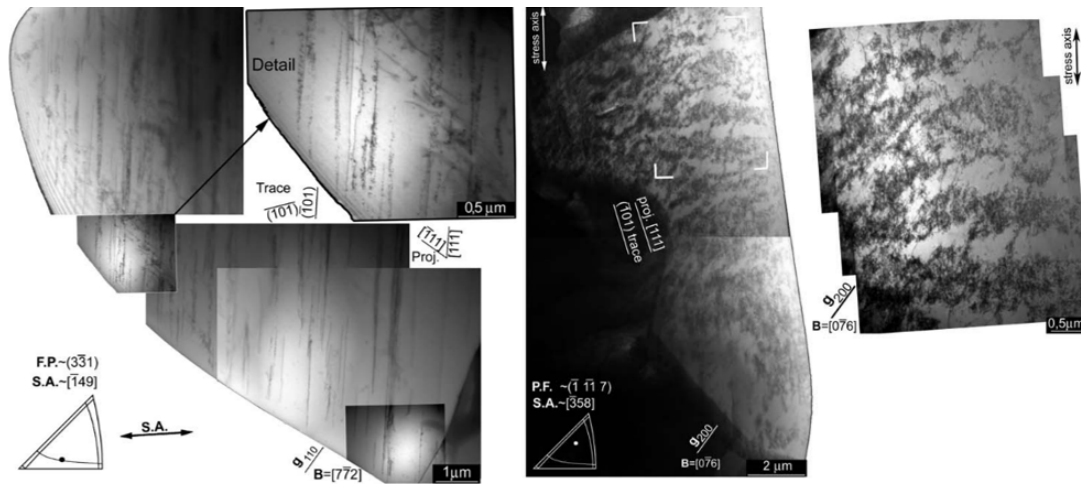


Figure 2.2.7: Planar and vein dislocation pattern in bcc X10CrAl24 steel at 5×10^{-5} strain amplitude (0.01% strain range) [37]

In Regime II, at 2×10^{-3} plastic strain amplitude (0.4% strain range) the dominant dislocations arrangements are wall structures (ladders, walls, and labyrinths) produced by the interaction of dislocations from two slips systems (Figure 2.2.8) [49]. The labyrinth configuration is formed when the second glide system is activated.

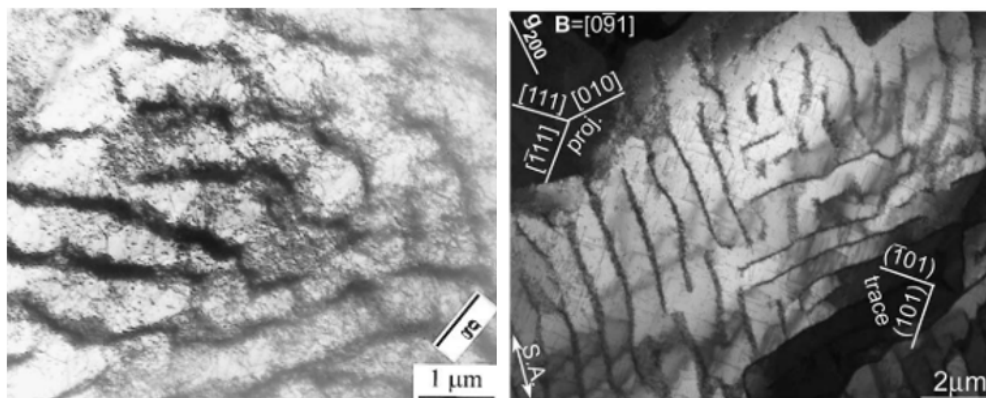


Figure 2.2.8: (left) Wall structure in bcc X10CrAl24 steel at 0.1% strain range (10^{-3} strain amplitude) and (right) labyrinth structure found at 0.4% strain range [37, 49]

Still in Regime II, at very high strain amplitudes 5×10^{-3} (1% strain range), the dislocations are assembled as a mixture of cells and walls. The cell configuration has the lowest energy, consisted of rich-dislocation boundaries and a nearly-dislocation-free interior. The cells accommodate the plasticity by the dislocation glide from their boundaries, this type of structure is very common in martensitic steels (Figure 2.2.9).

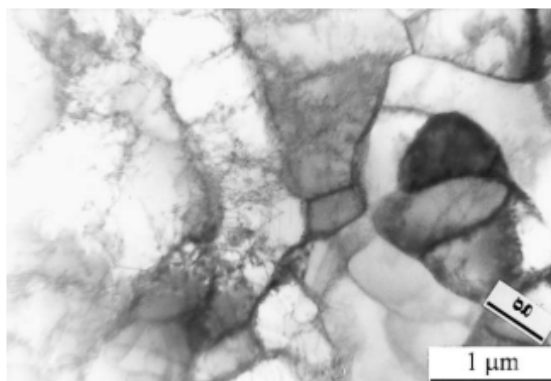


Figure 2.2.9: Cell structure in bcc X10CrAl24 steel at 1% strain range (5×10^{-3} strain amplitude $g = [010]$) [49]

It is already known that PSBs in fcc metals typically have a ladder structure at the end of fatigue life. For bcc metals, it was found that the PSBs consist of walls, cells, or dislocation poor channels. However, ladder-like structures were also reported when the material is cycled at medium strain levels (0.02% and 0.4% strain range) (Figure 2.2.10) [37].

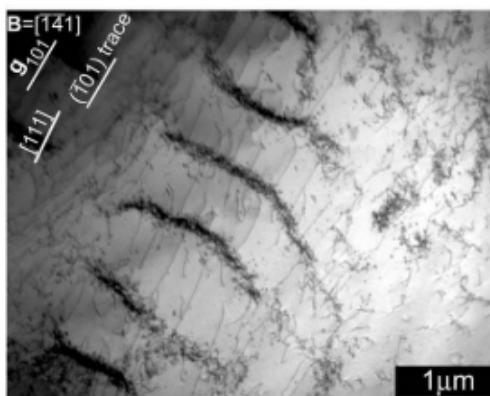


Figure 2.2.10: Ladder-like dislocation pattern in bcc X10CrAl24 steel cycled at 2×10^{-3} strain amplitude (0.4% strain range) [37]

The PSBs in polycrystals are not a bulk property like is commonly observed in single crystals. According to some observations, the dislocation substructure is different from the areas adjacent to the surface and the inner part of the material, the most dominant configurations are cells, subgrains, and labyrinth [47, 50]. Surface strain hardening is more evident, allowing the formation of these refined structures, caused by the loss of mobile edge dislocations that emerge at the surface causing secondary slip [43]. Although, there is no consensus about this evidence [51]. In the case of martensitic steels, it was pointed out that the laths can act themselves as a PSB, so no specific dislocation configuration is always seen at the vicinity of the Persistent Slip Marks (PSMs) [9, 30].

2.2.4 Surface Relief

The evidence of relief originated on the surface of cyclically strained crystalline materials has been remarked and attracts the attention of researchers for over 100 years. Those surface marks are evidence of the first signs of fatigue damage, being able to develop into fatigue cracks [7]. Studies of the nature of fatigue damage evolution started by Ewing and Humfrey [52], they observed a formation of surface marks after cycling the material. Afterward, the development of first-stage fatigue evidence characterization was done concerning extrusions, intrusions, and PSBs. The first sign of fatigue damage is now known as PSMs that are seen as a pronounced surface relief. Thompson, Wadsworth, and Louat were responsible to discover this phenomenon, revealing that the bands formed at the surface remain in the same position even after polishing [53]. The PSMs comprise the intrusions and extrusions, they develop at surface parallel to low index crystallographic planes [54], resulting from emerging PSBs with irreversible slip activity (dislocation movement) and they are the precursors of the fatigue crack.

The PSMs, very thin at the beginning of straining, widens progressively at early fatigue cycles. In his studies, Polák [55] confirms that the width of extrusions stabilizes very early and after this, they remain unchanged. The thin intrusions begin to develop sometimes parallel to the extrusions at about 1% of the fatigue life. As the number of cycles increases, the amount of PSMs accompanied by one or two parallel intrusions gets bigger. Parallel to this event, the intrusions deepen at a higher rate than the growth of the extrusions. According to reviews of Polák and Man [7] for 316L steel, at 15% of the fatigue life an amount of 87% of PSMs is composed of a wide extrusion paired with two thin intrusions, some of them already transformed into small cracks. Fatigue cracks preferably start from PSMs and continue growing along the PSM/matrix interface.

2.2.5 Shape of Extrusions

The shape of PSM is influenced by the grain size, strain amplitude, and temperature [7]. Some observations have taken into account that the intrusions are rarely found isolated, except for single crystals [56]. The intrusions are normally present on the side of the extrusions but sometimes they are not present, only extrusions were seen. Individual PSMs are observed both in the grain interiors and at the grain boundaries, and consist of ribbon-like extrusions often accompanied by parallel intrusions. Embryonic PSMs, consisting of alternating elevations and depressions, usually start in the middle of the grain and develop later into tongue-like extrusions and intrusion. The type of the activated slip system and its Schmid Factor influences the morphology of extrusions and intrusions [57].

There are several types of extrusions according to the literature, the concepts are well developed for monocrystalline [42, 56, 58–64] and polycrystalline aluminum and copper [54, 65–69]. Likewise, there are studies of ferritic [70, 71], austenitic [54, 72], and duplex steels [73–78]. On the other hand, there are only a few investigations concerning martensitic steels [9, 79]. The morphology of PSMs (Figure 2.2.11) diverges from single crystals and polycrystals. According to Polák [69], the macro-PSMs (protrusions or superimposed individual extrusions and intrusions) are usually found in single crystals. However, the individual PSMs are both observed in single and polycrystals. Individual PSMs comprise tongue-like extrusions alternating with intrusions (which are mainly at embryonic stages) and ribbon-like extrusions accompanied by intrusions on their side. Other definitions derive from those established for individual extrusions in fcc structure, such as band-like and cord-like [9, 76, 80]. The band-like extrusion is more similar to the ribbon-like extrusion, but it is less prominent. Moreover, the cord-like is more curved and comparable to the tongue-like extrusion. Despite presenting different microstructures, the shape of extrusions could be correlated and similarities were found to the ones observed by AFM technique in 12Cr martensitic steel [9].

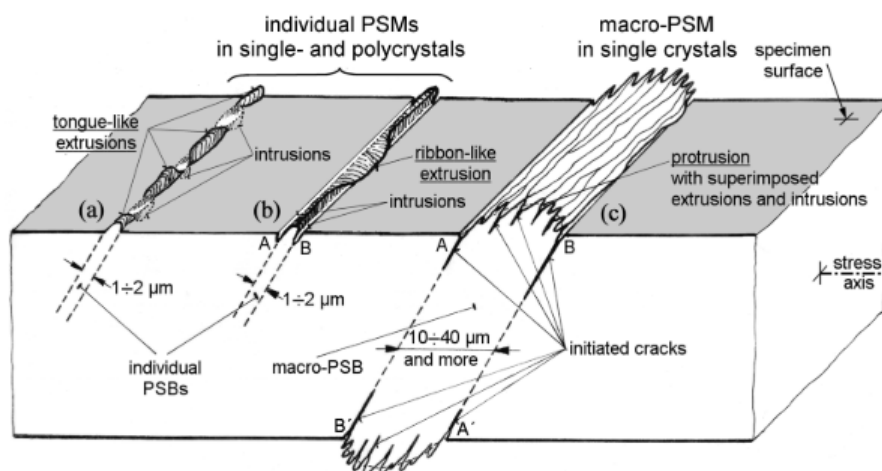


Figure 2.2.11: Persistent slips marks morphologies in fcc metals [69]

2.2.6 PSMs Visualization Techniques

Mughrabi et al [6] have identified that the PSBs are oriented at 45° to the load axis. This happens because the maximum critical resolved shear stress (CRSS) of a single crystal is at 45° from the load axis, having the maximum Schmid Factor. For polycrystals, when the grains are randomly oriented, PSM can be seen in a range of 20° to 60° from the load axis [81]. Extrusions and intrusions were usually studied by tapping methods, such as atomic force microscopy [9, 71] or using plastic replicas [54, 82]. Those techniques helped to catalog and differentiate the morphology of the extrusions and intrusions. Microscopy

techniques, such as SEM, TEM, and FIB milling allow an accurate visualization of the shape of the PSMs. A more detailed explanation about these techniques will be given in the Methodology section of this manuscript.

The PSM topography has been studied lately by SEM techniques, yet the SEM images miss the 3D information. SEM can image fine details of individual PSMs, mainly in polycrystals, with high resolution. The major problem for imaging the PSMs is that the perpendicular beam often misses some details, the extrusions can sometimes hide the intrusions beneath them due to the inclination. Tilting the sample is one of the solutions to this problem.

The Atomic Force Microscope (AFM) allows a quantitative study of the surface. Performing a scanning over the surface, by using a sharp stylus, the AFM is capable of imaging samples with a submicron lateral resolution and a sub nano vertical resolution [83]. Surface observation by AFM shows well the height of extrusions, but not the true shape due to the lateral resolution. The AFM tip does not detect as well the thin intrusions by observing the metallic surface as demonstrated in Figure 2.2.12, the use of plastic replicas was adopted but still lead to exaggeration of the dimensions of extrusions-intrusions.

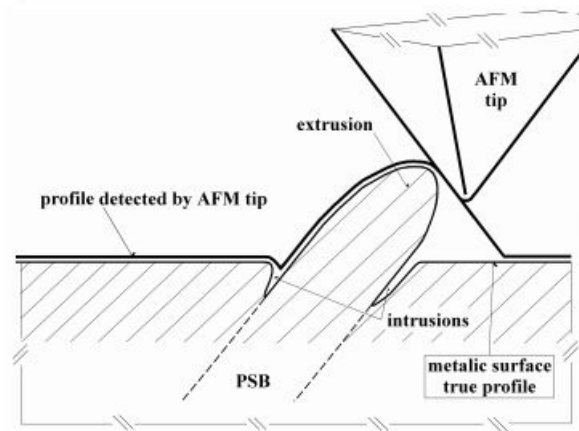


Figure 2.2.12: Extrusion profiles detected by AFM tip in austenitic steel [84]

Still, the combination of AFM and EBSD is very useful to make correlations of topography and crystallographic aspects of fatigue damage, providing 3D topographic images of the PSMs [9]. However, the scanned area by this technique is very restricted to a $100\ \mu\text{m} \times 100\ \mu\text{m}$ maximum size and the time for scanning is a limiting factor. To overcome those limitations, the Scanning White-light Interferometric Microscope (SWLI) appears as a feasible technique by using an incoherent light source, i.e. a white light, being capable to provide a non-contact 3D surface profile of the specimen. Compared to an AFM, an SWLI has a similar vertical resolution [85].

Among all the presented techniques, the best method to exhibit the true shape of PSMs is the cross-sectional view, but it is a destructive method. Some attempts were done with single crystals by making fine cutting or edge polishing [61]. Some authors have already performed the edge view for monocrystalline copper [56, 63, 86]. Two sophisticated techniques showed good results for monocrystalline materials, the micro-milling sectioning developed by Hunsche and Neumann [61] and sharp-corner polishing developed from Basinski and Basinski [62]. In the case of steels, there are some obstacles added to the procedure, which currently impossibilities some advance for a bigger profile view. In this context, the most applicable method for obtaining good results with polycrystals at this moment is the cross-sectioning technique using FIB milling and visualization by high-resolution SEM and TEM techniques [9, 54, 87–89] as represented in Figure 2.2.13 and Figure 2.2.14.

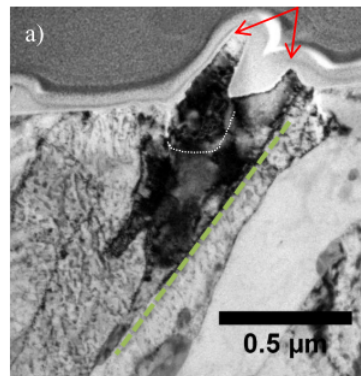


Figure 2.2.13: TEM-FIB cross sections of 12Cr steel [9]

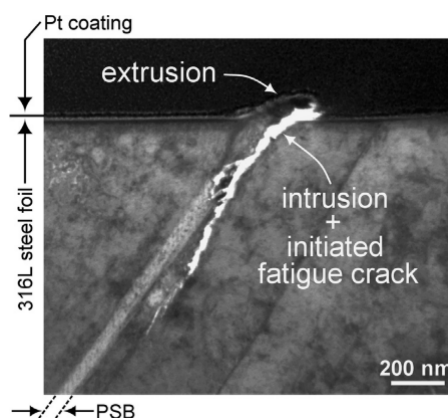


Figure 2.2.14: TEM of FIB foil covered by Pt, the sample was cut from the surface of 316L steel [90]

2.2.7 Fatigue Surface Relief Models

The development of the internal dislocation configuration contributes significantly to the fatigue crack initiation and in the same way for short crack growth. Several studies were proposed concerning the initiation of fatigue microcracks, the vacancy model considers the dislocation structure of the whole PSB, and the embryo cracks are related to vacancies.

The EGM is one of the vacancies models, founded on vacancies and their agglomerates produced by a non-conservative jog and opposite edge-dislocation annihilation. It was proposed by Essmann, Gösele, and Mughrabi [69], which is based on steady-state cyclic deformation in PSBs. This and other models of surface relief formation based on vacancies involve a temperature dependence, once the vacancy diffusion is a thermally-activated movement. This model explains the formation of high-density vacancy-type point defects within the walls of the ladder dislocation structure of PSBs as a result of dislocation interactions.

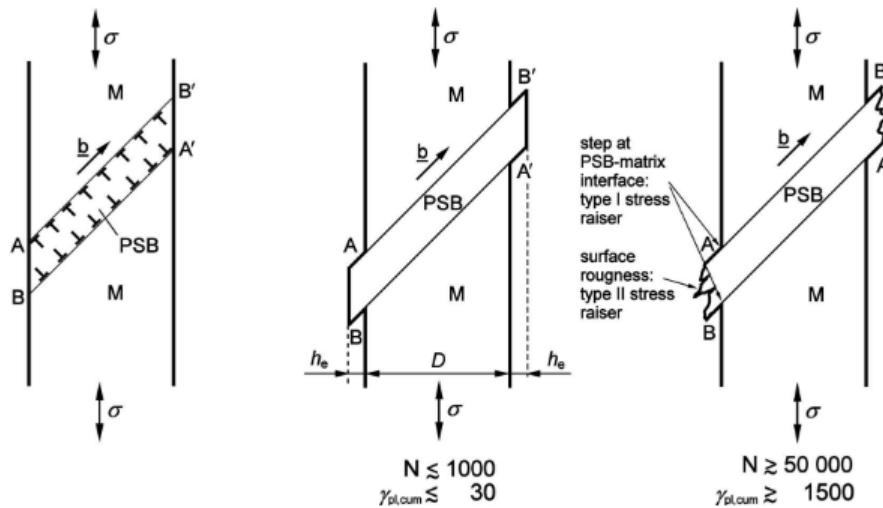


Figure 2.2.15: EGM-model of PSB surface profile formation [54]

Under an applied stress σ , the interface dislocations slide out of the crystal at A-A' when under tension and at B-B' during the compressive part of the fatigue cycle, as displayed in Figure 2.2.15. The vacancies that were originated in the dislocation walls cause the volume expansion of the PSB, this volume expansion increases the concentration of interface dislocation, their movement of slipping out of the PSB results in the elongation of the PSB lamella, developing a static extrusion. The additional volume of the extrusion formed on the surface is exactly the same volume produced by the increase of vacancy concentration in the PSB [7].

Polák [91] proposed an extension of the EGM model. Both models have been developed based on monocrystalline fcc copper, later they were extended to polycrystalline fcc materials. Polak's model also considers the dislocation arrangement, but the point defects are expected to be generated along the whole volume of PSB, both in the dislocation-rich walls and dislocation-poor channels. The vacancies are expected to distribute themselves homogeneously along the PSB-matrix interface with no agglomeration. Vacancies are created when vacancy-like dislocation dipoles are formed within the PSB. Their diffusion to the PSB-matrix interface which has a lower vacancy density forces a material flux into the PSB, leading to a volume increase [92]. The PSM appearance is based on matter redistribution inside the PSBs and at the interface PSB/matrix. The most important point of this model is that it considers the temperature dependence of point defects mobility. Vacancies produced at room temperature migrates from the channels to the matrix and annihilate when met edge dislocations, causing a constant mass redistribution between the PSB and the matrix (accumulation of mass in the channels and a reduction in the walls). This mass redistribution puts the inner part of PSB under compression stress and the adjacent thin-layer matrix under internal tension, those stresses increase with the number of cycles. The built-up due to this mass redistribution can be relaxed only in the loading direction of the specimen, thus creating the extrusions emergence at the surface where the channels are localized and an intrusion formation where the walls are present (Figure 2.2.17).

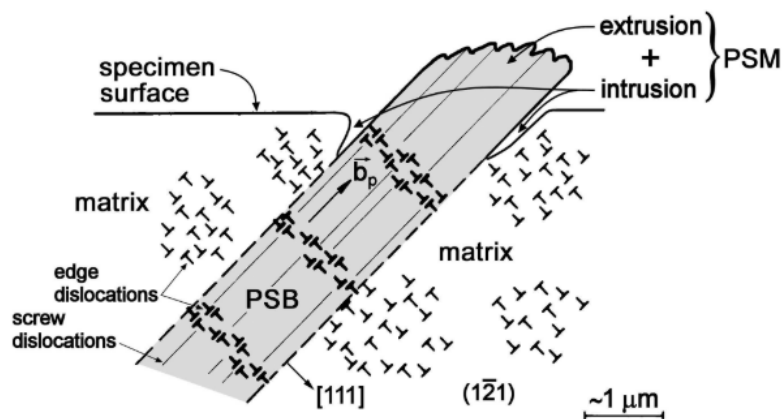


Figure 2.2.16: Representation of dislocation arrangement of a Persistent Slip Mark [54]

The relaxation of the means stress in the matrix is not as easy as it is in PSB. While the PSB deforms plastically, the matrix deforms only elastically since the critical yield stress of the PSB is lower than the matrix [7].

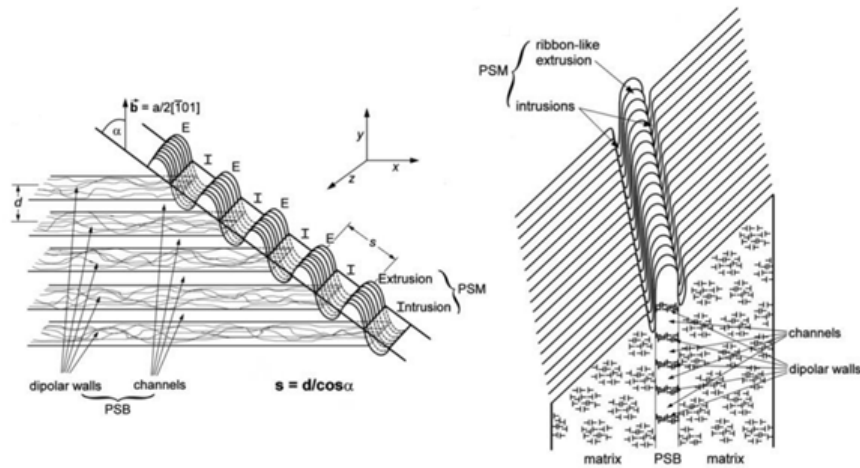


Figure 2.2.17: Polak's model of surface relief formation and surface profile of a PSM when point defects move back and forward from the PSB to the matrix [54]

The production of interstitial-type defects by the annihilation of edge dislocations brings to an intrusion and they are crack-like defects from which fatigue cracks can initiate. The vacancies can be formed by the interaction of positive and negative edge dislocations, abundant vacancies will then concentrate leading to micro-crack formation, which will then grow into fatigue cracks. In a few words, there are two basic mechanisms in charge of the formation of a row of point defects [82]:

1. The annihilation of two edge dislocations with opposite Burgers vector moving in the adjacent plane;
2. Movement of a jog on a screw dislocation inside the channel;

Mughrabi [93] emphasizes that at the very first cycles only the extrusions are formed. The intrusions appear only after few cycles, in a less evident dimension than the extrusions. It was discussed that the intrusions in fact do not develop by the same mechanism as the extrusions and they are not usually formed in parallel pairs to the extrusions, as proposed by Polák. The intrusions are in less quantity and they are frequently present at the side of the extrusion that the emerging active slip plane is inclined to surface in acute angle and this interface is preferable to form cracks. In other words, the intrusions develop as a result of the extrusions already formed and they are actually in the embryonic stage I shear cracks. Polák stated that the alleviation of the tensile internal stresses in the matrix happens only when they reach a value equal to the difference of yield stress of the matrix and the PSB, developing a delayed intrusion [7].

2.2.8 Crack nucleation

As already mentioned, during the cyclic loading, dislocation configurations strongly depend on imposed plastic strain amplitude, temperature and interstitial content. For martensitic steels, the plastic deformation which emerges during cycling is related to the $\{110\}$ slip system [17]. When the K-S relationships are fulfilled, the slip bands easily cross the phase boundaries. When there is no correlation between the phases, microcracks initiate at the slip band and converges into the phase boundary. The mechanism of strain accommodation in bcc metals might be noticeable by slip plane asymmetry or the formation of slip bands. The slip plane asymmetry is more frequently encountered in pure bcc structures while the commercial alloys present the formation of slip bands [81].

PSBs are the major factor in crack initiation, there are other mechanisms of crack propagation when the PSBs are not observed, below are described the principal sites of crack nucleation [48]:

- Slip Bands provoke localization of cyclic slip resulting in irregularities at the surface.
- Grain and twin boundaries (HAB), in the case of martensitic steels, fatigue site nucleation were also identified at laths and blocks boundaries (LAB) [9, 94].
- Initiation at heterogeneities at the metals, like inclusions and pores.

2.3 9Ni steel

Low carbon cryogenic steels are used for gas storage and transport, because of their excellent mechanical properties and good toughness at low temperatures. The 9Ni steel is included in the group of cryogenic structural steels and it is largely applied in the construction of natural gas storage according to American Society of Mechanical Engineers specifications (ASME). The 9Ni steel is used in the construction of gas pressure vessels of 50,000 m³ submitted to thermal fatigue without the necessity of tension alleviation after welding, being used as an alternative to stainless steels. This steel is indicated for storage of oxygen (-183 °C), argon (-186°C), nitrogen (-196 °C) and natural gas (-163 °C) [95]. The EN 10028-4 X8Ni9 and ASTM A333 standards specify the chemical composition of the 9Ni steel, as listed in Table 2.3.1.

Table 2.3.1: Chemical composition specifications according to ASTM A333 Gr.8 and EN 10028-4 standards

	Mass percentage %							
	C	Mn	P	S	Si	Ni	Mo	V
ASTM	≤0.13	≤0.9	≤0.035	≤0.04	0.15-0.3	8.5-9.5	-	-
EN 10028-4	≤0.13	0,3-0,8	≤0,020	≤0,005	≤0,35	8,5-10,0	≤0,10	≤0,05

The addition of nickel into the alloys is related to the interest of its good corrosion resistance and the ability to increase the resistance to brittle fracture, stabilizing the austenite, in this case, called reversed austenite. More details concerning the reversed austenite will be discussed in the *2.3.3 Reversed Austenite* section. The nickel element does not form carbide or nitrides, staying in a substitutional solid solution. Some studies pointed out that the presence of reversed austenite formed during the heat treatment influences the high toughness at cryogenic temperatures [96–101]. The nickel element contributes to the formation of bainitic and martensitic microstructures with high toughness, when it is in solid solution it can facilitate the dislocation formation at lower temperatures, ameliorating the relationship between the stress and the structure cohesion, increasing the metal strength [22, 102]. According to previous studies [3, 99, 103, 104], the presence of a “duplex microstructure” can promote a combination of toughness and mechanical resistance, delaying the fatigue crack propagation. After the heat treatment, the reversed austenite indirectly influences the impact strength by forcing the carbides to stay in a solid solution, preventing the formation of embrittling carbides and nitrides [4].

The 9Ni steel was primarily developed by the International Nickel Company in 1942. The 9Ni steel does not show a ductile-brittle transition temperature. Figure 2.3.1 demonstrates the relation between the nickel content and the energy absorbed at a significant temperature interval.

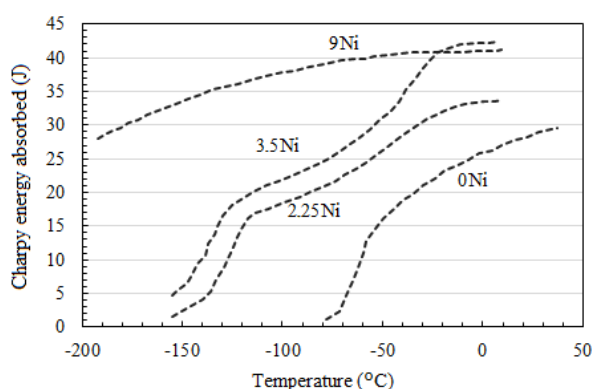


Figure 2.3.1: Effect of nickel content on impact toughness (adapted) [105]

2.3.1 Heat Treatment

Structural ferritic steels fabricated to work at cryogenic temperatures are thermally processed to reduce the ductile-brittle transition temperature to lower values than the working temperature. In the case of 9Ni steel, the heat treatment involves an intercritical tempering in a temperature that comprises the $\alpha + \gamma$ region in the phase diagram, ranging from 570 to 630°C (specifically between Ac1 and Ac3). Several investigations showed that heat treatment has an important impact on the mechanical properties of 9Ni steel [98, 99, 101, 106–108]. Frequently, normalizing and tempering thermal treatments are carried out to increase toughness and ductility. There are two specifications for producing the 9Ni steels:

- ASTM A353 - Standard Specification for Pressure Vessel Plates, Alloy Steel, Double-Normalized and Tempered 9Nickel;
- ASTM A553 - Standard Specification for Pressure Vessel Plates, Alloy Steel, Quenched and Tempered 7, 8, and 9Nickel;

The hardness values for both heat treatments are quite the same, ranging between 200 and 255 Brinell at room temperature [105]. Figure 2.3.2 summarizes all the heat treatments commonly adopted for the 9Ni steel in the industry, comprising the ASTM A353 and A553 standards, and the Quenching intercritical tempering (QIT), which is frequently found in the literature. The latter is consisted of the quenching, intercritical quenching, and tempering treatments and it is also referred to as the quenching, lamellarizing, and tempering (QLT) process. In this work, the heat treatment according to the ASTM A553 will be adopted (Quenching + Tempering).

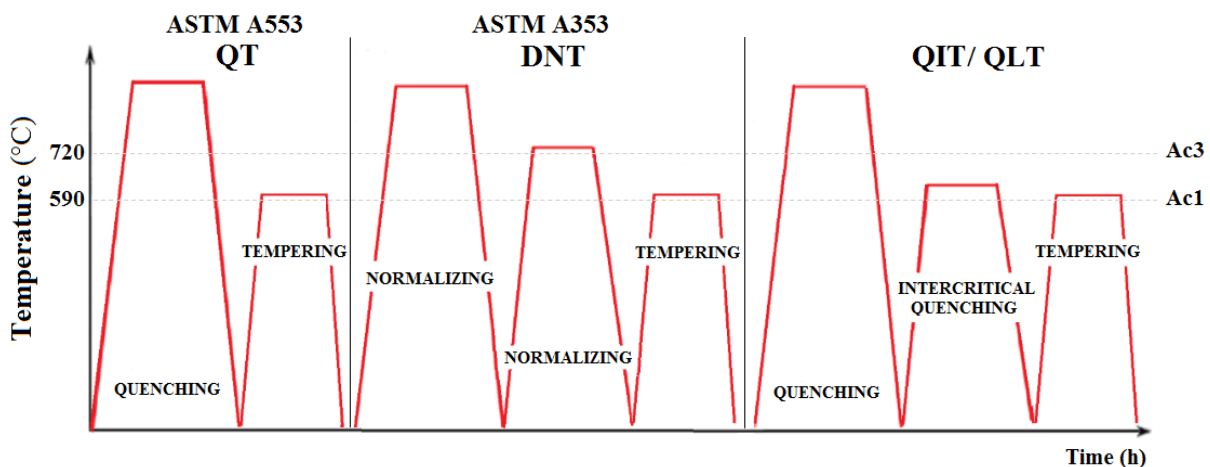


Figure 2.3.2: Thermal heat treatments existent for 9Ni steel [109]

As nickel is the principal alloying element, the binary Fe-Ni phase diagram (Figure 2.3.3) is useful to comprehend the 9Ni steel phase transformations, once the carbon content is low (≤ 0.13 wt.pct). As can be observed, the nickel element lowers the Ac1 temperature compared to the Fe-C diagram, the red line indicates the position at the diagram where the 9Ni steel lies. This element is also responsible for lowering the Ms temperature, this allows bainite to become present at lower temperatures as the Ni content increases.

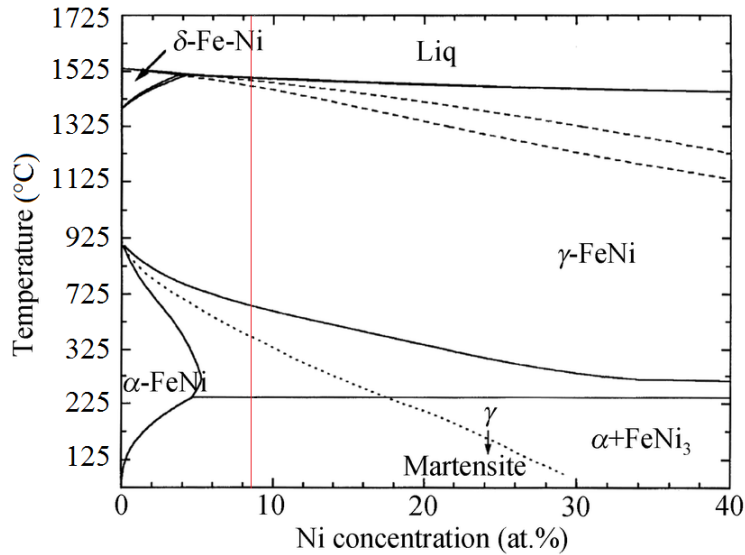


Figure 2.3.3: Iron-nickel phase diagram (adapted) [110]

The CCT diagram is useful to predict the phase transformations that can occur during the cooling at different rates. As can be observed on the CCT diagram of 9Ni steel (Figure 2.3.4), the microstructure of heat-treated 9Ni steel contains bainite, martensite, stable carbide, and manganese + nickel-rich austenite depending on the cooling rate. When submitted to tempering heat treatment at temperatures between 377 °C and 540 °C and during a long time, the 9Ni may suffer irreversible tempering embrittlement. This is attributed to the austenite instability that would be transformed into martensite upon cooling [4, 97, 111].

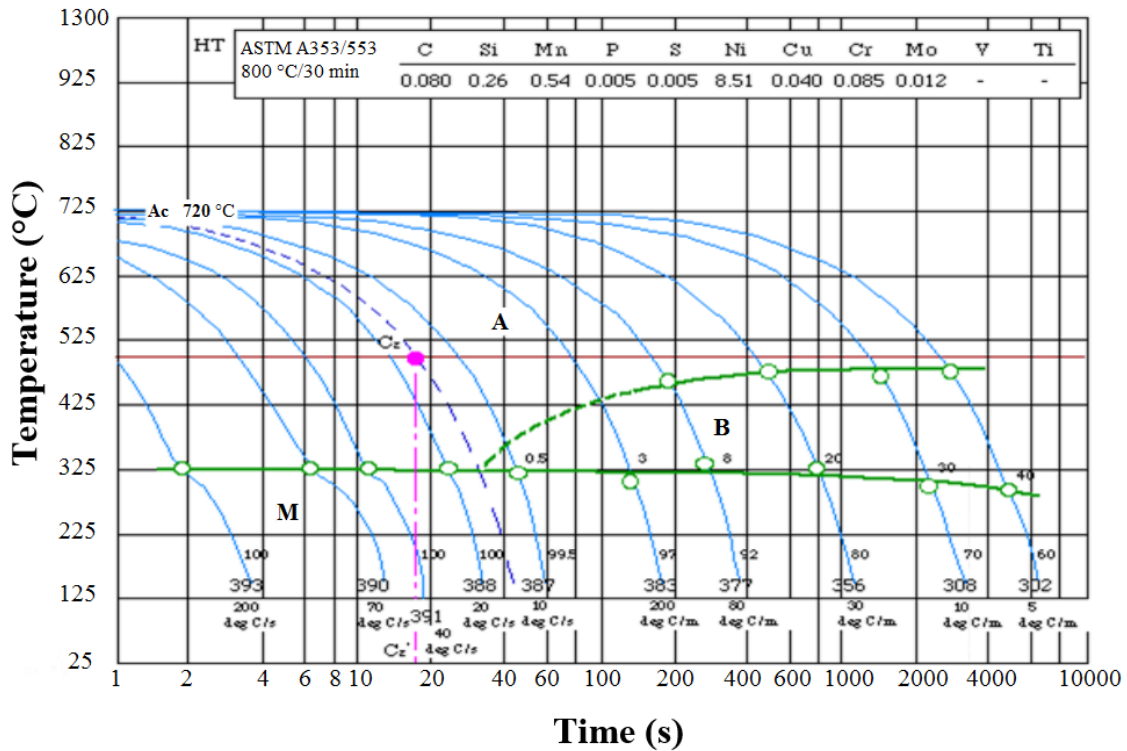


Figure 2.3.4: Continuous Cooling Temperature diagram for 8.5Ni steel (adapted) [109]

Current studies related to martensitic transformation in steels done by Maresca et al [112] have indicated that the transformation is never completely achieved and is influenced by the chemical composition of the alloy. Retained austenite segregated in the form of very thin films may be present after quenching at room temperature [112, 113]. In some cases, this austenitic phase may be undesirable because it can transform into a brittle form of martensite, causing premature failure of components. To avoid the presence of retained austenite, the steel must be cooled to temperatures below zero degrees Celsius, which sometimes is an unfeasible procedure. As a result, interlath austenite films may be retained after cooling to room temperature.

2.3.2 Microstructure of Quenched and Tempered 9Ni steel

After re-heating the sample for stress relieving, the zones containing very thin dispersed interlath films will be the sites for reversed austenite nucleation. Studies have shown that the amount and the stability of the reversed austenite depend on the time and temperature of the tempering heat treatment [2, 20, 101, 114]. As already mentioned, the quenching heat treatment consists of an austenitization above the Ac3 temperature and rapid water cooling. The Scanning Electron Microscopy (SEM) and optical micrographs of the quenched microstructure of 9Ni steel (Figure 2.3.5) show a typical lath-martensitic structure. The white parts characterized by Energy Dispersive X-Ray Spectroscopy

(EDS) are slightly concentrated in nickel and manganese elements. Transmission Electron Microscopy (TEM) images show the dislocation-rich martensite laths with more details (Figure 2.3.6).

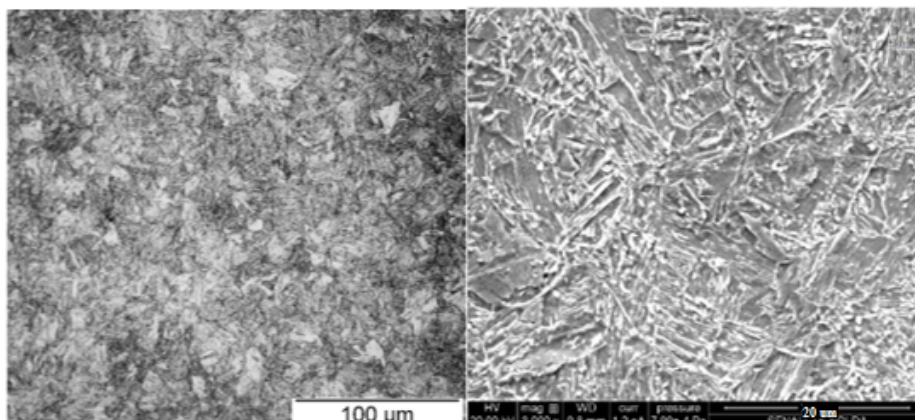


Figure 2.3.5: Optical and SEM microstructure of Quenched 9Ni steel [109]

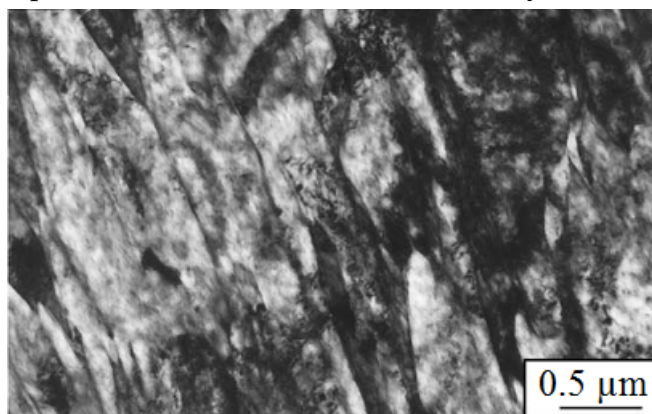


Figure 2.3.6: Transmission electron microscopy image from Quenched 9Ni steel [115]

Advanced techniques such as EBSD can distinguish between the fcc austenite and the bcc martensitic matrix present in the 9Ni steel after the complete heat treatment, as it is frequently done with similar dual-phase steels [116–121]. The EBSD data is displayed in Figure 2.3.7, under the same QIT treatment. The microsegregation bands are indicated by red arrows in the optical image (Figure 2.3.7-a), the yellow arrows point to the martensitic phase, the amount of reversed austenite measured by XRD technique indicated a volume fraction of 13.4% [22].

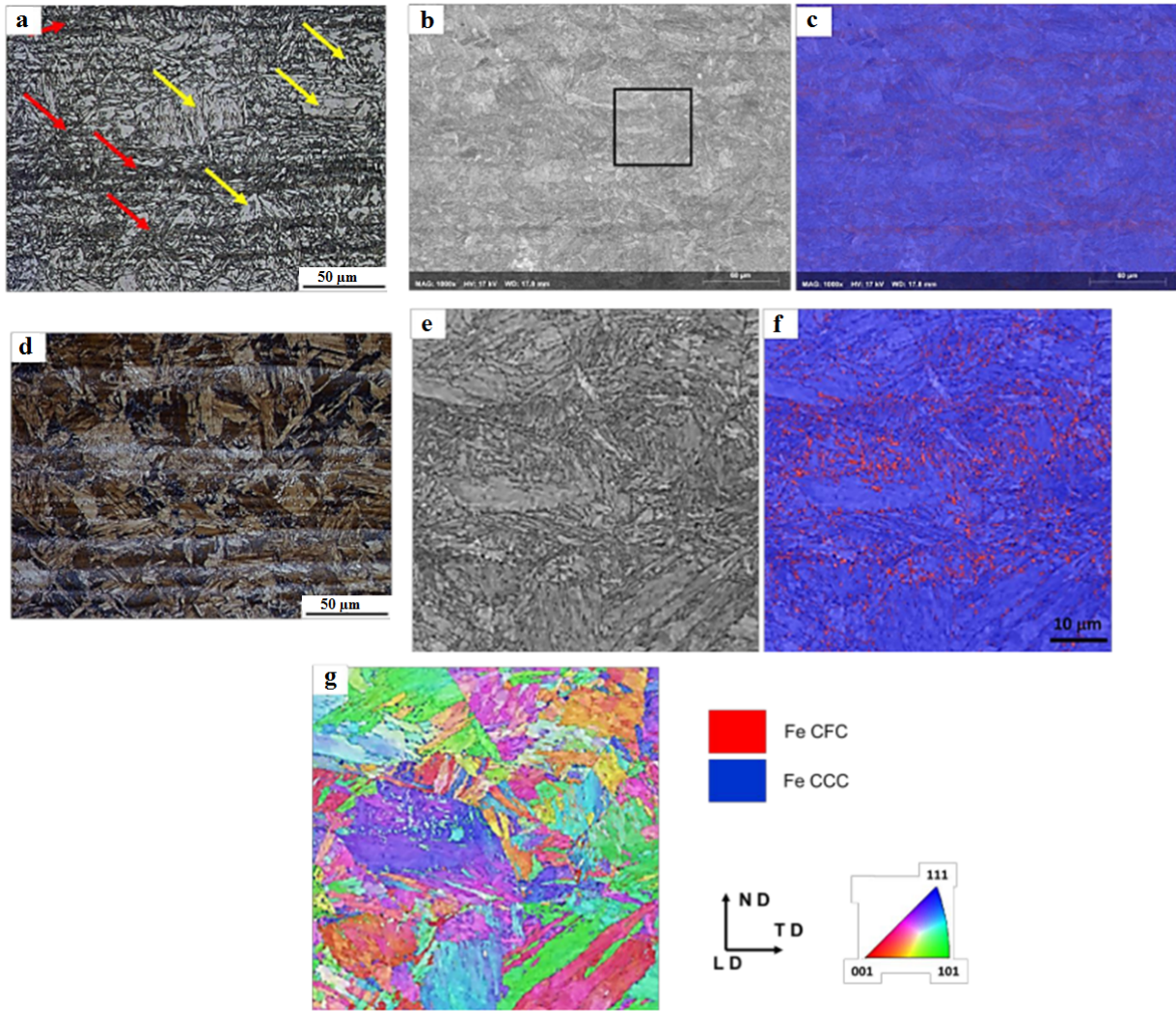


Figure 2.3.7: Microstructure of QIT 9Ni steel a) Optical micrograph d) Klemm's I etching showing the austenite as white bands. c) and f) EBSD phase map g) EBSD inverse pole figure [22]

Chemical analysis by EDS in the microsegregated lines revealed a higher concentration of nickel and manganese elements in this region (Figure 2.3.8).

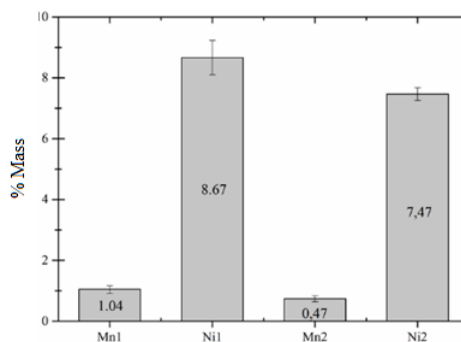


Figure 2.3.8: Chemical composition analysis by EDS. Mn1 and Ni1 are the chemical composition referent to the white bands. Mn2 and Ni2 as the zones without microsegregation [22]

EBSDB analysis of Quenched (800 °C/1 hour) + Tempered (600 °C/8 hours) 9Ni steel exhibits the cementite (in yellow) and austenite phases (in red) distributed homogeneously between the martensite blocks and grains (Figure 2.3.9). The Kernel Average Misorientation map (Figure 2.3.9-c) reveals regions of internal deformation and average misorientation.

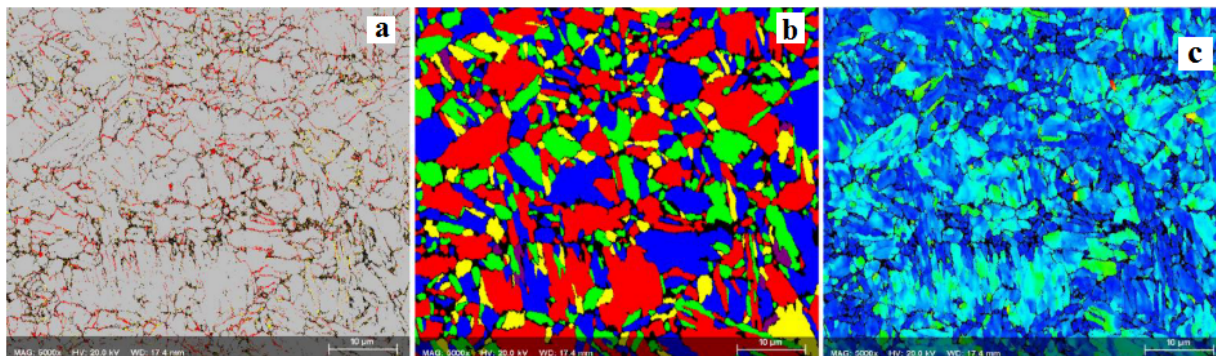


Figure 2.3.9: EBSD map of 9Ni steel Quenched (800 °C/1 hour) + Tempered (600 °C/8 hours) a) phase map, austenite in red and cementite in yellow b) grain size image c) Kernel Map d) Kernel Average Misorientation map [109]

TEM micrograph after quenching and 1-hour tempering at 590 °C shows an equiaxed lath structure with some regions rich in dislocations, 4.5% of austenite was detected in this sample (Figure 2.3.10). Another study done by Nakada et al [115] with a tempering temperature increased by 10 °C, but maintaining the same time, revealed the austenite islands in the martensitic matrix and the reversed austenite content raised to 9% (Figure 2.3.11). The observations suggest that, under the same tempering time, a very small increase in the temperature already exerts a strong influence on the austenite content.

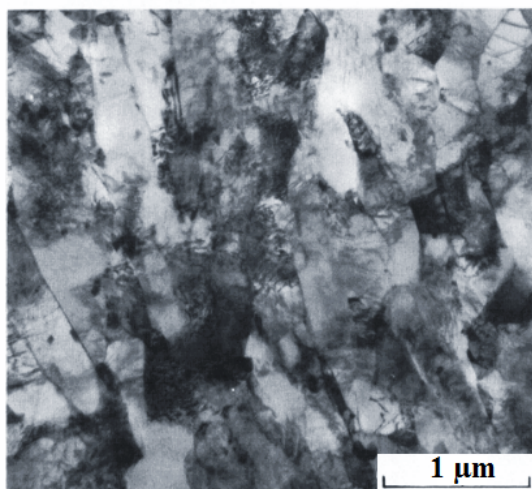


Figure 2.3.10: TEM micrograph of a structure obtained from quenching + tempering at 590 °C for 1h [99]

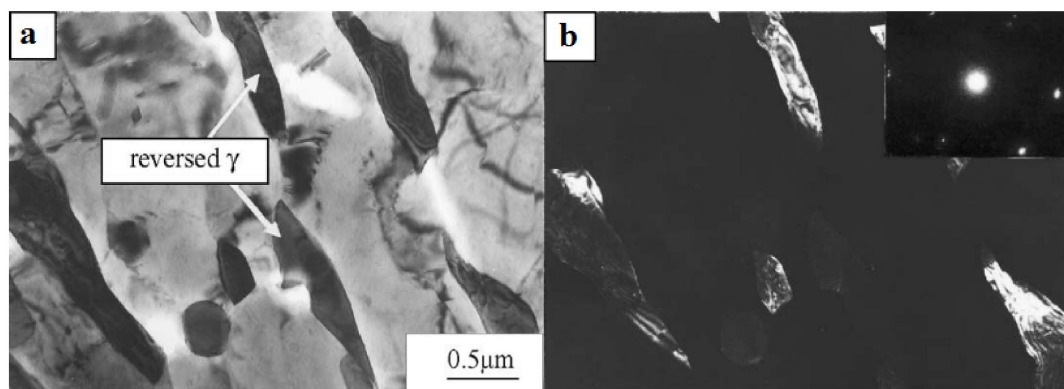


Figure 2.3.11: TEM micrographs of 9Ni steel tempered at 600°C for 1h indicating the presence of reversed austenite islands a) bright field image b) selected spot dark field image [115]

2.3.3 Reversed Austenite

In addition to stress-relieving, the tempering treatment causes several microstructural changes, such as a decrease in dislocation density, precipitation of cementite and the formation of reversed austenite. It is fundamental to distinguish the retained austenite from the reversed austenite, they differ from each other by the mechanism of formation, in their morphology, and finally they are distinct in their stability, where the retained austenite is meta-stable. The retained austenite remains in the structure after quenching (when the M_s temperature is below room temperature) while the reversed austenite appears in the tempering process, resulted from a memory effect from the previously retained austenite and their enrichment of gammagenic elements due to the diffusion process [122].

Reversed austenite is an important structure, which can not only keep the steel at a high degree of hardness but also improve its fracture toughness. In order to obtain the complete lath martensite, the quenching temperature should be above A_c3 . The reversed austenite appears gradually during the austenitization or maraging process, depending on the time and temperature. As a consequence of its significant influence on the mechanical properties of steels, this phase has received much attention in maraging steels together with martensitic steels [123].

The alloying elements strongly influence the stability of austenite. During the tempering heat treatment, the austenite phase precipitates along the grain boundaries or the martensitic laths as thin films or in a blocky shape (Figure 2.3.12) [96]. This reversed austenite is thermally stable upon cooling to at least -196 °C. The heat treatment also lowers the ductile-brittle transition temperature, breaking up the crystallographic

alignment of the martensite laths inside the packets by a toughening mechanism [124].

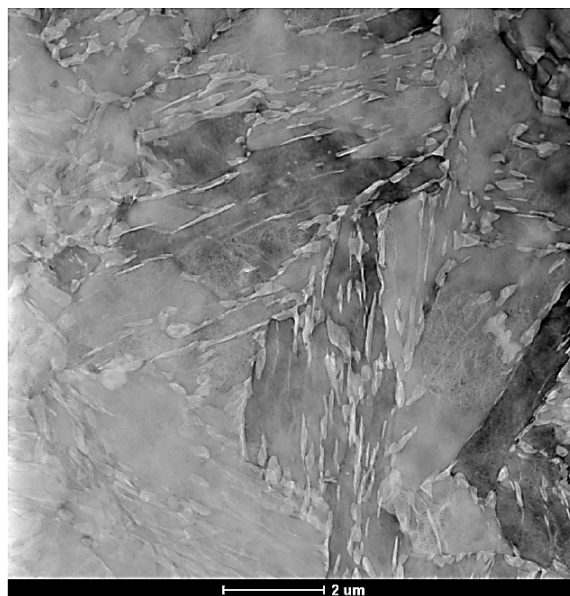


Figure 2.3.12: TEM image of Tempered 9Ni steel at 600 °C, the austenite phase was identified as the light phase between the martensite laths [109]

At the same time as the intercritical tempering occurs, the austenite phase is distributed along the boundaries of dislocated laths, packets, blocks, or prior austenite grains. The mechanism of this transformation is diffusional reversion, the austenite grows in those regions because they are low-energy sites for heterogeneous nucleation [124]. The alloy elements, such as C, Mn, and Ni are segregated from the martensite matrix to the reversed austenite during the tempering process. Studies have reported that manganese segregation into the austenite phase is originated from prolonged holding at an intercritical temperature [125]. The Ni-rich regions transform into austenite when the tempering temperature is near the A_{c1} . In consequence of those elements segregation, there are two regions with dissimilar A_{c1} temperatures, in that case, the martensite will transform at higher temperatures, rather than the interface rich in carbon/nickel, causing the two-stage austenite formation [100, 126, 127]. Therefore, nickel and carbon help to stabilize the austenite preventing the re-transformation during cooling. Figure 2.3.13 illustrate the steps of the reversed austenite formation. After cooling to room temperature, the amount of austenite lowers and more martensite can be transformed [126].

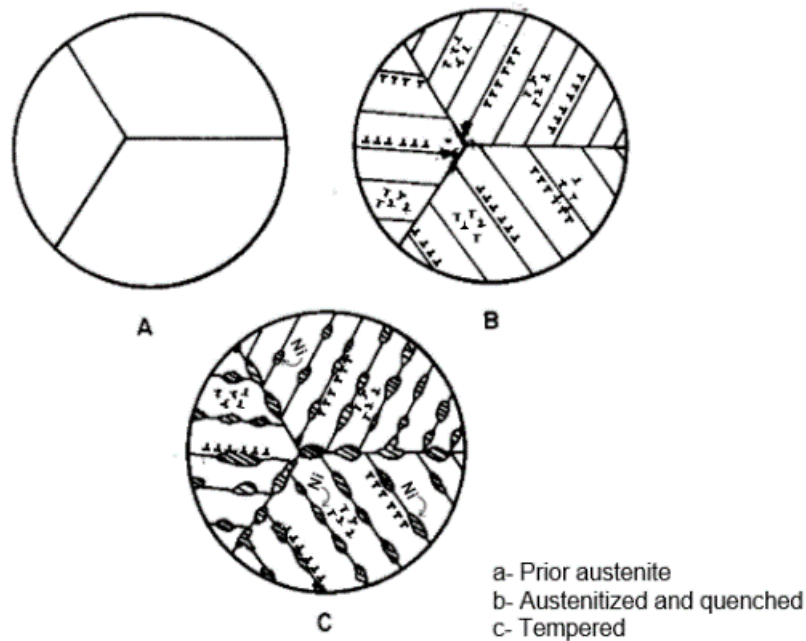


Figure 2.3.13: Schematic representation of microstructural development as a result of intercritical tempering of the as-quenched Fe-9Ni low carbon steel (adapted) [103]

The microstructure resulting from the heat treatment is composed of black and white bands, associated with alloying elements segregation. Figure 2.3.14 displays a three-dimensional combination of the micrographs in all directions of the 9Ni steel submitted to QIT treatment, the images were taken considering the rolling direction. Microsegregation bands are visible and they are originated from the rolling process. The white band is enriched in the austenite phase and the black zones with tempered martensite (ferrite).

After the heat treatment, the very fine austenite and the martensite are mixed forming a complex microstructure, which is very hard to be distinguished by optical microscopy. If the tempering is done above 600°C, the C, N, and Ni atoms can diffuse through a long-distance that alleviates the serious segregation, Figure 2.3.15 shows the partition of elements analyzed by EDS in the STEM technique, indicating the more concentrated elements at the lighter areas where the austenite is present.

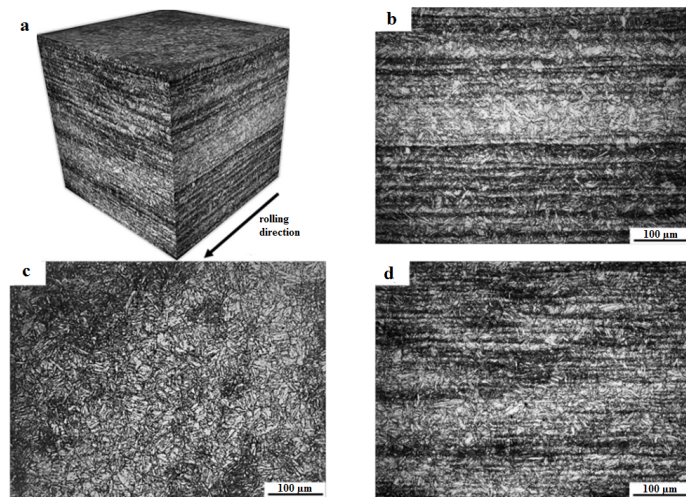


Figure 2.3.14: Microstructure of a 9Ni steel bar QIT treated represented in 3 directions. b) Longitudinal to the rolling direction c) Normal to the rolling direction d) Transverse to the rolling direction [22]

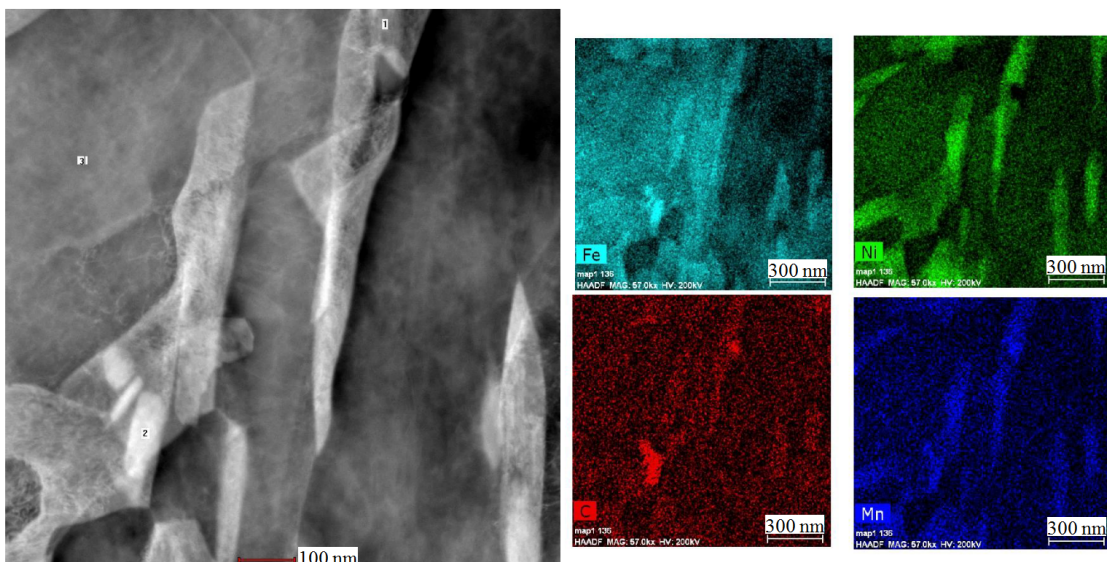


Figure 2.3.15: STEM-EDS map of tempered 9Ni steel at 600 °C, considering iron, nickel, carbon and manganese [109]

EBSD analysis of a sample quenched and tempered at 600 °C is shown in Figure 2.3.16. The reversed austenite is marked as red dots, the red and blue lines delimit the subgrain angles between 5° and 10°, respectively. This a piece of evidence that the austenite will form likely at the boundaries [96].

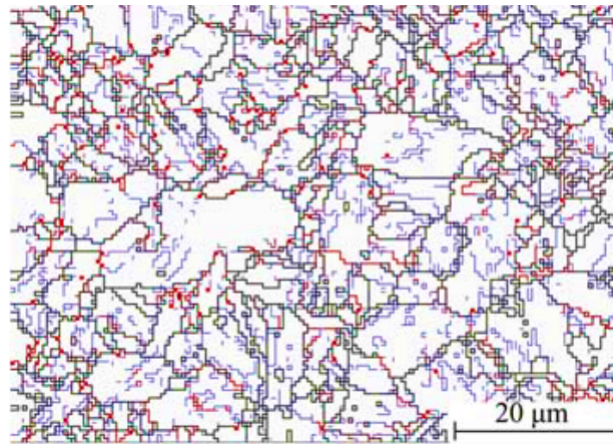


Figure 2.3.16: EBSD grain boundary map and phase map showing the distribution of reversed austenite. The red dots are the austenite phase, red lines are 5° low angle boundaries and the blue lines are 10° low angle boundaries [96]

If the steel is heat-treated above the temperature of 650-675 °C, the volume fraction of austenite tends to decrease, as indicated in Figure 2.3.17 [3, 96, 109, 115, 123, 128, 129]. This decrease has been attributed to the transformation of the unstable austenite formed during tempering into martensite on cooling [96, 128].

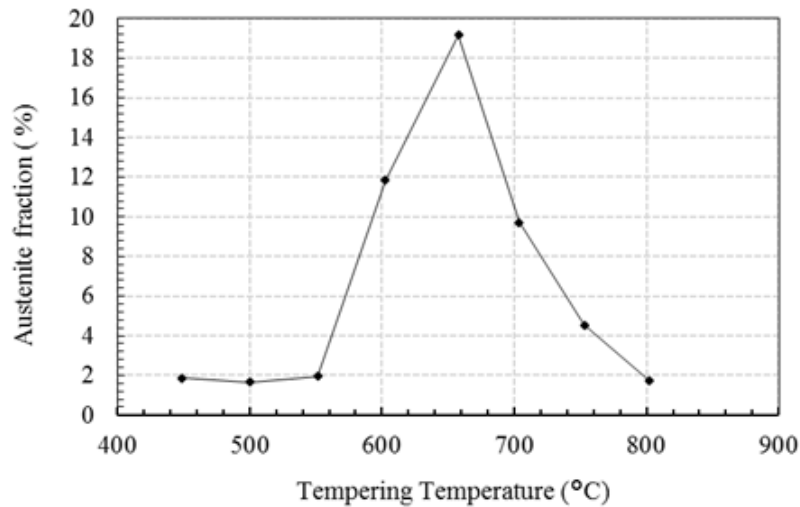


Figure 2.3.17: Volume fraction of reversed austenite at different tempering temperatures [128]

Kacem [5] in his studies showed that time has also importance on stabilizing the amount of reversed austenite, meaning that temperature is not the only parameter to be controlled. Figure 2.3.18 shows the variation of obtained reversed austenite according to the duration of heat treatment at 600 °C. Fultz et al [130] have done experiments with several tempering times and tested the material's response to cold deformation, verifying the thermal and mechanical stability of the reversed austenite, showing better stability at

short tempering times. They have noticed that after around 3 hours of tempering, the austenite is thermally and mechanically stable. The austenite begins to lose mechanical stability after few hours of tempering and it is very unstable after 100 hours of tempering. Most researchers rely on the theory that the amount of reversed austenite and its stability affects the cryogenic toughness of 9Ni steel [96, 114, 115, 130, 131].

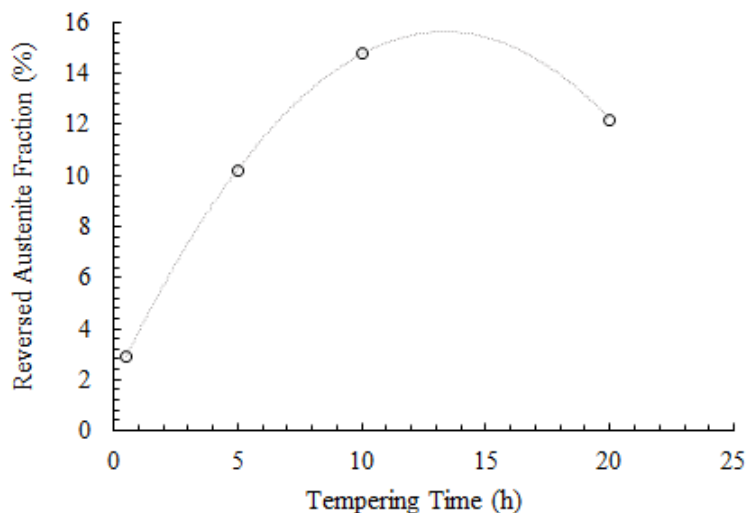


Figure 2.3.18: Evolution of reversed austenite fraction according to tempering times at 600 °C (adapted) [5]

An evaluation of the mechanical stability of the reversed austenite has been performed by several works correlating the XRD patterns to the austenite transformation within monotonic deformation [109, 132–134]. Figure 2.3.19 illustrates the diminution of austenite peaks according to the applied deformation from the tensile test. The $(111)\gamma$ and $(200)\gamma$ peaks become almost negligible at 6% of deformation. The austenite is mechanically transformed during the plastic regime, as can be seen in Figure 2.3.20, and at approximately 6% of deformation the sample is fully martensitic, as noticed in the XRD diffractogram (Figure 2.3.19). This is an important step to indicate that the 9Ni steel may exhibit strain-induced martensite when the stress values are over the yield point of the material which is the case in Low Cycle Fatigue tests. TEM and XRD investigations also pointed out an increase in dislocation density when the austenite transforms into martensite, this is one of the major impacts on the mechanical stability [130].

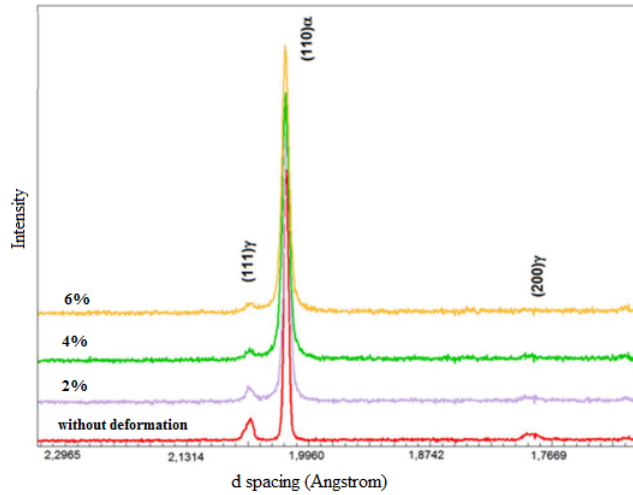


Figure 2.3.19: XRD diffractogram of Quenched (800 °C/1 hour) + Tempered (600 °C/8 hours) 9Ni steel at different deformation levels from a tensile test performed at room temperature [109]

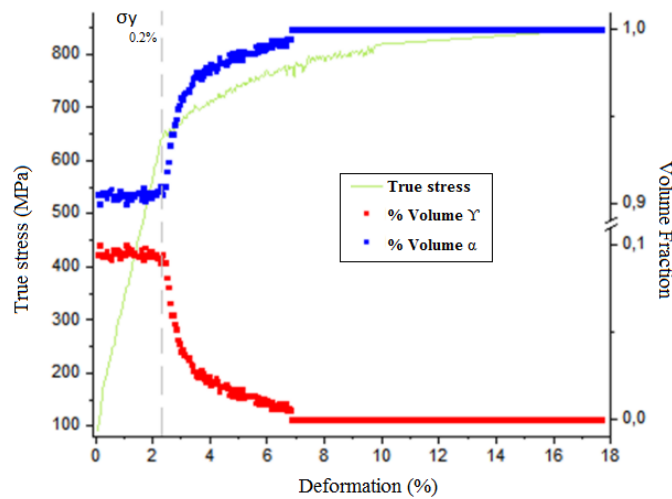


Figure 2.3.20: Evolution of austenite fraction in the stress-strain curve [109]

2.3.4 Mechanical Properties and Fatigue behavior of 9Ni steel

As opposed to Fe-Cr martensitic steels, cryogenic steels including 9Ni steel have not attracted so much attention from researchers in the investigation of the role of microstructure on mechanical properties. Indeed as mentioned above, 9Ni steel is used for LNG storage and transportation, in the form of tanks that are assembled by the welding process. As a result, the majority of the articles focus on the mechanical characteristics of welded 9Ni material, with the goal of verifying the structure before it is placed into service. The other motivation in the research program regarding this material and the possibility of decreasing the nickel content to combine the lower cost of product with

acceptable mechanical properties. To avoid losing the reader with an interesting, but borderline bibliography from the key topic of this PhD, this section will be limited to highlight the major mechanical characteristics of 9Ni steels. As well as presenting the primary facts needed to understand and create awareness about the contribution of the current PhD study.

The fracture toughness of 9Ni steel has been the subject of several studies. In addition, most studies are concentrated on methods of prediction of fatigue life for 9Ni steel welded joints at room and low temperatures [5, 135–138]. Still, no research strictly related to low cycle fatigue, crack initiation and surface relief of 9Ni steel has been found.

Tensile Tests

The mechanical properties from tensile tests of 9Ni steel are determined according to an ASTM A553 [139] standards, the minimum values required at room temperature are:

- Tensile strength: 690-825 MPa
- Yield strength 585 MPa

As demonstrated in Figure 2.3.21, the engineering tensile strength, yield strength and fatigue life at LNG temperatures increased at lower temperatures compared to room temperature [5, 138, 140], highlighting that the 9Ni steel has improved mechanical properties in cryogenic temperatures.

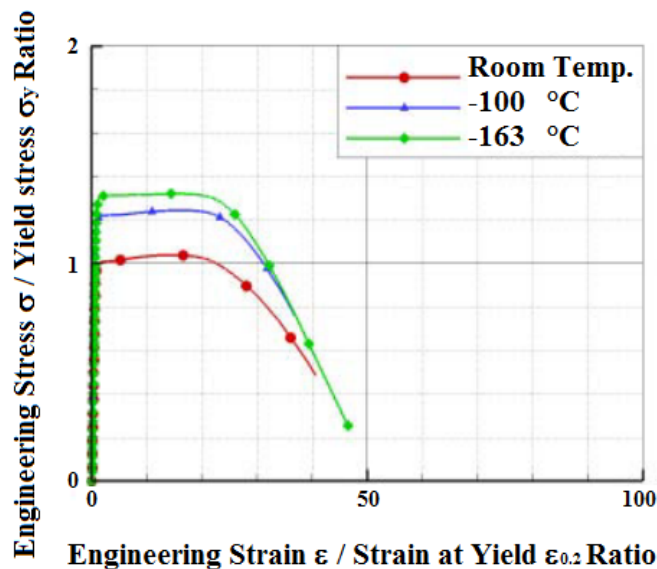


Figure 2.3.21: Engineering stress strain curve on 9Ni steel base metal [140]

Park et al [141] evaluated mechanical properties of nickel steels with various Ni contents between 3.5% to and 9% submitted to normalizing or quenching + tempering heat treatment. The materials were evaluated both at room and cryogenic temperatures. With increasing nickel content, there is a tendency for yield strength and tensile strength to rise (Figure 2.3.22).

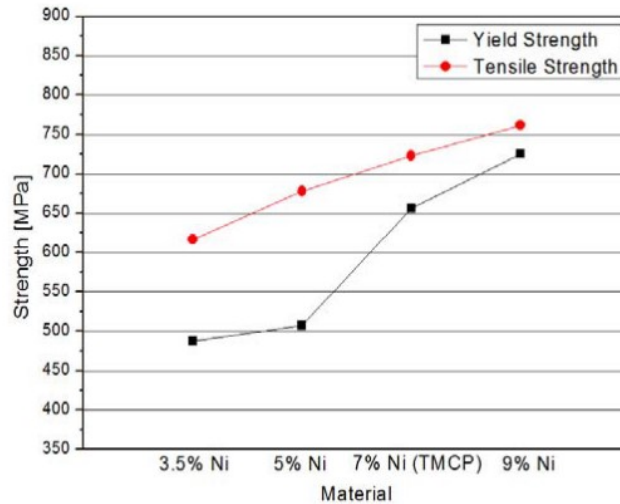


Figure 2.3.22: The variation of mechanical properties and nickel content for normalized or quenched+tempered Ni steels [141]

Tensile tests executed at room temperature by Kacem with the same material used in this study [5] indicated an average yield strength of 738 MPa and ultimate tensile strength of 772 MPa. At lower temperatures (-196 °C), the yield strength raises to 1055 MPa and ultimate tensile strength to 1112 MPa. The fracture surface shows a ductile behavior for both testing temperatures, as indicated in Figure 2.3.23.

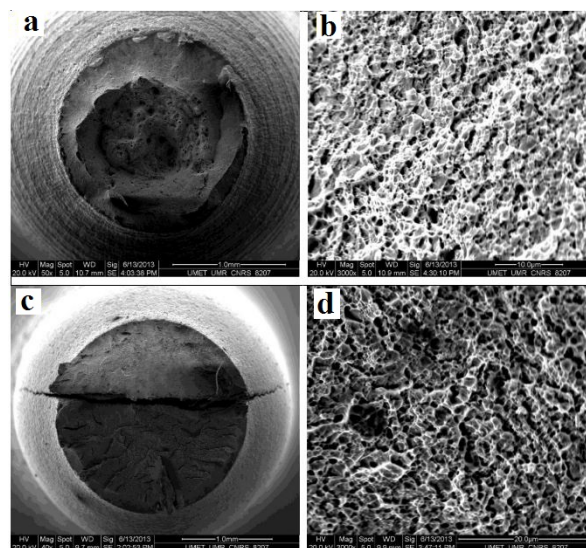


Figure 2.3.23: Fracture surface from tensile test at room temperature (a,b) and at -196°C (c,d) [5]

The effect of the tempering time was also evaluated by Choi et al [104], it was observed that the increase in tempering times induces a reduction of monotonic yield strength (940 MPa for quenched to 754MPa for 10 hours). However, a brief tempering treatment already improves significantly the toughness before the formation of detectable austenite, probably due to partial recovery of the lath martensite and carbon redistribution.

Toughness tests

It has been assumed that a substantial increase in impact resistance can be obtained by fixing a certain percentage of stable austenite dispersed in the martensitic structure [142]. Indeed, previously reported results of absorbed energy versus retained austenite concentration indicate a strong correlation for Fe-9Ni at all test temperatures [101, 106, 107, 114, 130].

The minimum impact value required by ASTM A553 at -196 °C is 27 J (transverse) and 34 J (longitudinal) [139]. As the curves in Figure 2.3.24 show, the toughness of 9Ni steel increases with increasing the amount of reversion austenite and it reaches the maximum 15% in volume, regardless of the temperature of the test and the values drop again with higher fractions of austenite.

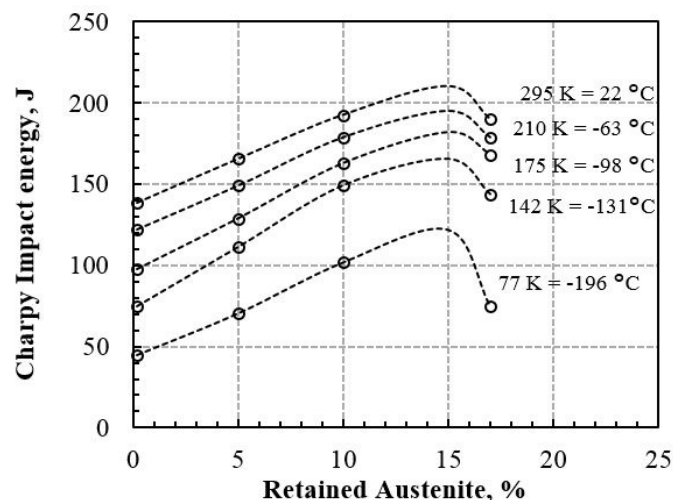


Figure 2.3.24: Evolution of toughness as a function of austenite content in 9Ni steel (adapted) [103]

Fatigue behavior

Fatigue life at LNG temperatures also increased in relation to temperature [137]. Park et al [141] evaluated fatigue crack propagation of nickel steels with various Ni contents between 3.5% to and 9%, both at room and cryogenic temperatures. It was identified that crack propagation rates increase as nickel concentration rises due to the growth in grain size.

In the studies conducted by Mu et al [137] with quenched+tempered 9Ni steel, the LCF test was performed with a triangular waveform and different strain ranges (0.6% to 1.6%) at room temperature (296 K). Cryogenic temperature (80 K) was also adopted to investigate the effects of the cryogenic environment on the LCF performance of welded 9Ni steel.

At room temperature, cyclic hardening and cyclic softening were evident, on the other hand, only cyclic hardening was observed at cryogenic temperature (Figure 2.3.25).

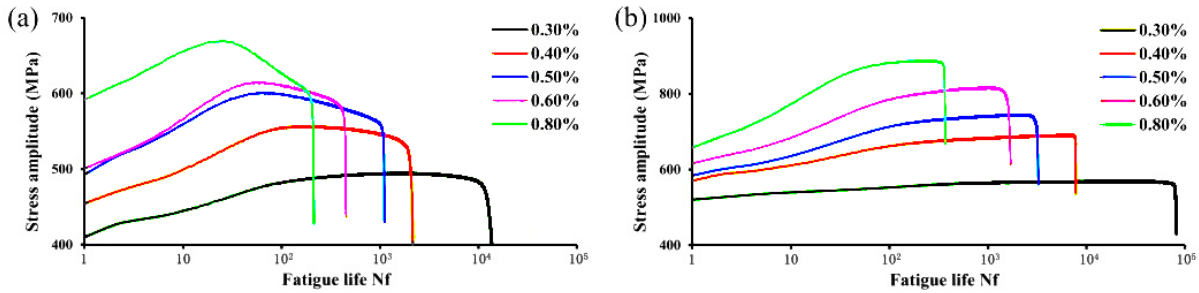


Figure 2.3.25: The cyclic stress response curves of welded 9Ni steel at a) room temperature, and b) cryogenic temperature (adapted) [137]

It was observed that specimens tested at cryogenic temperatures had a longer fatigue life than those tested at room temperature under the same controlled strain. Although, the performance was somewhat similar at $\Delta\epsilon_t/2=0.8\%$ (1.6% strain range) for both temperatures (Figure 2.3.26).

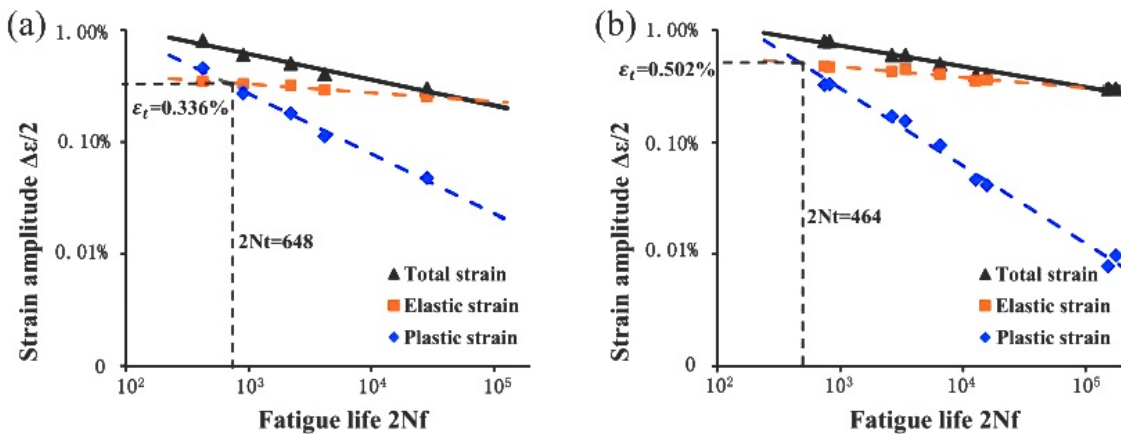


Figure 2.3.26: The relationship of the strain amplitude and the number of cycles to failure for welded 9Ni steel. a) room temperature b) cryogenic temperature (adapted) [137]

The influence of retained austenite in intercritical tempered Fe-9Ni-0.1C on the crack propagation in fatigue was also investigated by Choi et al [104] and it was observed that the as-quenched structure presents higher crack-growth rates than the tempered ones (Figure 2.3.27).

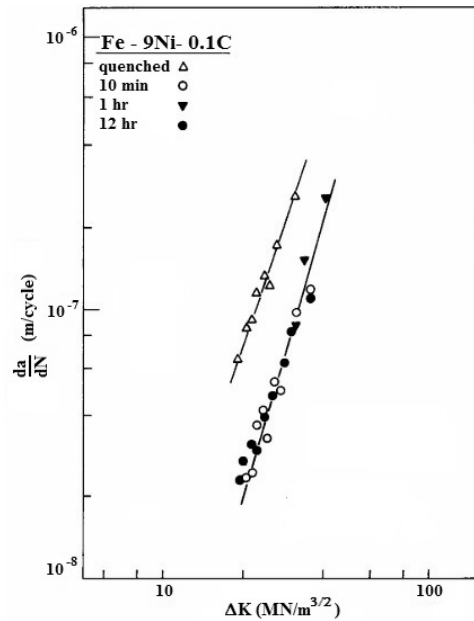


Figure 2.3.27: Crack propagation rate versus stress intensity factor for 9Ni steel tempered for 10 minutes, 1 hour and 12 hours [104]

What can be concluded here is that 9Ni steel indeed presents excellent cryogenic performance, still presenting a ductile behavior at lower temperatures. Not much information could be gathered from the literature regarding the deep analysis of the fatigue properties. One interesting point is a hardening effect seen in the first cycles followed by cyclic softening, and this effect is more prominent as the total applied strain increases. However, different fatigue behavior is observed at cryogenic temperatures, the cyclic hardening was dominant. The collected data done in this section will support the findings of the fatigue study of the 9Ni steel with several heat treatments.

Chapter 3

Materials and Methodology

3.1 Microstructure Characterization Techniques

Since the mechanisms of fatigue crack nucleation are based on the dislocation evolution, crystallographic aspects and surface observation, it is important to present the most relevant techniques used in the current work. The martensitic microstructure will be commented at different microstructural scales, prior to fatigue deformation and at the post deformation state. Figure 3.1.1 summarizes all the characterization techniques used in this research.

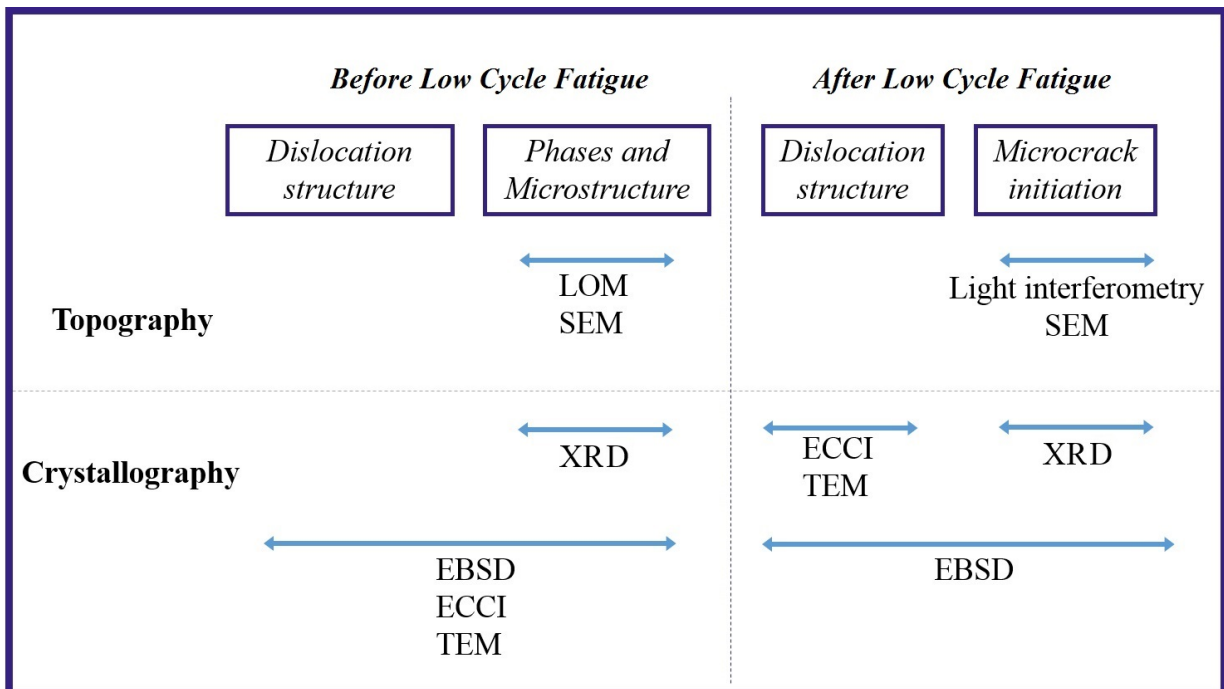


Figure 3.1.1: Characterization Methods used in this study

3.1.1 X-ray Diffraction

The detection of different phases present in the material can be performed by several techniques such as metallographic analysis, EBSD, chemical maps, magnetic methods, and X-ray Diffraction (XRD).

XRD is a crucial technique for characterizing crystalline materials. It is a non-destructive method that allows the evaluation of structural change in materials as well as phase identification based on Bragg's law:

$$n\lambda = 2d_{hkl}\sin\theta \quad (3.1)$$

Where,

- n : integer
- d_{hkl} : interplanar spacing between the diffracting planes
- θ : Bragg angle
- λ : wavelength of the primary electrons

According to Bragg's law, a diffraction pattern must have a path difference of a whole number of wavelengths (Figure 3.1.2).

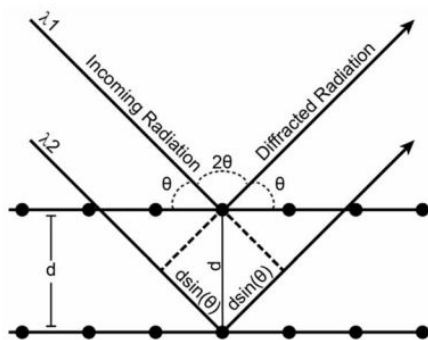


Figure 3.1.2: Bragg's law conditions [143]

Quantitative XRD assessment of the volume fraction of phases in distinct materials is based on the fact that the diffraction intensity for a given reflection of each phase is dependent on the phase volume in the material [144].

In this study, an estimation of the phases was done by X-ray Diffractometry with the Rigaku Smartlab diffractometer in a 38-120° 2θ range by using Cu $k\alpha$ radiation ($\lambda = 1.54056 \text{ \AA}$). The Cullity method [145] was applied to calculate the amount of the austenitic fraction. This method considers the intensity of the $(200)_\alpha$, $(211)_\alpha$, $(220)_\gamma$, $(311)_\gamma$ peaks. The Equation (3.2) shows how the austenitic fraction is determined.

$$f_\gamma = \frac{1}{4} \left(\frac{I_Y^{220}}{1.42 * I_\alpha^{200} + I_Y^{220}} + \frac{I_Y^{220}}{0.71 * I_\alpha^{211} + I_Y^{220}} + \frac{I_Y^{311}}{1.62 * I_\alpha^{200} + I_Y^{311}} + \frac{I_Y^{311}}{0.81 * I_\alpha^{211} + I_Y^{311}} \right) \quad (3.2)$$

The peaks $(110)_\alpha$, $(111)_\gamma$ are not considered for this calculation because they can lead to some uncertainties, they are too close from each other in the diffractogram.

3.1.2 Focused ion beam - FIB - Cross section visualization

The FIB instruments were created in the late '80s designed for the semiconductor industry. The FIB microscope now is an interesting tool for Materials Science because it can be used for micromachining and preparation of electron transparent foils to be analyzed by other techniques such TEM and Atom Probe [54, 87] and also for sectioning tomography to recreate 3D images [23, 73, 92, 146–149]. The FIB microscope can be composed of one of those two ion sources for milling: liquid metal ion sources (LMIS) and gas filed ionization sources (GFIS), mostly used for scanning ion microscopes [150]. The principle of working of the LMIS is consisted of heating a metal by a high electric field into the liquid state. This liquid metal ion source normally is composed of gallium and placed at the tip of a tungsten needle (Figure 3.1.3).

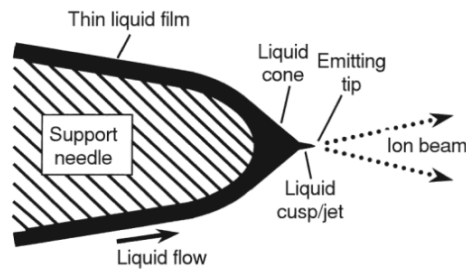


Figure 3.1.3: A working blunt-needle LMIS in ion generation mode [151]

During the cutting procedure, the surface is covered by platinum to protect the desired region from irradiation damages and improve cohesion. Next, the Ga^+ beam

is used to cut the slices being connected to the Tungsten needle by platinum and then separated from the bulk by using the gallium beam. Later, the extracted lamella is welded into a copper grid by using Pt-deposition, Figure 3.1.4 shows the procedure of a FIB lamella extraction in a region with PSMs. The extracted lamella is about 100 nm in thickness and 10 μm in width.

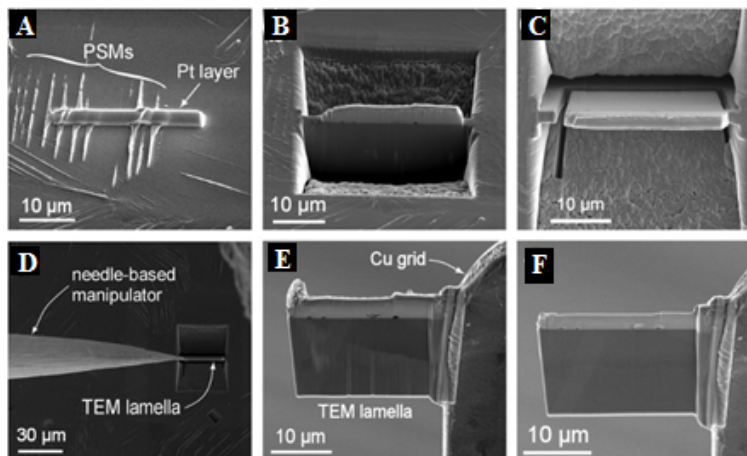


Figure 3.1.4: FIB lift-out steps a) Deposition of a protective Pt coating across the PSMs. b) Ion bombardment around the selected area c) Trenching the thin lamella d) Extraction with the tungsten tip and transportation e) Ion 'welding' to the copper grid. f) Final thinning of lamella ready for TEM observation [87]

3.1.2.1 Effects of the FIB milling on the bulk structure

The ion-sample interactions (elastic and inelastic) may cause some sample artifacts or damage. Gallium contamination may happen and some increasing disorder can be produced due to the presence of ions with sufficient energy, which can go into the solid. One of the possible changes by the energetic beam is the creation of dislocations at the surface and the bulk, also the production of point defects and their rearrangement [151–153], at it can lead also to the transformation of metastable phases [154]. Despite some little disadvantages, at this moment, the FIB lamella is the best procedure and more qualified to study with more details the constitution of the PSMs.

Cross-sectional thin lamellae were drawn out perpendicular to the surface of fatigued specimens with the help of the FIB technique using Ga^+ ions in a FEI Strata DB 235 SEM microscope located at the *Institut d'Électronique, de Microélectronique et de Nanotechnologie* (IEMN, Lille). First, the fatigued material was observed by SEM to select the region of interest. The surface was later covered by a thin layer of carbon, deposited by electron bombardment, and a thick layer of about 1 μm of platinum by ion bombardment. This allowed protection of the surface against the Ga^+ ion insertion employed for the machining of the lamella.

The extraction of the lamella started with the rough machining of the craters from their borders with a FIB accelerated at 30 kV, under a current of 20 nA. Then the lamella was cut, deposited on a copper grid, and finally thinned with a reduced energy of the FIB (10 pA and 5 kV) in order to remove or minimize the damage caused by the previous steps.

3.1.3 Transmission Electron Microscopy- TEM

The characterization of deformation substructures is normally performed by the TEM technique. The high spatial and angular resolution of TEM allows the characterization of crystal defects like dislocations, stacking faults, and point defects. Nevertheless, TEM presents some drawbacks such as sample preparation, where extremely thin sample disks (about 80-60 μm) are needed, and this method has reduced observation area [155]. When compared to Scanning Electron Microscopy (SEM), transmission microscopy uses much higher energy (between 80-300 kV). To generate TEM images, the electron beam incident traverses the thin disk, then the electrons are transmitted through the specimen, being subsequently focused by lenses and collected by a detector. The generated images can be visualized in real-time on a phosphor screen, or by a wide-angle camera. The images are recorded by a CCD camera (electronic charged coupled devices) which is a transducer that converts the electron signal into a pulse per pixel [156]. The diffraction patterns from several materials studied by TEM can be seen in Figure 3.1.5 and the concept of operation of the TEM microscope in the diffraction and imaging modes is shown in Figure 3.1.6.

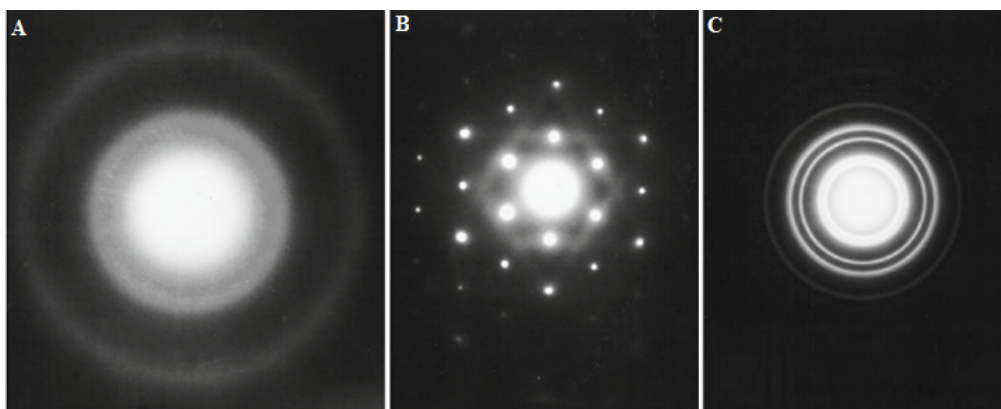


Figure 3.1.5: Different types of diffraction patterns obtained in a 100-kV TEM: A) amorphous carbon, B) an Al single crystal, C) polycrystalline Au (adapted) [157]

The possible basic operations of TEM are the bright field mode when the selected area electron diffraction pattern (SAEDP) is projected onto the detector, the pattern will show a bright central spot and the scattered beams will appear as spots or rings around

the direct beam. When the aperture is displaced to select the scattered electrons, the dark field image is formed. Concerning the dislocations, once the defects of the structure will deform the neighbor planes, the beam will be deflected, reducing the transmitted beam intensity. The dislocations in the TEM images will be visualized as dark lines.

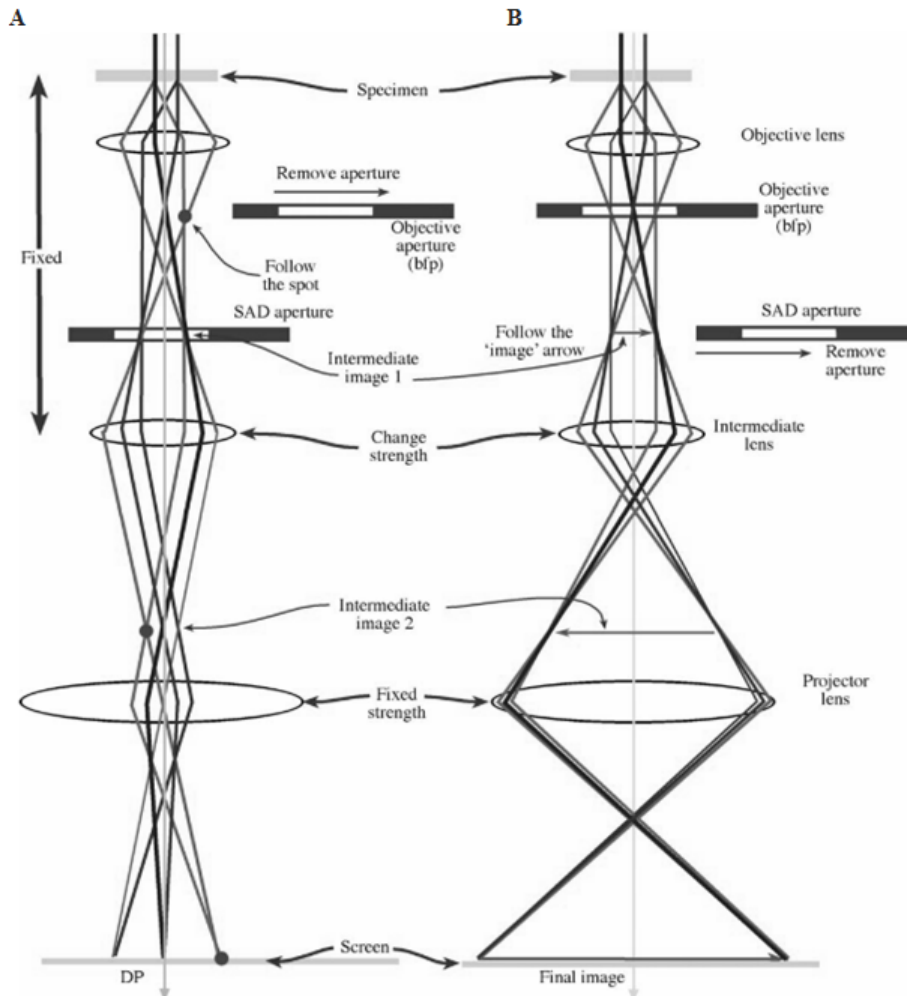


Figure 3.1.6: Two simplified basic modes of the TEM imaging A) diffraction mode: projecting the diffraction pattern and B) image mode: projecting the image [157]

In this study, the samples in the state previous to fatigue tests were mechanically ground and thinned up to 80 μm , 3 mm diameter thin disks were cut from the thin polished sheets. The center hole was made using a Struers Tenupol double jet polisher using a solution of 90% acetic acid and 10% Perchloric acid at 12 $^{\circ}\text{C}$ and 20.5V of applied tension, subsequently the surface was cleaned using Ar⁺ ion milling Precision Ion Beam Polishing (PIPS) with an accelerating voltage of 5 kV, average current of 15-20 μA , and a milling angle of 10 $^{\circ}$.

FEI Tecnai G2-20 twin microscope operated at 200 kV was used to take the TEM micrographs. The thin films of retained and reversed austenite were differentiated using

the selected area electron diffraction pattern (SAEDP), by choosing the d-spacing related to $(220)\gamma$ and $(311)\gamma$ planes on dark field mode (Cu $k\text{-}\alpha$ 1.267\AA).

3.1.3.1 High-resolution transmission electron microscopy HRTEM

The HRTEM is a technique that uses both transmitted and scattered beams to create an interference image, generating a phase-contrast image. This technique can analyze crystal structures and lattice imperfections, showing images at the atomic level, with the possibility to reveal details finer than 0.2 nm. Under some imaging conditions, the patterns will correspond to atom positions [156, 158]. If the specimens are very thin, about 100 nm thickness or less, the elastic scattering will be majoritarian in relation to the inelastic scattering. Interference patterns, normally visible starting from 400k of magnification, will be generated by the interaction of the beam and the crystal lattice [159, 160]. Figure 3.1.7 shows one example of an image obtained by HRTEM, the IFFT (Inverse Fast Fourier Transformation) is a lattice-fringe representation that corresponds to the d-spacing, useful to identify the family of planes and linear defects. In the case of Figure 3.1.7, the IFFT was able to highlight the twin structure present in that region.

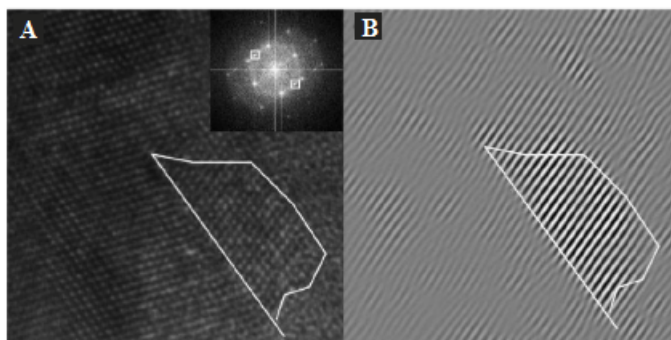


Figure 3.1.7: a) HRTEM image of a monocrystalline Si and its twin structure b) IFFT image highlighting the twin [161]

TEM analysis from the FIB lamellae were done only on samples extracted from low cycle fatigue deformed specimens. The analysis was undertaken on FEI Tecnai Transmission electron microscope G2-20 twin operated at 200 kV and HRTEM images were conducted in FEI Titan Themis 60-300 kV microscope.

The foils were further cleaned by Ar^+ ion milling precise ion polisher (PIPS, Gatan) at an accelerating voltage of 5 kV, an average current of 15-20 μA , and a milling angle of 10° .

3.1.4 Scanning Electron Microscopy-based diffraction techniques

The scanning electron microscopy (SEM) technique gives detailed information of the surface, which may be by chemical composition via backscattered electrons (BSE) or topography by secondary electrons (SE). Furthermore, crystallography information can be obtained by electron backscatter diffraction (EBSD) and near-TEM lattice defects imaging by the electron channeling effect (ECCI) that will be detailed hereafter. In comparison to TEM analysis, the SEM-based diffraction techniques present inferior spatial resolution, on the other hand, it allows the visualization of bulk specimens, providing more statistical data.

3.1.4.1 Electron backscatter diffraction - EBSD

In this technique, an electron probe is focused into a small area of a crystal and the angular distribution of backscattered electrons emerging from the sample is recorded. The signal of electron backscatter diffraction pattern (EBSP) is singular and depends on the crystal structure (for example, bcc and fcc) as well as crystal orientation. An EBSP pattern is presented in Figure 3.1.8, the bands are known as Kikuchi lines, each line represents a single family of planes and the intersections form the zone axes. Figure 3.1.9 summarizes the generation of the Kikuchi lines [20, 162].

For image acquisition, the sample is tilted 70° inside the microscope chamber, which is the optimal position for analyzing the backscattered signal, at this position the diffraction patterns are captured [20]. The EBSD analysis is very convenient to identify, with high spatial resolution, the phase distribution of polycrystals, local texture, individual grain orientations on the surface, crystallographic relationships between phases, among other things [156].

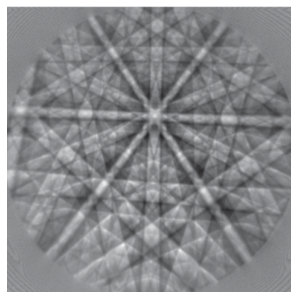


Figure 3.1.8: EBSP pattern of Fe 36% Ni (fcc crystal structure), acquired with 15 kV [162]

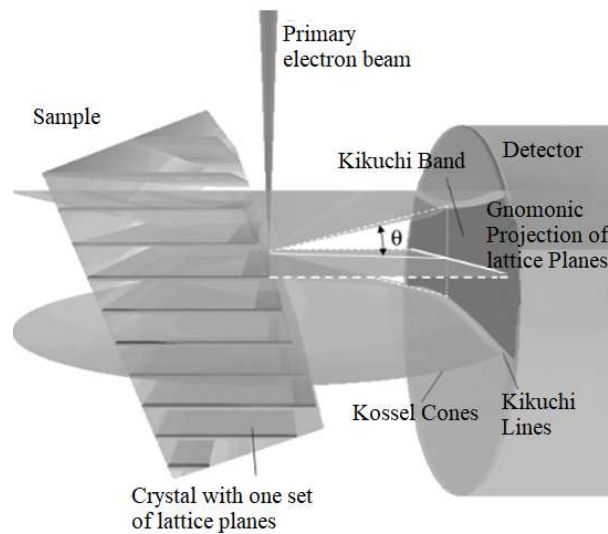


Figure 3.1.9: Representation of the acquisition of EBSD patterns. Only one Kikuchi band is displayed in the image (adapted) [162]

While the electron beam scans the sample over a regular grid measuring crystal orientations, the EBSD patterns are collected and evaluated step by step, being indexed according to a database. The orientation imaging microscopy mapping (OIM) is then executed and the data are used to generate orientation or phase maps of the sample's scanned area (Figure 3.1.10). The OIM technique is extremely powerful, allowing the investigation of particular characteristics of the material's microstructure. The post-processing data allows the extraction of several types of information.

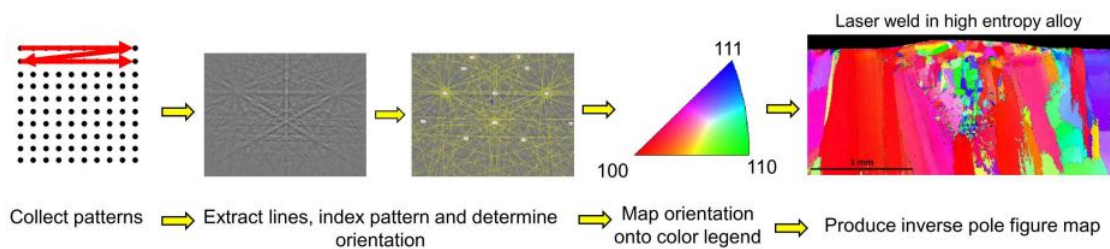


Figure 3.1.10: Steps of EBSD data acquisition [163]

The EBSD acquisition was carried out in a Hitachi SU-5000 FEG-SEM system operated at 20 kV with an Oxford Instruments Symmetry system, having a high-resolution camera with angular precision below 1° and acquisition speed up to 3000 patterns per second [164]. Automated collection and analysis of EBSD patterns were performed by the orientation OIM technique in the Oxford Aztec system.

There are few requisites to acquire a good pattern and perform proper and reliable post-processing with the EBSD data:

1- Mean Angular Deviation – MAD: Also known as pattern misfit, it determines how well the Kikuchi bands match. Showing the maximum angular deviation allowed from the EBSP collected and the one present in the database used as reference. The lower the value, the better it is.

2- Angular resolution: It means the ability of measuring angular changes in the diffraction pattern with a certain precision. The Symmetry system presents different indexing modes that can be chosen depending on the desired analysis that will impact the pixel-resolution of the patterns.

The refined accuracy mode is recommended for achieving the greatest precision misorientation measurements (for example, to characterize minor sub-grain structures), revealing details below 0.1° . This mode was used in this study due to out focus on revealing very thin substructures.

The binning was adjusted to keep an angular resolution better than 0.08° by choosing the highest possible image resolution for pattern processing of the CMOS camera and optimising the Hough transform parameters [165, 166]. More precisely, the resolution mode has been selected allowing a resolution of 1244 x 1024 pixels and the Hough transform parameter was set to 60.

3- Step size: This means the distance between each step of the data acquisition, will depend on the intrinsic parameters of the SEM/EBSD, and nowadays it can reach a dozen of nanometers. The step size should be on a scale that reflects the microstructural details, if dislocation substructures like cells are of importance, the step size should be near their diameter [167]. The scan step size of 100 nm was adopted focusing on optimization of the acquisition data according to the methods proposed by Chen et al and Kamaya et al [168–170]. A big step size leads to loss of information and very small values may collect background data, inducing errors. The step size value should be on a scale that reflects the microstructural details. The ideal value of step size in this experiment was achieved after several trials in the same area to get reliable data.

The EBSD system is capable of displaying standard maps while the sample is still scanned, such as phase maps, image quality maps and orientation maps. Those features will be detailed as follows.

Band contrast- Image Quality

It represents the quality factor of the image (IQ), originated from the Hough

Transformation. It is the average intensity of the Kikuchi bands with respect to the total intensity of the scanned area, varying from 0 to 255 on a grayscale. The lowest the value, the less quality the captured region has, showing as darker regions. The IQ value is affected by grain boundaries, dislocation density, precipitates, topography, microscopy settings and of course, sample preparation.

Euler and IPF orientation mapping

The Euler angles ϕ_1, Φ, ϕ_2 , are used to display the texture of the overall microstructure and represent a rotation of the crystal according to an external reference, following Bunge's notation. Changing in colors indicates an alteration in the rotation, such as low-angle sub-grain boundaries, for example. Euler maps have some limitations, when the Euler angles are near the limit, the RGB component can vary between maximum and minimum, showing a big color difference, but in fact, there will be just some little or no orientation change. Due to this limitation, the inverse pole figure maps (IPF) can help better to interpret the data.

The pole figures are used for texture analysis and to study slip systems. This tool is useful for understanding preferred orientations in terms of the sample coordinate system (rolling direction, transverse direction, and normal direction). The IPF uses a basic RGB coloring scheme, and is plotted on a standard stereographic triangle, they can be used in place of the traditional pole figures.

The post-processing after the data acquisition was performed for all samples by both the EDAX/TSL Orientation Imaging Microscopy and Aztec CHANNEL 5 softwares. Grain dilation with a tolerance angle of 15° was applied to clean up the artifacts present on the material's surface [171].

3.1.4.2 EBSD - Advanced use

The quality of the Kikuchi pattern depends directly on the diffraction on the crystal volume, the less perfect it is, the more diffuse the Kikuchi pattern will be [172]. A blur in the pattern can also be caused by a deformation layer from inadequate sample preparation and sometimes, non-indexing of patterns will happen at grain boundaries by overlapping.

The image quality (IQ) is an important factor to measure the "pattern quality". The IQ maps of coarse-grain materials display grain boundaries and topography changes, being an indirect tool to differentiate deformed and recovered or recrystallized grains in a microstructure. According to some authors, this feature is also helpful to differentiate the bainitic constituent and the ferritic phase in TRIP steels [173, 174]. Petrov and Ryde

[116] have observed that the martensite shows a low pattern quality, bainite medium quality pattern, and higher quality is observed for the ferritic phase. Those findings are also coherent with studies done by Bouquerel [175] in TRIP steels. In advanced mapping, particular attention is paid to misorientation measurement. From the literature, those variations in the pattern can correspond to the presence of Geometrically necessary dislocations (GNDs) and grain curvature due to strain or the presence of GNDs that are originated from phase transformation.

The martensitic and bainitic phase transformation occurs under a volume change, generating internal stresses. When a material is deformed plastically or heat-treated, two types of dislocations are created. The statistically stored dislocation (SSD), which does not promote any lattice rotation, and the Geometrically necessary dislocations (GND) generates a representative and measurable lattice rotation. Moreover, the GNDs are associated with long-range distortion and the SSDs are associated with homogeneous deformation because their distortion fields are canceled by the other neighboring dislocations [176]. During the straining, the GND will arrange themselves into low-energy structures, developing small angle grain boundaries. Those two types of dislocations will affect the IQ map, when the dislocation is introduced into the material, the distortion of the lattice is created, resulting in a degradation of EBSD patterns as demonstrated in Figure 3.1.11.

The EBSD can identify qualitatively and quantitatively the gradient produced by the creation of the GNDs. Figure 3.1.12 shows two different EBSD patterns emphasizing the distortion in the pattern caused by deformation, this evidence is used to measure local plastic strain. However, we need to pay attention to GND inherited from a heat treatment that may affect the overall analysis.

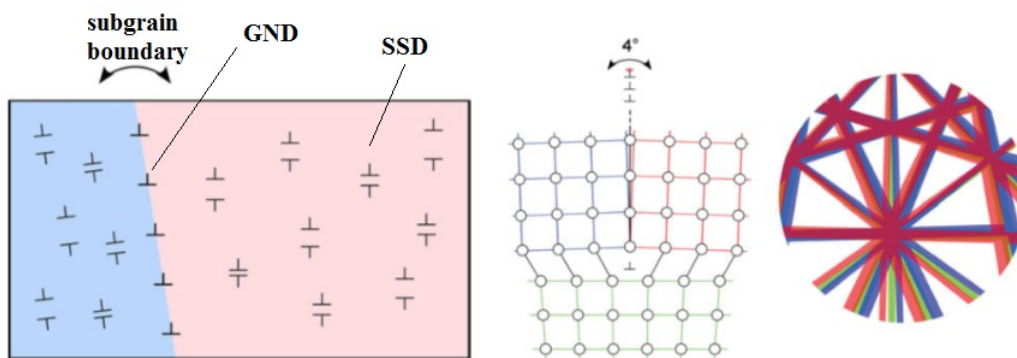


Figure 3.1.11: Schematic of dislocations and subgrain boundaries and the effect on the EBSD pattern (adapted) [177]

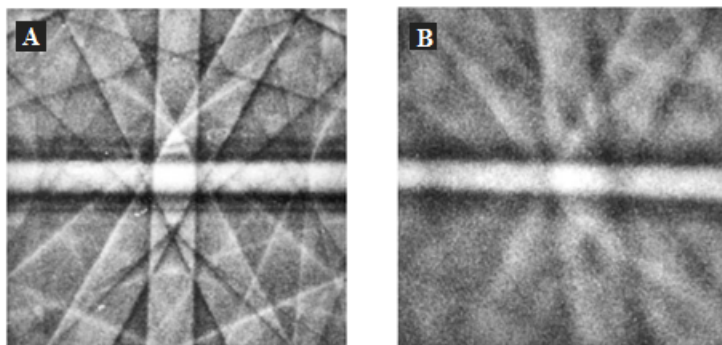


Figure 3.1.12: EBSD pattern of Al 6061 alloy a) annealed b) 8.5% strain deformation, blurred pattern [178]

Some misorientation methods will be now explored based on their feasibility regarding the complex martensitic structure and considering the GNDs already present in the matrix due to phase transformation.

Interface Boundary-based approach: Line Segment Method

The smallest misorientations admitted between grains or subgrains obtained by automated EBSD are typically between 0.5° and 1.5° . These very low values are achieved only with high-resolution parameters such as FEG-system, high-resolution cameras, good surface conditions, and a well-calibrated system. The LSM maps can distinguish boundaries by the applied threshold, being capable to resolve subgrains with the average size of hundreds of nanometers [179]. In the general approach used in the orientation imaging analysis software, called here the line segments method (LSM), grain boundaries (grain boundary traces, strictly speaking) are represented by line segments separating adjacent EBSD points associated with specific misorientation ranges. The HAB segments are usually associated with misorientations higher than a threshold, typically set at 15° . Whereas low-angle grain boundary (LAB) segments are associated with misorientations between 5° and 15° . In addition, line segments associated with misorientations lower than 5° are considered as intragranular boundaries (IBs) or dislocation cell boundaries [180].

Kernel-based approach

Numerous EBSD misorientation parameters allow the evaluation and quantification of strain-induced changes in the structure. Grain-based approaches such as GOS and GROD and the Kernel-based approach. When these parameters are averaged across a significant area, they show a strong correlation with the degree of plastic strain.

The GOS (Grain Orientation Spread) technique is based on the average misorientation within the whole grain, by comparing a reference pixel inside a grain with the other pixels of the same grain. This approach indicates restored zones after heat treatment or plastic

deformation. It is more suitable when a shift in the grain and a moderate increase of density of dislocation are observed. The GROD (Grain reference orientation deviation) technique measures the relationship between plastic deformation and misorientation, giving the extent of deformation in a grain. It shows the magnitude of the orientation changes referent to the initial crystal orientation. This technique is being used as a complement to the Kernel Average Misorientation (KAM) technique, displaying a strain distribution on a larger scale when compared to the Kernel methods. For the case of the martensitic steels, the grain-based approaches do not suit very well due to the hierarchical structure.

At the present, the angular and spatial resolutions provided by EBSD are not enough to resolve information about individual dislocations. Nevertheless, lattice misorientations or gradients can still give information about the dislocations. The formation of dislocations substructures is one kind of energy storage mechanism, thus the spatial distribution of stored energy can be calculated by the measurement that comes from those subgrains.

The Kernel methods quantify the angle differences between indexed EBSD pixels within a grain, which is also correlated to GNDs [181, 182]. Kernel Average Misorientation (KAM) calculates the average misorientation between a pixel i and its surrounding pixels, as long as the misorientation does not exceed a predefined threshold value (5° for example, to avoid HAB in the calculation), showing a local orientation (Figure 3.1.13). The KAM value is usually higher in deformed grains due to the increase of dislocation density, this approach is often used as a qualitative measure of plastic deformation localization [176, 182–186]. The KAM describes better areas with strong interactions between dislocations and places where sub-boundaries are created.

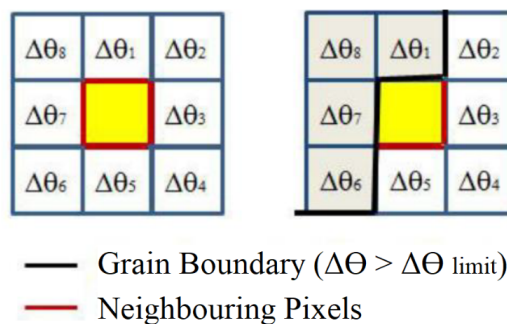


Figure 3.1.13: Schematic representation of KAM calculation [187]

The KAM approach can show the GND due to defects induced by plastic deformation or GNDs originated from the accommodation during the phase transformation (e.g. Fe- γ fcc to Fe- α bcc). In the case of the 316 stainless steel and nickel polycrystals [184, 188], microstructural evolution was observed for different degrees of applied strain. The magnitude of the local misorientation increases with the strain amplitude. It was observed

by EBSD that the strain distribution was not uniform for LCF specimens, the material tended to form clusters of dislocations and their appearance was proportional to the applied strain. Schayes [182] in her study for Fe-3Si steel has also used the misorientation bases criteria, investigating the relationship between the KAM values and the dislocation structures found in the material, and strain localization in the vicinity of grain boundaries. If the GNDs are already present in a considerable amount in the material because they were originated from phase transformation, which is the case of the martensite structure, the analysis turns out to be the more complicated for further evaluation.

The measured GND density depends strongly on the step size used to measure the lattice distortion, in other words, the adopted step size affects the KAM values. Very small step sizes can induce errors in the measurements, as well as high step size, which may result in loss of information [182, 189]. The step size used for EBSD analysis should not exceed 1/5 of the average grain size. For accuracy of 5%, 8 pixels per grain are required, at least. Additionally, a high sufficient number of points must be collected [179]. The optimal step size varies for each material and it is achieved by comparing the results under several values adopted for scanning [167].

For this study, the KAM maps were generated with a 100 nm step size and it was based on the calculation for the first nearest neighbors. A maximum misorientation of 5° was adopted in the post-treatment. In that way, any boundary with a misorientation of less than 5 degrees will be recognized as an area of increased dislocation density.

3.1.4.3 t-EBSD or TKD (Transmission Kikuchi Diffraction)

The TKD technique uses the SEM with an EBSD detector performing orientation mapping on transparent thin foils, the EBSD patterns will be produced by transmission rather than scattering, which is why this method is also called t-EBSD. The sample thickness is very important, the best pattern quality is obtained when the thin sheet thickness is between 75 and 200 nm [154, 190]. In very thin areas, the Kikuchi bands can be blurred due to the thickness dependency, on the other hand, in thicker areas the electrons have difficulty being transmitted, decreasing the pattern quality.

The TKD analysis was performed by Jeol JSM-7800F FEG-SEM microscope, with the operating conditions of 30 kV, a sample holder with a pre-tilt of 60°, and an additional tilt around -44° was applied, resulting in an effective angle of 16°.

3.1.4.4 Electron channelling contrast imaging - ECCI

Coates [191] discovered the electron channelling effect in crystals in 1967, it was reported the strong crystal orientation dependence of the intensity of high energy backscattered electrons. The intensity of Back Scattered Energy Electrons (BSEs) varies quickly with the orientation when it is close to Bragg conditions, the Kikuchi-like patterns superposed with the BSE topographical images are then observed. When the primary electron beam can excite the two-beam diffraction condition in the crystal, the electron channelling contrast is generated. By this phenomenon, it is possible to image dislocations lying near crystal surface [178, 192] such as stacking faults (SFs), individual dislocations, and dislocations arrangements originated by tensile loading or fatigue because they can variate the backscattering by changing the crystal orientation [193].

There is a dependence of the crystal lattice orientation in relation to the primary beam, the electron wave field density inside of the crystal differs, leading to a variable inelastic backscattering. After multiple scattering, the electrons may be reflected by the surface, and the intensity of the resulting signal will depend on the crystallographic direction parallel to the primary beam [194]. Figure 3.1.14 describes the channeling effect when a lattice defect is present.

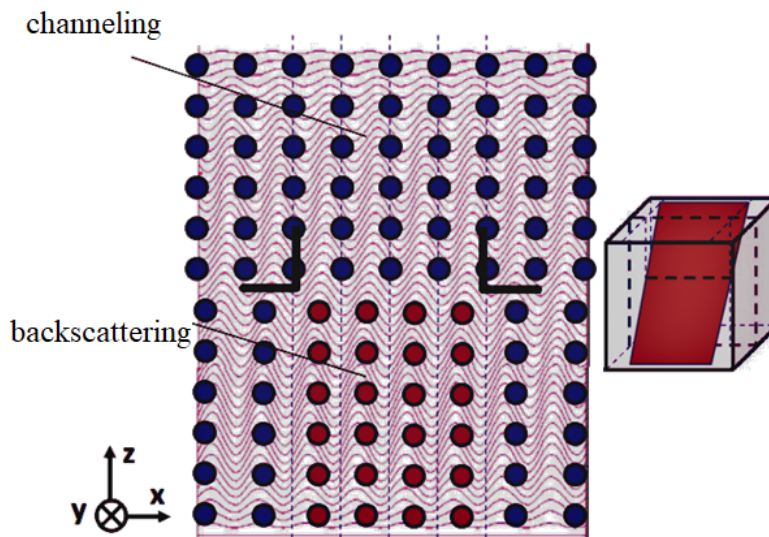


Figure 3.1.14: Schematic representation of the defect contrast formation in ECCI [194]

Under the proper two-beam condition, the crystal becomes quasi electron transparent, consequently, it appears dark in the ECC image. The bright areas are the ones in which the crystal is disturbed by dislocations, causing the backscattering. Figure 3.1.15 summarizes the ECCI imaging conditions and a representation of the ECC image obtained after the fatigue test, showing the dislocation arrangement.

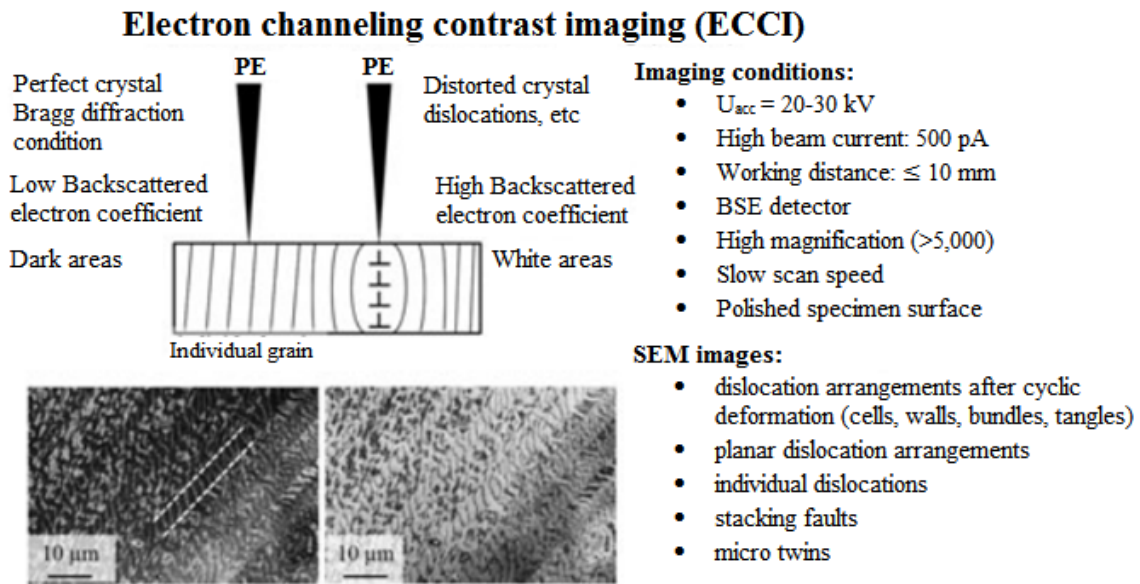


Figure 3.1.15: ECC image of the dislocation arrangement after fatigue test. The dislocation dense regions (walls, veins) appear as a bright contrast. The image on the side is in inverted contrast, being comparable to TEM studies [193]

The first attempt to image dislocations used the collected ECPs (Electron Channeling Pattern). But unfortunately, it does not determine crystal orientations of fine grain polycrystalline materials, combined with the lack of spatial resolution [195]. The selected area electron channeling pattern (SACP) technique was then built to solve this limitation. This technique works by rocking the electron beam at a certain location, reducing the region from which a pattern may be gathered. Rocking beam diffraction was firstly proposed in TEM [196], the sample stays in a fixed position and the beam is deflected. In SEM, this can be achieved by the use of two coils, where the beam is deflected mechanically [197]. The drawbacks encountered for this technique is that the rocking point does not coincide with the exact sample surface and the spherical aberration of the SEM objective lens affects the accuracy of the rocking beam mode, so the beam does not rock around a point but instead scans a much broader region [198]. On polycrystalline materials, this restriction indeed excludes the use of the standard rocking beam method. Some improvements have been done, but this method is limited to certain types of SEM [199].

The ECCI images can be done with two different approaches, without orienting the crystal or by using the ECP. Former studies have been done with the ECCI technique but without the control of the imaging conditions. Morin et al [200] have introduced the combinations of the ECP and the observation of the BSE images after tilting the samples in a good condition. The specimen was tilted until a dark Kikuchi line in the ECP coincides with the center of the pattern, indicating the channeling condition. However, the visualization of dislocation can be performed more precisely with various methods that have nowadays been developed to be used with modern equipment. The current

ECCI technologies comprise the R-ECCI, A-ECCI and the C-ECCI.

The Rotational-Electron Channeling Contrast Imaging (R-ECCI) [201] has one benefit over regular ECCI, which is the enhancement of the dislocation contrast homogeneity across wide regions by combining the images obtained at each rotated angle. Even though an automated rotation-acquisition technique custom-built software is required, this method may be used in any FEG-SEM with a BSE detector and a motorized goniometer with a rotation accuracy of 0.5° . One inconvenience from this technique is the lack of orientation information.

Other approaches are based on controlled oriented ECCI conditions, both A-ECCI and C-ECCI work by this technique. With the development of the EBSD, the ECP/SACP ended up falling into disuse, however, there is still an Accurate ECCI (A-ECCI) technique which shows some advances over the EBSD-aided techniques, with high spatial resolution [198]. The A-ECCI technique is based on the live acquisition of patterns collected by an aperture alignment to rock the beam in a Zeiss Gemini column. To do this pseudo-rocking, the electron beam is first deviated from the center of a predetermined aperture, causing the electron beam to be moved far away from the region of interest while hitting the sample at an angle. Then, using the beam shift control, the electron beam is moved back to the region of interest. This procedure is repeated to rock the beam on the region of interest, with the pattern being acquired as a function of rocking angle. However, this is only possible to execute at certain types of microscopes.

The alternative technique is the electron channeling contrast imaging under controlled diffraction conditions (c-ECCI), which was the one adopted for this research. The random method and EBSD approach for revealing dislocations was also ameliorated by the combination of the EBSD technique and the simulation of ECP patterns by using the Tools for Orientation Determination and Crystallographic Analysis (TOCA) program created by Zaefferer [202]. The software determines the tilt and rotation conditions to obtain the channeling contrast for the defined set of lattice planes. This is done by providing a simulated ECP pattern based on the inserted Euler angles observed during the EBSD scan. After the development of this technique, some authors have explored to control the specific condition for imaging dislocations [182, 203].

At present, c-ECCI micrographs have resolution comparable to TEM images. Figure 3.1.16 shows a comparison between ECCI and TEM dislocation visualization in γ -TiAl.

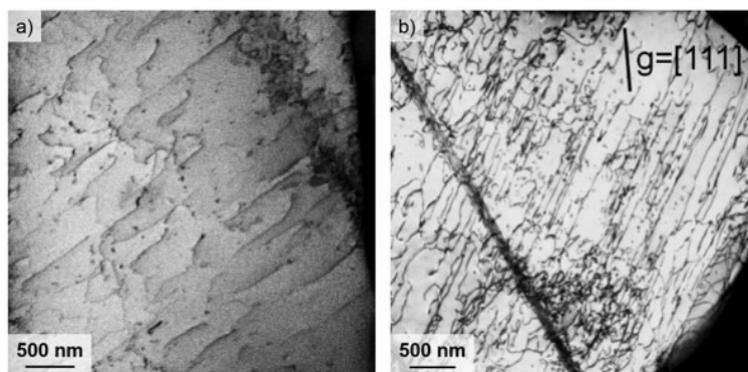


Figure 3.1.16: Comparison between a) inverted c-ECCI and b) conventional TEM micrograph of the dislocation arrangement in a globular γ -TiAl grain [193]

As TEM provides only small areas of observation, the c-ECCI technique shows as a good option to acquire a wider area and considerable amount of information. Another advantage is the sample preparation, once there is no need to make thin foils. Furthermore, the sample can be observed by ECCI several times, during the fatigue test, whereas for TEM the sample must be destroyed. However, despite having faster analysis, the ECCI technique is incapable to identify phases, nor quantify the amount of each of them. Therefore, it is necessary to use complementary techniques such as XRD to specify the phase fraction or EBSD to confirm by imaging the presence of the phases and make a microstructural correlation [86, 203].

A very good surface polishing, free of artifacts and damage is necessary for ECCI investigations, once the c-ECCI is destined to visualize dislocation arrangements near the surface, any artifact can affect the imaging quality. In this research, the dislocation structure in a broader area was analyzed in all heat-treated samples before and after LCF tests by c-ECCI in a Hitachi SU-5000 FEG-SEM system with 30 kV of applied tension. The two-beam diffraction condition for a well-oriented crystal was obtained with the aid of the TOCA software using the c-ECCI methodology developed by Zaefferer and Elhami [194].

3.1.5 Scanning White Light Interferometry

Scanning White Light Interferometry (SWLI) is a profilometry method, which uses light to reconstruct a 3D surface. The measurement is based on the light interference of a beam reflected from the surface and a reference light beam. The interference fringes or patterns are obtained according to the variations on the relief, the height difference between to detection the point will help to construct the sample surface. Light interferometry is a faster mode, which can measure vast surfaces in few minutes.

For the 2D analysis, the surface profile is obtained by a cross-sectional line considering several scans (Figure 3.1.17). Differently, the 3D profile comprises one scanned area (Figure 3.1.18). In previous works, it was reported that the 2D parameters are sometimes inadequate or unsuitable for surface characterization [204, 205].

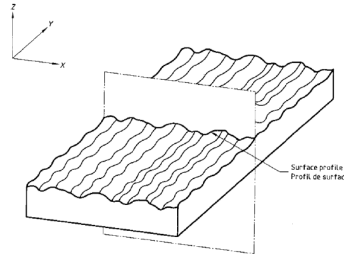


Figure 3.1.17: 2D Surface profile according to ISO 4287:1997

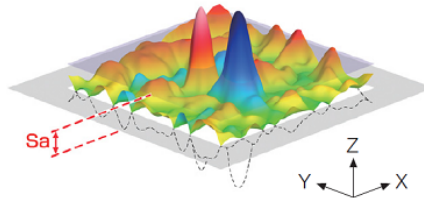


Figure 3.1.18: 3D acquisition according to ISO 25178-2:2012 (adapted) [206]

Quantitative measurements of the surface roughness were carried out by SWLI in a Bruker Contour GT-K 3D Microscope. The 2D surface roughness evaluation was based on ISO 4287:1997. Parameters such as arithmetical mean roughness value (R_a), Root mean square roughness (R_q), mean roughness depth (R_z), symmetry of surface (R_{sk}), and sharpness of profile peaks (R_{ku}) were considered. The ISO 25178-2:2012 norm was used for the 3D approach. The arithmetical mean height of the surface (S_a), superficial energy (S_q), the height of the highest peak (S_p), the absolute value of the height of the largest peak (S_v), the largest peak height value and the largest pit depth value (S_z), Skewness-asymmetry of the roughness shape (SSk), and sharpness of the surface (Sku) were chosen for being compared [207].

3.2 Experimental Procedure and basic observations

The 9Ni steel used in this study to investigate the mechanism of crack initiation was previously employed in another study for LNG application [5]. The chemical composition according to the supplier is available in Table 3.2.1.

Table 3.2.1: Chemical composition of the 9Ni steel given by the supplier

Chemical element	% Weight
C	0.04
Mn	0.53
P	0.006
S	0.001
Si	0.23
Ni	8.99
Mo	0.01
V	0.003
Al	0.048
Cu	0.06
Cr	0.04
Ti	0.001
Nb	0.004
N	0.004

The investigation of the mechanism of fatigue crack initiation in 9Ni steel involves the three following steps:

1. Thermal treatment to obtain different microstructures
2. Mechanical characterization to observe their behavior
3. Microstructural characterization that will be linked to mechanical properties

Based on the effect of the thermoprocessing routes available for the 9Ni steel that affect the microstructure (e.g presence of austenite and matrix morphology), blocks of the raw material were subjected to several heat treatments. The heat treatments adopted focused on structure modifications in the matrix as well as incorporating an iron-fcc structure within the iron-bcc matrix, this phase will stay localized at the interfaces. The heat-treated blocks were divided according to the heat treatment adopted and subsequently characterized by several techniques for comprehending the microstructural changes performed.

3.2.1 Heat Treatment

Based on the literature review, four different tempering heat treatment times were proposed to achieve the highest and lowest amount of reversed austenite. The samples were austenitized at 900 °C for 1 hour and 45 minutes, the parameters were adopted to obtain wide packets allowing a better microstructure visualization. The duration of each tempering treatment was defined according to the investigations done by Kacem [5]: 30 minutes, 5 hours, 10 hours, and 20 hours at 600 °C. Figure 3.2.1 summarizes all the heat treatment routes for the first step of the experiment. The water-quenched microstructure (WQ) was also evaluated in this work because it has a more clear lath martensitic structure and the matrix morphology is somewhat comparable to that of 12Cr martensitic steel (which already has a proposed mechanism for fatigue crack initiation).

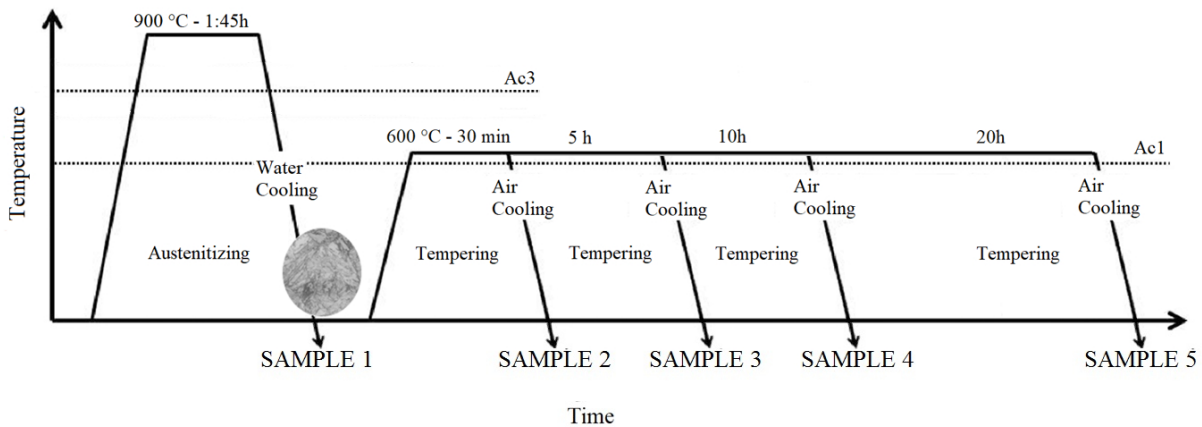


Figure 3.2.1: Heat treatments routes adopted for this work

The XRD analysis was used to measure the amount of phases present in the heat-treated samples. The results indicate that the austenite content follows a near-parabolic trend, where the peak is reached at 10 hours of tempering heat treatment, with an amount of 11% in volume (Figure 3.2.2). The sample that has only been submitted to quenching heat treatment showed an amount near 8% of austenite. As reported in the literature [130], as tempering time increases, the diffusion of carbon in a longer distance is permitted, enriching the existing austenite located at the boundaries. However, after the peak is reached after a certain time, this austenite becomes mechanically unstable, transforming back to martensite when the sample is cooled down.

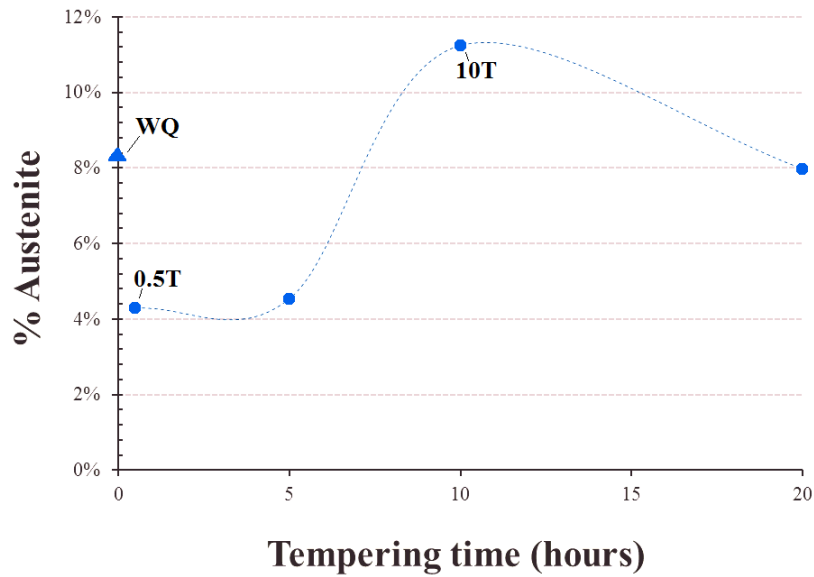


Figure 3.2.2: Austenite fraction measured by XRD as a function of the tempering time. WQ: water-quenched, 0.5T: tempered for 30 minutes and 10T: tempered for 10 hours.

Based on the XRD results and the two natures of obtained austenite (retained and reversed austenite), three microstructures were chosen to be analyzed. The samples were chosen relying on their austenite content together with the tempering time to reach a sufficient amount to be analyzed. The quenched microstructure with 8% of retained austenite (from now on labeled as WQ), the microstructure tempered for 30 minutes with 4.5% of reversed austenite (0.5T), and the microstructure tempered for 10 hours with 11% of reversed austenite (10T).

For the considered thermoprocessing routes, the corresponding Vickers hardness are displayed in Table 3.2.2.

Table 3.2.2: Vickers Hardness

Water Quenched (WQ)	Tempering 30 min (0.5T)	Tempering 10h (10T)
362 HV10	242 HV10	233 HV10

In order to get an overview of the obtained microstructure, the samples were first characterized by light optical microscopy (LOM), using two different chemical etchants:

- Nital 4% (4 ml HNO_3 in 96 mL of Ethanol);
- Klemm's etching ($\text{Na}_2\text{S}_2\text{O}_5$, water and $\text{K}_2\text{S}_2\text{O}_5$);

The Nital etching is used to create a contrast of the high angle boundaries present in the microstructure. Since the tempering time is long enough to allow the formation of bainite [109], there is a need to investigate and differentiate all the phases and microconstituents, once the bainite and tempered lath martensite are quite similar in morphology. Klemm's etching is a useful tool to optically differentiate those microconstituents and also indicate the presence of austenite. The Klemm's tint etchant colors the ferrite (bainite) in blue; martensite in brown/yellow and does not etch the austenite, appearing as white in the micrograph.

To reveal the microstructure, the samples were cut parallel to the rolling direction and prepared following the metallographic standards. The specimens were ground into smooth and mirror surfaces by SiC paper and fine polished by diamond paste until 1 μm . Finally, the samples were submerged for 3 seconds in a Nital solution. For revealing the different micro constituents, the Klemm's etchant was poured into the polished surface until it turns into a dark blue color.

The optical micrographs are divided in Figure 3.2.3 according to each heat treatment and etchant used for revealing the microstructure. The LOM technique gives a general idea of the hierarchical martensitic structure but still is incapable to resolve the laths nor making the differentiation of the martensitic units.

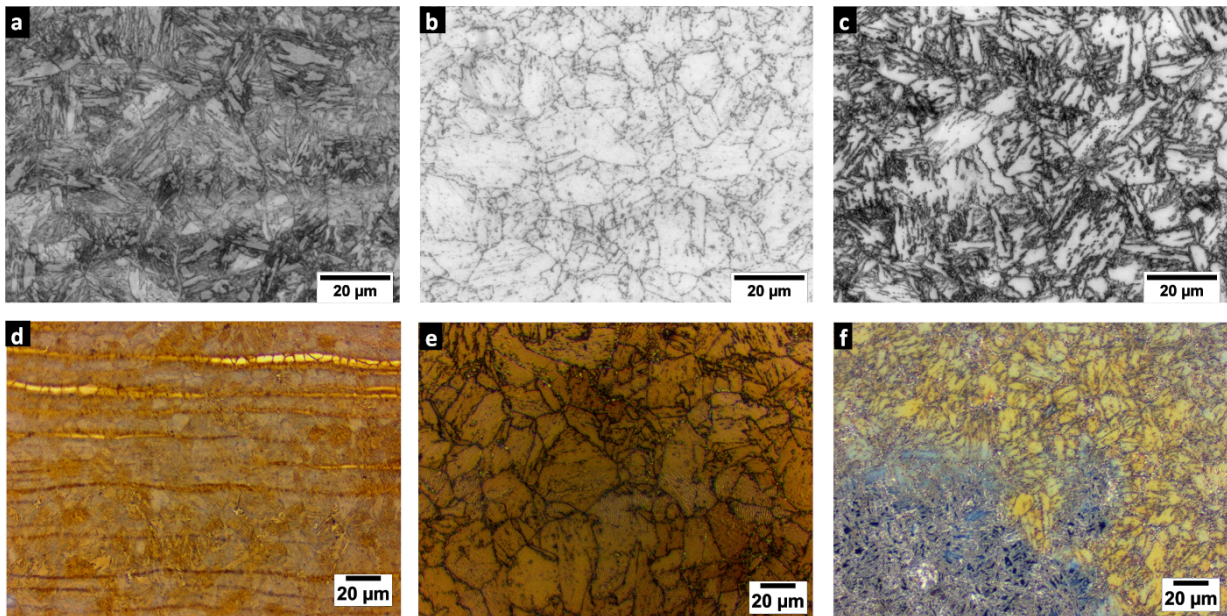


Figure 3.2.3: Nital 3% and Klemm's II solution: sample WQ (a and d), sample 0.5T (b and e) and sample 10T (c and f). The yellow/brown zones indicates the martensitic constituent, blue zones corresponds to the bainitic constituent and the lighter dots or bands are the austenitic phase

SEM micrographs from the same materials (Figure 3.2.4) show more refined details of the microstructure etched by Nital, the white phase present at the interfaces increases with the tempering time. Energy-dispersive X-ray spectroscopy (EDS) analysis indicated distinct contents of gammagenic elements (Ni and Mn) in the matrix and the white zones of the 10T sample (Figure 3.2.5) thus, we can infer that the white phase, richer in Ni and Mn, correspond to reversed austenite. The findings are in accordance with the same observation on the QIT heat treatment reported in the literature [22]. The area fraction of the white zones was calculated by Image J software [208] and 15% of each observed micrograph corresponds to the white zones for the 10T microstructure and 5% for the 0.5T microstructure. Those results are closer compared to the fraction estimated by the XRD technique, reinforcing that they correspond to the reversed austenite.

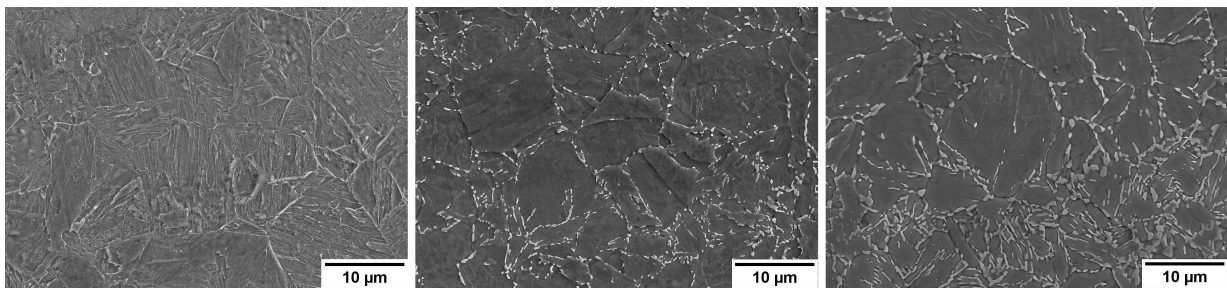


Figure 3.2.4: SEM micrographs of 9Ni steel. WQ sample (left), 0.5T (middle), 10T (right)

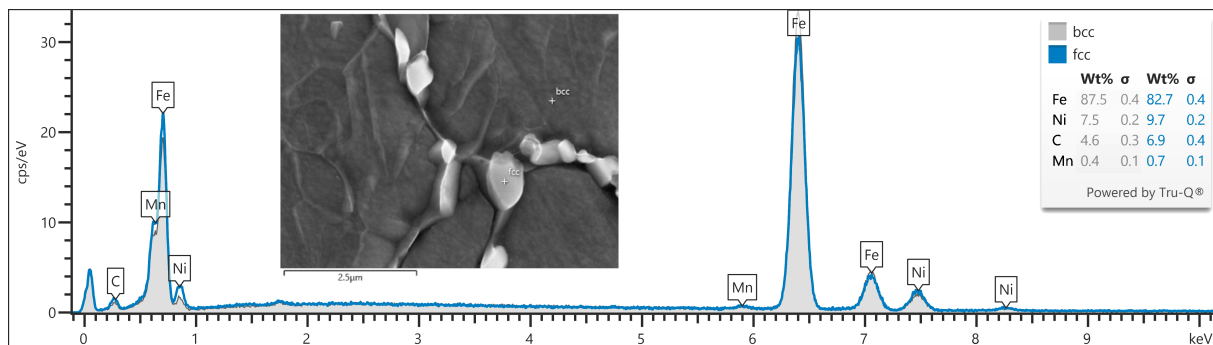


Figure 3.2.5: EDS point analysis indicating element segregation into the white zones, identified as reversed austenite

3.2.2 Low cycle fatigue Testing

Flat LCF specimens were cut by spark erosion according to ASTM E606. The geometry of the specimen has a gauge length of 12 mm and a cross-section of 6 mm x 3 mm. The vertical axis of the specimen is parallel to the rolling direction (Figure 3.2.6).

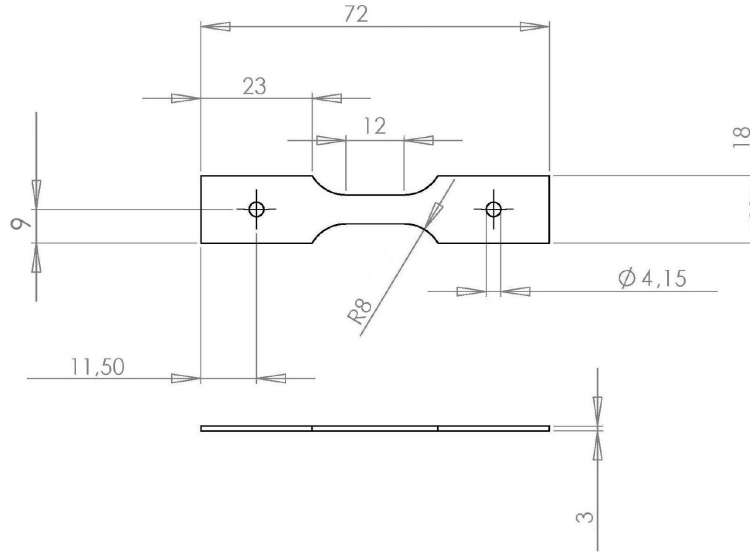


Figure 3.2.6: Low cycle fatigue specimen geometry according to ASTM E606

The flat geometry was chosen to facilitate the EBSD/c-ECCI acquisition and proper surface analysis. For further crystallographic analysis by EBSD and c-ECCI, a smooth surface free of artifacts must be achieved. For that purpose, LCF specimens were prepared by mechanical polishing and finished with a $\frac{1}{4}$ μm diamond paste. Additionally, a fine-polishing step with Struers OP-U 0.04 μm colloidal silica suspension was performed with a variable time according to the hardness of the sample. Two EBSD maps with an approximate area of 80 μm x 40 μm parallel to the rolling direction were taken prior to deformation for each specimen.

LCF tests were conducted on an electromechanical Instron Schenck Trebel RMC10 machine under total strain control by using a strain gauge extensometer stuck on the specimen. The tests were performed at room temperature in a fully push pull mode (strain ratio $\epsilon_{\min}/\epsilon_{\max} = -1$) using a triangular waveform with a constant strain rate of $4 \times 10^{-3} \text{ s}^{-1}$. The strain variations $\Delta\epsilon_t$ were ranging from 0.8% to 1.6% for the WQ sample. For the 0.5T and 10T samples the total applied strains were: $\Delta\epsilon_t = 0.8\%$, 1.2% , and 1.6% . The fatigue life N_f , is defined as the number of cycles needed for a 25% drop in the tensile stress taking as a reference the (pseudo) stabilized hysteresis loop. Tests were repeated twice in order to confirm the results. Moreover, interrupted LCF tests were also realized at defined fatigue life fractions to observe the microstructural and topographic evolution.

3.2.3 Post Fatigue Characterization

Successive cyclic loadings in the material are known to provoke permanent changes in the dislocation structures that will lead to surface topography. The material's response is also known to be dependent on its microstructure. Therefore, observing and correlating the surface changes will help us to understand the material's response and by combining the dislocation changes, a mechanism that could explain fatigue crack initiation can be proposed.

The topography of the deformed specimens WQ, 0.5T, and 10T was evaluated by SEM in an area comprising about 300 Persistent Slip Marks (PSMs) (0.5% of the total gauge area). A categorization of the PSMs according to the literature was realized for the specimens with 1.2% of applied strain. This level of deformation was chosen as a reference because it has the most proper surface to make the topographical evaluation with a sufficient number of PSMs for the three microstructures. At the failure stage, the austenite content was measured again by XRD to determine the austenite stability. Quantitative measurements of the surface roughness were carried out by SWLI-Light Interferometry. The surfaces were scanned three times and five areas with dimensions of 120 μm x 160 μm were collected from each specimen. Once the data follows a normal distribution, the results were submitted to Analyze of Variance calculation (ANOVA).

At each stage of the interrupted LCF tests (σ max, 5%, and 50% of fatigue life), EBSD scans were performed to observe changes in the microstructure throughout the cycling straining, reference points were marked in each specimen in order to help to recover the same scanned zone. In addition, concomitant c-ECCI imaging was used to observe the dislocation structures at the same region. The same conditions used at the initial state characterization were adopted. The average EBSD scanned zone was 60 μm x 40 μm with a 100 nm step size, covering about 100 blocks and 47 packets. Two zones were recorded by EBSD and evaluated at each level of strain to get a significant amount of data.

A cross-section view by EBSD comprising half part of the total gauge length was also done (Figure 3.2.7) focusing on the visualization of the microcracks and intrusions and their relation to the microstructure. Several scans of 2 x 2 μm were done with a step size of 30 nm to follow the intrusions path, this smaller step size was chosen to allow the identification of the possible presence of nanograins around the cracks.

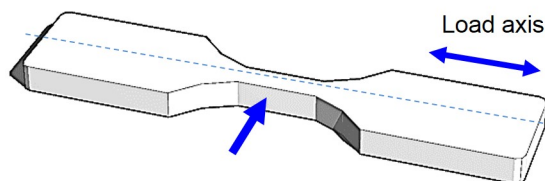


Figure 3.2.7: Broad cross-section cut on fatigued specimens

To achieve a better understanding of the relationship between crystallography character and the susceptibility to fracture, the martensite parent grain was reconstructed. As the orientations relationships (OR) such as Greninger-Troiano, Nishiyama- Wassermann, and Kurdjumov-Sachs are approximations and differ from each other by a small degree [209], the 24 Kurdjumov-Sachs variant orientation relationship was adopted for the martensite parent grain reconstruction in this study. The martensite parent grain reconstruction based on the 24 Kurdjumov-Sachs variant orientation relationship was accomplished by an algorithm developed for MTEX analysis toolbox in MATLAB [29]. For the best fit, in this reconstruction, a minimum grain boundary threshold of 3° is used to ignore the dislocation arrangements.

It is also necessary to comprehend the deformation mechanism on a very small scale (dislocations) to establish a parallel to the findings in the literature. The deformation in metals is originated from dislocation motion, slip, and twinning mechanisms. The slip mechanism is more prominent for polycrystals [8]. High-resolution techniques were used as support allowing the observation of dislocation changes beneath the deformed surface. The cross-sectional FIB cuts also helped the observation of the shape of the PSMs and the sites of crack nucleation with finer details. Specific zones with pairs of extrusions-intrusions were chosen from the samples and FIB lamellas were extracted for deep analysis with TEM, HRTEM, and TKD techniques.

Chapter 4

Results and Discussion

In this chapter, each material, that was briefly introduced in the previous one, is investigated in detail at each respective subchapter. First, it starts with a complete description of the microstructure of each considered heat-treated material. Then the fatigue behavior is studied in terms of cyclic accommodation and fatigue resistance. Finally, the fatigue feature is explained based on deep analysis of the evolution of the microstructure, accurate determination of intrusions and extrusions to reach the ultimate goal: the mechanism of crack initiation in the 9Ni steel in regards with the material metallurgy.

4.1 Water Quenched 9Ni steel - WQ sample

4.1.1 Non-deformed state

4.1.1.1 Matrix Evaluation

After austenitization at 900°C for 1h 45min and water quenching, the WQ sample exhibits a matrix composed of thin laths. The average prior-austenitic grain size measured by the line segment method is 14 μm , with a packet size of 5 μm , and a block size of 3 μm . The laths have approximately 400 nm of width measured in the TEM micrographs and are fulfilled by dislocation tangles spread throughout the analyzed area (Figure 4.1.1).



Figure 4.1.1: TEM micrograph of the WQ sample

In order to visualize a partial crystallographic orientation of the microstructure, a representative area was taken from the EBSD IPF map along the rolling direction and it shows that this material does not have any preferential texture (Figure 4.1.2).



Figure 4.1.2: Inverse Pole Figure of a representative zone showing absence of any preferential texture in the WQ material

The austenitic phase is suggested by only very few dispersed indexed pixels (Figure 4.1.3), however this can not guarantee that only a single pixel is the austenitic phase. For that reason, no cleanup procedure was used trying on revealing the secondary phase, not only for the amount measurement but also for attesting the austenite homogeneous distribution. The 8% volume fraction of austenite measured by XRD is not confirmed by the EBSD phase maps. The reasons that may affect the austenite indexation are their

thickness, the effect that the time and dose of incident radiation in a zone can induce the phase transformation or the approach adopted for surface preparation [210]. Another technique such as TEM should allow a more deep and precise investigation concerning the very thin austenite films. In an investigation of austenite stability conducted by Knijf [121], it was noticed a 40% divergence in the determination of the volume fraction of austenite by EBSD and XRD, demonstrating the need for proper detection method selection.

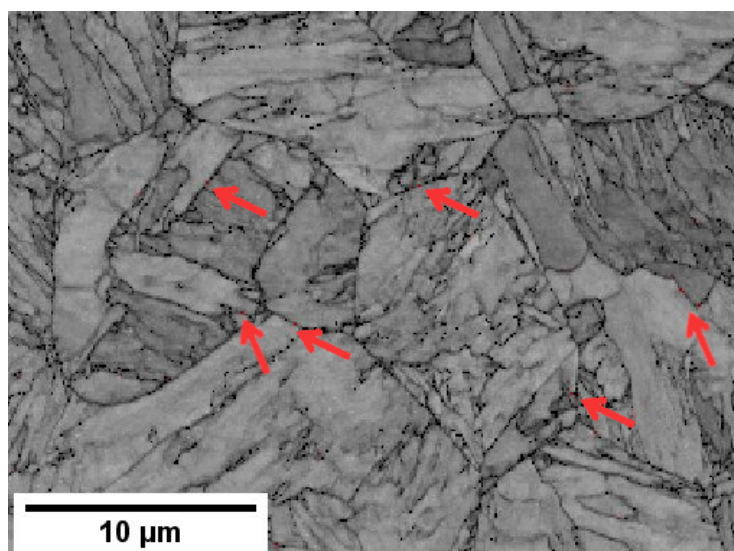


Figure 4.1.3: Phase map showing very few indexed pixels as austenite pointed by red arrows in the WQ material

Contrarily to EBSD Phase Maps, TEM in the imaging mode and in the Selected Area Diffraction (SAED) was successful to image the retained austenite. The 220γ diffraction plane was chosen by Selected Area Diffraction Spot (SAED) and dark-field imaging highlighted the nanometric austenitic films, with an average width ranged between 20 nm to 200 nm (Figure 4.1.4). Those very thin austenite films have already been reported in the literature [112, 113].

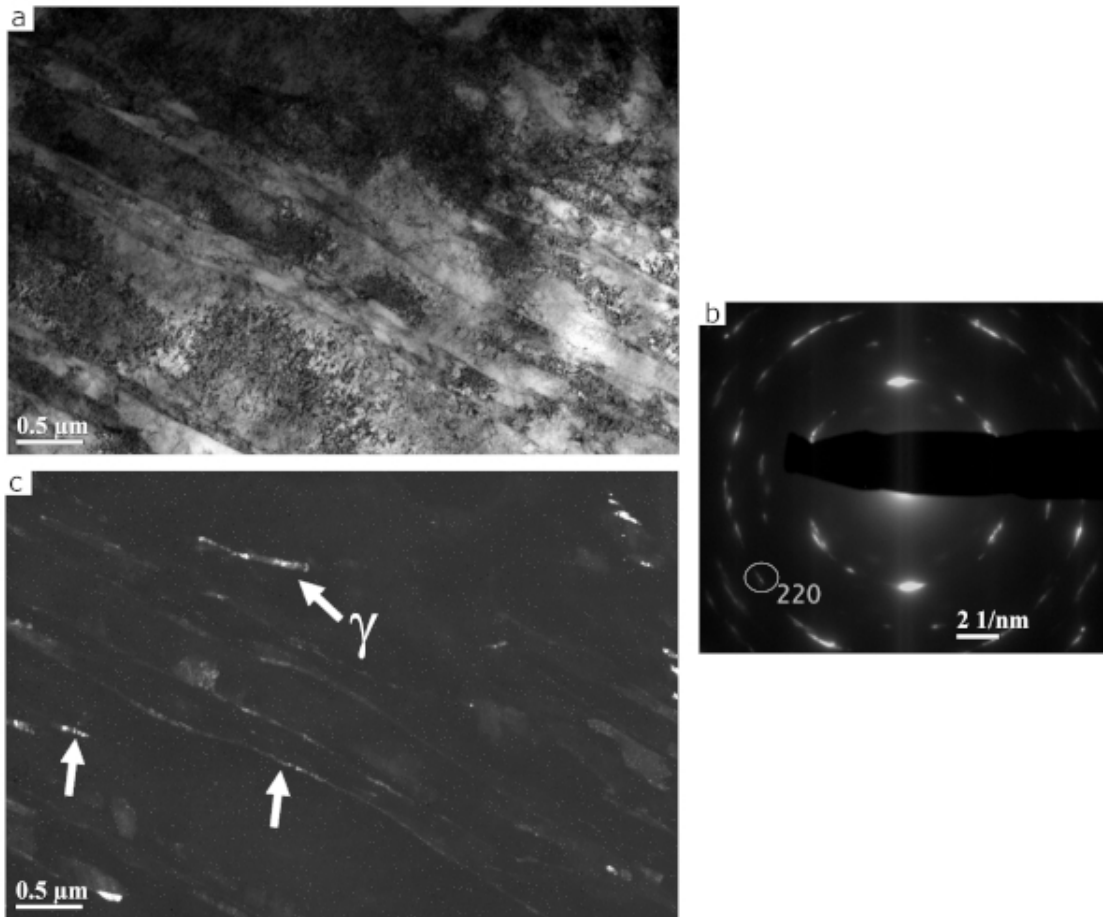


Figure 4.1.4: a) Bright field image TEM of WQ 9Ni steel, b) Selected Area Diffraction Spot (SAED) of $(220)\gamma$, c) dark field image of the same area highlighting the austenitic phase

The c-ECCI technique allows a broader view of the dislocation's distribution in a selected crystallographic plane (Figure 4.1.5). The thin laths are very well visible with a large amount of dislocations spread through the entire microstructure, the darker zones belong to $\vec{g} = 0\bar{1}1$ oriented plane. A closer look at the same scanned area points to very thin lighter spots distributed along the boundaries is shown in Figure 4.1.6. Considering the morphology and the difference in contrast seen by TEM, we can correlate, by analogy, those very thin light spots to the austenite films. Figure 4.1.7 also shows some twins found in the microstructure in the $\vec{g} = \bar{1}01$ oriented plane, as already demonstrated by this technique in TWIP steels [211].

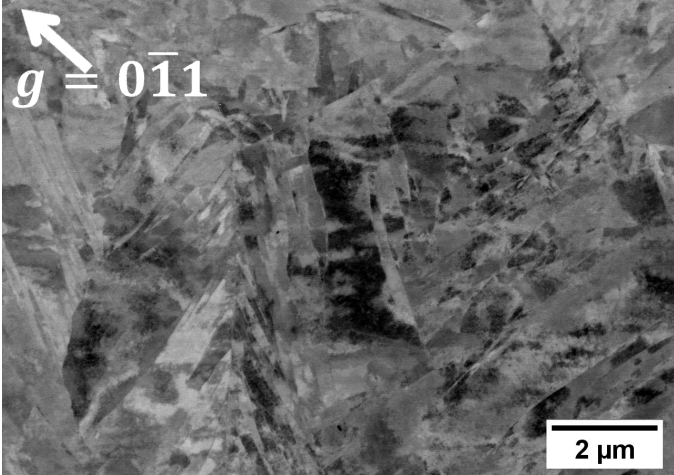


Figure 4.1.5: ECCI image showing the WQ structure of 9Ni steel

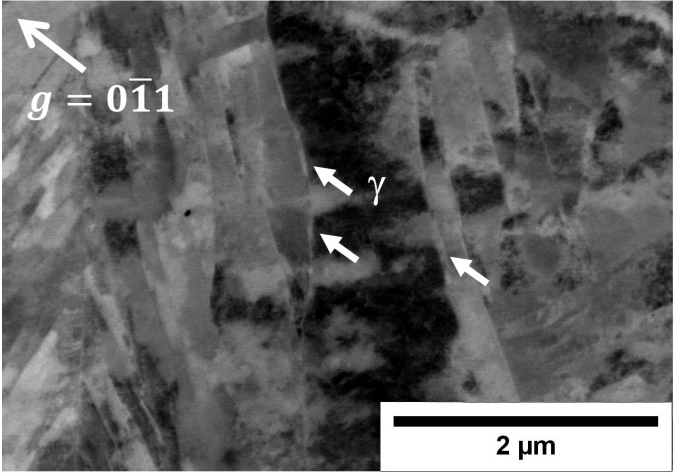


Figure 4.1.6: ECCI image showing the WQ structure of 9Ni steel, the austenite is indicated by the white arrows

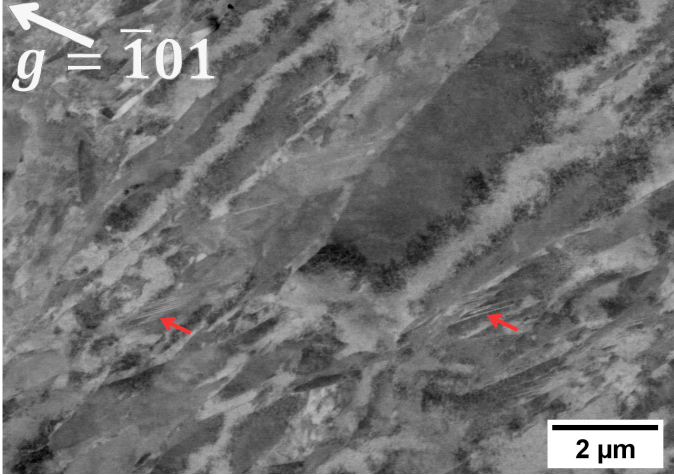


Figure 4.1.7: Twins identified by ECCI technique in WQ sample as indicated by the red arrows

The KAM approach was used for measuring the local misorientations at the initial state and helped to get a general idea of the distributions of strains generated by dislocations originated from the quenching heat treatment. A representative area of the EBSD KAM maps shows a very misoriented structure (Figure 4.1.8). Misorientation with less than 1° is displayed by the blue color, green color indicates misorientations between 1° and 2° , yellow between 2° and 3° , orange between 3° and 4° , and red between 4° and 5° . Even without applied deformation by LCF, the initial microstructure shows misoriented zones induced by the quenching heat treatment. The blue zones are those that are free from lattice distortion and almost free from strain. When a parallel is established between the LSM+IQ maps (Figure 4.1.9) and the KAM maps, it is observed that the misorientations highlighted by KAM surround low-angle boundary configuration comprised between 1° to 5° (dislocations) highlighted by the LSM+IQ maps. These observations are relevant with the previous ECCI investigations (Figure 4.1.6). Part of the structure, such as the martensite lath well oriented for ECCI in the center of the micrograph shows a few amount of entangled dislocations in its core, and will induce a slight misoriented area. The arrays of GND may, on the other hand, correspond to some lath/lath or lath/block interfaces.

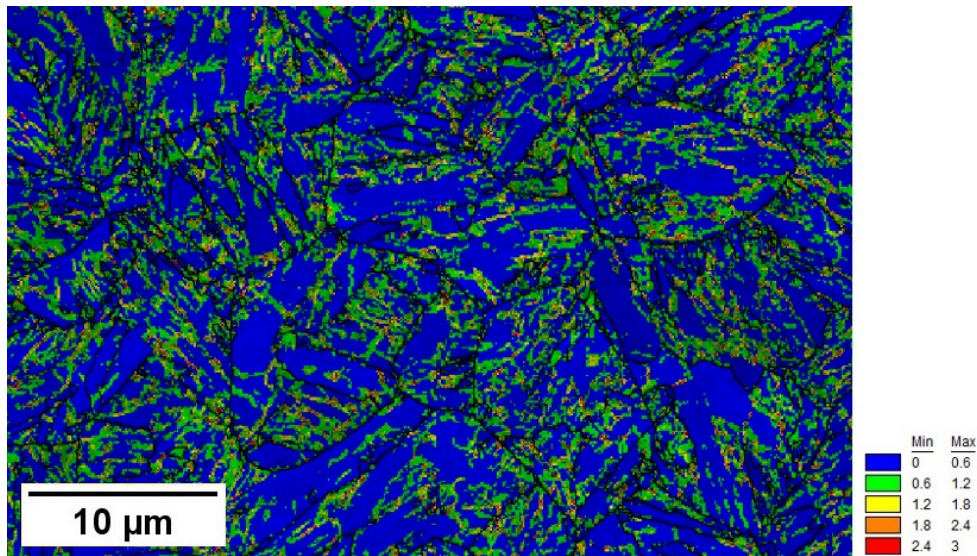


Figure 4.1.8: Kernel Average Misorientation maps showing an initial microstructure composed of highly misoriented zones

The LSM presents the spatial distribution of the boundary traces associated with a specific misorientation. High angle boundaries (HAB) corresponds to 15° misorientation between the measured points and usually, they are equivalent to the grain boundaries highlighted by LOM. Although this is not the case for the martensite, where those misorientations can also correspond to packets or sometimes blocks, a parent grain reconstruction is necessary to differentiate the martensitic structure based on the

variant orientation (this topic will be further discussed). In LSM maps, the low angle boundaries (LAB) comprised between $1\text{-}15^\circ$ can be correlated to laths, subgrains and dislocations substructures or tangles. The LABs were subdivided into groups of misorientations between $1\text{-}5^\circ$, corresponding to dislocation tangles, and $5\text{-}15^\circ$ were classified as microstructural substructures such as laths, subgrains or dislocation cells.

The observations indicated that the material in a pre-deformed state already shows a significant amount of GNDs inherited from martensitic phase transformation that were highlighted by the KAM maps as local misorientations. The martensitic transformation also reflects in a rich and finer structure indicated by the LSM maps. The finding goes in an opposite way that would have been taken by analyzing a simple structure like the ones found in ferritic and austenitic steels.

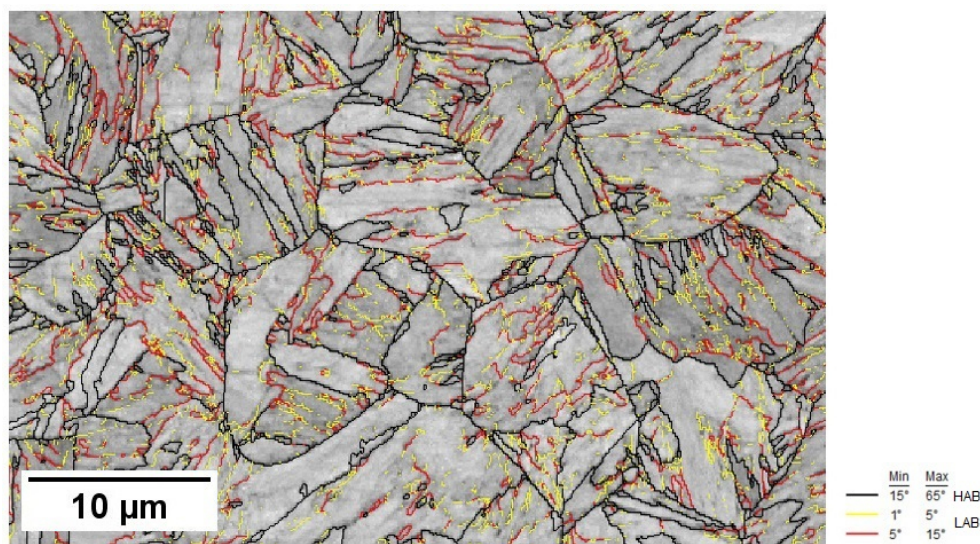


Figure 4.1.9: Line Segment Misorientation + Image Quality - Misorientation distribution EBSD maps for WQ sample at the initial state

4.1.2 Cyclic stress-strain response and fatigue resistance

The cyclic accommodation of the WQ material is represented by the evolution of the stress amplitudes with the number of cycles and with the life fraction at different strain levels in Figure 4.1.10.

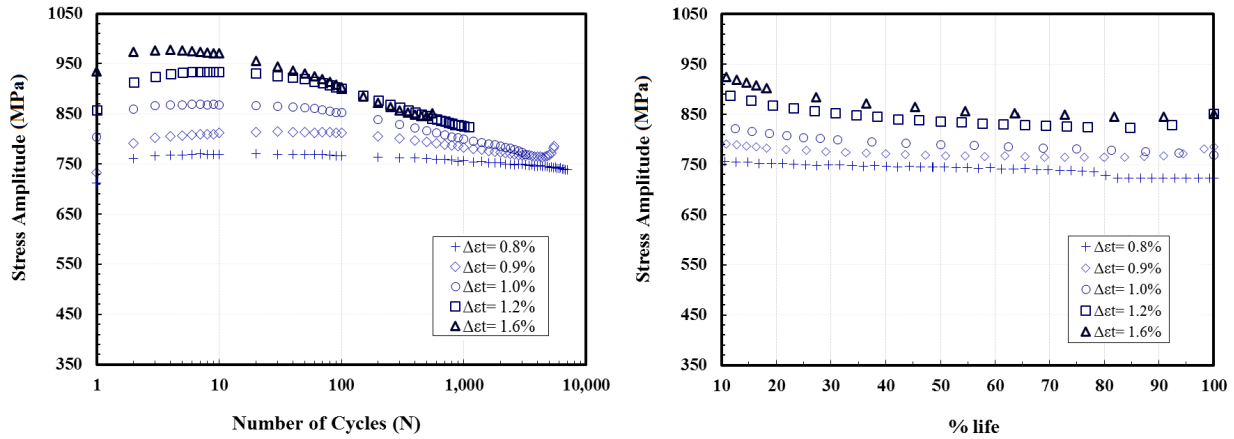


Figure 4.1.10: Evolution of the stress amplitude versus the number of cycles (left) and versus the fatigue life fraction (right) for the different total strain tests for WQ sample

The curves present in the graph show that the material response consists of a cyclic hardening accompanied by a cyclic softening. The hardening period gets shorter as the applied total strain rises, and it only accounts for a minor portion of the fatigue life (less than 2 %). When the applied deformation is higher, however, the softening period appears to last longer. The multiple entangled dislocations with limited mobility in martensite laths can be freed when an external force is applied. High strain loading causes high stress and a greater number of unlocked dislocations that can glide and recover the laths, resulting in significant softening. It is also expected that dislocations will reorganize, resulting in a more stable structure.

The cyclic stress-strain curve obtained from the quasi stabilized hysteresis loops is shown in Figure 4.1.11 together with the curve obtained from the peak stress of cyclic accommodation and the monotonic hardening curve. The stress softening is more noticeable at greater strain levels during the stable stage of the cycling. As can be seen, the initial hardening is comparatively constant at all applied levels of total strain and the softening more pronounced as the total applied strain increases.

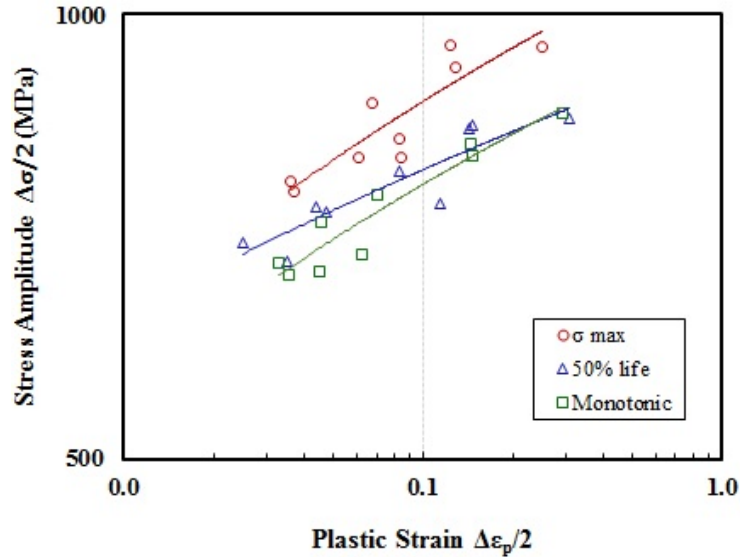


Figure 4.1.11: Cyclic and monotonic stress-strain curves

The fatigue resistance is presented in Figure 4.1.12 in terms of the relationship between strain ranges and fatigue life. The elastic strain range was essentially consistent throughout all experimental strain ranges, and the related line (the Basquin curve) remained above the plastic strain range data. This behavior is seen for several martensitic steels [212]. In general, the Manson-Coffin law fits well with a linear relationship in double log coordinates between the plastic strain and the number of cycles of fatigue to failure, which is not the case here. Nevertheless, the non-linear relationship of the plastic strain was observed in Nickel-based alloys, Aluminium-Lithium alloys, bainitic steels, low carbon steels, and 12Cr steels [171, 213–219]. The WQ microstructure follows this same trend, exhibiting a change in slope at $\Delta\epsilon_t=1\%$ ($\Delta\epsilon_p=0.2\%$). The above-cited research attributed this bi-linear behavior to the change in deformation mode, crack propagation modes and localization of plastic slip due to microstructural aspects.

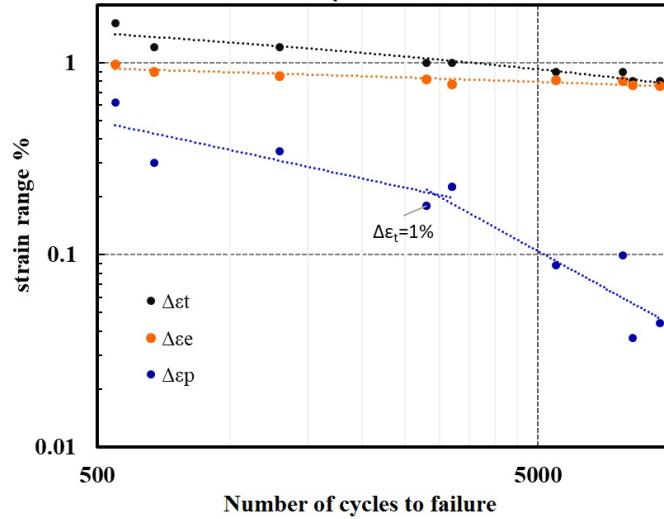


Figure 4.1.12: Manson-Coffin curves showing a point of changing in slope at $\Delta\epsilon_t=1\%$ ($\Delta\epsilon_p=0.2\%$)

Together with the main objective to provide a mechanism of crack initiation in 9Ni steels, the origin of the dual-slope in the fatigue resistance curve of this water quenched structure appeared as a motivating fact. It was thus decided to investigate the microstructure after fatigue tests at low and high strain levels ($\Delta\epsilon_t=0.9\%$ and 1.2%). The evolution of the microstructure and the damage was also considered at three stages of cycling: at the peak stress in the cyclic accommodation curve (σ_{\max}), 5% and 50% of the fatigue life. For these two selected strain ranges and the fatigue life fractions, the plastic strains are reported in Table 4.1.1.

Table 4.1.1: Plastic strain at several stages for each applied strain

$\Delta\epsilon_t$	$\Delta\epsilon_p$	
	0.9%	1.2%
σ_{\max}	0.16	0.31
5%	0.19	0.36
50%	0.22	0.41

The first stage of the proposed investigation is the surface evaluation of each specimen. Followed by dislocation structure analysis and cross section visualizations.

4.1.3 Topography Overview

In addition to the microstructural changes in the bulk of the material, during the cyclic plasticity, deformations at the surface will appear. Figure 4.1.13 displays the

topographical changes for all applied total strain levels at the end of fatigue life. At lower strain levels, a very smooth surface topography comprising very few isolated extrusions is evidenced. At high levels of deformation, a large number of coalesced extrusions have been identified. It is worth mentioning here that at $\Delta\varepsilon_t=1.6\%$, a network of extrusions is observed. In all levels of deformation, the extrusions on the specimen surface are generally positioned closely to $30-45^\circ$ from the load axis. The intrusions are identified in a lower amount than the extrusions, sometimes the intrusions identification gets be mixed up with the microcracks. The distinction between them is not easily done with a perpendicular incident electron beam, special sectioning techniques, in that case, are recommended. A detailed extrusion profile identification will be realized in a dedicated sub-chapter comparing the three microstructures.

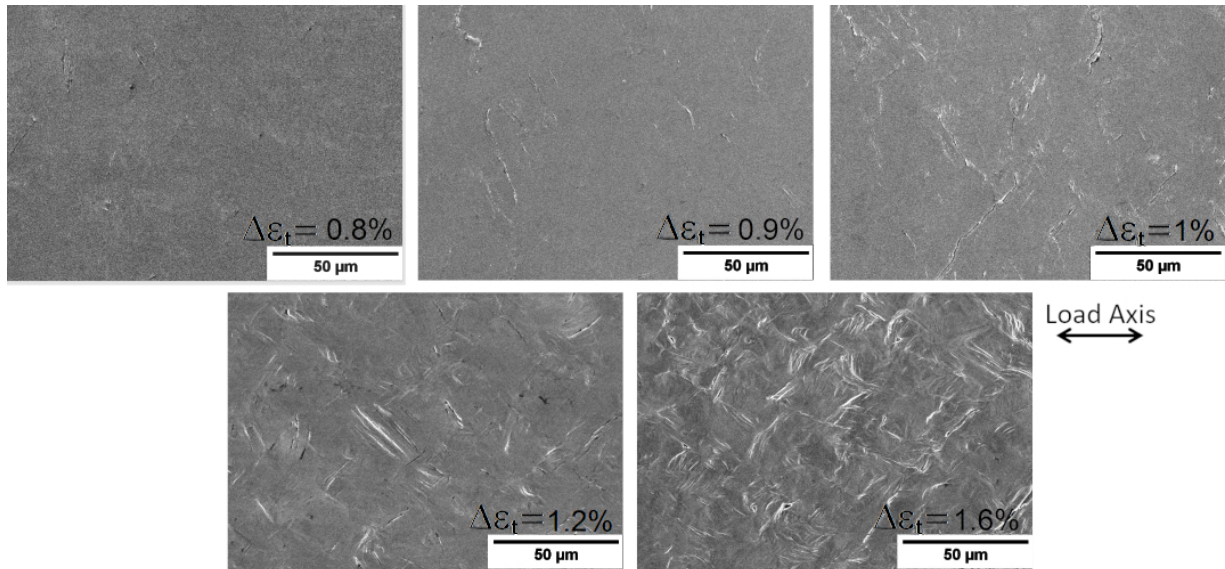


Figure 4.1.13: Surface roughness at life end of different LCF tests

4.1.4 Dislocation Structure and Microstructural Response

As mentioned just above, the bi-linear feature of the Manson-Coffin curve will be studied in detail from the dislocation structure analysis and the development of extrusion-intrusions pattern effect at two levels of imposed strain representative of each portion of the curve.

4.1.4.1 Extrusions – intrusions evolution at $\Delta\varepsilon_t=0.9\%$ low strain level

Figure 4.1.14 exhibits the progression of the same scanned surface evaluated by c-ECCI in the $\vec{g} = 0\bar{1}1$ plane during the course of the fatigue life. This zone was not scanned prior to cycling since it could not be anticipated whether or not it would be

triggered afterward. The slip steps are already present in the test done at $\Delta\varepsilon_t=0.9\%$, at σ_{\max} , although they are not abundant or immediately visible, as shown in Figure 4.1.14- σ_{\max} . The slip steps confirmed the quenched steel's capacity to accommodate plastic deformation. They are the earliest signs of an upcoming extrusion rising. After 5% of the fatigue life, the extrusions were easily formed, as seen in Figure 4.1.14. The existing extrusion grew as the number of cycles increased, and new extrusions developed. In addition, intrusions around the extrusion are noticeable. Extrusion and intrusion both made it difficult to define their exact position by direct observation.

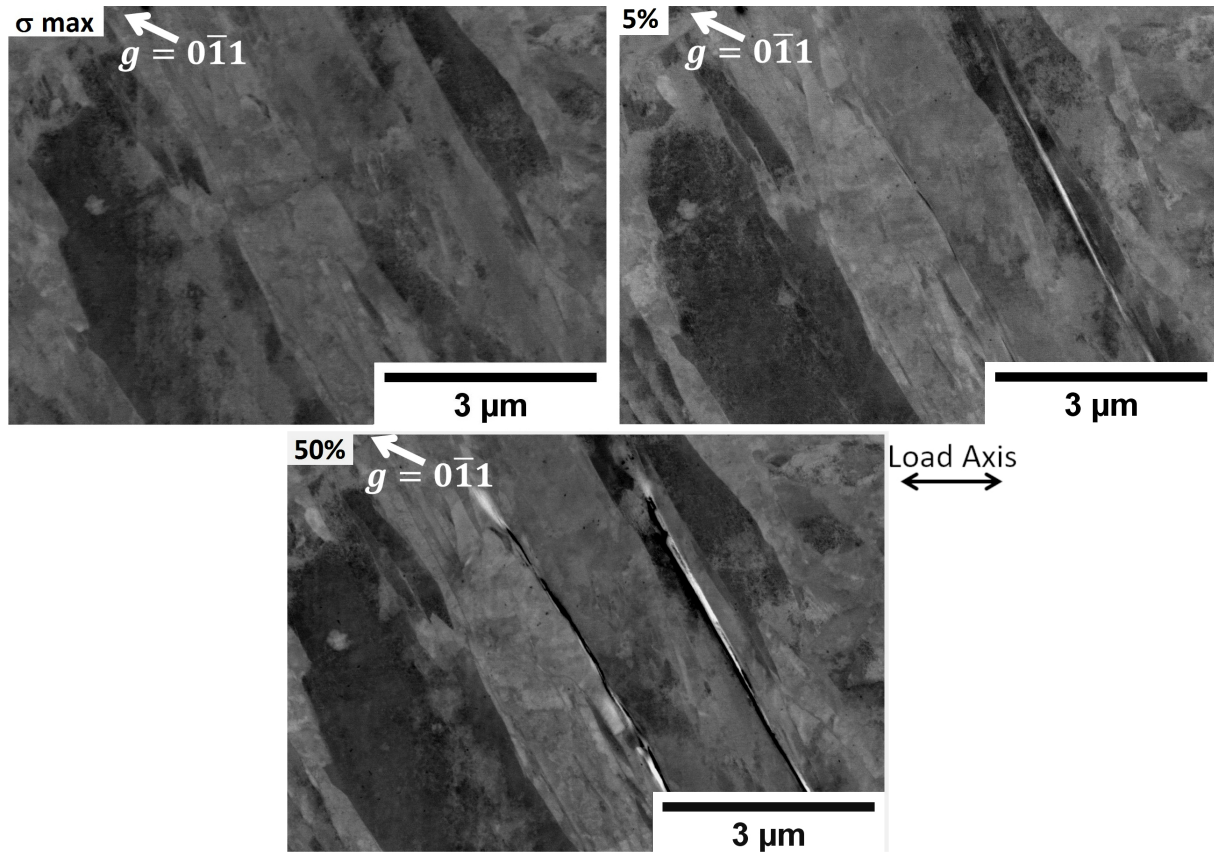


Figure 4.1.14: c-ECCI images showing the dislocation and topography of the WQ 9Ni at each stage of cycling ($\Delta\varepsilon_t=0.9\%$)

The EBSD analysis has been used to target a particular zone, and the $\vec{g} = \bar{1}01$ plane was then orientated with the help of the TOCA software to accentuate the dislocations. It was found by the contrast variation on the image that dislocations have a propensity to be swept and concentrate towards deformed zones (extrusions-intrusions), leading to the formation of new cells and subgrains, and the cleansing of the interior of these structures. A closer look at an extrusion in the region at 50% fatigue life in the $\vec{g} = \bar{1}01$ oriented plane showed a dislocation arrangement composed of very thin fragmented walls (Figure 4.1.15).

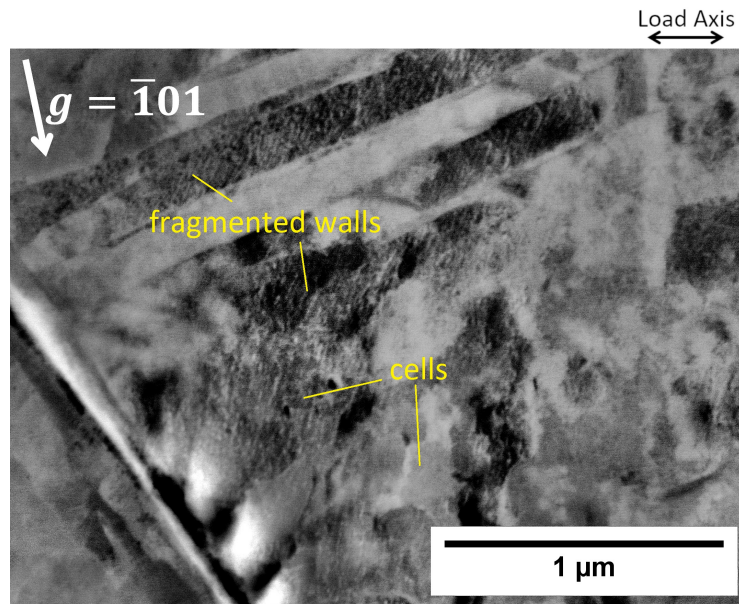


Figure 4.1.15: Planar dislocation structure localized within the laths next to the persistent slip marks at 50% of the fatigue life for the test at $\Delta\epsilon_t=0.9\%$

Contrarily from the pre-deformation state analysis where the measured KAM showed pre-strained structure due to the presence of the GNDs inherited from the $\gamma \rightarrow \alpha'$ phase transformation, the interest by doing a KAM approach after the LCF tests is to show the evolution in terms of local deformation that may be associated to the evolution of the local density of GNDs originated by the interaction of dislocations [170, 184–186].

A complementary approach from the EBSD analysis of deformation and recovery substructures was then accomplished by the KAM approach and LSM method. Figure 4.1.16 shows a small representative area from the total scan, exhibiting the evolution of the KAM at each stage of applied deformation. IPF and c-ECCI images were also included to give a clearer understanding of where the PSMs and the strain fields were located. The KAM does not evolve significantly along with cycling, only a very small increase in misorientation is observed at 50% of fatigue life.

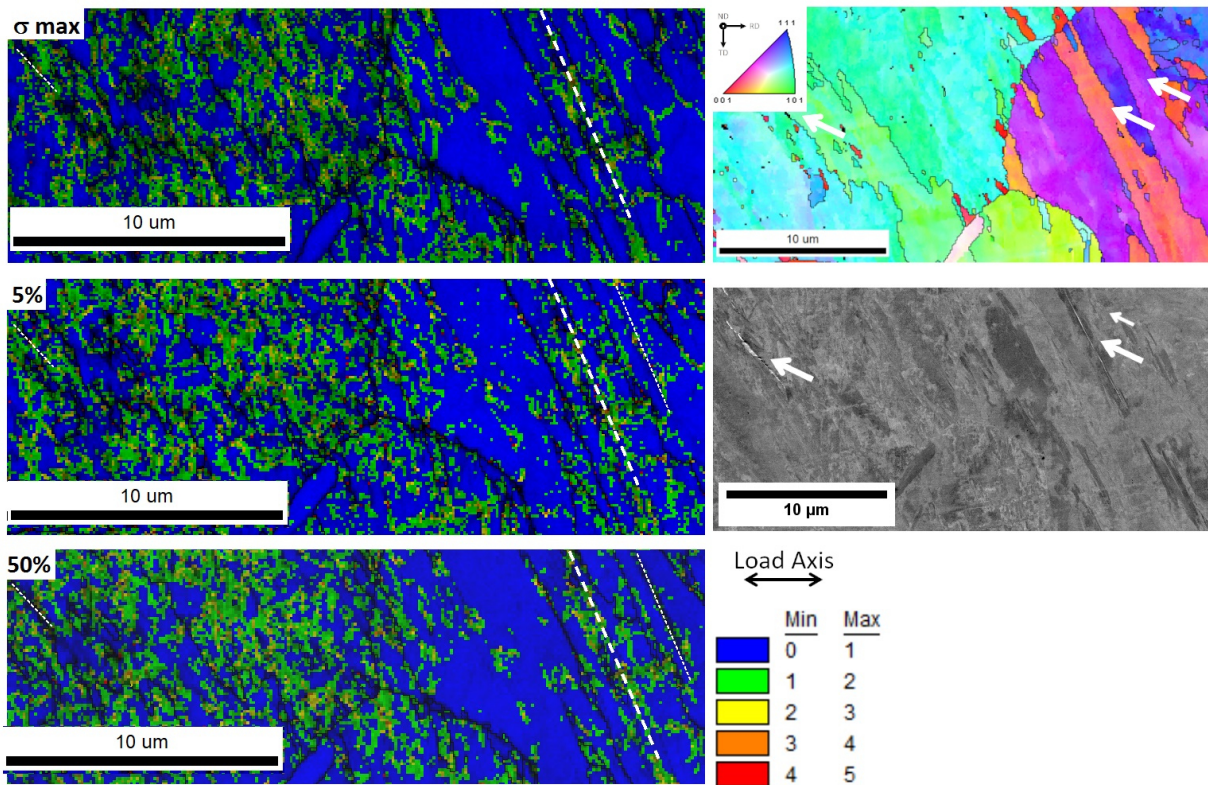


Figure 4.1.16: KAM maps evolution of WQ 9Ni steel at $\Delta\epsilon_t=0.9\%$. The white arrows and the dashed lines indicate the extrusions. c-ECCI and IPF images shows the scanned zone at 5% of life

Since the slip activity seemed to be concentrated near the extrusion and the KAM maps were not sufficient to provide any conclusion, LSM maps were analyzed to understand whether dislocation configurations and restructuration near the extrusions had happened (Figure 4.1.17). However, globally there was no significant variation between the different locations inspected after each life fraction. Some zones, shown by blue arrows, display different levels of misorientation, ranging from $1-5^\circ$ to $5-15^\circ$.

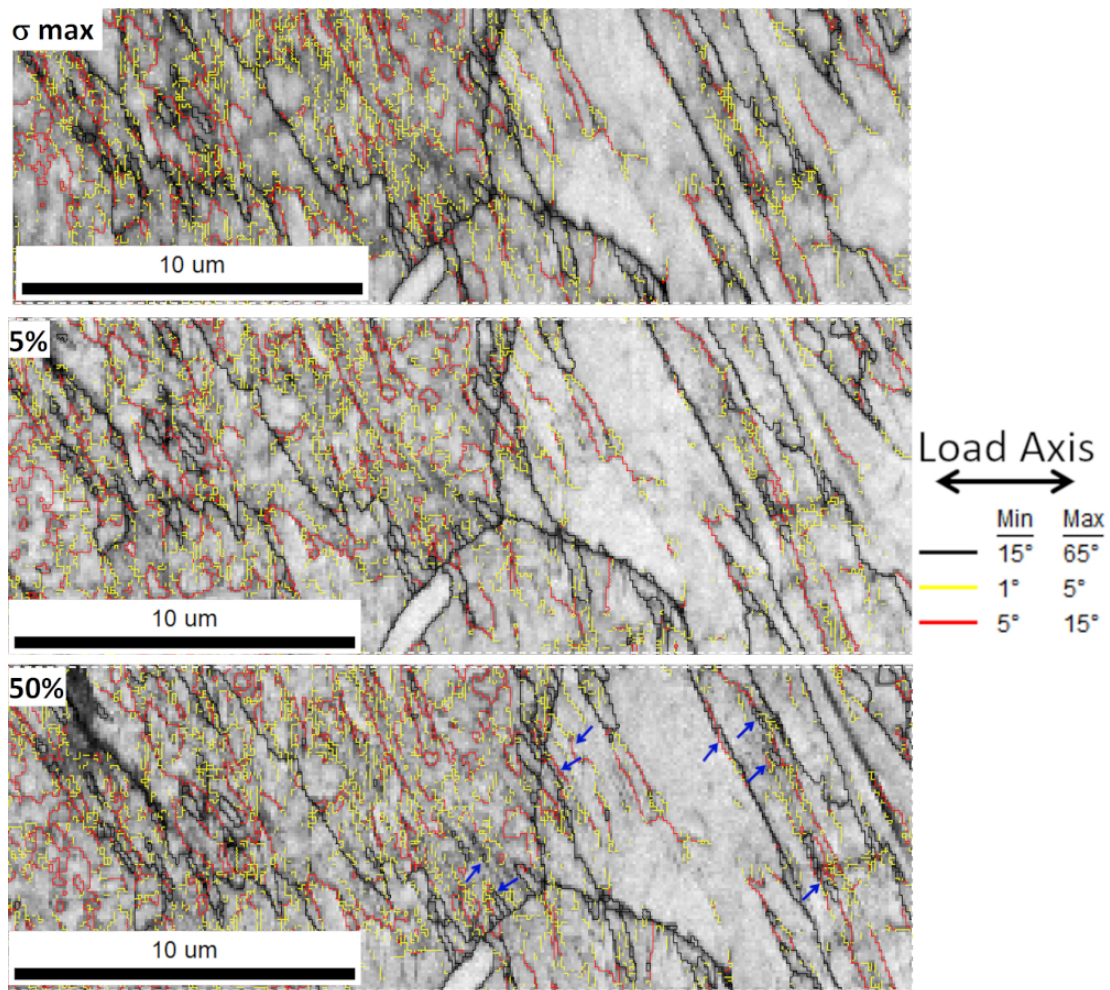


Figure 4.1.17: Image Quality + LSM EBSD maps at $\Delta\varepsilon_t=0.9\%$. The darker zones indicate the regions with the presence of extrusions. Blue arrows indicate the changing of misorientation level

As metallurgical interfaces such as grain boundaries or twin boundaries can cause strain incompatibility, they can be a location for crack initiation. Furthermore, because martensitic steel has so many distinct interfaces, this question comes more often. Despite the fact that the description of the martensitic structure in terms of hierarchical features (grain boundary, block, packet, lath) is now well recognized and accepted, trying to determine the orientation relationship of the block with the parent austenite established during the martensitic transformation is not that evident.

Recent research in dual-phase ferritic-martensitic steels has identified the previous austenite grain boundaries as crack nucleation sites [220]. Moreover, it has also been observed that the martensite properties are likely related to block size and its misorientation [26]. The main limitation from the first EBSD observations is that neither IPF maps nor LSM maps can discriminate martensitic units effectively, especially in the case of austenite parent grain. To overcome this issue, a parent austenitic grain

reconstruction is required, which distinguishes the various martensitic structures such as packets, blocks, and grain boundaries, helping to establish a link between mechanical qualities and fatigue response. The martensitic transformation involves a specific set of 24 Kurdjumov-Sachs variants in which the same closed packed plane in austenite is parallel to the transformed martensitic closed packed planes $\{111\}_\gamma//\{110\}_\alpha$, as well as the directions: $[110]_\gamma//[111]_\alpha$, with a very small reconstruction deviation ranging from 1.5 to 3°. The average angular deviation error derived from the reconstruction was between 2° and 4° in this experiment, implying an appropriate match.

The grain reconstruction of the same zone showed by the LSM and KAM maps led to the identification of variants, referred to sub-blocks or laths, by means of different shades. A packet comprises a short gradient of a single color made up of three parallel blocks, each with a very modest color shift. The gradient bar in Figure 4.1.18 will help to illustrate this notion. Figure 4.1.18 presents the martensite parent grain reconstruction for the deformed zone based on the Kurdjumov-Sachs orientation relationship, comprising a total of 27 scanned grains, 43 packets and 119 blocks. The parent grain is defined by the dark line and an analogous IPF map was also provided to contrast the findings.

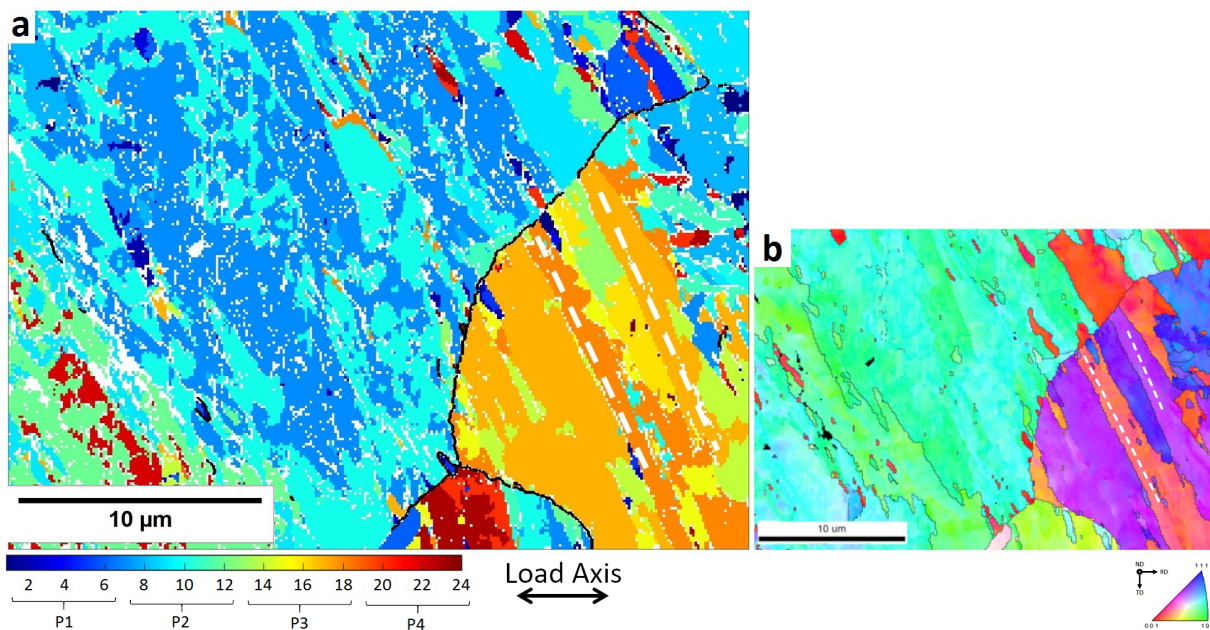


Figure 4.1.18: Martensite parent grain reconstruction based on the Kurdjumov-Sachs orientation relation for the WQ 9Ni steel deformed at $\Delta\epsilon_t=0.9\%$. (b) Corresponding IPF map. The white dashed lines indicate the extrusions

The two broader EBSD-scanned zones containing extrusions were reconstructed to provide a general sense of the material's behavior. It was revealed that the extrusion development is limited to structures with approximately the same orientation (lath/lath and lath/block) belonging to the martensitic grain. Such less misoriented structures are

represented in the reconstructed picture as a single color, representing the laths and blocks. The conclusion, supported by the c-ECCI data, is that the dislocations are restricted to moving exclusively across the LAB, inside the less misoriented structures, and the strain is accommodated in this situation by blocks and laths.

4.1.4.2 Extrusions – intrusions evolution at $\Delta\epsilon_t=1.2\%$ high strain level

At this level of imposed strain, few extrusions have already emerged at the surface during the test after the number of cycles where the peak stress value was achieved - σ_{\max} (Figure 4.1.19). With continued cycling, the initially formed extrusions evolved and new ones appeared.

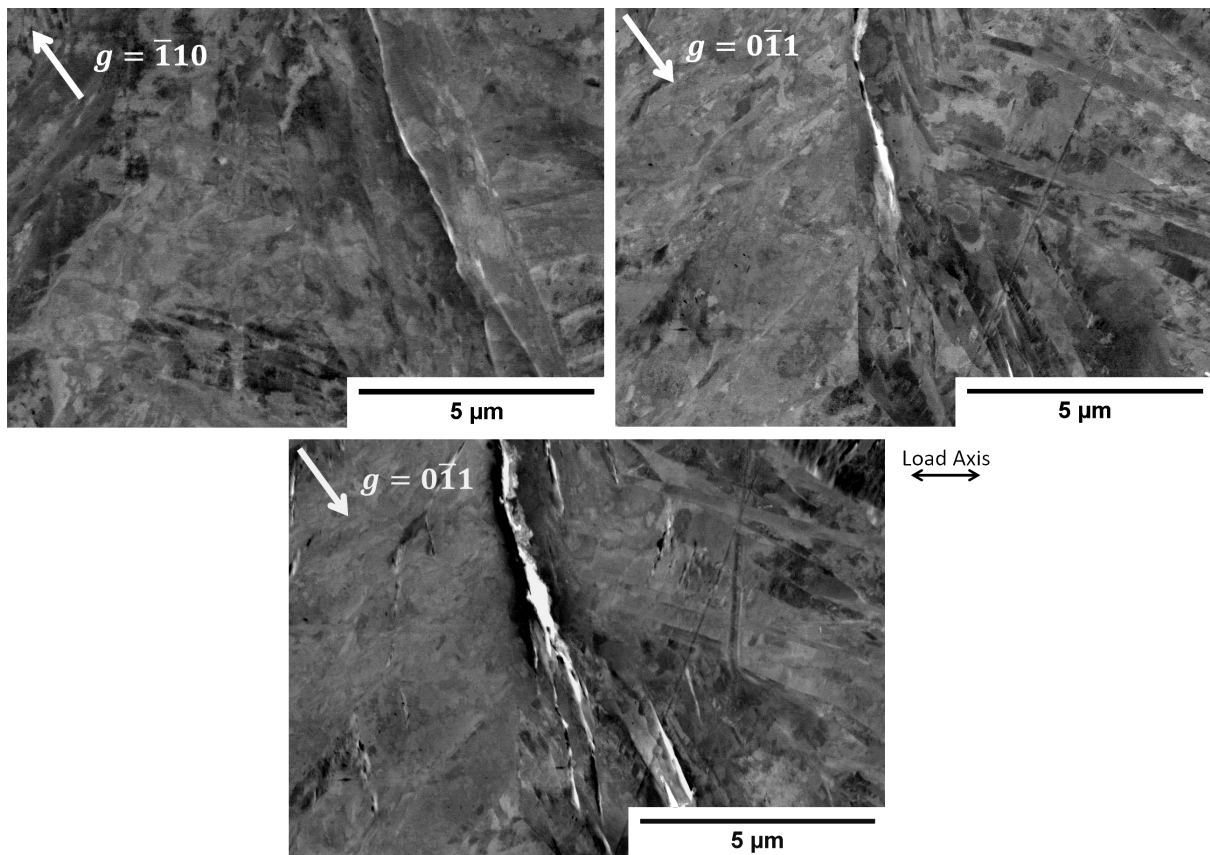


Figure 4.1.19: c-ECCI images showing the dislocation and topography of the WQ 9Ni steel at several stages of fatigue life ($\Delta\epsilon_t=1.2\%$)

Arrays of dislocations were observed close to extrusion at the $\vec{g} = \bar{1}10$ plane during the softening stage and cell arrangement was also seen (Figure 4.1.20). These dislocation arrays might be the very thin highly dense dislocation walls (HDDW), as seen in TWIP steels, CrMn steels, Fe3Si steels, and austenitic stainless steels. [211, 221–227]. HDDW is a term used to describe fine linear structures formed by coplanar slip orientated in

the most favorable slip direction and they can obstruct the dislocation glide. It was also discovered in this material that the zones previously occupied by dislocations have been replaced by more organized structures such as cells and subgrains, and this dislocation configuration limits as well the mean dislocation free path.

In order to get more information of the same area visualized by c-ECCI, the strain fields and recovery substructures were analyzed using the KAM and LSM EBSD methods. The corresponding KAM maps indicate a different behavior than observed at the lower level of plastic strain ($\Delta\varepsilon_t = 0.9\%$). The maps at σ_{\max} correspond an adjacent zone. A significant change in average misorientation is detected at 5% of fatigue life (Figure 4.1.21).

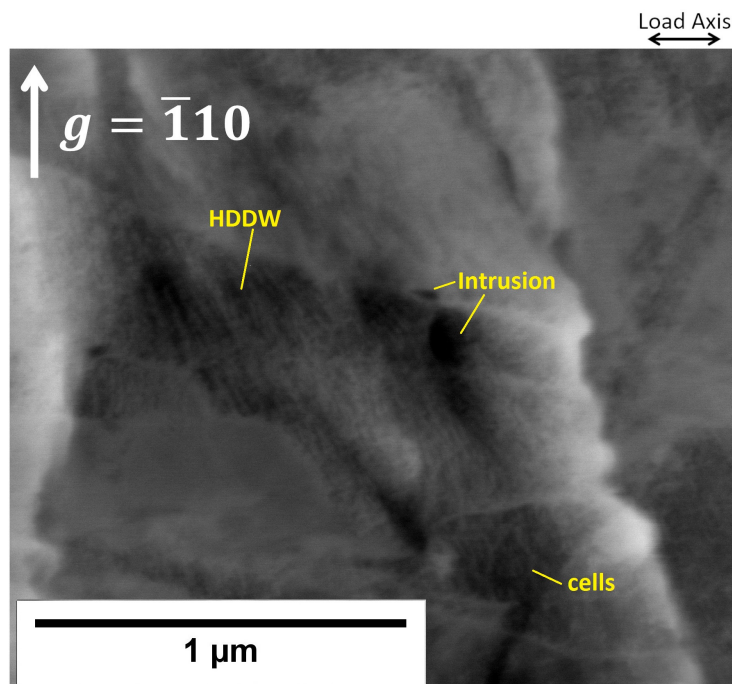


Figure 4.1.20: Highly dense dislocation walls (HDDW) aligned to a persistent slip mark that crosses a block boundary. One intrusion in the process of forming at the interface ($\Delta\varepsilon_t = 1.2\%$)

The local misorientation raises again at 50% with a high level of strain localized at places corresponding to LAB confirmed by the LSM maps (Figure 4.1.22), strain is mostly concentrated at 1-5° boundaries. The KAM method is not able to distinguish an array of dislocations with net Burgers vector equal to zero, such as dipoles, where dislocation annihilation may happen [228]. So, the decrease in KAM values at 5% of fatigue life may be linked to the HDDW structures found next to the PSMs, where annihilation is mostly probable to happen due to coplanar slip. After few cycles, the crystal lattice strain gradient would develop through plastic deformation, being detected again by the KAM method.

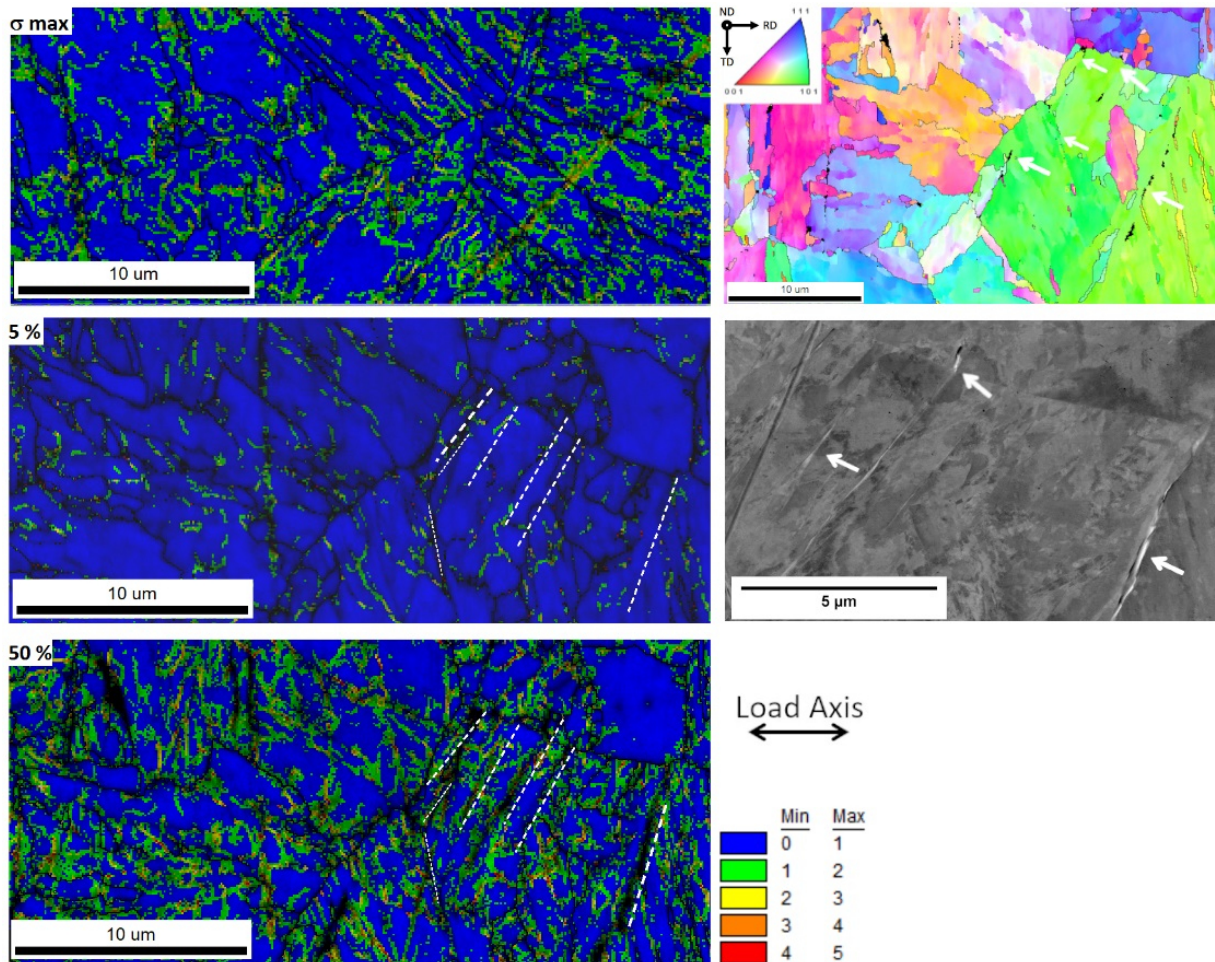


Figure 4.1.21: KAM maps evolution of WQ 9Ni steel at $\Delta\varepsilon_t=1.2\%$. The white arrows and the dashed lines indicate the extrusions. c-ECCI and IPF images indicating the scanned zone at 5% of life

By coupling KAM (Figure 4.1.21) and LSM maps (Figure 4.1.22) it can be observed that deformation is predominantly distributed at $1\text{-}5^\circ$ boundaries revealed by LSM maps which correspond to the dislocation rearrangement during the cyclic straining. There was a growth in 1° -type LAB, as well as their evolution into 5° of misorientation. Nevertheless, no evolution to 15° type of boundary inside a grain was detected; yet, the pre-existing HAB were sites for extrusion development.

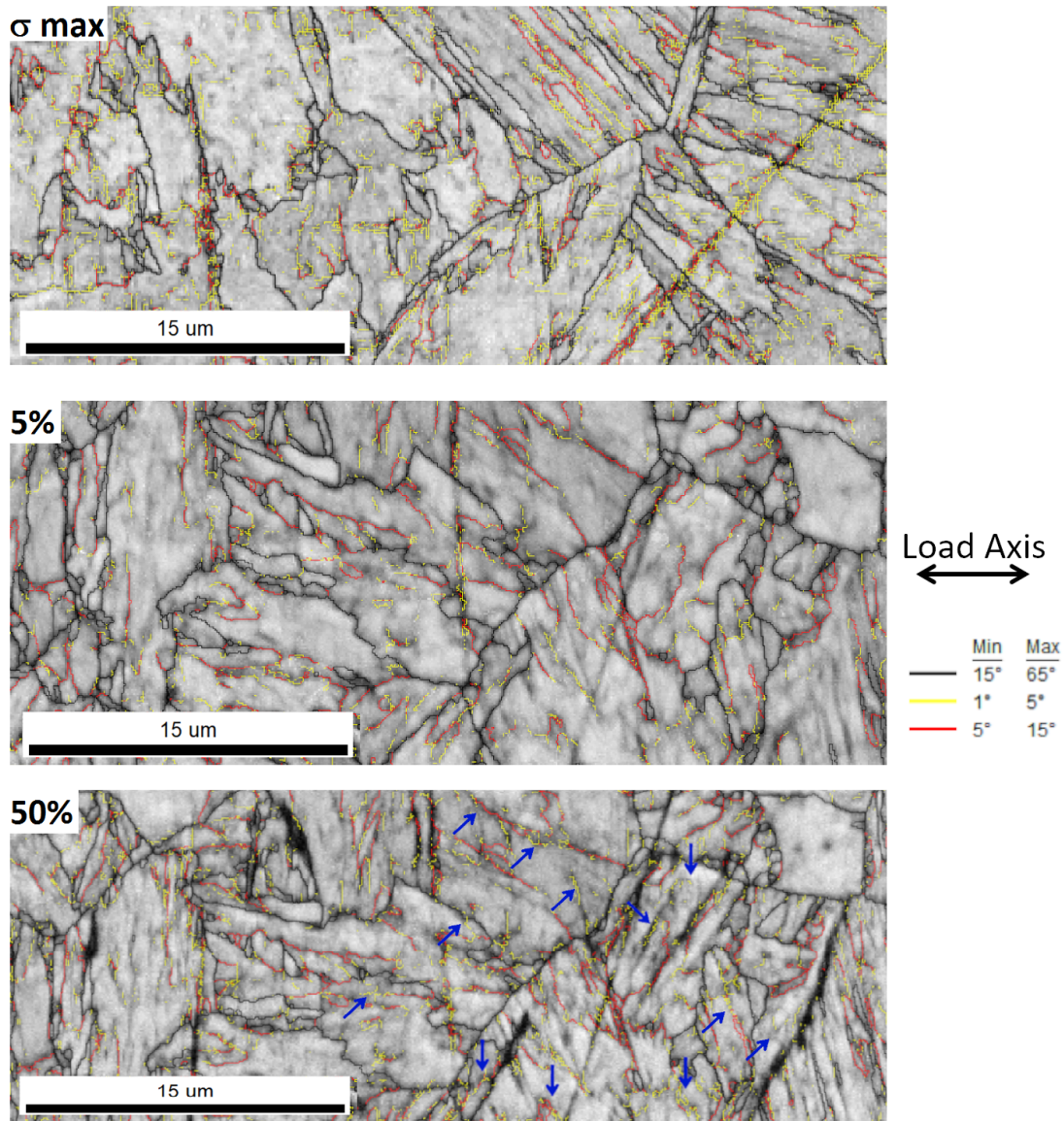


Figure 4.1.22: Image Quality + LSM EBSD maps of WQ 9Ni steel at $\Delta\varepsilon_t = 1.2\%$. The darker zones indicate the regions with the presence of extrusions. Blue arrows indicate the changing of misorientation level

Martensite parent grain reconstruction based on the Kurdjumov-Sachs orientation relationship (Figure 4.1.23) shows that differently from the lower level of applied deformation, the extrusions emerge more often at HAB, across all types of LAB and low angle misoriented structures.

The main extrusions are present along HAB belonging to packets and grain boundaries (GB), sometimes growing within a packet crossing the LAB or developing in a grain boundary. As the cycling continues, the extrusions may coalesce or even propagate trespassing all kinds of interfaces present in the material. These findings suggest that at high degrees of deformation, the boundaries can no longer obstruct the growth of extrusions.

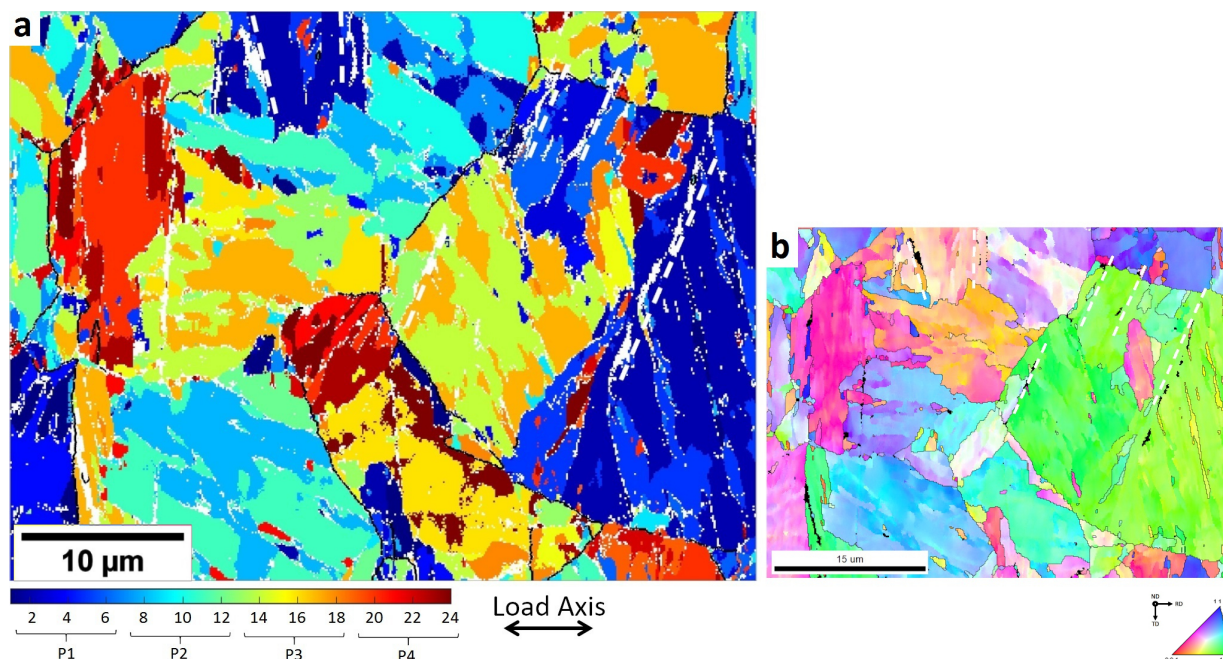


Figure 4.1.23: a) Martensite parent grain reconstruction based on the Kurdjumov-Sachs orientation relation for the WQ sample deformed at $\Delta\varepsilon_t=1.2\%$. b) Corresponding IPF map. The white dashed lines indicate the extrusions

Those crack formation observations, as well as their relationship to the extent of misorientation in the microstructure, were also seen in macro tensile testing of lath martensite [229]. At low strains, the deformation is governed by crystallographic slip parallel to the lath boundaries, although at high strains, the deformation is dictated by crystallographic slip at HAB. To get dislocations to travel across a long distance, a specific amount of energy must be applied. At very small strains, the slip activity tends to concentrate within the laths; however, at greater strains, the dislocations might overcome the LAB but then tend to pile up at the HAB. Since dislocations cannot flow through the grain boundary due to grain mismatch, the grain boundary serves as an obstacle, raising the stress levels in those zones. Microhardness in situ tests have proven this point, when a high amount of charge is applied, the dislocations tend to cross laths interfaces transmitting the strain. On the other hand, the behavior of the dislocation “sink” at the high-angle grain boundary is observed and no transmission of strain is identified [31].

4.1.5 Cross-sectional view

The surface analyses done by c-ECCI together with EBSD were very useful to observe the plastic accommodation of the material at two levels of deformation. However, no information is given in respect of what was going on few microns beneath the surface. In addition, the confirmation of the precise location of the pair of extrusions-intrusions is

needed to establish a mechanism of fatigue crack initiation for this microstructure. To overcome those limitations, cross-section visualizations may help to answer the remaining questions.

4.1.5.1 Accurate determination of extrusion/intrusion shape and location

To have a real view of the shape of the extrusion and its exact location, TEM observation was performed on FIB lamellae extracted from identified extrusions as the one showed in Figure 4.1.24. The sample fatigued at $\Delta\epsilon_t=1.2\%$ was chosen for this investigation because they presented more prominent and numerous sets of PSMs at several stages of fatigue life. Cross-sectional cuts were performed on the specimen surface, parallel to the load axis from the sample after 5% of life and after failure.

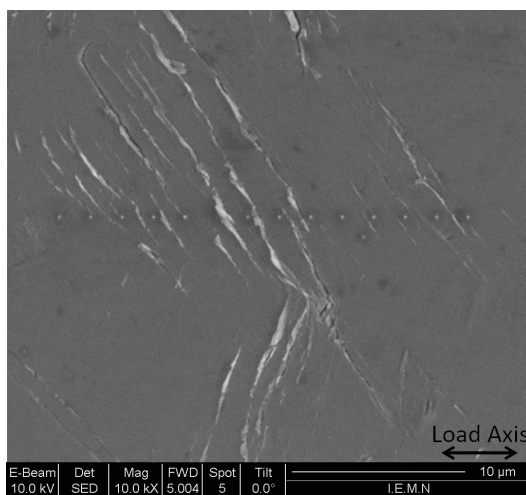


Figure 4.1.24: Selected zone comprising PSMs for FIB lamella extraction of the WQ sample fatigued at $\Delta\epsilon_t=1.2\%$ at the end of fatigue life, the dots correspond to the Pt deposition mark the exact position of extraction

Single extrusions were already substantial and noticeable at 5% of life (Figure 4.1.25). Extrusions predominate the surface, only a modest development close to an extrusion was identified as an intrusion. It can be seen that the extrusions are located at the border of a lath interface while the intrusion is in the middle of the lath. Sometimes the extrusions are placed in the middle of the lath, but coinciding with a cell wall.

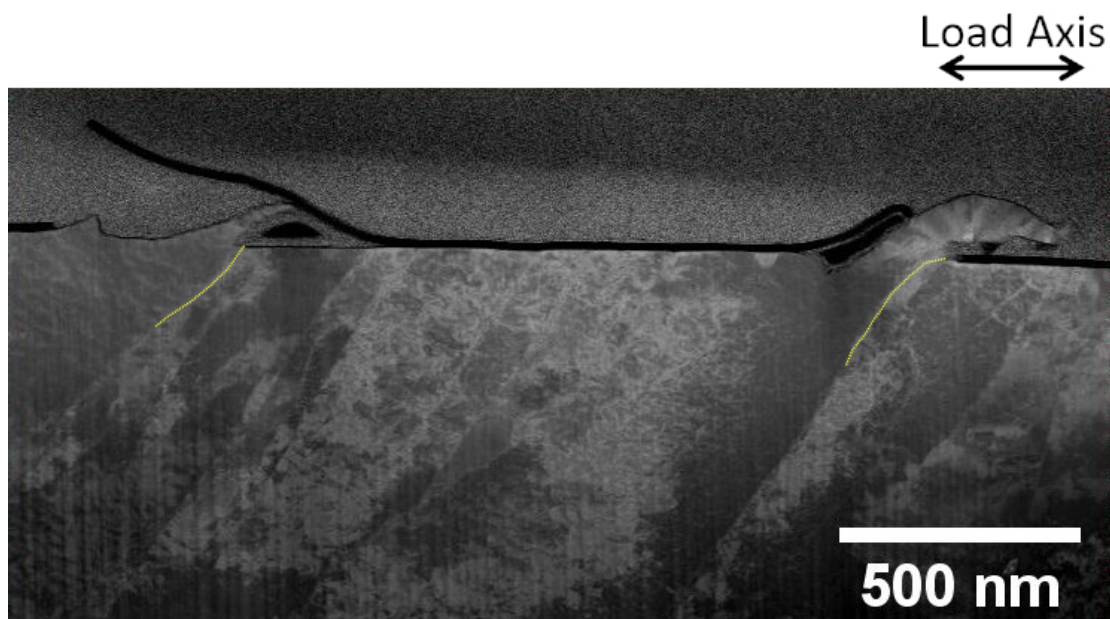


Figure 4.1.25: HRTEM image of WQ sample thin lamella showing accurately the sites of extrusions and intrusions at 5% of the fatigue life ($\Delta\varepsilon_t=1.2\%$). The yellow lines highlight the laths boundaries

As it could be feared, the thin films of retained austenite were not revealed even at very high magnification as a result of the FIB technique. Indeed, the FIB lamella preparation tends to transform the austenite due to the high amount of energy applied during the machining. Other clues for attesting the presence of austenite at lath boundaries were searched. Bright-field micrographs closer to the extrusion zone shows a distortion near the boundary (Figure 4.1.26), characterized as Moiré fringes. Those interference fringes were already noticed at the austenitic/martensitic interface in 9Ni steel, representing a small mismatch between the $(111)\gamma$ and $(110)\alpha'$ parallel planes [130]. However, here, this distortion could not yet be surely assigned to the austenite. Nanograins/subgrains clusters were also identified next to the boundary, right beneath the surface, indicating a high plasticity activity in that zone or a tentative to blunt an embryo intrusion to form.

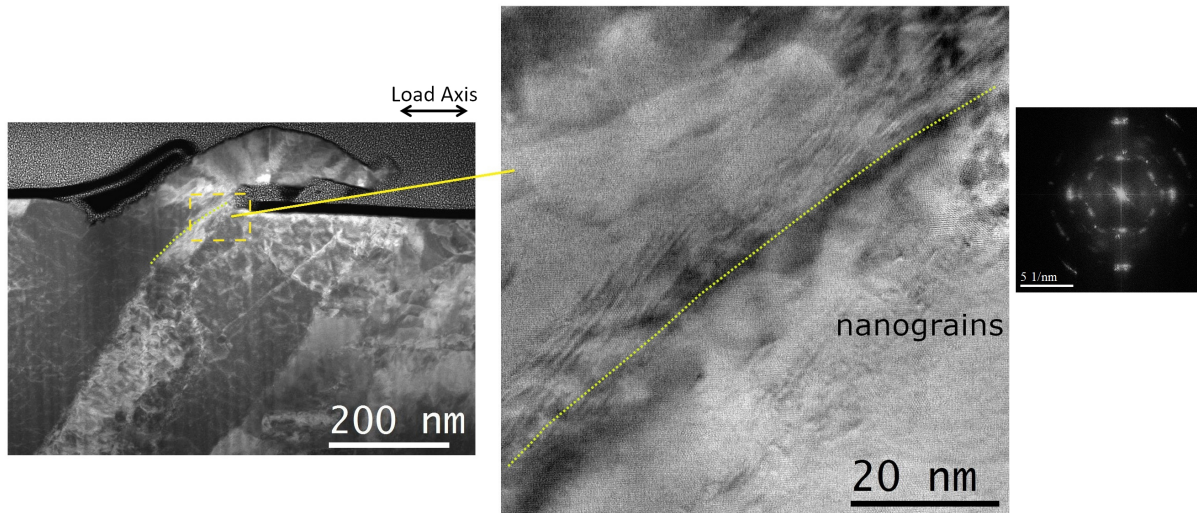


Figure 4.1.26: HRTEM image of an extrusion formed at 5% of the fatigue life ($\Delta\epsilon_t=1.2\%$). Enlarged view of the yellow dashed zone showing nanograins the yellow dashed line indicates the lath boundary)

The intense interest in identifying the exact location of austenite resides in the fact that this softer phase can influence the plasticity mechanism of the martensitic matrix. For that reason, a second extrusion placed at the boundary was analyzed and a chemical map indicates a higher concentration of carbon at the interface (Figure 4.1.27). Atom probe investigations done by Morito et al [113] have shown a significant change in the carbon content at the interface due to the presence of the very thin austenitic films in as-quenched martensitic steels. This might lead to the conclusion that the identified carbon enrichment is linked to an austenite film that existed at the interface and was transformed by the FIB machining. XRD analysis performed after the LCF test in this study indicated a small decrease in the austenite content, from 8% to 5%, meaning that the retained austenite is quite stable upon cycling due to the high content of gammagenic elements. Those pieces of evidence help to conclude that the austenite films do not transform entirely into stress-induced martensite (TRIP effect), but instead, the retained austenite sandwiched between martensite laths is suspected to take part in the accommodation of the cyclic plasticity.

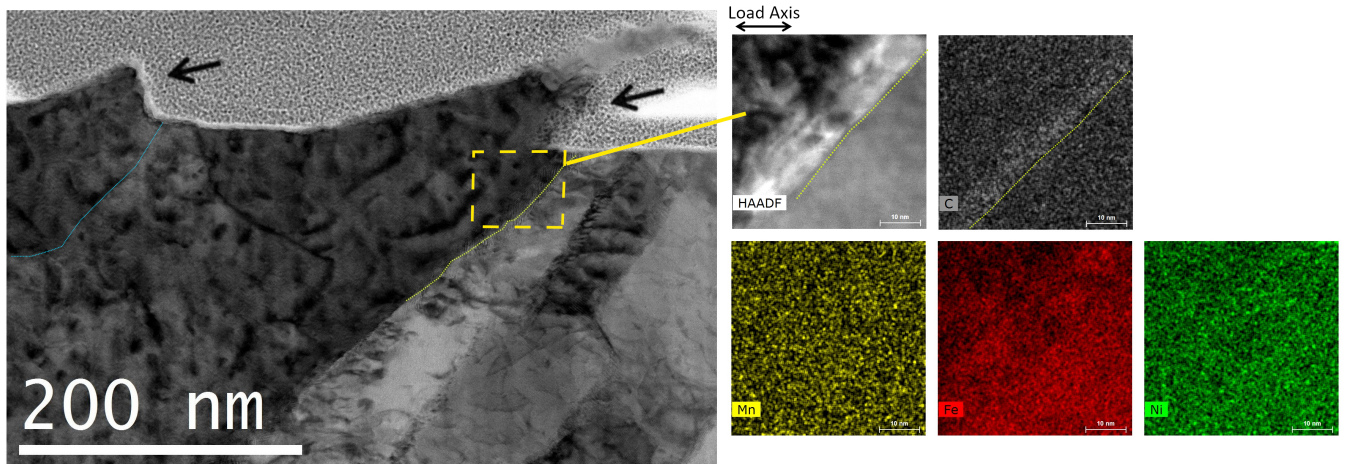


Figure 4.1.27: HRTEM image of two extrusions formed at 5% of the fatigue life ($\Delta\epsilon_t=1.2\%$). HAADF-STEM and EDX map of the yellow dashed zone. Yellow dashed lines indicate the lath boundary with small increase of carbon next to it

The existence of extrusions at lath boundaries is suspected to result from a slippery property of the interface caused by the presence of retained austenite as suggested by Du [30] on water quenched martensite deformed by micro tensile test. Cretegy [230] in AFM analysis on fatigued PH 13-8 Mo stainless steel also considered the hypothesis of the influence of an interlath soft-reversed austenite phase which accumulates plastic deformation, confirming our hypothesis, but without any proof of the fact. So it is interesting to find a way to visualize these austenite nanofilms verifying if they exert any influence on the plasticity mechanism. The experimental evaluation of this plasticity is not very common in the literature and, sometimes, the retained austenite may transform rapidly into martensite while cycling, not being able to carry the plasticity through the entire plastic straining [17] [113], but this is not the case of the 9Ni steel, as demonstrated. The very thin austenitic stable films present in 9Ni steel allow the matter to flow along the interface, acting as an interlath lubricant for boundary sliding.

Finally, on the sample taken at the end of life, short cracks stemming from the intrusion were identified and a transition in the behavior from an intrusion to a short crack is evident (Figure 4.1.28). A closer look at the central intrusion indicated that it starts in the middle of the lath changing its path towards the HAB boundary, where it will finally meet the requirements to grow and propagate.

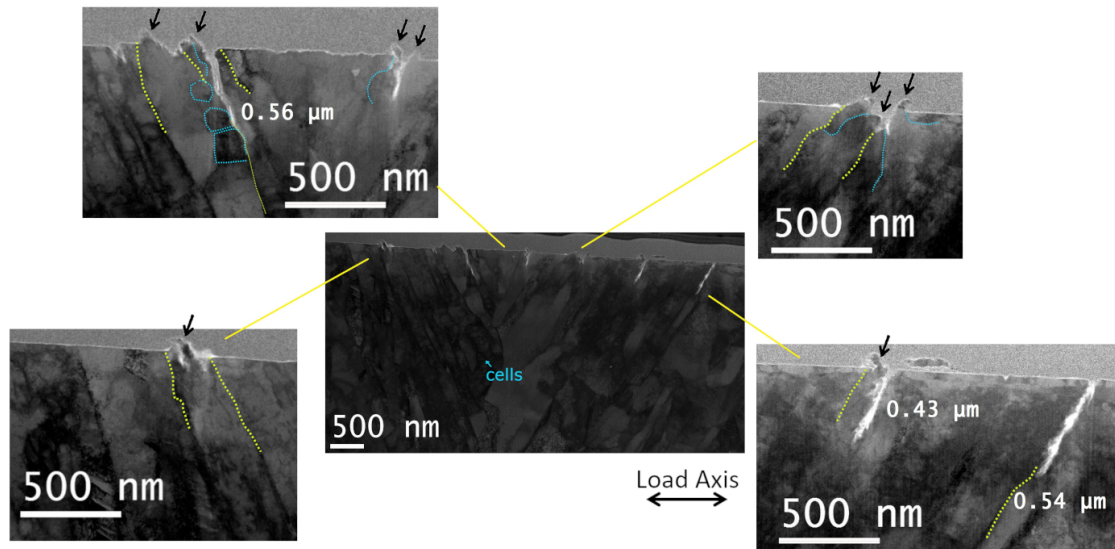


Figure 4.1.28: HRTEM images of thin lamellae accurately indicate the sites of extrusions and intrusions at the end of the fatigue life ($\Delta\epsilon_t=1.2\%$). Yellow dashed lines indicate the lath boundary and the blue dashed lines indicate the cell walls

Well-developed intrusions and extruded laths positioned along the load axis, at the end of fatigue life were also identified (Figure 4.1.29), both following the same trend, i.e. located at the boundaries. Nanograins or subgrains were discovered around the intrusion tip, suggesting a highly activated plastic zone (Figure 4.1.29-c). No specific dislocation structure such as PSB that would express cyclic strain localization inside a martensitic lath was identified. Nevertheless, the volume of the extrusion suggests a high activity of plastic deformation, which is confirmed by the very small dislocation cells inside the lath.

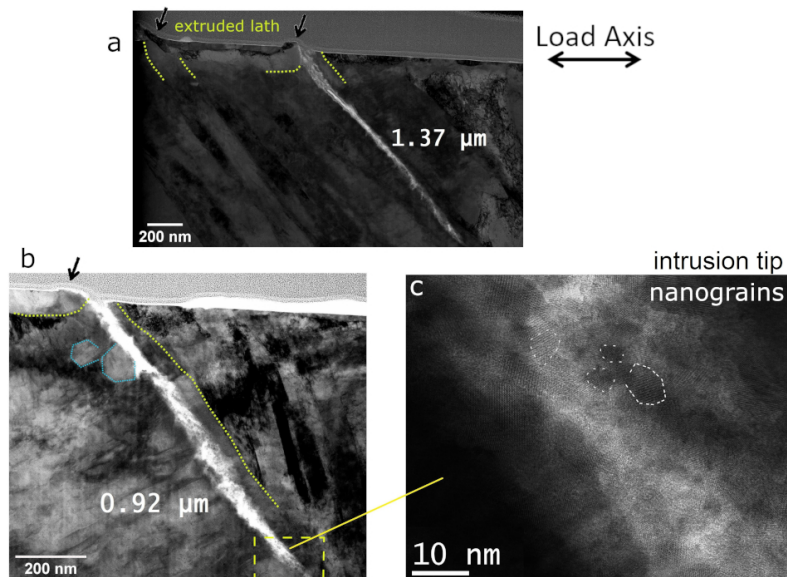


Figure 4.1.29: HRTEM images of thin lamellae showing the microcracks ($\Delta\epsilon_t=1.2\%$), cells identified next to the cracks highlighted by the blue dashed lines and nanograins were also identified at the intrusion tip

4.1.6 Conclusions

When the 9Ni steel is austenitized at 900°C for 1h 45 min and water quenched, the microstructure comprises a martensitic matrix with nanofilms of retained austenite along martensite laths. The austenite volume fraction of 8% determined by XRD diverges from that measured by EBSD. The latter tends to minimize the volume fraction due to the thickness of the austenitic film compared with the electron beam size and the excited matter volume.

In the case of a highly dislocated structure such as martensite, the combination of the several techniques adopted in this study (EBSD, c-ECCI, TEM/HRTEM) are extremely necessary for giving the information needed to have a conclusion, one isolated technique would not solve the problem investigated.

The cyclic accommodation consists of a short primary hardening followed by softening. The Manson-Coffin relation exhibits a bi-linear behavior with the change in slope at $\Delta\varepsilon_t=1\%$. This can be related to the interactions of moving dislocations and their interactions with LAB interfaces, the latter being "coated by the lubricant" retained austenite. At lower strains, the entangled dislocations formed during the quenching are loosened and move with difficulty at short distances within the martensite laths. As a result, they fail to cross the first LAB (lath/lath and lath/block), which works as a structural barrier and inhibits them from advancing. Instead of developing a pile-up of dislocations, which would have increased stress at the interface, the presence of retained austenite, which remains partially stable and serves as a lubricant, permits the localized displacement of matter along the martensitic lath. Inside this zone, a highly localized plastic slip occurs, resulting in an extrusion rising along the LAB interface and the nucleation of the intrusion inside the lath.

Nevertheless, at high strain levels, mobile dislocations inside martensite laths reach the LAB interface, but because they are under high stress, they can overcome this barrier. This time, they are not hindered, so no matter displacement at the LAB happens. Those mobile dislocations can overcome the LAB until they reach a HAB, and there the matter will flow towards the surface with the aid of the lubricant austenitic film. An extrusion develops along the HAB boundary, followed by an intrusion nucleating inside a martensite lath adjacent to the HAB interface.

The investigations done here can be explained by considering Pólak and Man's argument that the pair of extrusions-intrusions are the precursors of a crack [231]. The significant difference between the present work and those on copper, austenitic stainless steels, or even 12Cr martensitic steel is that the intrusion is not located exactly

at the interface. The graphical abstract (Figure 4.1.30) summarizes the process of extrusion/intrusion nucleation and growth through the fatigue life of WQ microstructure and the dependence upon the applied strain.

HIGHLIGHTS

- Thin retained austenite films are present at martensite laths
- Manson-Coffin curve exhibits a bi-linearity, associated with two different mechanisms of crack nucleation
- Extrusions form at the LAB at low strain and HAB at high strain
- Extrusions emerge at the laths interfaces, while intrusions nucleates inside the laths
- Retained austenite may be responsible for promoting the matter flowing at interfaces

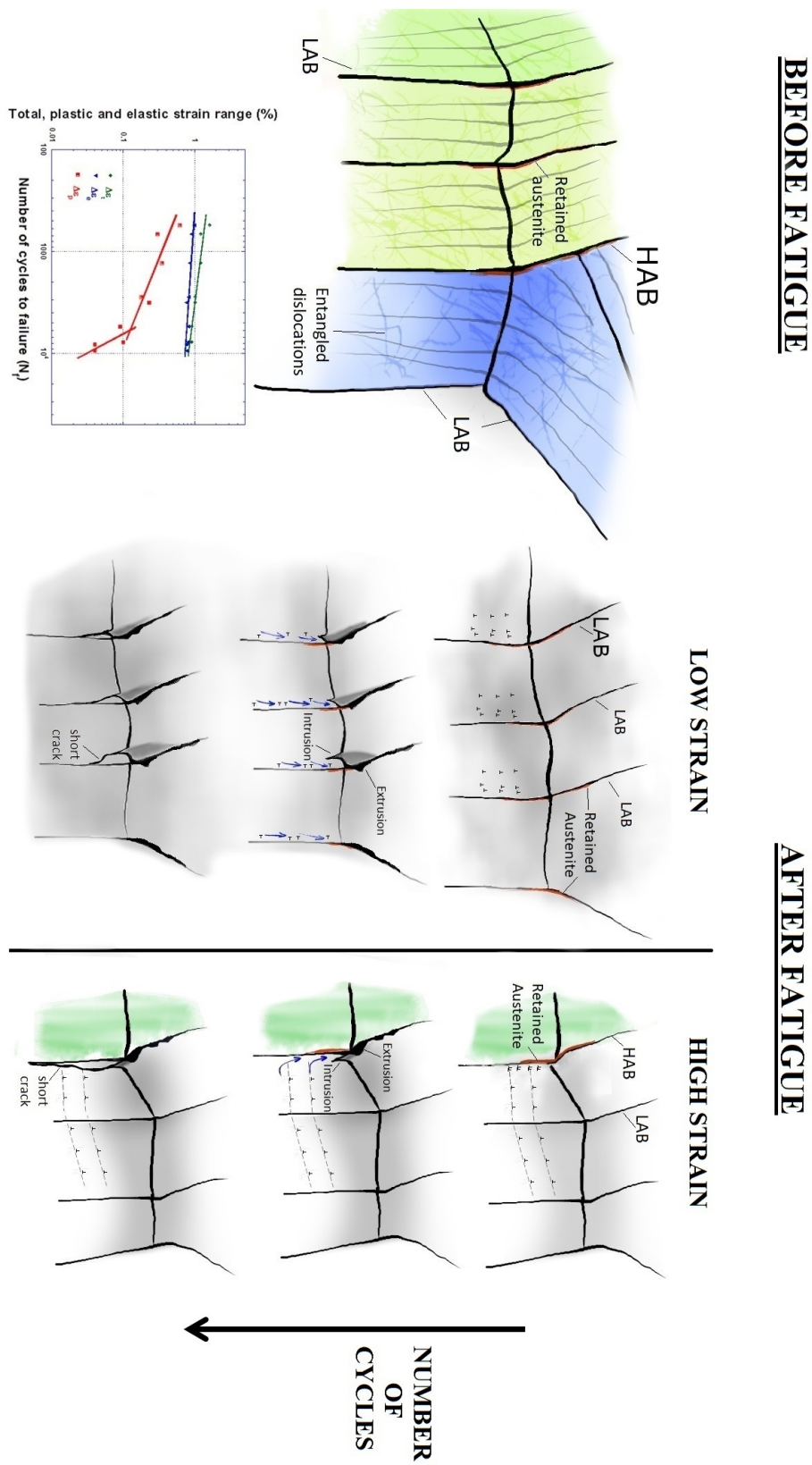


Figure 4.1.30: Representation of extrusions and intrusions nucleation sites for the WQ sample during fatigue at low and high strain

4.2 30 Minutes Tempered 9Ni steel - 0.5T sample

4.2.1 Non-deformed state

4.2.1.1 Matrix Evaluation

When a steel with a quenched microstructure is reheated to temperatures below A_{c1} , diffusion takes place and partitioning of the alloy elements to minimize the material's free energy happens. In the case of the 9Ni steel, the gammagenic elements will then migrate from martensite to the residual austenite, as well as to the borders of prior austenitic grains and martensitic laths. Once the concentration of gammagenic elements at these boundaries becomes substantial enough, germination and growth of phase rich in these elements occur transforming the retained austenite into a stable form, the reversed austenite. The result is a matrix rich in recovered zones, less rich in dislocations more or less organized in cells and filled with islands or films of reversed austenite in the interfaces (as reported in the literature, see section *2.3.2 Microstructure of Quenched + Tempered 9Ni steel*). It should be remembered here that the austenite shows a memory effect [122]. In the case of the 9Ni steel, the morphology of the reversed austenite will be different from the retained austenite, they will be also encountered in the form of islands instead of just thin films distributed along any type of boundary.

The obtained microstructure from the quenching and subsequent 30 minutes tempering heat treatment at 600 °C already shown in Figure 3.2.3 and Figure 3.2.4 present the following features for the martensitic matrix: an average grain size of 19 μm , packets with 5.5 μm , and block size of approximately 2 μm . The time of tempering heat treatment will be a key factor to determine the extension of changing in the matrix as well as the concentration of reversed austenite located at the boundaries.

The crystallographic orientation of the sample surface was evaluated by EBSD using the IPF maps. It is found that the tempering treatment did not affect the crystallographic texture since no preferential texture along the rolling direction was revealed (Figure 4.2.1 shows a representative area from the scanned zones). In addition, to evaluate the location and the shape of the reversed austenite, the EBSD phase map (Figure 4.2.2) was used and it assigned very well the austenitic phase in this microstructure, with their islands placed at the boundaries. However, as for the WQ sample, the EBSD technique indicated an amount far below than measured by XRD (0.3% of the scanned areas)- more than ten times lower than 4.5% in volume detected by XRD.

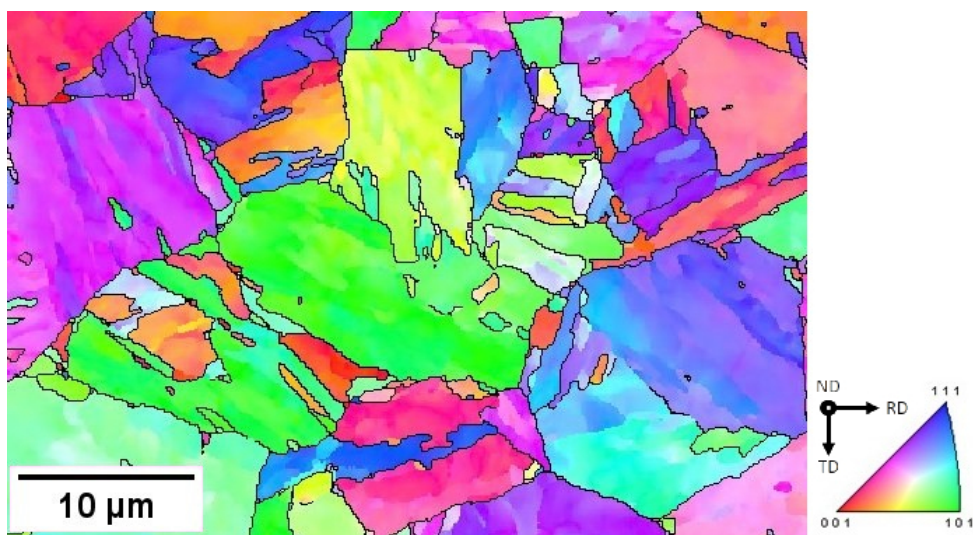


Figure 4.2.1: Inverse Pole Figure of a representative zone from the 0.5T sample

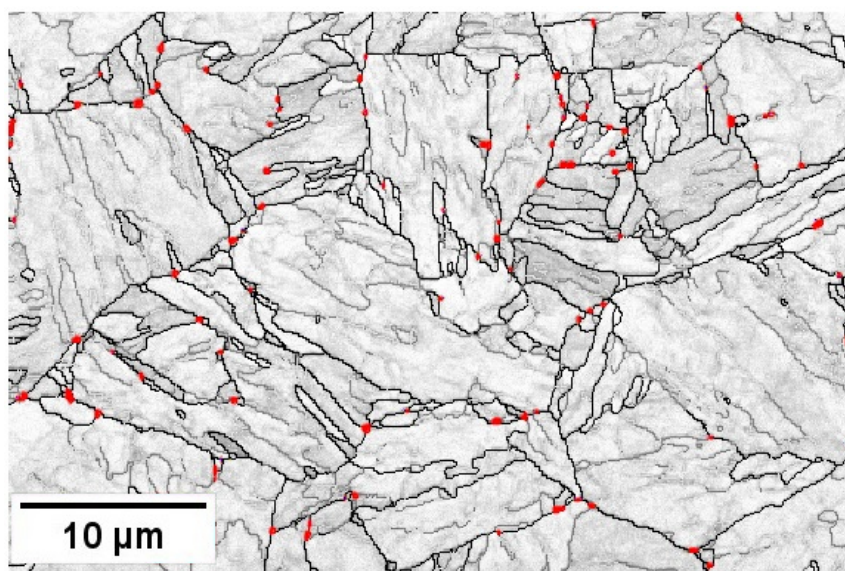


Figure 4.2.2: Phase map of the 0.5T sample, the reversed austenite is represented by the red color

TEM images in dark field mode show that the austenite was sometimes identified with a thickness of less than 50 nanometers (Figure 4.2.3). The reversed austenite was identified by selecting the $(220)_\gamma$ spot in the Selected Area Diffraction (SAED) mode. By contrast to the microstructure of the WQ sample, for which the retained austenite was encountered in the form of very thin films, the average width of the reversed austenite islands was around 200 nanometers, some austenitic islands were 300 nm or wider, but some of them were only tens of nanometers in size (Figure 4.2.3).

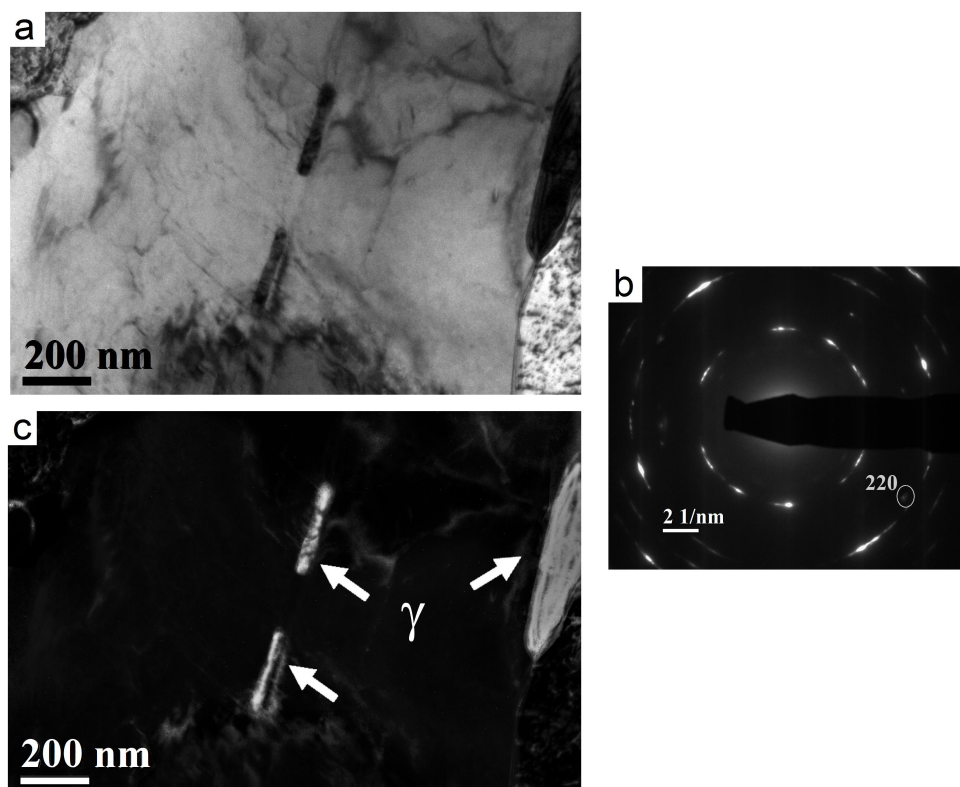


Figure 4.2.3: a) Bright field image TEM of 0.5T sample, b) Selected Area Diffraction Spot (SAED) of $(220)\gamma$ plane, c) dark field image of the same area highlighting the austenitic phase

The dislocation structure obtained from the 30 minutes tempering treatment was firstly revealed by TEM (Figure 4.2.4). The laths have an average width of 1 μm , but very thin laths were still present and dislocation tangles were less prevalent. Moreover, several zones of lath coalescence were discovered, showing an equiaxed shape.

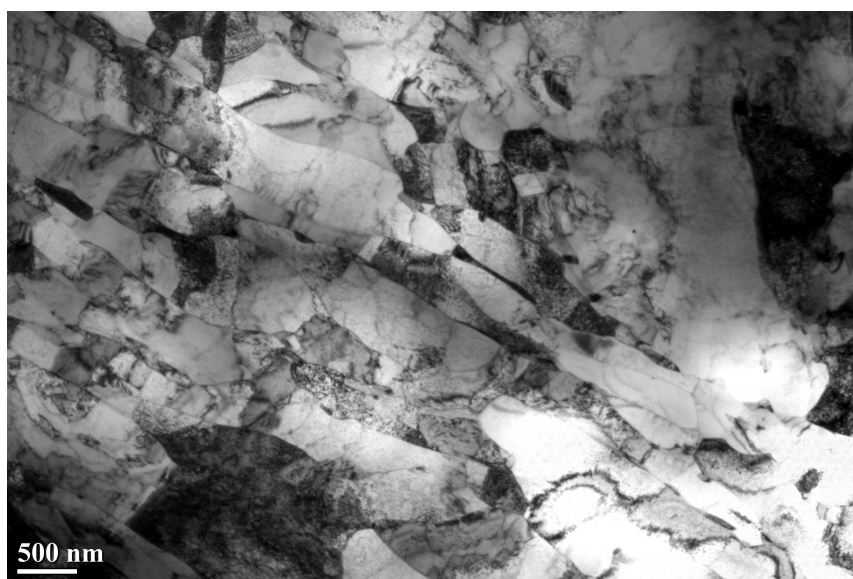


Figure 4.2.4: TEM micrograph of the 0.5T microstructure of 9Ni steel

c-ECCI images show a broader area highlighting the martensitic laths and the recovered cells. Following the same logic as adopted for the retained austenite, lighter zones are seen at the boundaries, being assigned as reversed austenite according to the difference in contrast and morphology (Figure 4.2.5). A closer look in Figure 4.2.6 shows dislocation networks and pile-ups in the cell walls and laths boundaries. The dislocations are less entangled when compared to the quenched structure, so it is expected a different behavior during the fatigue cycling.

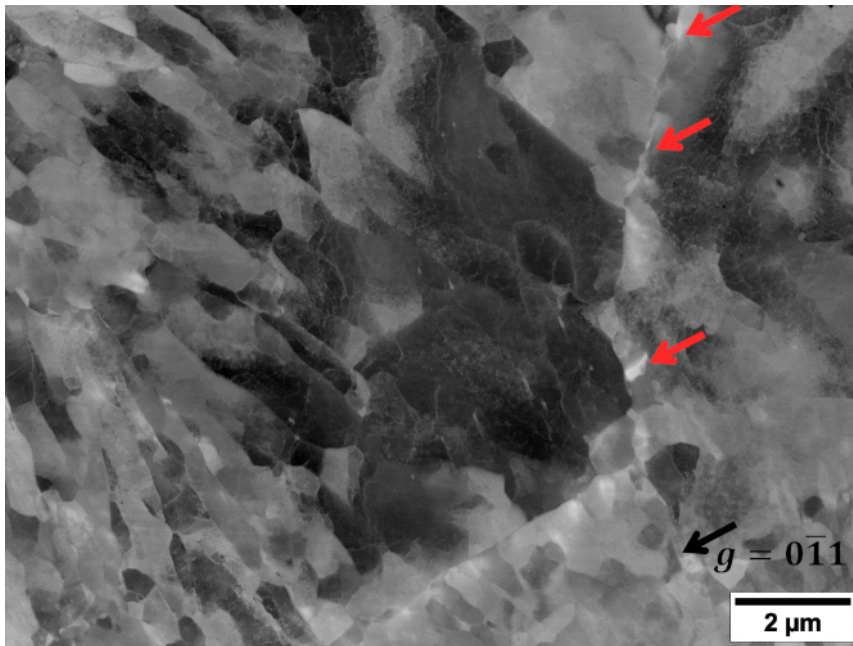


Figure 4.2.5: c-ECCI image of the 0.5T microstructure of 9Ni steel, the red arrows point to the reversed austenite

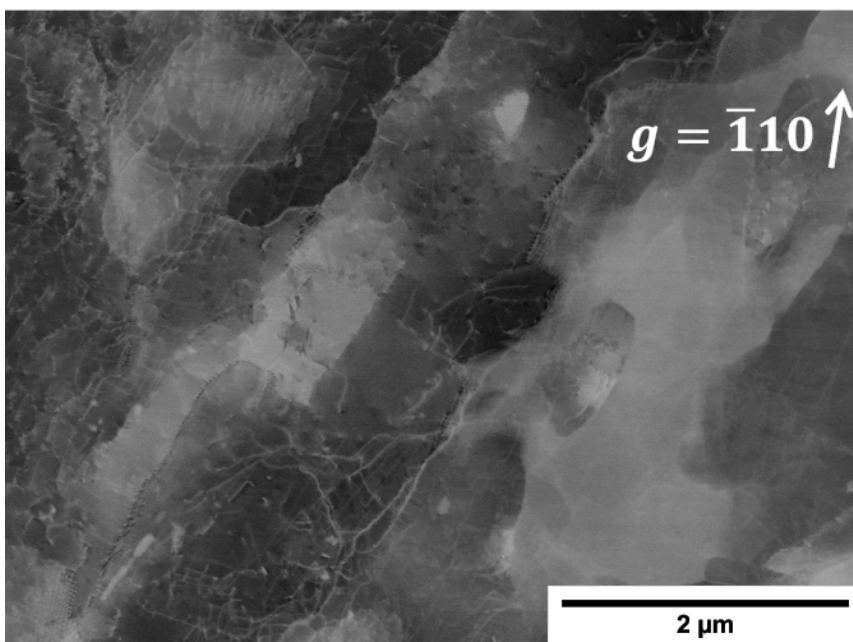


Figure 4.2.6: c-ECCI image of the 0.5T microstructure of 9Ni steel

Local strain distribution in the non-deformed state was evaluated by means of the KAM map. Figure 4.2.7 shows a less misoriented structure when compared to the quenched martensite which is quite frequent for the martensite structure. No widespread high-value KAM was detected and strain is mostly localized in the LAB of 2-5° or next to them, as highlighted by the LSM+IQ maps. The LSM maps were used to distinguish the types of boundaries (LAB or HAB) encountered in the microstructure (Figure 4.2.8).

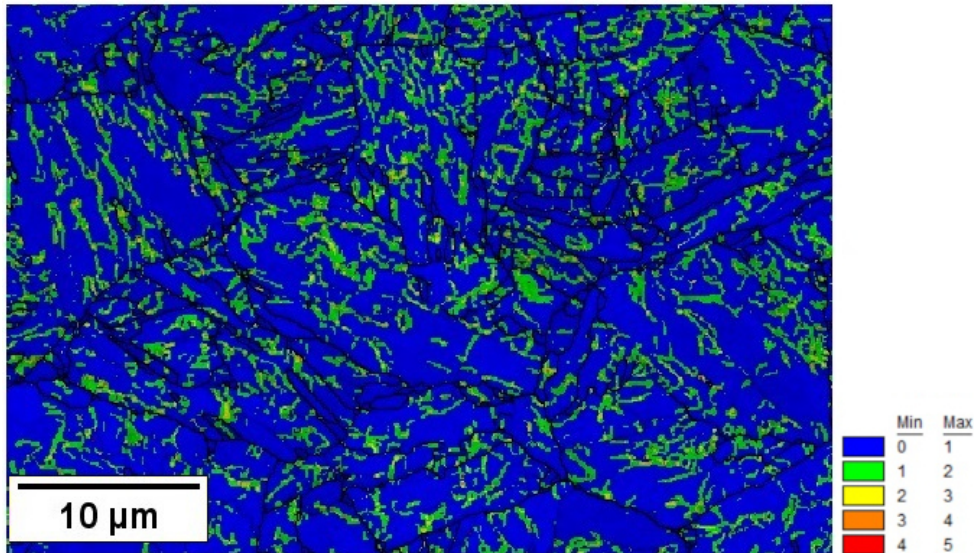


Figure 4.2.7: Kernel Average Misorientation map of the 0.5T sample at the initial state

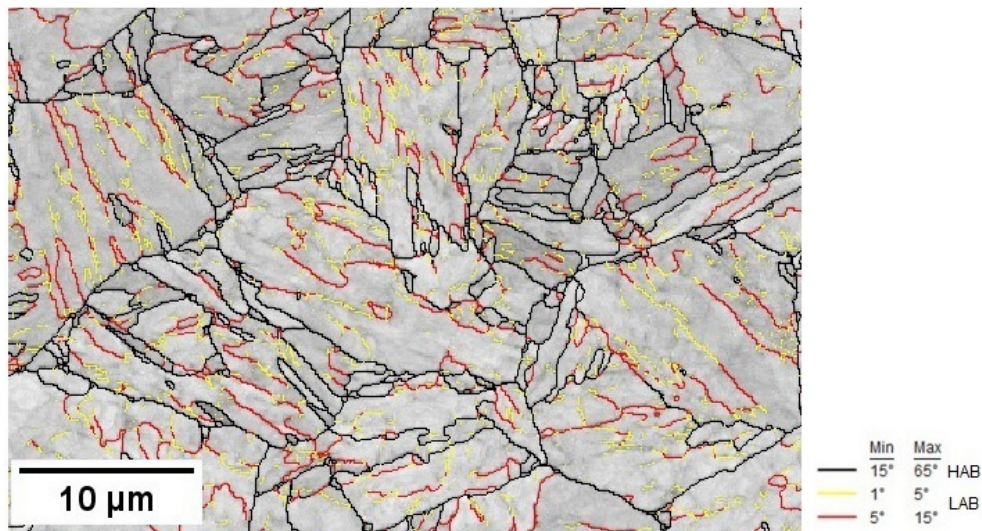


Figure 4.2.8: Line Segment Misorientation + Image Quality - Misorientation distribution EBSD map for 0.5T sample at the initial state

4.2.2 Cyclic stress-strain response and fatigue resistance

Figure 4.2.9 exhibits the cyclic accommodation curves at different strain levels for the 0.5T microstructure as a function of the number of cycles (left) and the stress response as a function of life fraction (right).

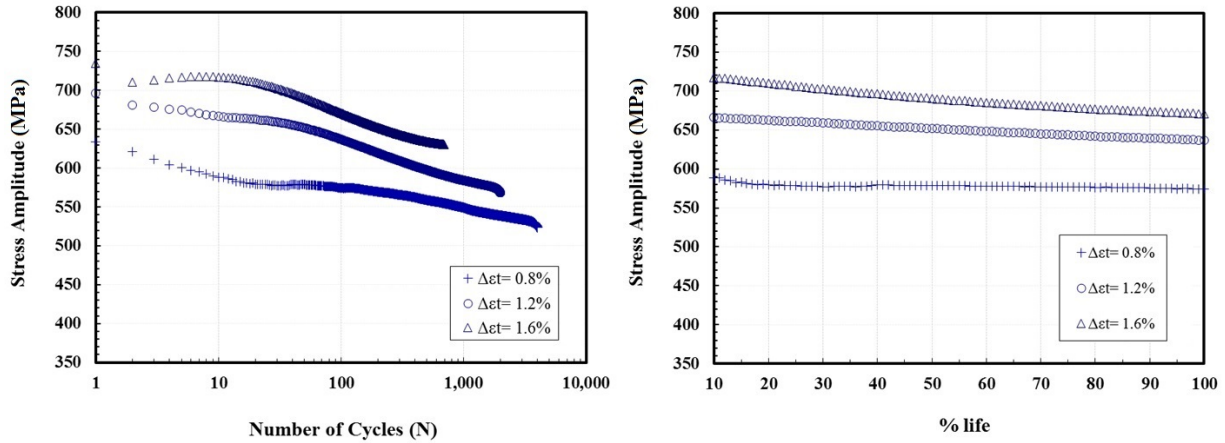


Figure 4.2.9: Evolution of the stress amplitude versus the number of cycles (left) and versus the fatigue life fraction (right) for the different total strain tests for 0.5T sample

The graph's curves demonstrate that the material behavior consists of a continuous cyclic softening which starts first moderately at the very beginning of the fatigue life (about 0.2% of the fatigue life) and then is more pronounced for the rest of the fatigue life. The change in the softening rate arrives faster as the applied strain increases. The rate of the secondary softening appears to be dependent on the total applied strain. Many variables have been linked to cyclic softening in the literature, including cell structure development, increase in subgrain size with low dislocation density, dynamic recovery/recrystallization, grain rotation, and dislocation annihilation [40, 232–234].

In comparison with the WQ material which started to cyclically harden during the first applied cycles (see again Figure 4.2.6), the continuous cyclic softening of the 0.5T suggests that the tempering has decreased the dislocation density so that the remaining dislocations are now less entangled, easily mobile and in sufficient quantity to accommodate the required deformation. In addition, if the quenched microstructure's subgrains and laths tend to coalesce by the tempering heat treatment producing a coarser equiaxed microstructure, the Hall-Petch effect related with dislocation pile-ups, subgrain size, and subgrain misorientations reduce, so the softening then becomes more pronounced due to a larger mean free path of dislocations.

Figure 4.2.10 presents the cyclic stress-strain curve derived from the quasi stabilized hysteresis loop, together with the monotonic curve. The stress softening is almost stable

for all levels of applied strain, being slightly stronger at greater strain levels.

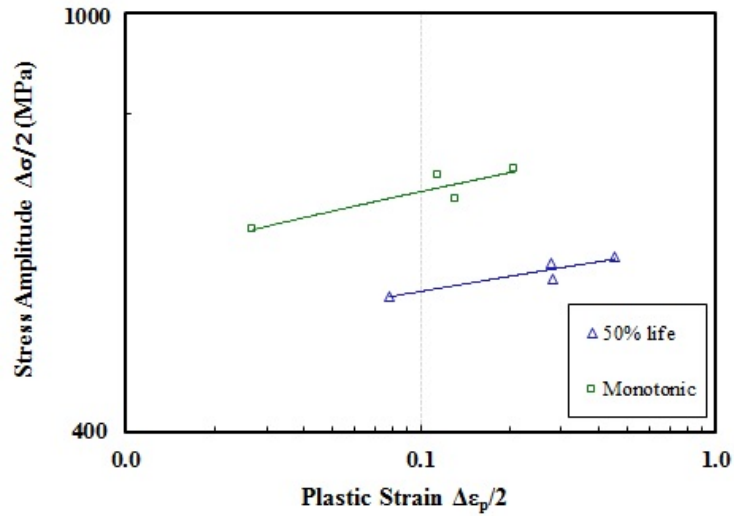


Figure 4.2.10: Cyclic and monotonic stress-strain curves for the 0.5T sample

Manson-Coffin curve combined with the Basquin curve (elastic strain) is represented in Figure 4.2.11. The evolution of the plastic strain range and the elastic strain range fit well with a single slope. At the higher levels of strain, the Basquin curve stays below the plastic strain, switching to values above the plastic strain at lower levels of deformation. It means that at some levels of applied strain, the plastic or elastic component is dominant in the total strain amplitude. This tendency is frequently reported in the literature for ferritic-martensitic steels [212, 234–237], but also for welded joints of 9Ni steel [137].

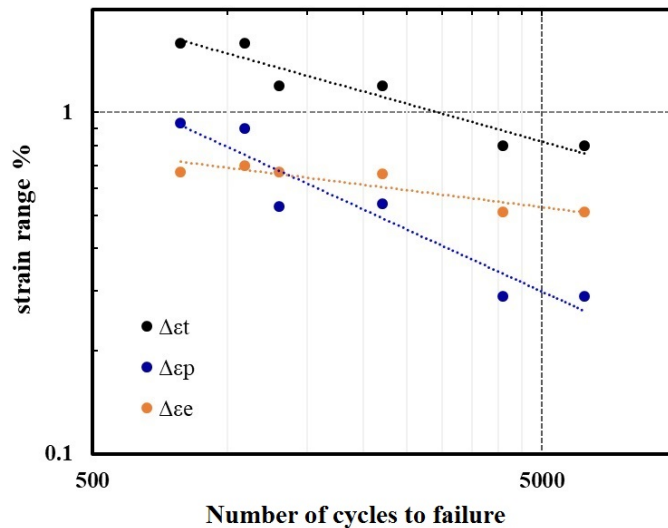


Figure 4.2.11: Manson-Coffin curves of the 0.5T sample

4.2.3 Topography Overview

The surface deformation for the three levels of applied strain is displayed in Figure 4.2.12. Extrusions and protrusions, which is a group of accumulated extrusions (a more detailed analysis regarding the morphology will be done later) are already visible at $\Delta\varepsilon_t=0.8\%$. A considerable amount of surface topography is already present at 1.2% of applied deformation, with pairs of extrusions and intrusions mostly aligned around 35° to 45° from the load axis. At $\Delta\varepsilon_t=1.6\%$ the surface is substantially deformed and remarkable microcracks are present linking one group of extrusions to another. These observations are similar to the behavior observed for AISI 410 tempered martensitic structure. The position of extrusions has also been reported along the lath boundaries oriented around 45° to the load axis [232].

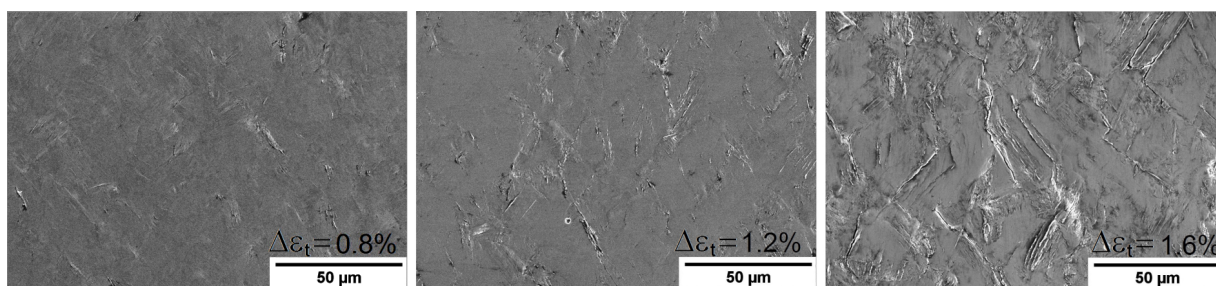


Figure 4.2.12: Evolution of surface damage accumulation resulted from LCF tests for the 0.5T sample, as a function of the total applied strain

4.2.4 Dislocation Structure and Microstructural Response

Since the fatigue resistance of the 0.5T sample could be represented with a single slope in the Manson-Coffin relation, only the 1.2% level of total applied strain was chosen to observe the microstructural response in the course of the LCF test, this intermediate level of applied strain was chosen because it already shows a sufficient amount of deformation at the surface that could be indexed by the EBSD technique and c-ECCI, higher levels of deformation would lead to a less well-indexed pattern, inducing too much noise and interfering the microstructural analysis. The plastic strains measured from the hysteresis loops at each stage of fatigue life chosen to compare to the same stages for the other microstructures are displayed in Table 4.2.1.

Table 4.2.1: Plastic strain at the evaluated stages of fatigue life with $\Delta\epsilon_t=1.2\%$

% life	$\Delta\epsilon_p$
5%	0.665
50%	0.723

Figure 4.2.13 shows the development of the same scanned surface analyzed by c-ECCI throughout the fatigue life in the $\vec{g} = 1\bar{1}0$ plane. Extrusions were apparent at 5% fatigue life and were located inside a martensitic grain. At 50% of fatigue life, well-developed extrusions are seen grouped in parallel from each other, but in other cases staying isolated. Protrusion emerging from an entire block was also present.

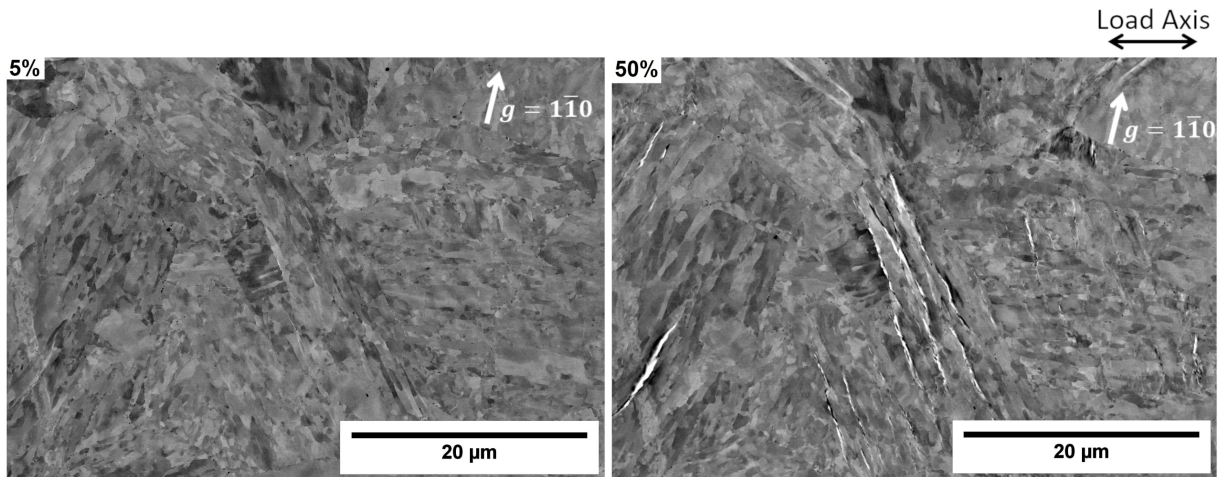


Figure 4.2.13: c-ECCI images showing the dislocation and topography of the 0.5T sample at 5% and 50% of fatigue life

Dislocation cells and HDDW are present already at 5% of fatigue life located next to a PSM (Figure 4.2.14) in the selected $\vec{g} = 0\bar{1}1$ plane. A closer look into a zone with several PSMs shows places with intense dislocation lines and HDDW (Figure 4.2.15). Figure 4.2.15-b indicates that those dislocation structures are the precursors of emerging extrusions. At 50% of fatigue life, cell formation with well-defined walls is observed next to the PSMs and the intense dislocation lines are still present in the $\vec{g} = 0\bar{1}1$ plane. The differences in contrast between the zones around the emerging extrusions evidence the presence of an interface at the exact position of the extrusion.

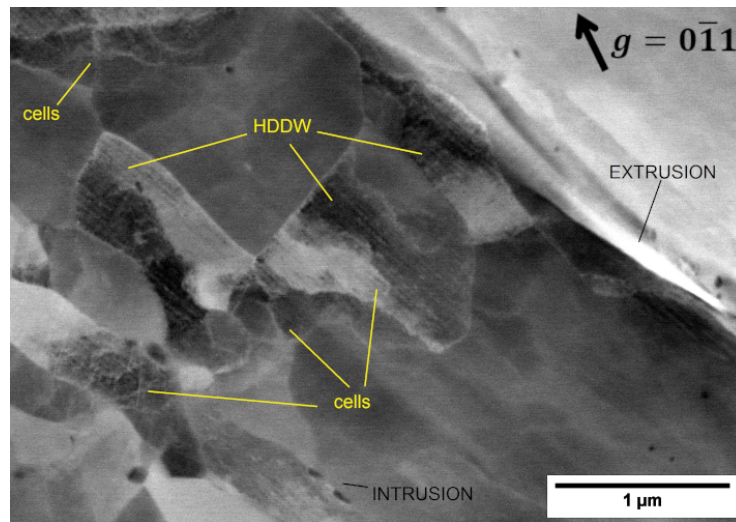


Figure 4.2.14: Highly dense dislocation walls (HDDW), cells and dislocation bands next to a persistent slip mark (extrusion) of the 0.5T sample at 5% of fatigue life

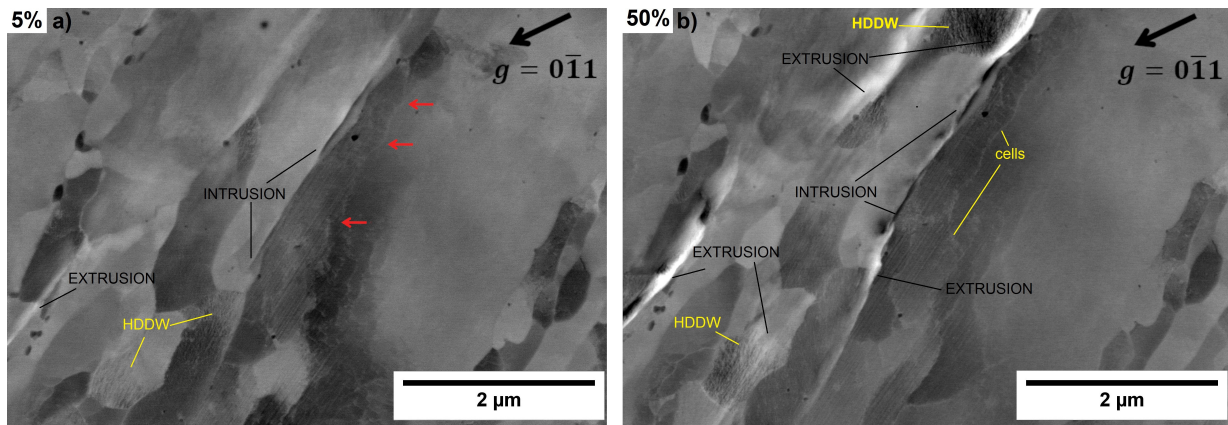


Figure 4.2.15: A closer look of c-ECCI images showing the dislocation and topography of the 0.5T sample at 5% and 50% of fatigue life. The red arrows point to the dislocations

An intense dislocation activity was also noticed in the $\vec{g} = 0\bar{1}1$ plane (Figure 4.2.16), which was characterized by dislocation lines adjacent to a depression in the surface, i.e., an area with tension stresses that will lead to an intrusion. HDDWs condensed at the interface next to the tip of the intrusion are already identified at 5% of fatigue life. The KAM method was used to characterize the strain distribution in the microstructure after the LCF test. Strong misorientation localization was observed possibly linked to strong plastic activity in this exact region (Figure 4.2.18). The evolution of the microstructure at 50% of fatigue life demonstrates that those HDDW will trigger an extrusion raising precisely at the lath interface, next to the intrusion placed only a few nanometers away from that boundary. Since the extrusions appear before the intrusions, at 5% of fatigue life (4.2.16-b) at least one slip step should be already present at the interface close to the HDDW, yet, the surface was scanned with an incident beam perpendicular to the surface,

making the exact visualization of the extrusion difficult when no contrast is obtained.

It is known that the interaction of dislocations in the zones with intense plastic activity will lead to their annihilation, producing vacancies or interstitial-type defects [7]. The development of the pair of extrusion-intrusion observed in Figure 4.2.16-b demonstrates an effort to make a mass balance due to the dislocation interaction in a tentative of trying to relax compression-tension stresses developed in that region, leading to an extruded volume of matter and depression in the vacancy-rich zone. At the right part of the PSM, the dislocation lines are still visible, on the other hand, the preexistent small dislocation cells coalesced, and a more intense dislocation cell's walls are noticed. Those new coalesced cells appear almost free of dislocations in their interior. In addition, an accumulation of dislocations is observed next to the intrusion on the top.

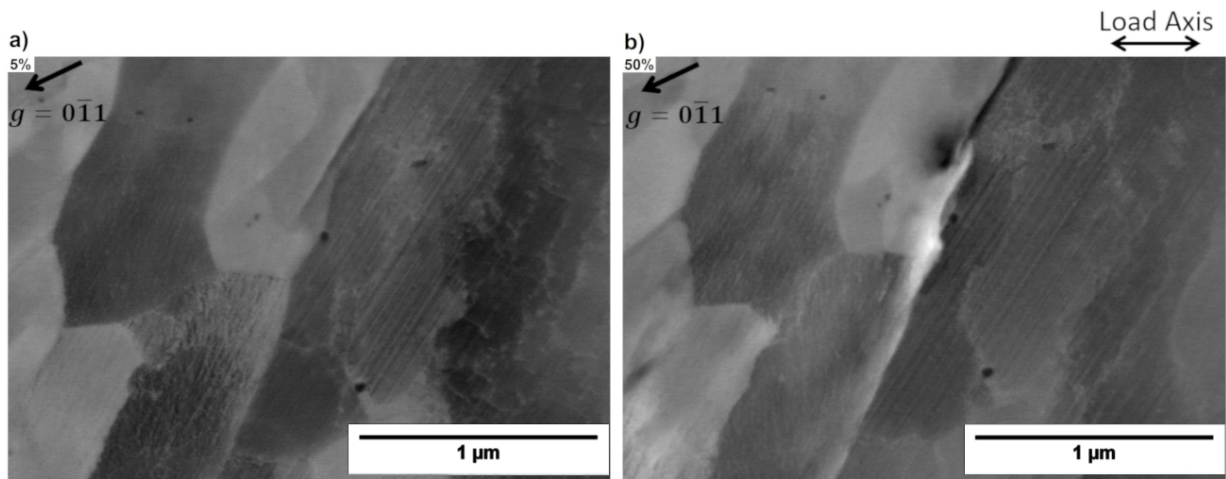


Figure 4.2.16: Highly dense dislocation walls (HDDW), cells and dislocation lines next to an intrusion of the 0.5T sample ($\Delta\epsilon_t=1.2\%$)

EBSD-LSM maps show a minor change in the LAB distribution, no new HAB was identified. The identified extrusions coincide mostly with HAB ($15-65^\circ$) and sometimes with LAB in the $5-15^\circ$ range, LSM maps at 5% of fatigue life already indicate this tendency (Figure 4.2.17). KAM map indicates light misoriented zones surrounding the extrusions and a global reduction of the low misoriented areas (or an increase in blue strain-free areas), which is more than expected due to the cyclic softening and the dislocations arrangements encountered in this microstructure, with a resultant Burgers vector equals to zero (Figure 4.2.18). IPF map and c-ECCI image were added to give more details and facilitate the visualization of the scanned zone.

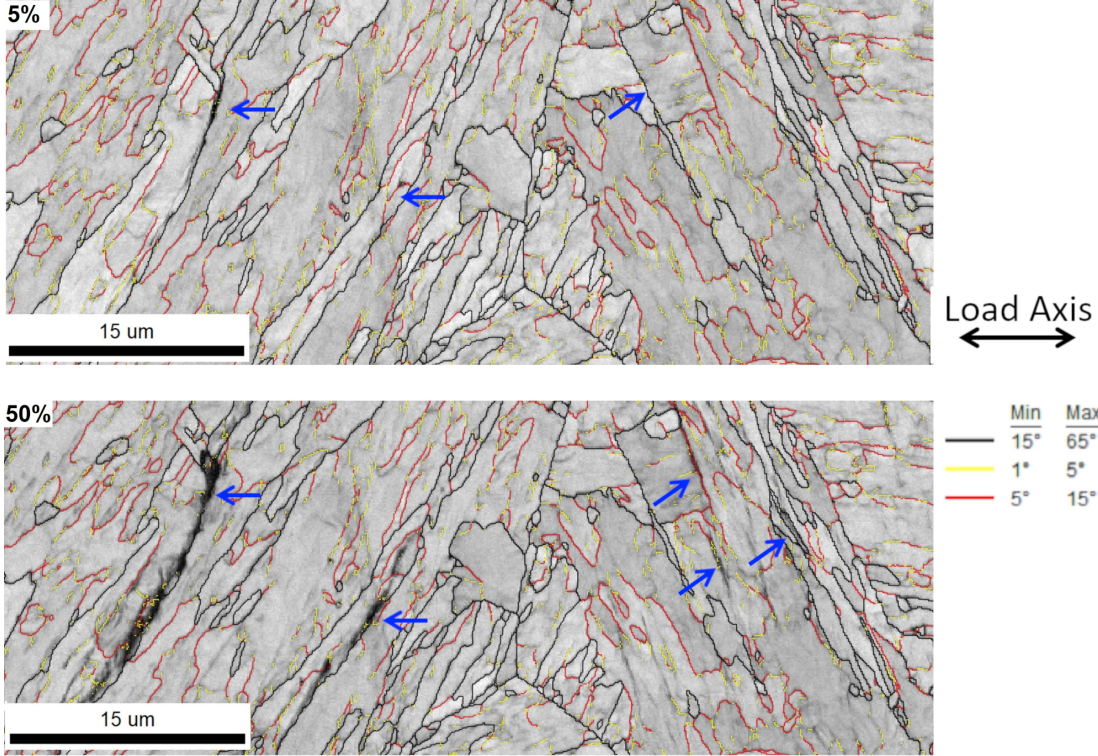


Figure 4.2.17: Image Quality + LSM EBSD maps of 0.5T sample at $\Delta\epsilon_t=1.2\%$. The blue arrows indicate the regions with the presence of extrusions

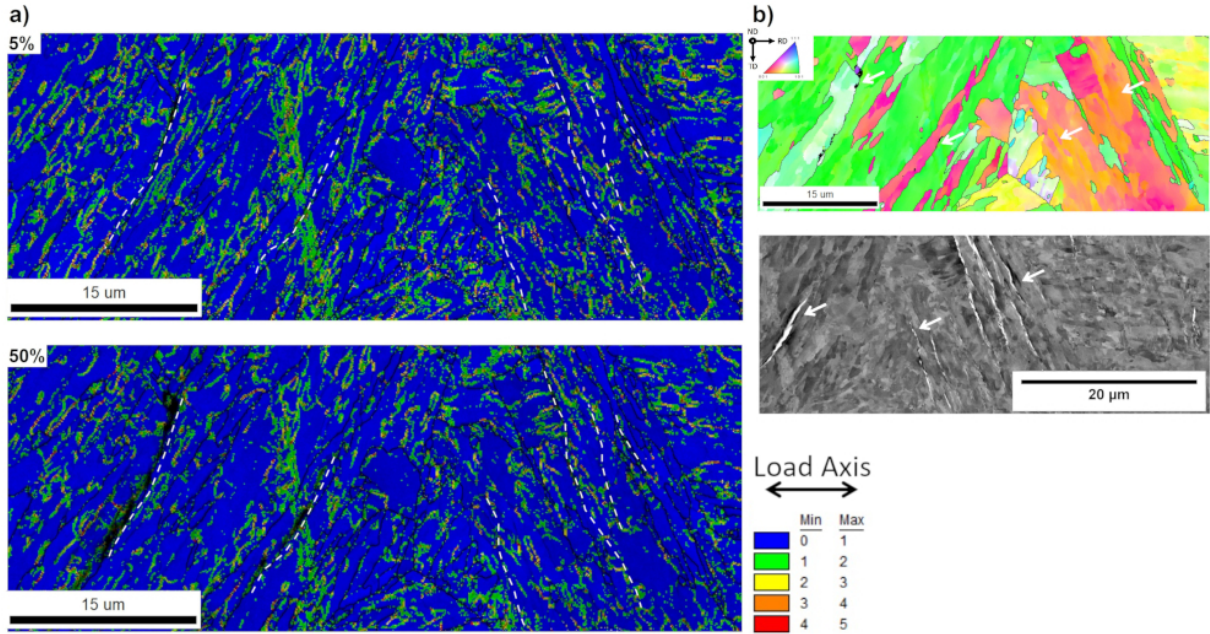


Figure 4.2.18: a) KAM maps evolution of 0.5T sample at $\Delta\epsilon_t=1.2\%$. The white arrows and the dashed lines indicate the extrusions. b) c-ECCI and IPF images indicating the scanned zone at 50% of life

Martensite parent grain reconstruction in Figure 4.2.19 indicates the grain boundaries delimited by the black lines, the packets appear as a group of four different nuances, the blocks are represented by a group of a slight color change, and finally, the laths or variants are represented by one singular color. The grain reconstruction helps to confirm the exact location of the extrusions and allowed the identification of 24 grains, 38 packets and 98 blocks in in each zone, in average. The pair of extrusions-intrusions identified coincides mostly with the block or laths boundaries (LAB), but in some cases, they may develop at packet boundaries (HAB). The common point is that the PSM is always confined inside a martensitic grain, most precisely next to lath/block interfaces. This level of applied strain is not capable to make the extrusions overpass the grain boundaries. The slip activity is in general concentrated within the laths and in some cases involves an entire block as expressed by the observation of protrusions. The preexisted pile-ups detected at the laths boundaries may perhaps be the driving force for the strain incompatibility at those boundaries during cycling. Incompatibility of plastic strain between two adjacent variants was documented in the literature for the quenched 8Ni steel, and indeed the blocks were the preferential sites of crack nucleation [94].

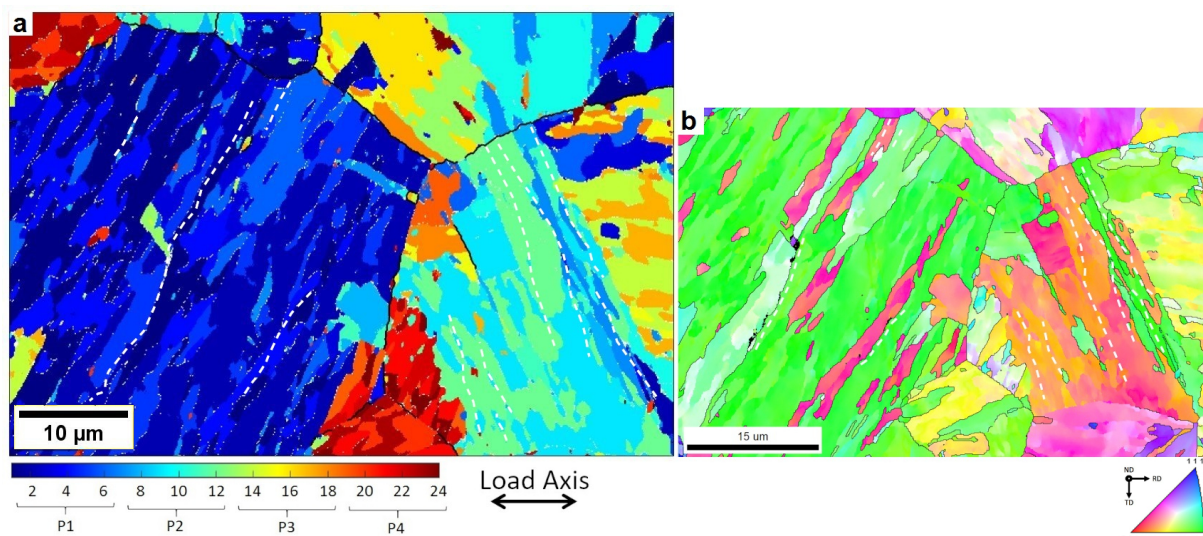


Figure 4.2.19: a) Martensite parent grain reconstruction based on the Kurdjumov-Sachs orientation relation for the 0.5T sample deformed at $\Delta\varepsilon_t=1.2\%$. b) Corresponding IPF map. The white dashed lines indicate the extrusions

4.2.5 Cross-sectional view

4.2.5.1 Accurate determination of extrusion/intrusion shape and location

To reinforce the conclusions taken from the EBSD and c-ECCI analysis done on the surface, the same procedure was done here as the one adopted for the WQ structure

providing a clear understanding of the extrusion's shape and specific location.

Figure 4.2.20 exhibits one of the selected extrusions typically found in the 0.5T material for the lamella extraction. TEM, HRTEM and TKD analyses were performed on the extracted FIB lamellae.

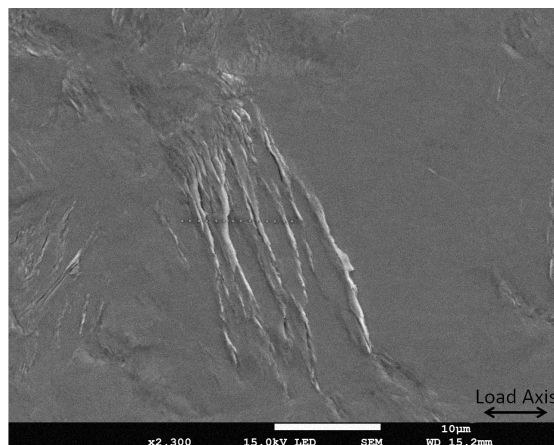


Figure 4.2.20: Selected zone comprising PSMs for FIB lamella extraction of the 0.5T sample with $\Delta\epsilon_t=1.2\%$ at the end of fatigue life. The dots correspond to the exact position of lamella extraction

A wide view of the extrusions profile comprising a microcrack is displayed in Figure 4.2.21. Even being at the end of fatigue life, the extrusions were still more numerous than the intrusions, which is more than expected, according to the literature [7, 9]. The 0.5T microstructure follows the same trend as the WQ microstructure, where the extrusions are placed at the boundaries and the intrusions in the middle of the lath. In some rare cases the intrusions were found at the interfaces and extrusions in the middle of the laths have also been found, but only when the laths were wider than the average. Besides the cell configuration within the laths indicating intense dislocation activity, no other specific dislocation configuration was observed at the vicinity of the pair of intrusion-extrusion.

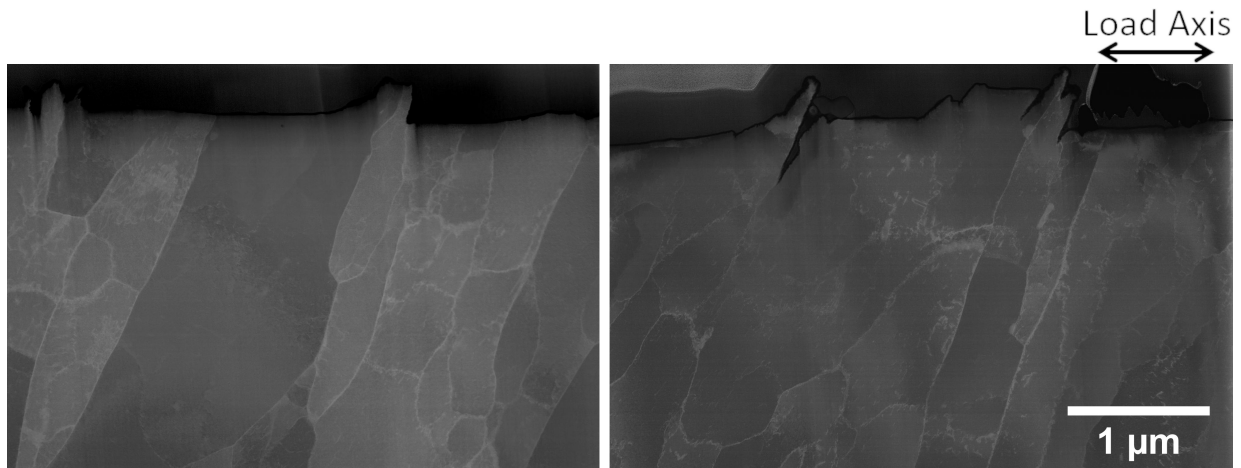


Figure 4.2.21: HRTEM images of two thin lamellae indicating the sites of extrusions and intrusions for the 0.5T sample at $\Delta\epsilon_t=1.2\%$ at the end of fatigue life

Another FIB lamella containing a microcrack and an austenite island placed at the martensitic lath boundary is shown in Figure 4.2.22. The extrusions are placed next to the martensitic boundary or cell walls, and one intrusion is located in the middle of the lath. The well-developed microcrack located in the central part of the lamella starts in the middle of the lath deviating later to the boundary. The very thin FIB lamella may fold depending on the extension of the microcrack, leading to a loss of details around this zone, although the crack path was still visible.

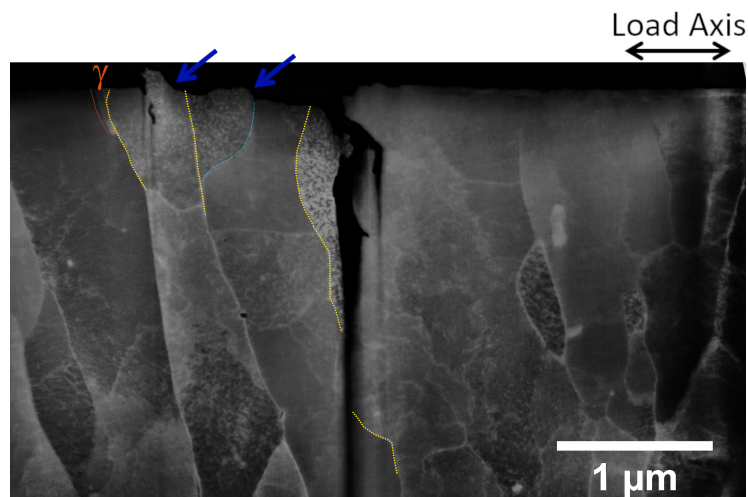


Figure 4.2.22: FIB lamellae showing a zone containing a microcrack and pair of extrusion-intrusion next to an austenitic island for the 0.5T microstructure at the end of fatigue life ($\Delta\epsilon_t=1.2\%$)

Figure 4.2.23-a is an HRTEM image of the martensite/austenite interface observed in Figure 4.2.22. The austenite remained stable even after FIB machining due to the increased content of gammagenic elements. The idea of recognition of the austenitic islands

at the boundaries and their role in the mechanism of plastic accommodation remains the same as for the WQ sample. Since the amount of austenite stabilizing elements like Ni, Mn, and C is often higher in reversed austenite than in the martensitic matrix, a chemical map of this zone was made to examine the distribution of those elements.

As expected, a higher concentration of nickel and manganese is observed in the zones where the austenite is present (Figure 4.2.23-b). Inverse Fast Fourier Transform (IFFT) was also performed to select the austenite lattice planes, highlighting the austenite/martensite interface. Figures 4.2.23-c), d), and e) are the corresponding IFFT/FFT images showing the existence of both martensitic and austenitic phases and the well-delimited interface. In this microstructure, the austenitic phase was more clearly identified in comparison to the WQ microstructure.

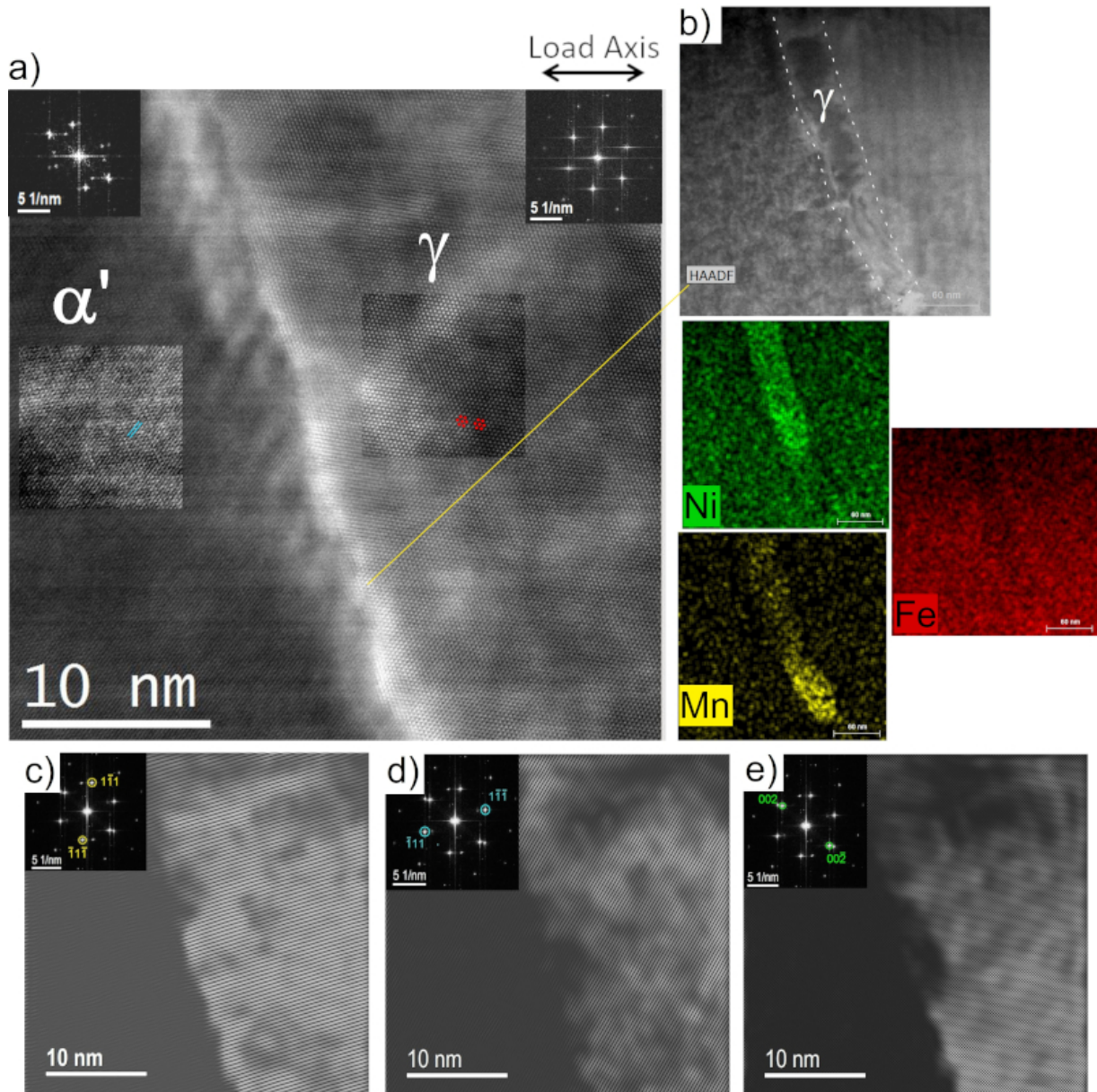


Figure 4.2.23: a) HRTEM image the interface between martensite and austenite of the 0.5T sample, b) HAADF and EDX mapping of the chemical elements of the selected zone, c), d) and e) Austenite planes enhanced by IFFT

In some cases, in TEM mode, the distinction between austenite with a zone axis along $\langle 110 \rangle$ and martensite along $\langle 111 \rangle$ remains difficult, because the diffraction spots may coincide or stay very close to each other. The TKD analysis, in this case, has been used as a complementary method to validate the existence of austenite in the interface [154]. Figure 4.2.24 shows the IPF and phase map of the same scanned zone, confirming the presence of austenite.

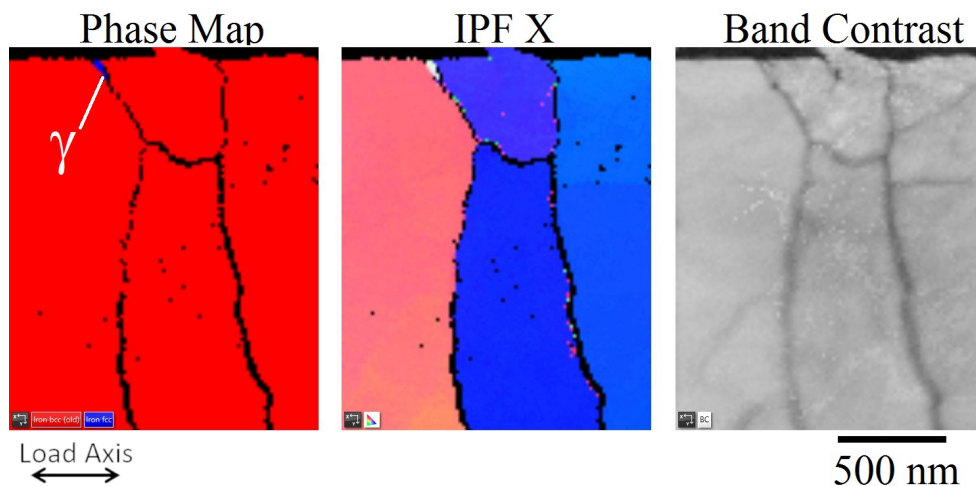


Figure 4.2.24: Phase Map, IPF and Band contrast images of the TKD scan conducted on a FIB lamellae of the 0.5T sample ($\Delta\epsilon_t=1.2\%$)

4.2.6 Conclusions

It may be inferred from the microstructural analysis of the 0.5T material that the 30 min - 600°C tempering heat treatment favored a considerable increase in the lath size, some of them coalesced transforming into equiaxed structures or recovery cells. The dislocations were less entangled and less numerous, having an easiness to glide. Pile-up originated from the tempering treatment was also observed. The reversed austenite after the tempering treatment, in a volume fraction of about 4.5%, may be found at the interfaces and seems to be more stable.

Advanced analysis techniques are still necessary to be employed for the characterization of the reversed austenite, and more generally for the tempered microstructure. Even if the size of reversed austenite lamellae has increased, leading to easier indexing, there were still significant differences between the XRD and EBSD techniques for the volume fraction measurement.

The results of this heat treatment were already seen in the fatigue performance. Compared with the WQ material, lower stress levels were reached in the 0.5T material and the cyclic hardening was not observed, being replaced by a continuous softening due to the facilitated dislocation glide and preexisted pile-ups. No bi-linear behavior was observed in the Manson-Coffin relation, suggesting that one type of mechanism of cyclic accommodation is present for this microstructure at the applied levels of deformations analyzed.

The surface exhibited several types of Persistent Slip Marks, comprising both isolated extrusions and protrusions and a more deformed surface as the total applied strain increases.

Regarding the appearance of extrusions, the 0.5T sample follows the same trend compared to the WQ sample, where the extrusions are located at the interfaces, mostly LAB. The intrusions were found to be in the middle of the laths, no specific dislocation arrangement was observed other than the dislocation cells. In this microstructure, intense dislocation bands were found next to the PSMs and it was clear that the HDDW placed at the laths and cell boundaries are directly linked to the emerging extrusions. The prior martensitic grains can exert an influence on the dislocation movement by blocking the development of the extrusions across them, plastic activity is typically restricted to martensite blocks due to the plastic incompatibility between the variants. Combined with the preexisting pile-ups and the short distance motion of dislocations causing strain incompatibility, the boundary sliding also seems to contribute to the plastic accommodation mechanism as remarked by the cross-section analysis, aided by the presence of the austenite island located at the interface acting as a "greasy film".

HIGHLIGHTS

- 30 min tempering at 600°C recovers the quenched microstructure and transforms the retained austenite into reversed austenite
- Reversed austenite films are present at martensite interfaces (laths, blocks, packets, and GB)
- Surface relief is identified already at lower strains and comprises both isolated extrusions or protrusions
- Extrusions emerges at the laths interfaces, while intrusions nucleates inside the laths
- Extrusions form at laths and block boundaries (LAB) or covers one entire block
- Reversed austenite was identified and may help matter flowing at interfaces

The graphical abstract (Figure 4.2.25) summarizes the process of extrusion/intrusion nucleation and growth through the fatigue life of 0.5T microstructure.

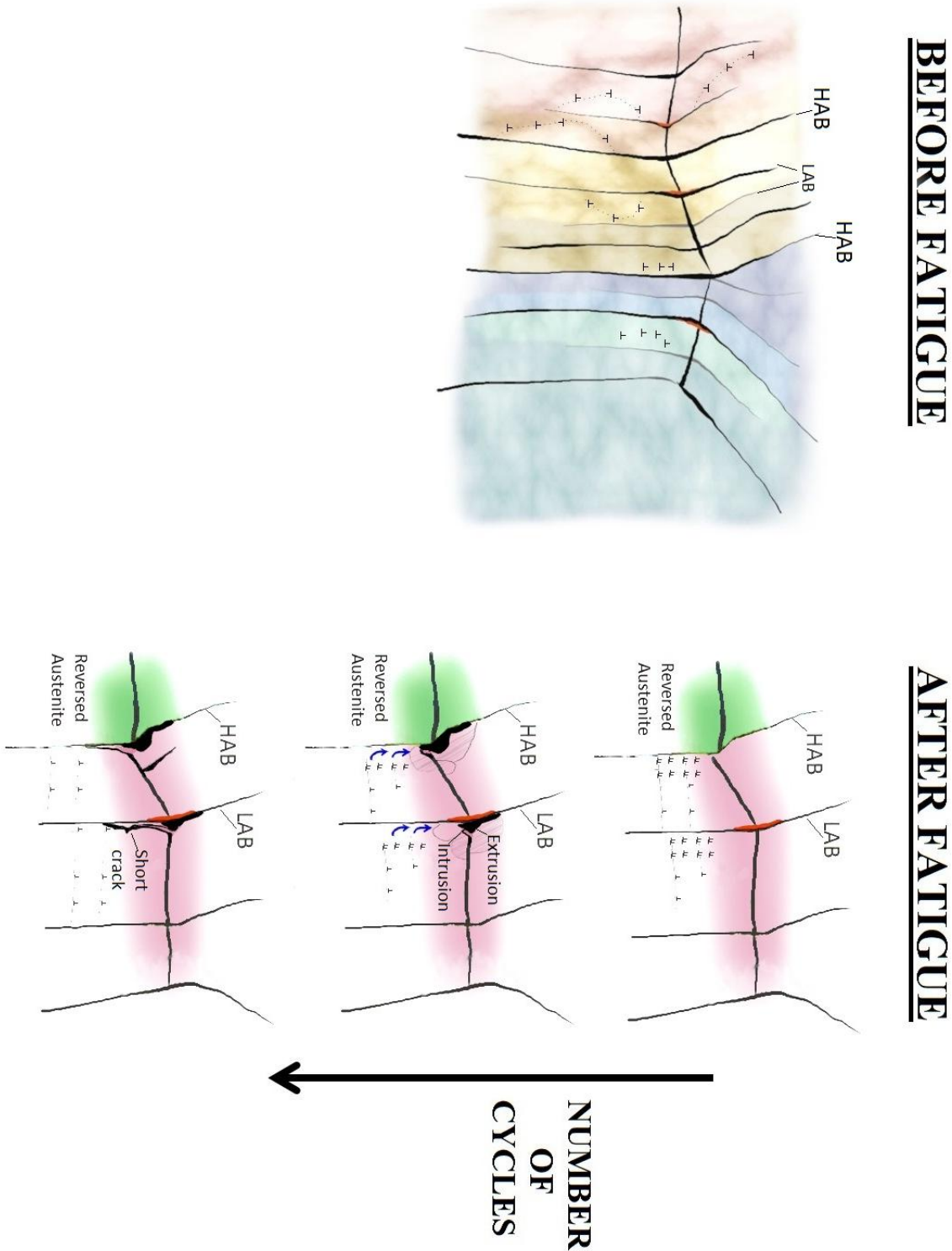


Figure 4.2.25: Representation of extrusions and intrusions nucleation sites for the 0.5T sample during fatigue

4.3 10 Hours Tempered 9Ni steel - 10T sample

4.3.1 Non-deformed state

4.3.1.1 Matrix Evaluation

As long as the tempering time increases, substantial changes happen in the matrix together with an increase in the austenite content. The microstructure tempered for 10 hours is considerably different from the one that has been submitted to quenching heat treatment, having an average grain size of 18 μm , packet size with 6.2 μm in dimensions, and a block size of 3.2 μm . The time and temperature also allowed the bainitic reaction to take place. The result is a matrix composed of a mixture of tempered martensite and bainite. In addition, the amount of austenite increased substantially and segregation of this phase was observed in the regions with a higher concentration of bainite in agreement with the statements of Bhadeshia [12], as shown in Figure 3.2.3.

In order to capture the distribution of the martensitic and bainitic zones, five different areas of the specimen were scanned in the EBSD analysis. The optical micrographs indicated that the bainite is segregated in bands aligned in parallel to the rolling direction (load axis). Thus, a vertical scan perpendicular to the rolling direction is displayed in Figure 4.3.1, showing slight differences between the two constituents. The bainite is supposedly in the center, where the austenite is more concentrated. The bcc and fcc phases can be easily distinguished by the EBSD technique, the main difficulty is to differentiate the tempered martensite from the ferrite and bainite constituent, because they have the same bcc structure. In the case of martensite, the pattern quality is usually lower when compared to the other phases because it is more distorted and richer in dislocations. Concerning bainite and ferrite, some studies have shown that the bainite presents a higher dislocation density (10^{13} m^{-2} - 10^{14} m^{-2}) than ferrite (10^{12} m^{-2} - 10^{13} m^{-2}) [175].

The mean angular deviation (MAD) represents the mismatch between the measured and calculated angles between bands. Hence, the larger the MAD value, the greater the mismatch, and the lower is the indexing confidence. The MAD is also an excellent predictor of lattice strain or defect density. In this microstructure, the MAD values, the zero solutions, and the austenite segregation were considered to distinguish the martensite from bainite, where the martensite presents higher MAD values and higher zero solutions due to the dislocation density, even though they have a very similar structure. The IPF maps in Figure 4.3.1-a shows that the material does not show any preferential texture.

The local misorientation mapping was used to evaluate the state of the microstructure after a long tempering treatment, the KAM maps (Figure 4.3.1-b) indicate very few strain fields originated from the martensitic and bainitic transformation, and the LSM maps (Figure 4.3.1-c) points that those strain fields are mainly concentrated in LAB from 1° to 5° that mostly represents the dislocations arrangements, such as restored cells. Finally, the detection of reversed austenite has attracted attention, since this microstructure revealed the largest quantity of this phase by XRD. The phase map shows the austenite placed at the interfaces and concentrated in the central scanned zone (Figure 4.3.1-d).

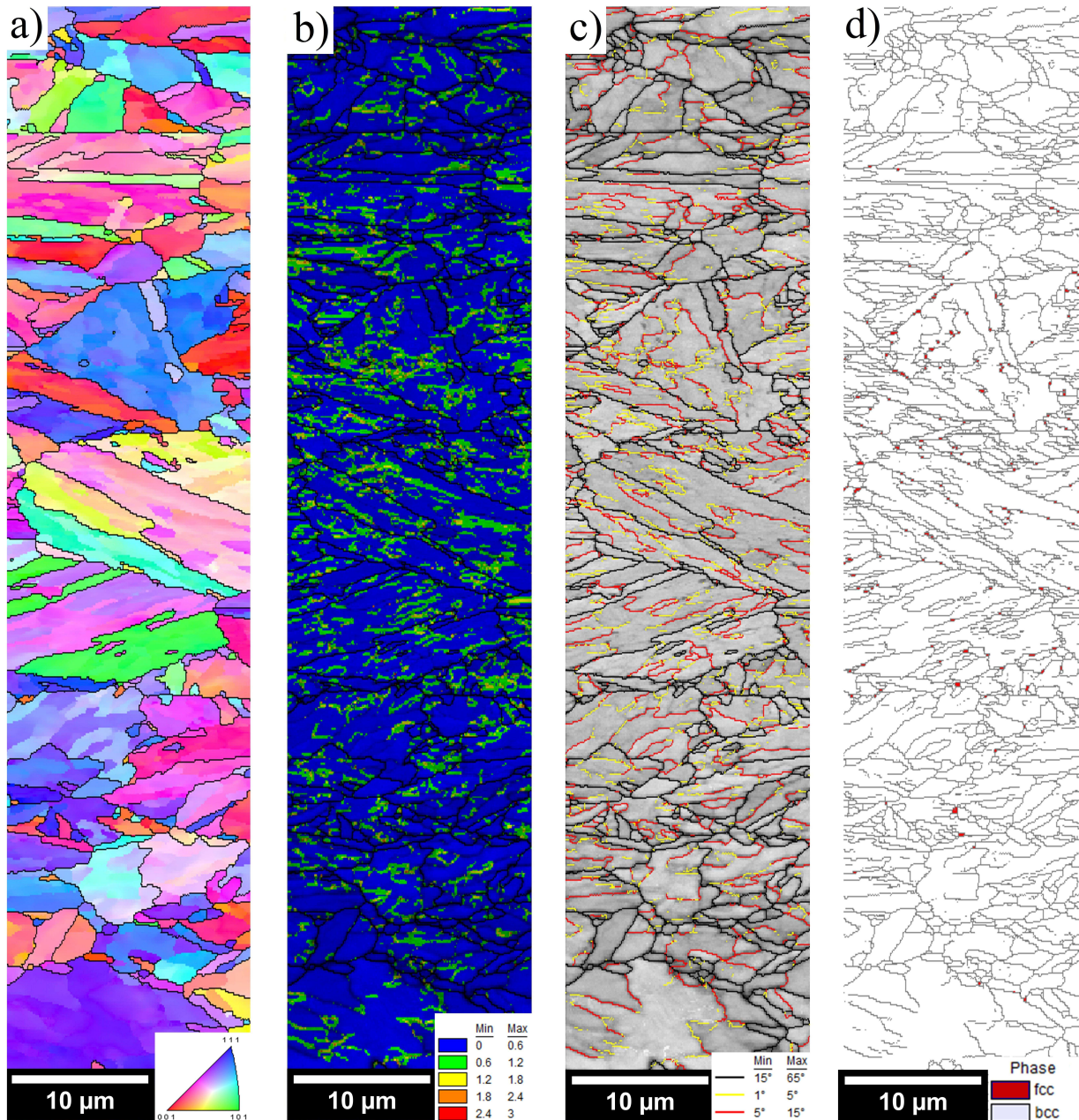


Figure 4.3.1: a) IPF, b) KAM, c) IQ +LSM and d) Phase Map of the 10T sample

The reversed austenite was properly imaged using TEM by Selected Area Diffraction (SAED) mode. Figure 4.3.2-a shows the bright-field image, the corresponding SAED pattern from the imaged zone is present in Figure 4.3.2-b and the dark field of the selected $(220)\gamma$ spot shows the austenite films and islands aligned in parallel (Figure 4.3.2-c). The austenite films, with an average thickness of 300 nm, were found to be aligned in parallel with an average spacing between them of one micron, a distance that represented the average lath width from the WQ structure.

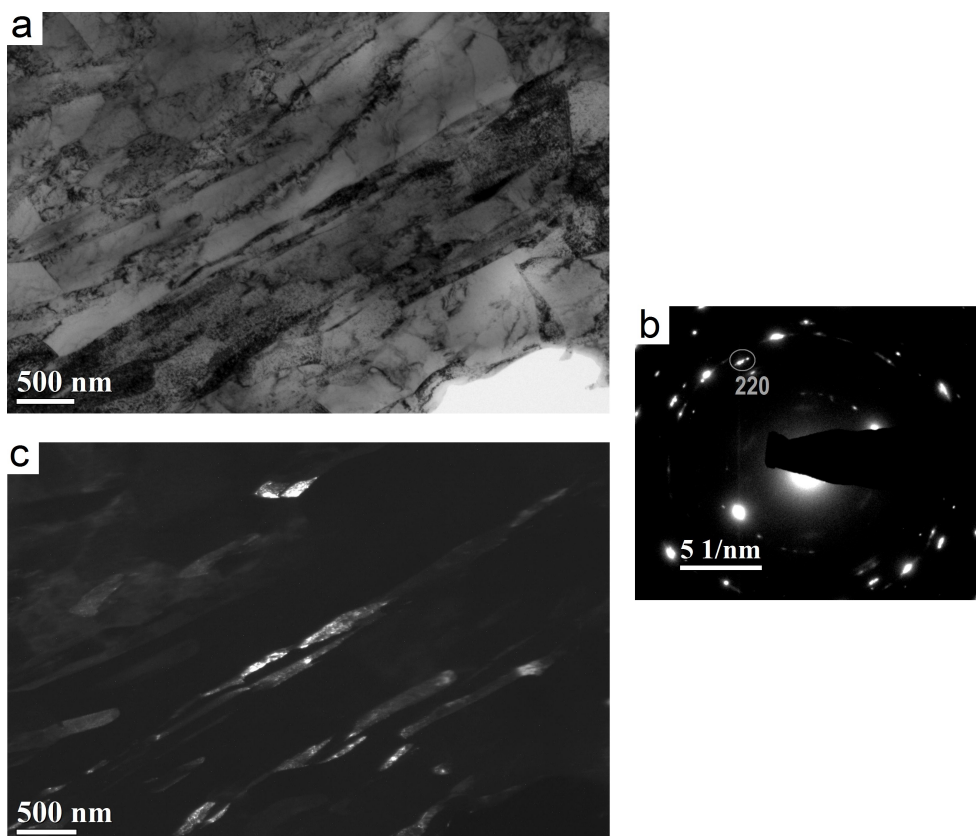


Figure 4.3.2: a) Bright field image TEM of 10T sample, b) Selected Area Diffraction Spot (SAED) of $(220)\gamma$ plane, c) dark field image of the same area highlighting the austenitic phase

TEM investigations allowed visualization of the dislocation distribution in the matrix (Figure 4.3.3). Few laths are still visible, some of them are practically dislocation-free, while others have some entangled or isolated dislocations. Wider laths presented the recovered cells in their interior with their walls filled with entangled dislocations.

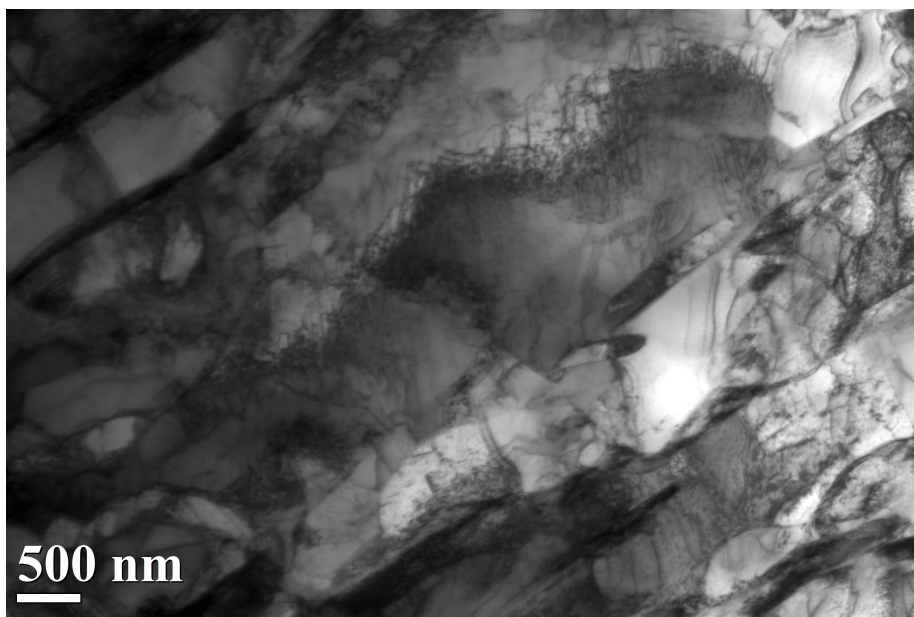


Figure 4.3.3: TEM micrograph of the 10T sample

The c-ECCI images reveal on a large scale that the matrix was almost completely changed by the long-time tempering heat treatment (Figure 4.3.4). Well-defined subgrains and cells are visible together with a more equiaxed structure, the sharp laths as the one seen in WQ microstructure are rarely observed.

By association with the shape and contrast difference, the c-ECCI also confirms the presence of longer and more noticeable reversed austenite islands decorating the laths interfaces, sometimes aligned in parallel at the preexisted laths boundaries originated by the quenching heat treatment (Figure 4.3.5). The average size of the encountered reversed austenite islands was about 300 nm, with a minimum width of 50 nm and a maximum width of 600 nm.

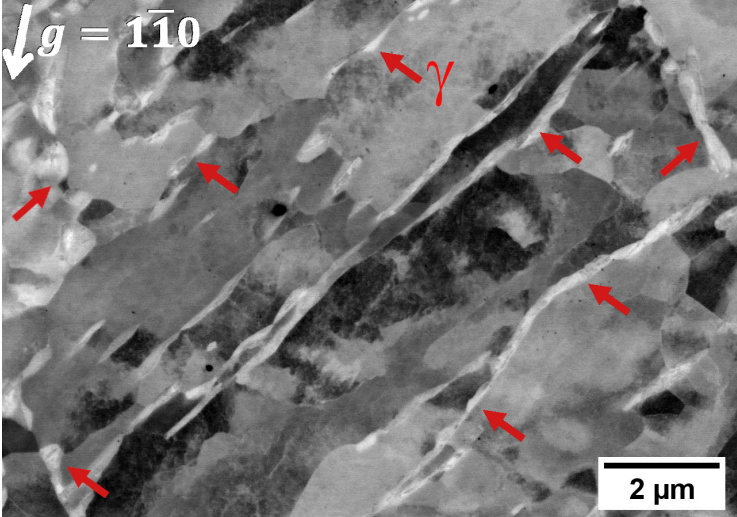


Figure 4.3.4: c-ECCI image of the 10T microstructure, the red arrows point to the reversed austenite

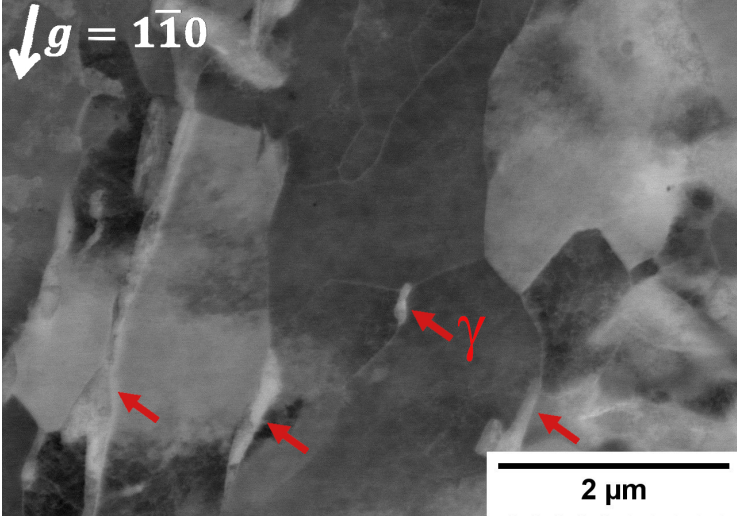


Figure 4.3.5: c-ECCI image of the 10T microstructure, the red arrows point to the reversed austenite

4.3.2 Cyclic stress-strain response and fatigue resistance

The cyclic behavior with regards to the number of cycles and the fraction of fatigue life for different total strains is shown in Figure 4.3.6.

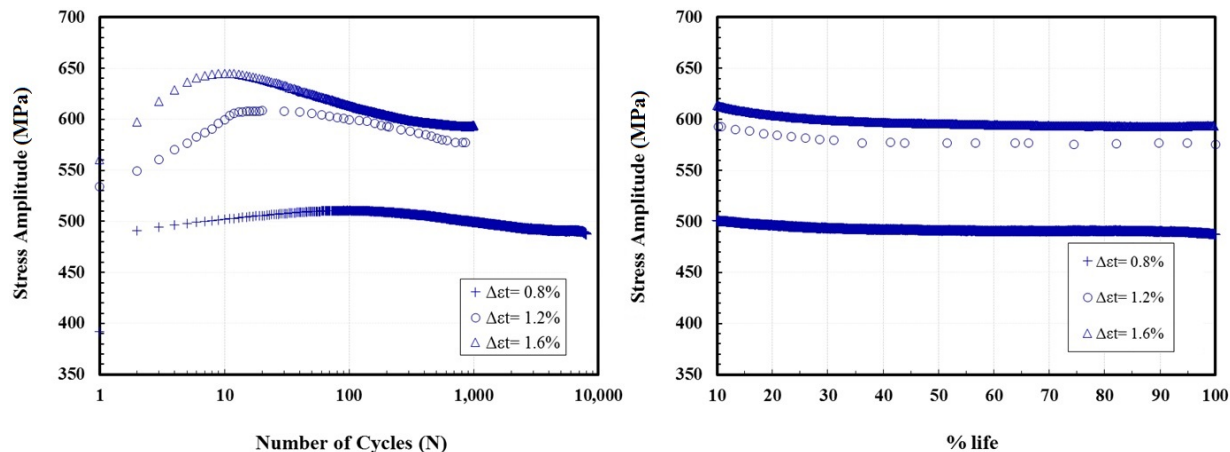


Figure 4.3.6: Evolution of the stress amplitude versus the number of cycles (left) and versus the fatigue life fraction (right) at different total strains for the 10T sample

The cyclic response of the 10T sample is characterized by an initial hardening, occupying approximately 1% of the fatigue life. This hardening period lasts longer and is less evident as the total applied strain decreases. The subsequent step is cyclic softening and quasi-stabilization. As noticed for the primary cyclic hardening, the softening rate is more noticeable when the applied total strain is higher. XRD analysis indicated a small decrease in the austenite fraction from 11% to 7% in the sample deformed at $\Delta\varepsilon_t=1.2\%$. Nevertheless, the link between the cyclic hardening with the austenite transformation is far to be obvious if the results on TRIP steels with nearly the same austenite content is considered. The tentative of releasing the entangled dislocations present in some laths and the generation of dislocations in laths containing cells is also to be taken into account. In further cyclic loading, dynamic recovery takes place with dislocations moving and annihilating by interacting with opposite sign dislocations.

Figure 4.3.7 shows the cyclic stress-strain curve derived from the quasi-stabilized hysteresis loops, together with the curve generated from the peak stress and the monotonic hardening curve. The cyclic hardening is more apparent at higher strain levels during the peak stress of cyclic accommodation. A decrease in stress levels is remarked and is even more evident at increased levels of strain, meaning that a higher strain level is necessary to release the previously entangled dislocations allowing them to glide.

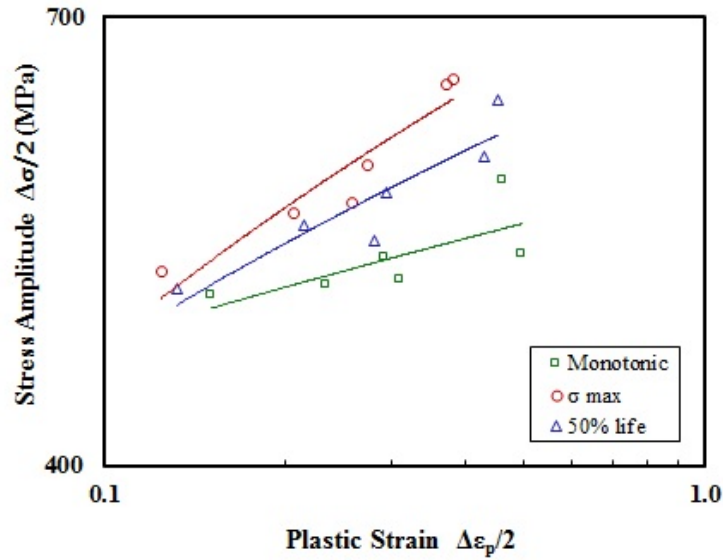


Figure 4.3.7: Cyclic and monotonic stress-strain curves for the 10T sample

The elastic (Basquin) and plastic parts (Manson-Coffin) of the total strain at the fatigue life is plotted in Figure 4.3.8. Following the same trend as the 0.5T sample, no bi-linearity was observed and the elastic strain curve stays above the plastic strain, except at the higher level of total applied strain.

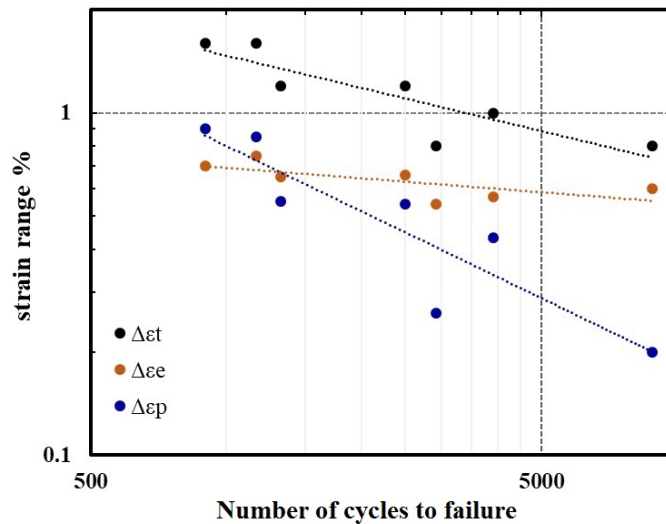


Figure 4.3.8: Manson-Coffin and Basquin curves of the 10 T sample

4.3.3 Topography Overview

The surface damage for the three levels of applied strain can be seen in Figure 4.3.9. The surface is mostly composed of severe deformation already at lower levels of applied strain, with coalesced microcracks linking one group of extrusions to another. The surface

is mostly composed of protrusions, very few isolated extrusions were identified. Meaning that an increased amount of austenite located at the laths interfaces together with the mixture of bainite and martensite in the matrix favors the plastic accommodation as surface damage.

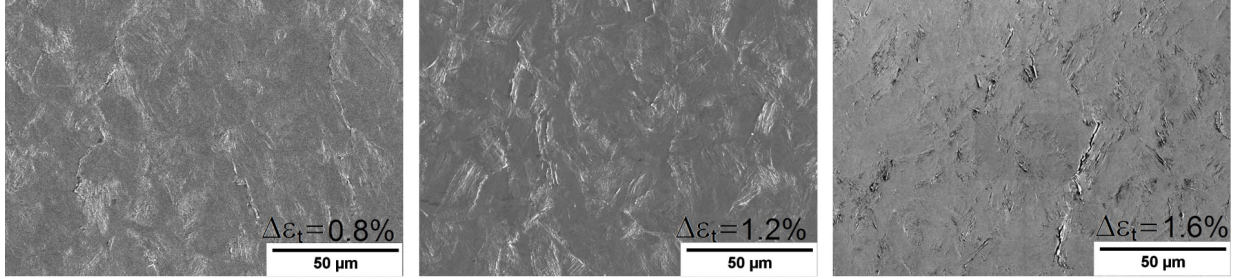


Figure 4.3.9: Surface damage accumulation resulted from LCF tests for the 10T sample

4.3.4 Dislocation Structure and Microstructural Response

Like the 0.5T sample, the fatigue resistance of the 10T sample could be also represented with a single slope in the Manson-Coffin relation. Because of this, only the test performed at $\Delta\epsilon_t=1.2\%$ was chosen to observe the microstructural response during the LCF test. Table 4.3.1 shows the plastic strain range measured from hysteresis loops at each step of fatigue life.

Table 4.3.1: Plastic strain range of 10T sample at the evaluated stages of fatigue life with $\Delta\epsilon_t=1.2\%$

% life	$\Delta\epsilon_p$
σ_{\max}	0.31
5%	0.36
50%	0.72

The visualization of the slip steps at the peak of stress (σ_{\max}) for the sample tested at $\Delta\epsilon_t=1.2\%$ was complicated by the presence of austenite, the difference in topography and contrast leads to some confusion among them. To solve this issue, several zones were scanned and in some cases, the lighter areas could be related to the emerging extrusions.

Figure 4.3.10 shows the dislocation evolution seen by the c-ECCI technique in the course of the fatigue life in the $\vec{g} = \bar{1}10$ plane. The scanned zone at (σ_{\max}) was filled by dislocations and recovered cells coming from the tempering heat treatment. At 5% of life, the microstructure changes drastically, with dislocations being vanished in the selected crystallographic plane. Extrusions appeared aligned in parallel, the exact position of

the extrusion was not possible to be determined by this technique. In general, at 5% of fatigue life, coalescence of the substructures (cells or subgrains) is remarked. As the cycling continues, at 50% of fatigue life, the extrusions become more prominent and some new extrusions emerge in between, showing a highly deformed surface. Even at 50% of fatigue life, the intrusions were hardly found, only depressions next to the extrusions were identified, as seen in the Figure 4.3.10.

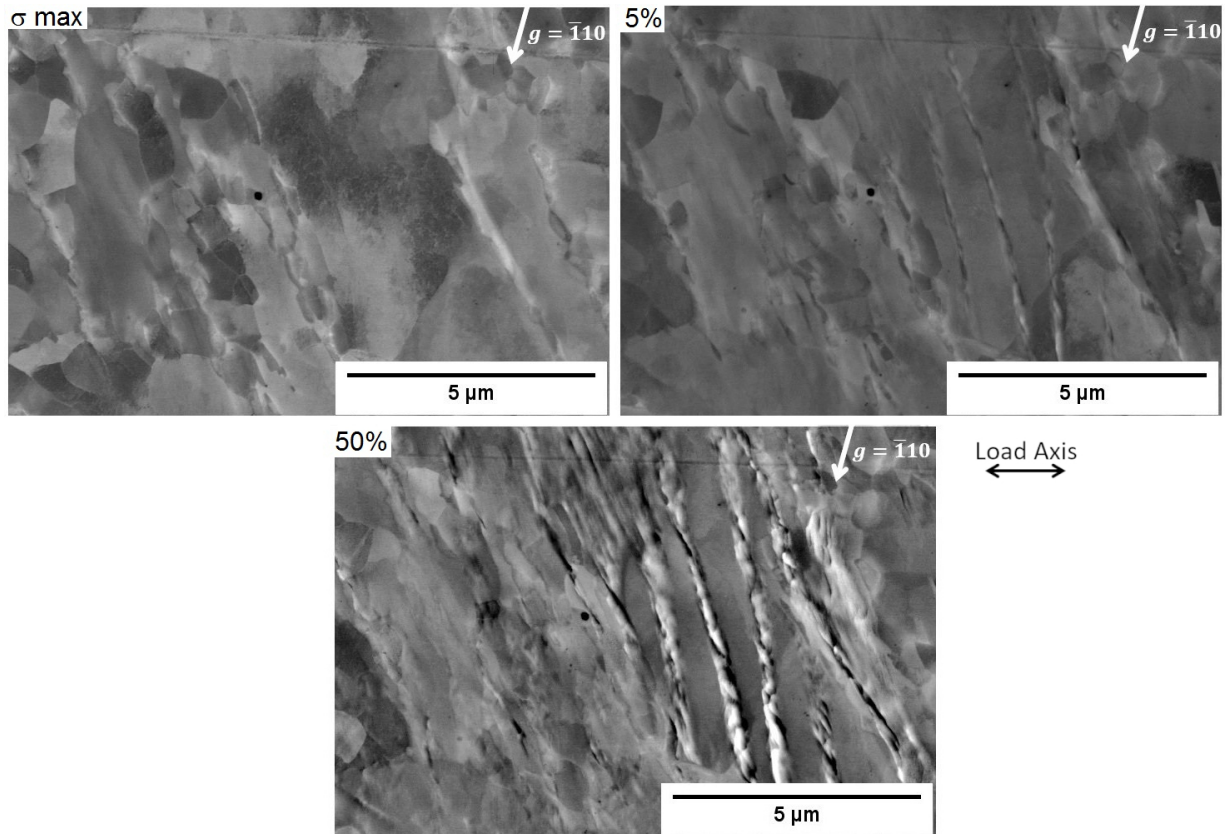


Figure 4.3.10: c-ECCI images showing the dislocation and topography of the 10T sample at each stage of cycling

A closer view in another zone at all stages of fatigue life highlights the dislocation structures that have been found (Figure 4.3.11). As encountered for the 0.5T sample, HDDW and dislocation lines are visible 5% of fatigue life. The previously encountered cells coalesced at 50% of fatigue life and more defined walls are seen with dislocation bands evident inside them. The austenite islands are highlighted by the red arrows, it can be observed that in the course of cycling, the zones around the austenite will deform developing into an extrusion (Figure 4.3.11-c). Plastic accommodation is seen in the bcc phase (martensite or bainite). Establishing a parallel with duplex steels, the bcc phase is known to accommodate the plastic deformation, leading to stress concentrations and finally the appearance of microcracks [76, 77, 238]. Differently for the results found in the literature for duplex steels, where both phases exhibit more or less the same plastic

deformation distribution, no PSM has been seen here in the austenite islands at this level of applied strain ($\Delta\epsilon_t=1.2\%$), or even crossing them, respecting very well the phase boundaries. The bcc phase in this steel is richer in dislocations compared to the fcc phase and during the cyclic straining, the dislocations will arrange themselves. As a result, the higher plastic activity seen in this phase might explain microcrack nucleation in the bcc matrix during LCF, together with the fact that the austenite can act as a greasy film, facilitating the boundary sliding.

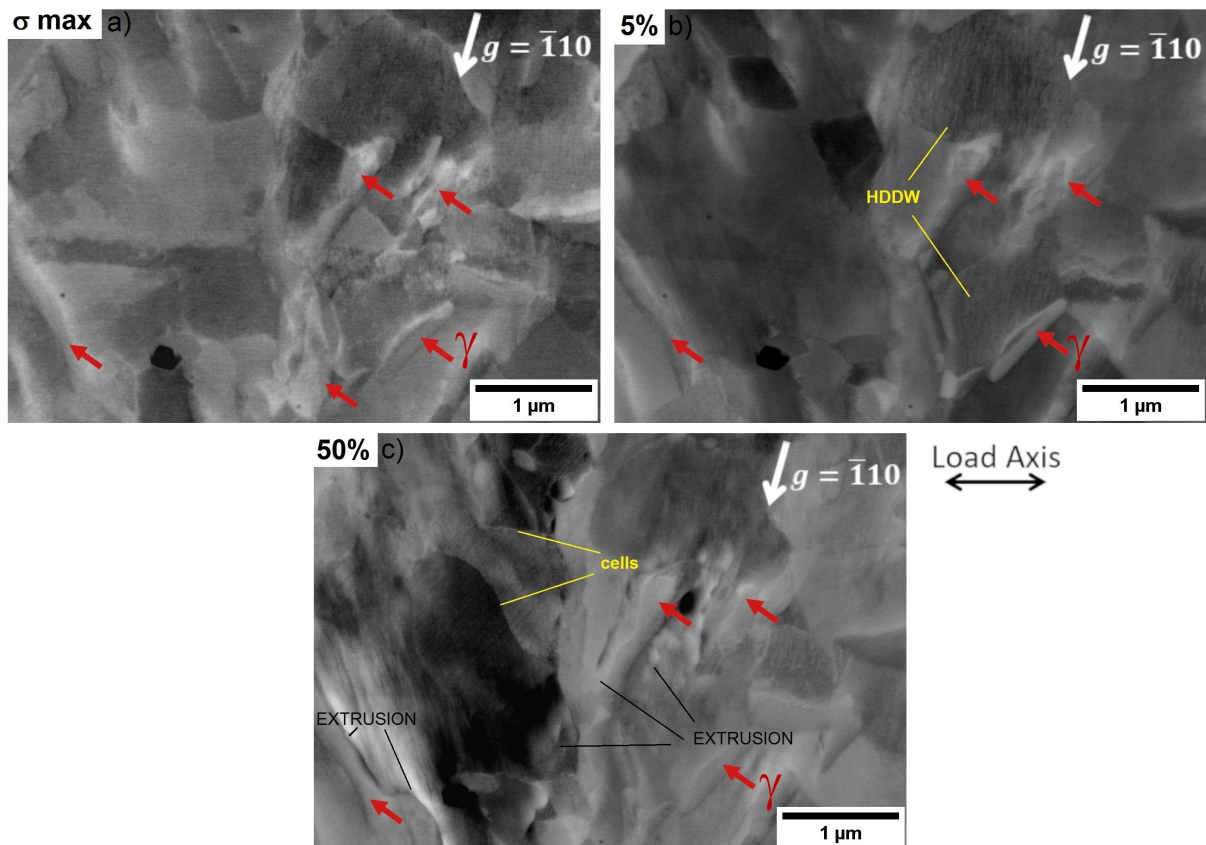


Figure 4.3.11: c-ECCI images showing the dislocation evolution of the 10T sample at each stage of cycling

Local plastic gradients that may correspond to misorientation induced by GNDs were evaluated by the KAM method. It has been observed by the KAM maps (Figure 4.3.12) that stronger strain fields, comprised between 1.2 and 3 degrees misorientation in the KAM method, are related to the pre-existing 1-5° misorientations detected by LSM at σ_{\max} (Figure 4.3.13). An increase in strain fields towards the zones with the emerging PSMs at 5% of fatigue life is observed, however, no extrusion was still detected in that zone at this stage. The fragmented zones with small misorientation (0.6° to 1.2°) in the KAM maps present at 5% of life were not identified as any type of substructure by the LSM method, but upon further cycling, new substructures were found next to those zones and they correspond to the new 1-5° LAB. Additionally, the new-created

1-5° misorientations at 50% of fatigue life came from the strain fields observed at 5% of cycling by the KAM method. The c-ECCI and IPF images are used together with the KAM maps to bring a better understanding of the location of the strain fields and the extrusions found. The preliminary observation indicates that some extrusions are comprised within a grain, but highly deformed zones at the possible grain boundaries were also seen. The grain reconstruction of the zone will help to get a better conclusion about the location of the extrusions.

Regarding the LSM maps, no big change was detected from σ_{\max} to 5% of fatigue life, only a small decrease in dislocations and a discrete increase of 5-15° LAB was observed. At 50% of fatigue life, an increase of 1-5° was seen and few HAB were detected next to the PSMs.

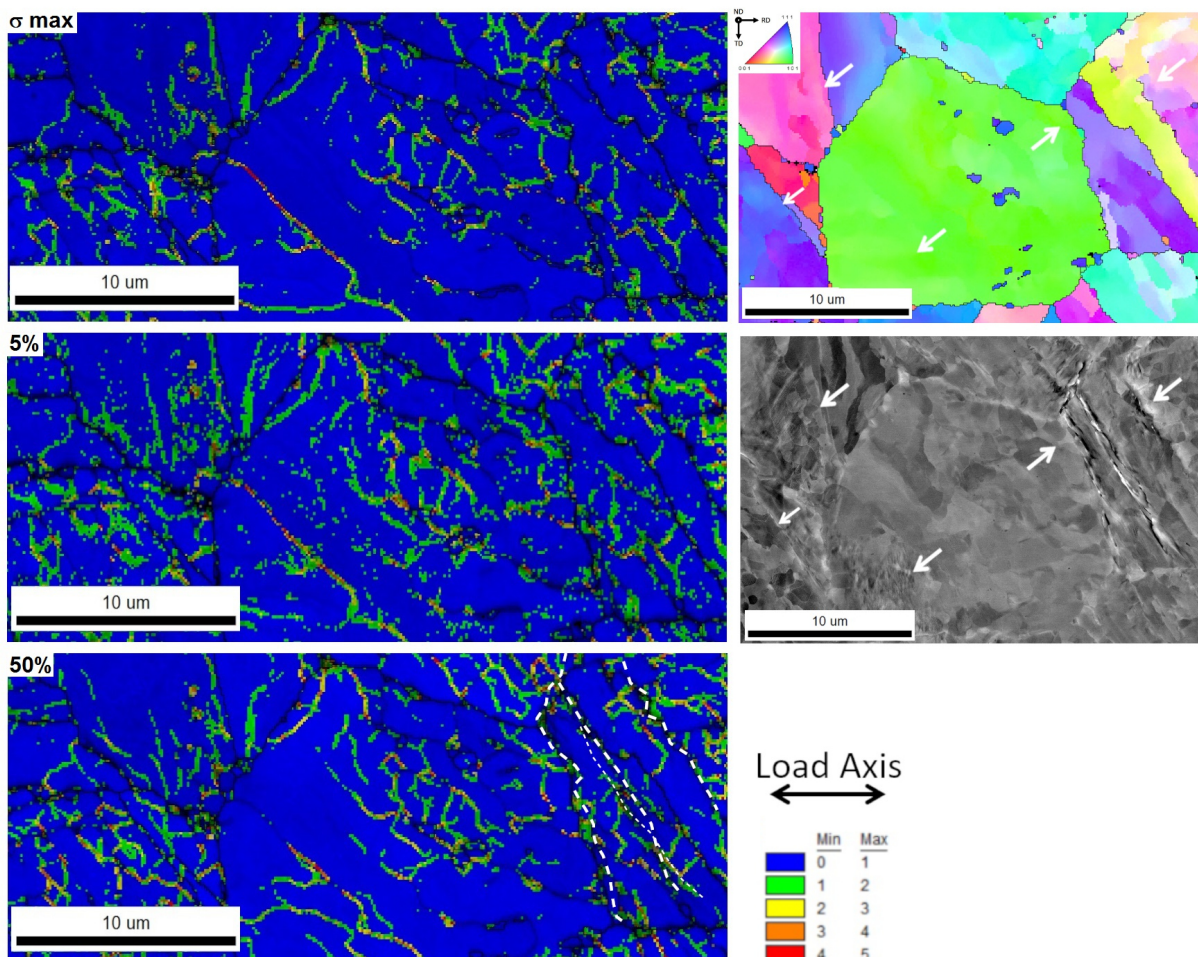


Figure 4.3.12: a) KAM maps evolution of 10T sample at $\Delta\epsilon_t=1.2\%$ b) c-ECCI and IPF images indicating the scanned zone at 50% of fatigue life. The white arrows and the dashed lines indicate the extrusions

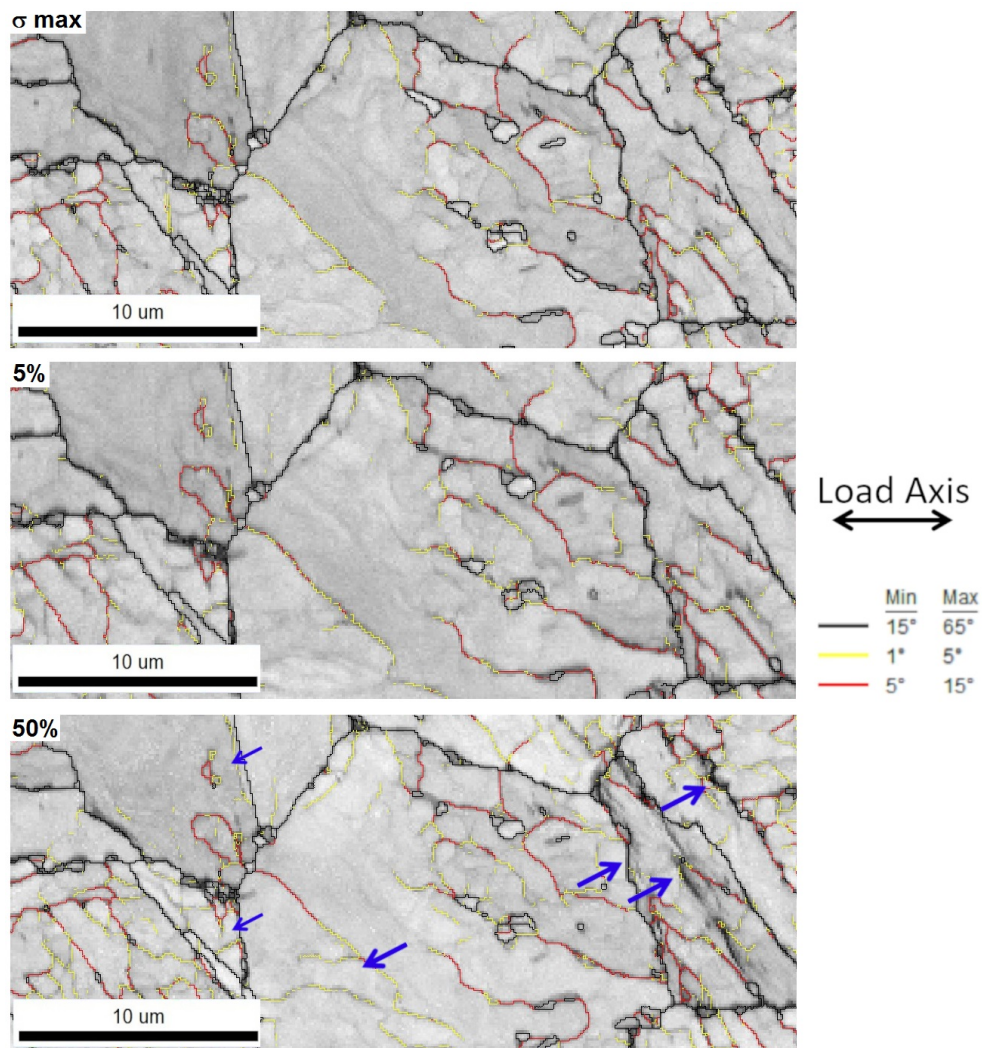


Figure 4.3.13: Image Quality + LSM EBSD maps of 10T sample at $\Delta\epsilon_t=1.2\%$. The blue arrows indicate the regions with the presence of extrusions

Four scanned zones comprising the PSM were reconstructed and Figure 4.3.14 shows one of the several reconstructed zones, in average a total of 35 grains, 60 packets and 88 blocks were identified. The same region previously represented by the KAM and LSM maps was selected to be shown here. As the other reconstructed maps for the WQ and 0.5T samples, the black lines delimit the martensitic grains, the packets are represented by a group of four different colors, the blocks by a group of two light color changes, and the laths or variants are represented by a single color. Some extrusions are placed exactly at the HAB (GB or a packet boundary) or starting at them and growing in parallel within a block or a packet. A high number of groups of extrusions, and protrusions as well, were found comprising an entire single block. PSMs at block boundaries were found too.

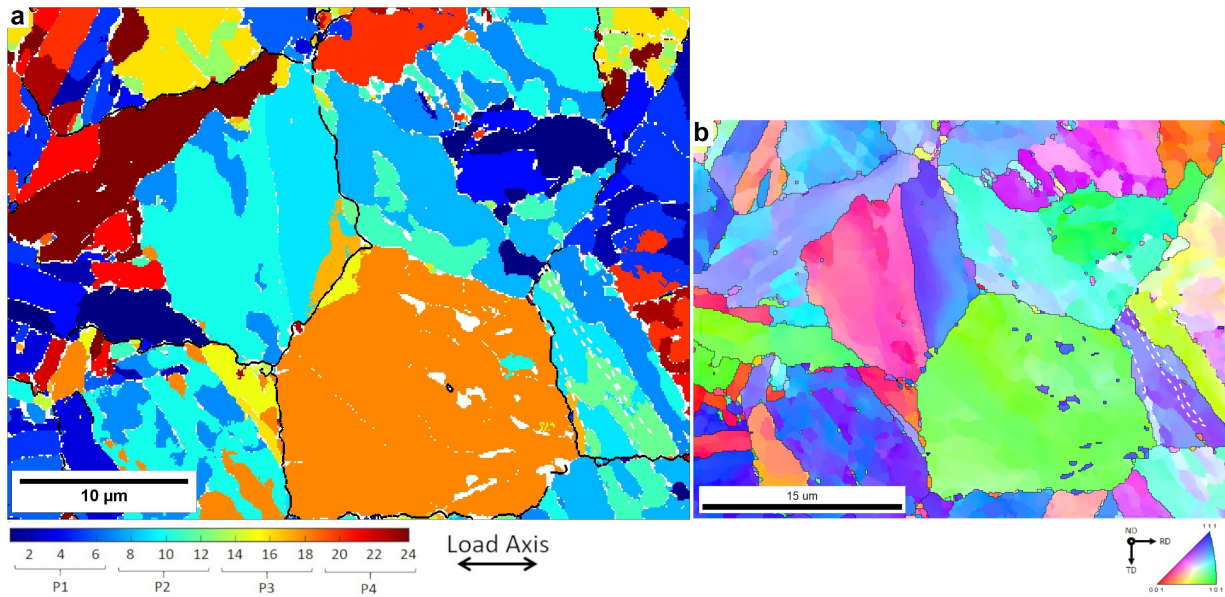


Figure 4.3.14: a) Martensite parent grain reconstruction based on the Kurdjumov-Sachs orientation relation for 10T sample deformed at $\Delta\varepsilon_t=1.2\%$. b) Corresponding IPF map. The white dashed lines indicate the extrusions

In contrast to the other two microstructures (WQ and 0.5T), the austenite islands were still detected by EBSD after the LCF tests. XRD analysis has indicated a reduction from 11% to 8% of the austenite content (30% of decrease), EBSD phase maps (Figure 4.3.15) also exhibited a diminution around 30% of the austenitic phase. Due to its scale limitation regarding very thin structure, EBSD appears here only as a qualitative tool to describe this phase evolution. Furthermore, the austenite content measured by EBSD is almost ten times lower than the value measured by XRD.

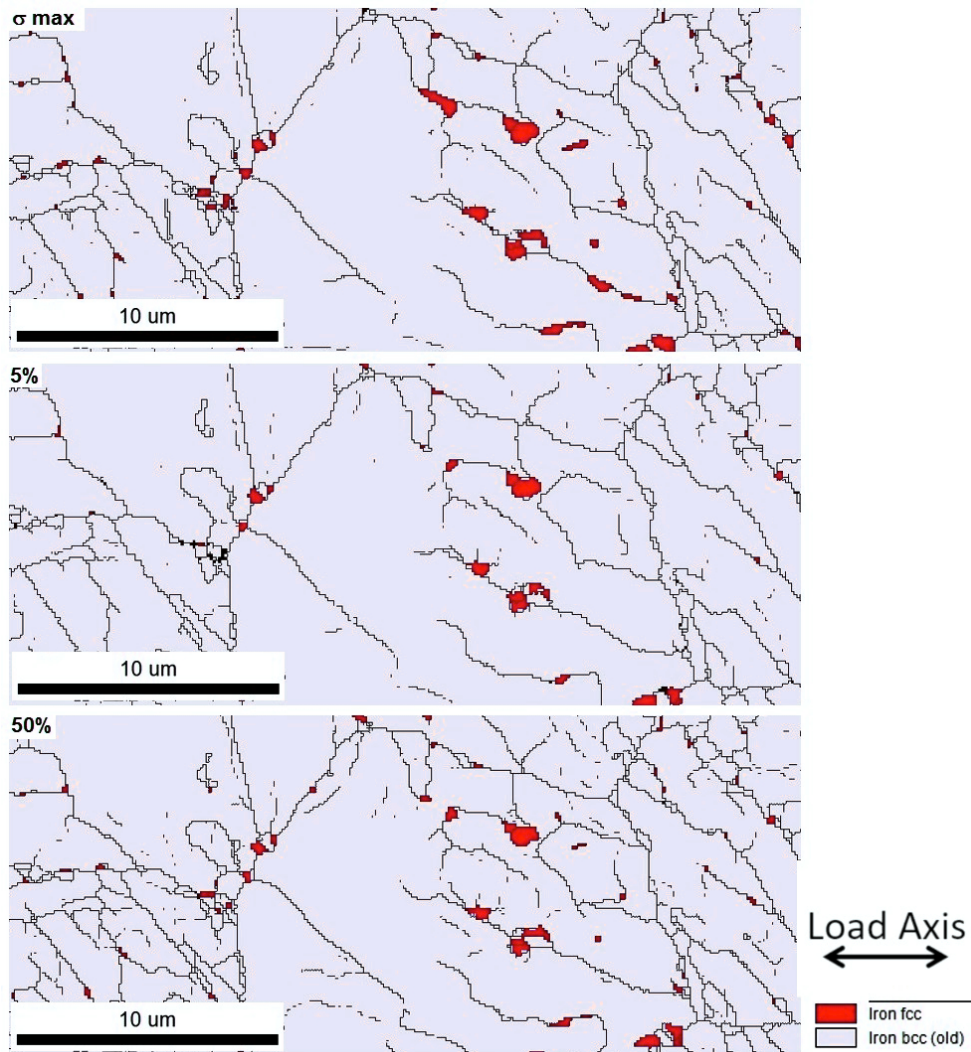


Figure 4.3.15: EBSD phase maps evolution of 10T sample at $\Delta\epsilon_t=1.2\%$

4.3.5 Cross-sectional view

The same method was used here as it did for the WQ and 0.5T structures to support the findings drawn from the EBSD and c-ECCI analysis performed on the surface, providing clear knowledge of the extrusion's shape and particular position.

4.3.5.1 Accurate determination of extrusion/intrusion shape and location

Figure 4.3.16 shows one group of PSMs selected for FIB lamella cut.

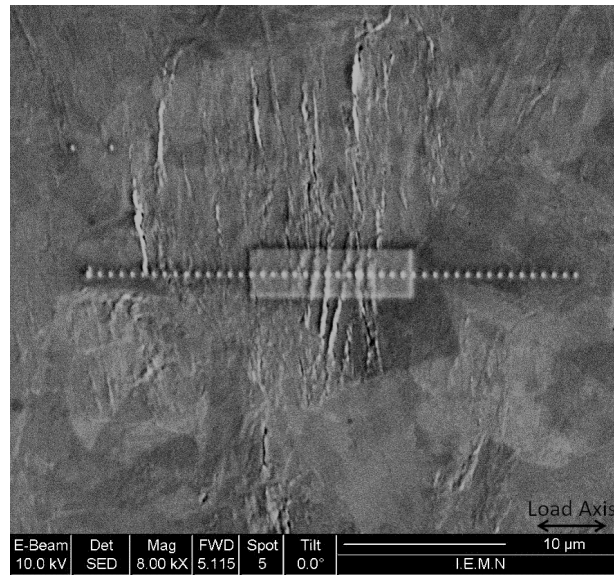


Figure 4.3.16: Selected zone comprising PSMs for FIB lamella extraction of the 10T sample with $\Delta\varepsilon_t=1.2\%$ at the end of fatigue life. The dots correspond to the Pt deposition marking the exact position of extraction

A global view of the extracted lamellae is shown in Figure 4.3.17. Few laths are noticeable, extrusions presented the lowest height when compared to the other two microstructures. The extrusions are in general placed at the boundaries with the intrusions in the middle of the laths or the equiaxed structures.

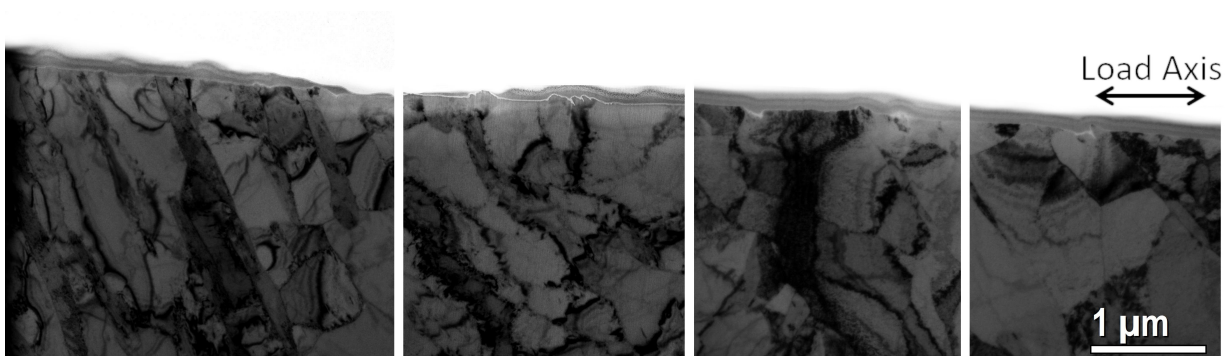


Figure 4.3.17: HRTEM images of two thin lamellae indicating the sites of extrusions and intrusions at $\Delta\varepsilon_t=1.2\%$ at the end of fatigue life for the 10T sample

TEM in the Selected Area Diffraction (SAED) mode allowed the imaging of the films and islands of the reversed austenite. The $(220)\gamma$ and $(311)\gamma$ diffraction planes were selected and dark-field imaging highlighted the austenitic phase placed at the interfaces, as demonstrated in Figure 4.3.18. The extrusions are located next to the austenitic films and in the majority of the cases, between two austenite islands.

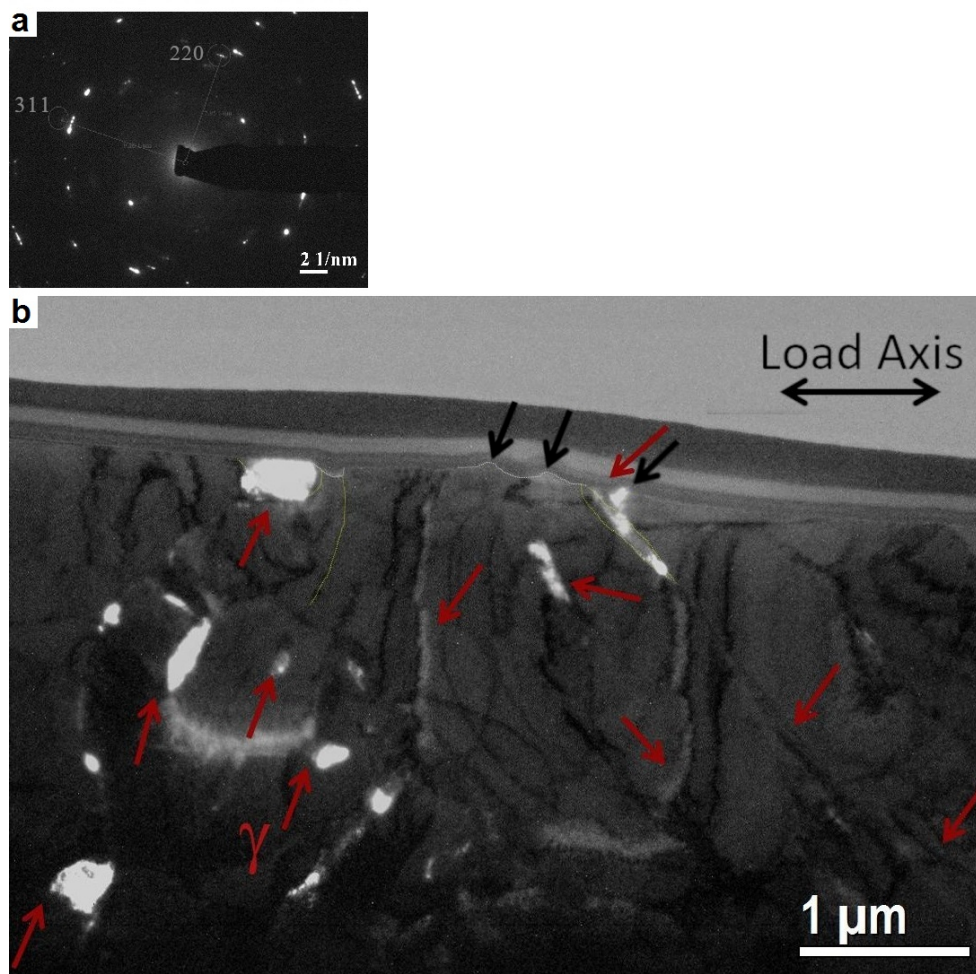


Figure 4.3.18: a) Diffraction pattern b) SAED and TEM images superposed indicating the austenite and the sites of extrusions marked by the black arrows at $\Delta\epsilon_t=1.2\%$ at the end of fatigue life for the 10T sample

Figure 4.3.19 shows several zones where the dark field images obtained from SAED $(311)\gamma$ was superposed with the bright field images. The extrusions are frequently placed at the boundaries, usually between the surrounding austenite islands. Although, few extrusions were found when the lath's width exceeds 500 nm and no austenite is seen around, but those extrusions were placed in a cell boundary. Few intrusions were found located in the middle of the laths.

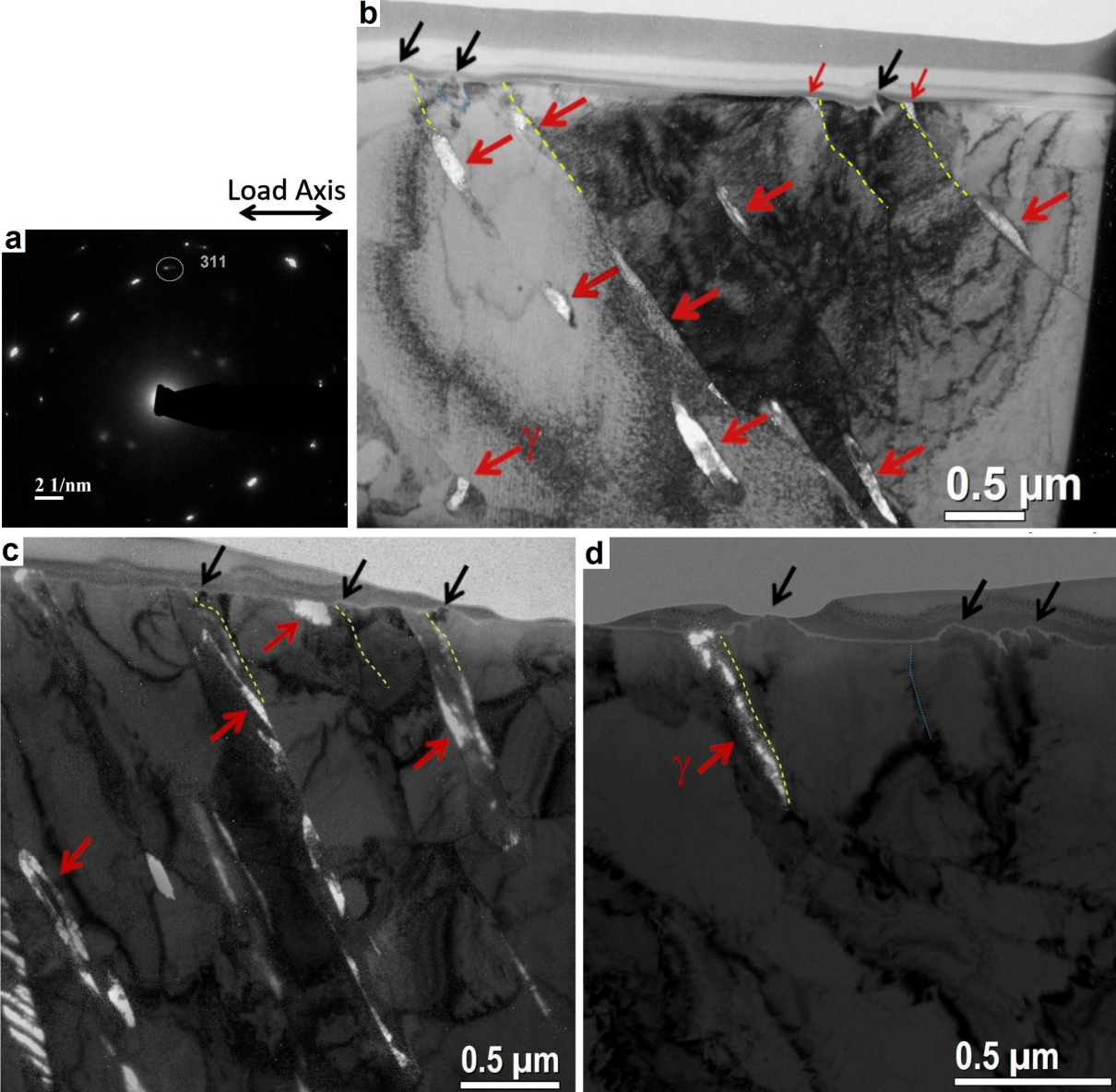


Figure 4.3.19: a) Diffraction pattern; b), c) and d) dark field-TEM images obtained with the (311) γ spot indicating the austenite and the sites of extrusions marked by the black arrows at $\Delta\epsilon_t=1.2\%$ at the end of fatigue life for the 10T sample. Blue and yellow dashed lines indicate the cells boundaries and lath boundaries, respectively

4.3.6 Conclusions

The microstructure of the steel tempered for 10 hours is composed of tempered martensite, bainite and 11% of reversed austenite. The latter was measured by XRD and LOM. The reversed austenite was found as larger films or islands, aligned in parallel with an average spacing between them of one micron, where the old lath interfaces from the quenching treatment were present. Moreover, the austenitic phase was more concentrated at the bainitic zones. Laths were not evident nor abundant anymore, this structure was partially replaced by some type of wider equiaxed structure and a high number of recovered cells. Dislocations were found to be entangled at the cell walls.

The Manson-Coffin relation showed no bi-linear behavior, suggesting that this microstructure accommodated the cyclic plasticity with the same mechanism along the deformation levels studied. A brief initial cyclic hardening was observed and may involve a partial TRIP effect of the austenitic phase and the releasing of the entangled dislocations. Subsequent cyclic softening was observed influenced by the mobility of dislocations and their interaction.

The surface was filled in the majority by groups of condensed PSM denominated as protrusions. Very few isolated extrusions were found at the beginning of cycling, placed at HAB or LAB. The PSMs were found in the matrix, mostly around the austenitic islands and no extrusion was identified at this phase. Cross-sectional views allowed the observation of the extrusions-intrusions locations and they were discovered in majority between two austenitic islands, with the extrusion being close to the interface and the intrusions in the center of the lath. With increased lath size or the absence of austenite, the extrusions were found coinciding with the cells walls. Apart from dislocation cells and HDDWs found in the middle of fatigue life, no particular dislocation pattern was identified in the high-resolution cross-section view.

Following the same mechanism as adopted for the other two microstructures independently of the strain level, after releasing the dislocations, they will be able to reach the boundaries being annihilated or generating point defects in those zones. A matter flow by the boundary sliding mechanism aided by the presence of the austenite films will then happen.

The graphical abstract (Figure 4.3.20) summarizes the process of extrusion/intrusion nucleation and growth through the fatigue life of 10T microstructure.

HIGHLIGHTS

- The microstructure is a mixture of tempered martensite, bainite, and reversed austenite
- Reversed austenite films are present at martensite interfaces aligned in parallel and were detectable by XRD, LOM, and EBSD techniques thanks to their larger size
- Surface relief is identified already at lower strains and comprises mostly protrusions
- Extrusions emerges at the laths interfaces, while intrusions nucleates inside the laths
- The austenite content diminishes by 30% after the LCF, partial volume of the austenite islands remains stable next to the extrusions
- The austenitic phase was found located at the boundaries and the extrusions were most of the time next to them or between two austenitic islands.
- Sites of nucleation of extrusions were identified LAB and HAB, but always delimited to by the HAB (packet and GB), sometimes covering one entire block

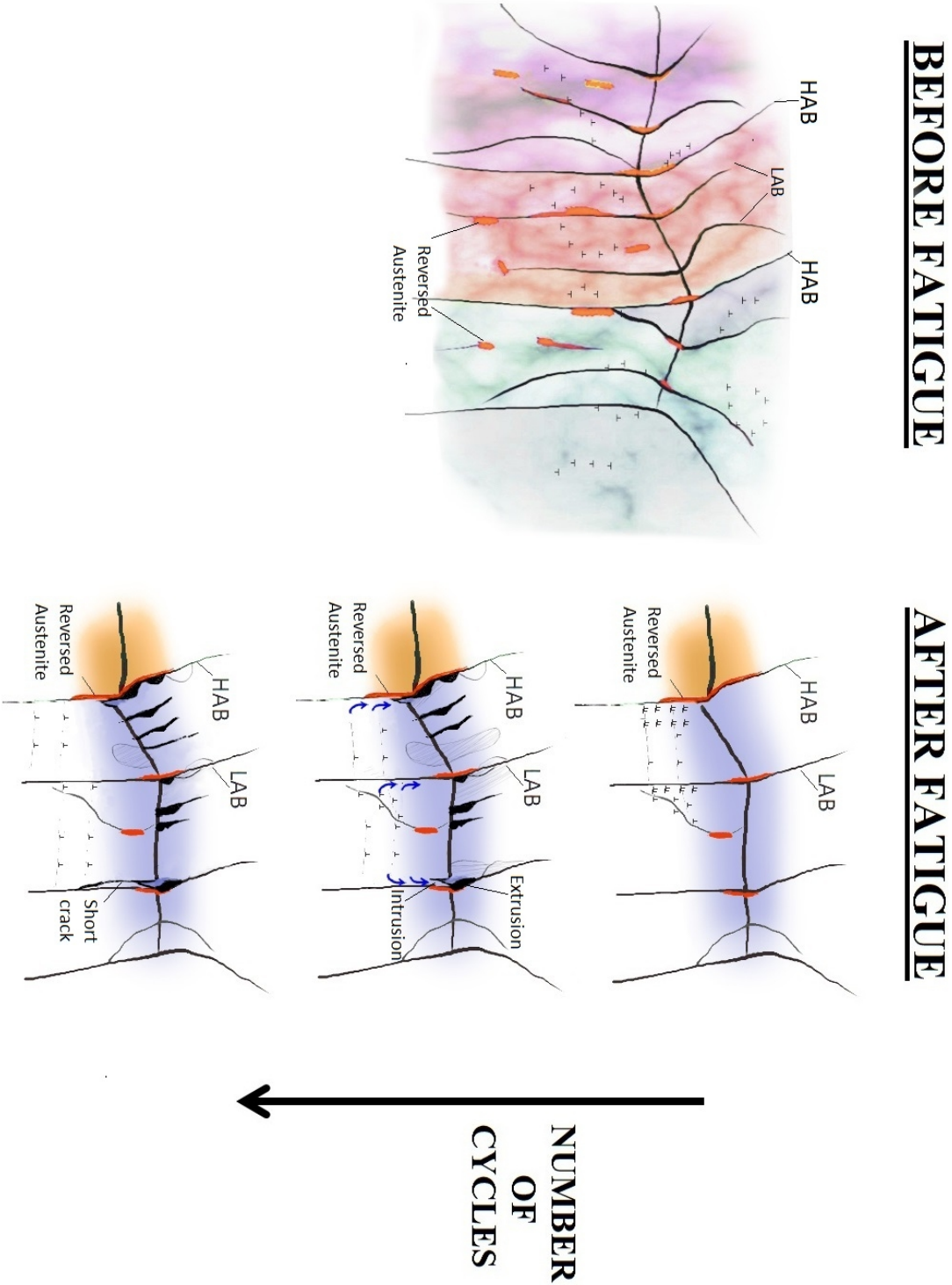


Figure 4.3.20: Representation of extrusions and intrusions nucleation sites for the 10T sample during fatigue

Chapter 5

Outcome, Emerging Findings and Conclusions

The basic background of the research that has been initiated three years ago was to understand the mechanisms of fatigue crack initiation in a martensitic steel. Among the different grades of martensitic steels, the selection of the 9Ni alloy appeared relevant because the experimental research route led us to unexpected situations or technical issues to overcome. This allowed us to address not only the initial PhD topic but to bring ideas or answers to more general questions. Indeed, heat treatments were scheduled as a way to modify the nature of the lath interface. But at the same time, it modified the nature of the matrix, which turned from a hard fully martensitic to a softer bainite-martensitic matrix. SEM-EBSD was employed for a large part of the investigation of the microstructures. Strong attention was paid to the data processing of very small substructures along cracks tips resulting then in a clear definition of intrusions and microcracks. Finally, the key element in this study was the presence of austenite. Whatever the latter was retained or reversed, it has been shown that the employed technique had an impact on the volume fraction evaluation. The one providing the most reliable content has been pointed out. Imaging unambiguously the austenite of small size, however, appeared critical. Thanks to a collaboration with Dr. Jean-Marc Olive from Bordeaux University, impressive results were obtained on fatigued materials. Even though these results came very close to the end of the PhD thesis, they need to be included in the present document considering its importance and how it is proposed as a new characterization approach. These points will be highlighted in this chapter.

The first sub-chapter deals with a brief comparison between the three microstructures focusing on contrasting the fatigue behavior and observations done in the course of the experiments. The main interest is to point which microstructure shows more advantages regarding fatigue performance and to determine if a most efficient microstructure for fatigue resistance exists or not. Then, in the second sub-chapter, the differentiation between intrusions and microcracks will be proposed as an extra key on identifying the stages of fatigue crack initiation. With our analysis, we want to show that intrusion and

very short crack is really a question of semantic. The third sub-chapter concerns the imaging of small domains of austenite embedded in a martensitic matrix. Because of the difference in magnetic properties, the magnetic force microscope (MFM) has been employed, and the power of this technique is highlighted for the identification of the exact location of the austenite. And finally, in the fourth sub-chapter, a general mechanism will be proposed for the martensitic structure with a small interface modification.

5.1 Which microstructure is the most efficient?

The microscopic and mesoscopic characterizations of the three considered materials (WQ, 0.5T, and 10T) have pointed out some similarities, but also differences between them. Here, the results will be compiled together as a comparative in order to propose the most efficient microstructure with regards to fatigue performance.

5.1.1 Topography Overview

Figure 5.1.1 displays the surface relief, as observed by SEM, for the three considered microstructures at three levels of total applied strain ($\Delta\varepsilon_t = 0.8\%$, 1.2% and 1.6%). All the observations have been carried out on LCF tests up to fracture.

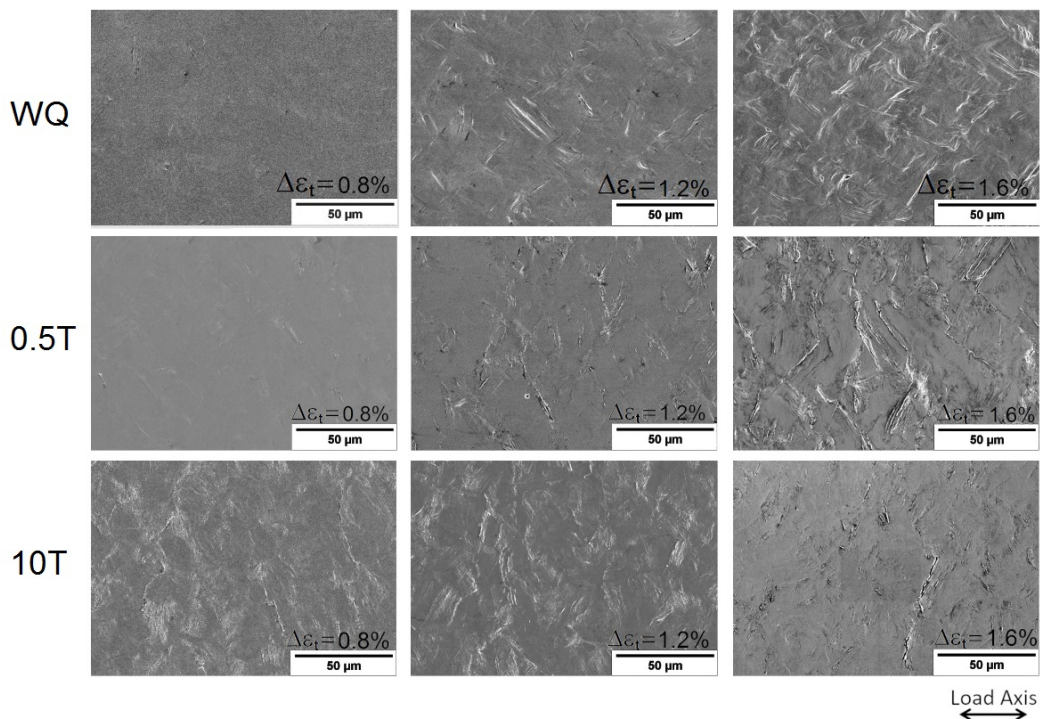


Figure 5.1.1: Surface topography after LCF tests for all microstructures analyzed at three different strain levels

At $\Delta\varepsilon_t = 0.8\%$ very light surface relief is observed for the WQ and 0.5T microstructures, while the 10T sample already exhibits a surface filled by grouped extrusions. As the total strain increases, more deformation and more pronounced extrusions are developed. Those first observations indicate that both the WQ and 0.5T conditions may have a more homogeneous dislocation distribution. By contrast, the 10T sample has a heterogeneous microstructure composed of tempered martensite, more austenitic zones, and bainite. The addition of bainite in the matrix may cause non-uniform distribution of the dislocations, leading to an increase in stress levels at the first cycles or the appearance of new sites for plastic activity. Moreover, as determined by neutron diffraction [239], the bainite constituent has a lower yield strength than austenite and martensite.

The various constituents do not react at the same time when the sample is submitted to the fatigue loading. Bainite, which is the softest constituent, will be able to accommodate first the deformation until the dislocations present in this constituent are annihilated. Then, it is expected as the same case for duplex steels that, when a threshold deformation level is reached, the austenitic phase would be the next soft phase to be activated and finally, the deformation will be accommodated by the martensitic phase. Although, as observed by us, the austenitic phase will behave on facilitating the slip between the martensitic laths, not participating actively on strain absorption as observed for duplex steel grades. So, in our case, once the fcc slip systems in austenite films should be aligned with the boundary, slip in the films should occur at lower resolved shear stress than in the laths where the austenite is not present, allowing the hard laths to slide, generating more extrusions. At higher levels of total applied strain, more slip systems should be activated, leading to a more prominent topography.

5.1.1.1 Classification of Extrusions

Each sample analyzed by SEM had its surface evaluated in order to classify the types of extrusions found based on previous studies from other authors, as described in the section *2.2.5 Shape of Extrusions*.

The extrusions shape changes were attributed to the simultaneous action of numerous slip mechanisms [72]. The bcc structure contains 48 possible slip systems, which can be activated concomitantly during the straining, leading to grouped extrusions with different morphologies. Figure 5.1.2 comprehends all the types of extrusions found in this study.

After labeling the extrusions by their morphology, they were categorized as individual or grouped extrusions (protrusions). Over 300 types of extrusions were classified for each microstructure (0.5T and 10T). The 0.5T microstructure exhibited a distribution of about

50% of the isolated type, and the other 50% of grouped extrusions. The protrusions were predominant for the 10T structure, corresponding of 96% from the total PSMs analyzed (Figure 5.1.3). For the WQ microstructure, it was found that its surface is largely composed of individual extrusions (only 3% of them were identified as a protrusion).

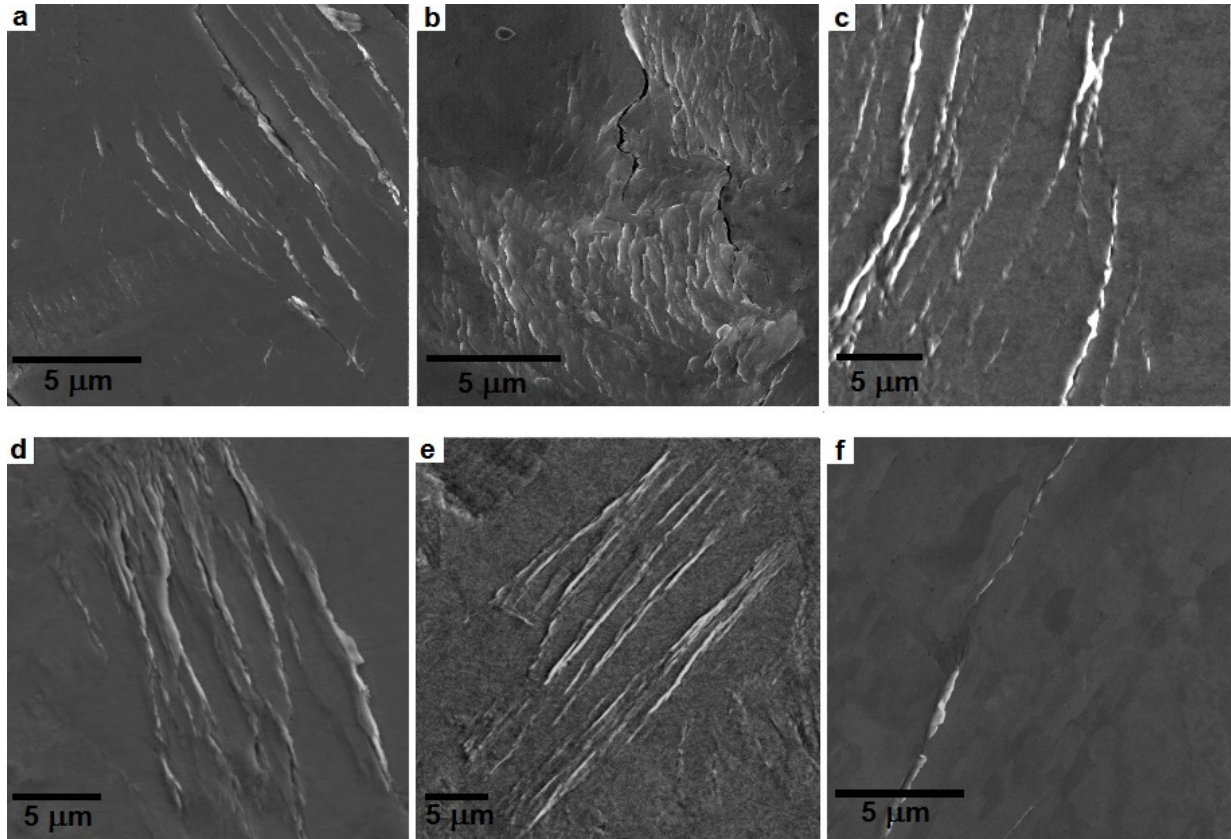


Figure 5.1.2: Types of extrusions found on 9Ni steel. a) Band-like b) Coarse c) Cord-like d) Protrusion e) Ribbon-like f) Tongue-like

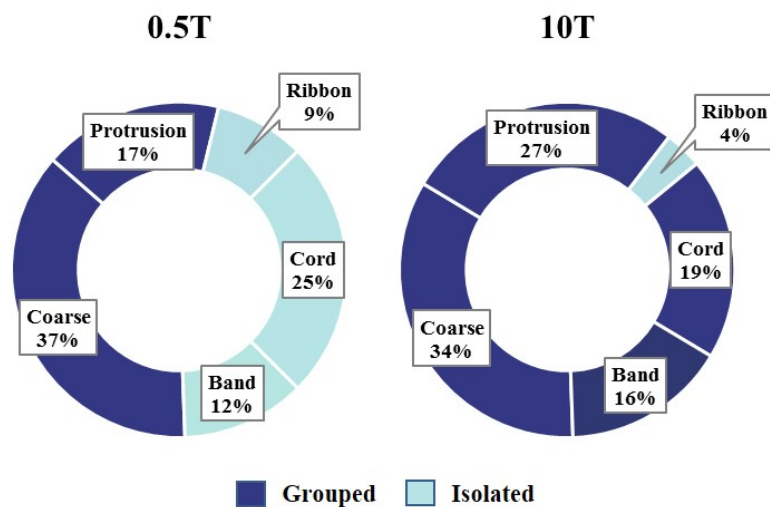


Figure 5.1.3: Distribution of extrusions for the 0.5T and 10T samples

5.1.2 Light Interferometry

The surface texture of the three microstructures at $\Delta\epsilon_t=1.2\%$ was obtained by the Scanning White-light Interferometric (SWLI) method and the roughness parameters described in the section 3.1.5 *Light Interferometry* were compared to get an idea of the extrusions profile. Figure 5.1.4 shows the reconstructed surface roughness of the three microstructures after fatigue tests. For instance, it can be seen from these profiles that they are already not very similar, where the 10T sample exhibits more deformation-red peaks spread along the scanned area.

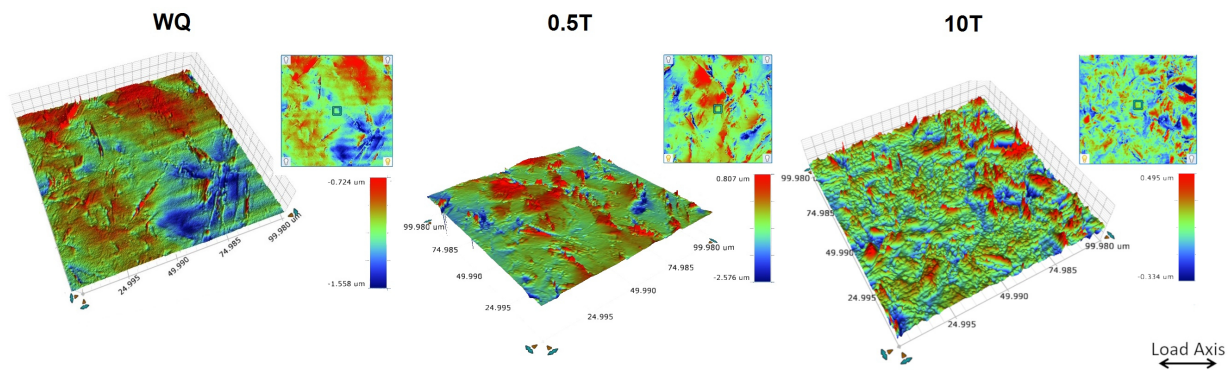


Figure 5.1.4: Surface profile of the LCF tested specimens

Together with the reconstructed image, SWLI provided various measured roughness parameters. Figure 5.1.5 and Figure 5.1.6 exhibits the box-plot charts for the evaluated parameters collected from the three microstructures in 2D and 3D, respectively. To see if there is any statistically significant difference between the measured roughness parameters, a one-way analysis of variance (ANOVA) at a 0.05 level was performed (results present in the *Appendix 5.5*).

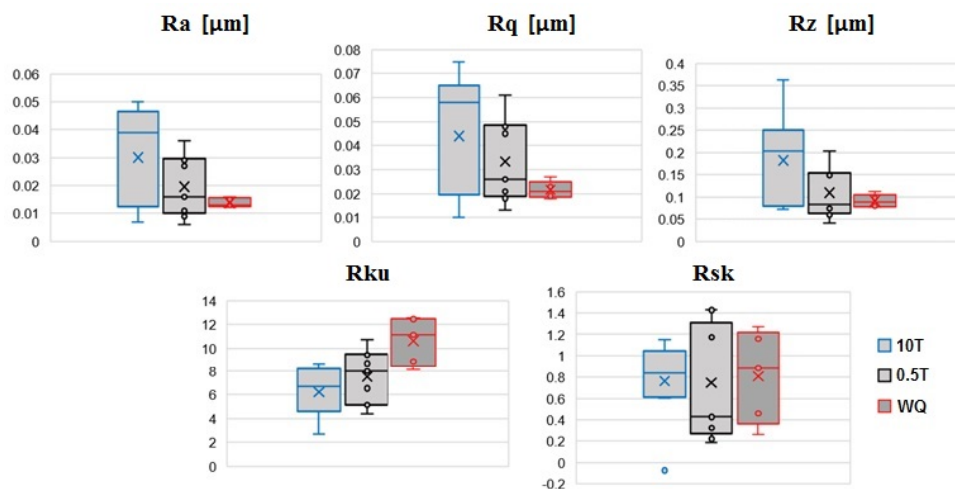


Figure 5.1.5: Box-plot charts of the 2D measured parameters

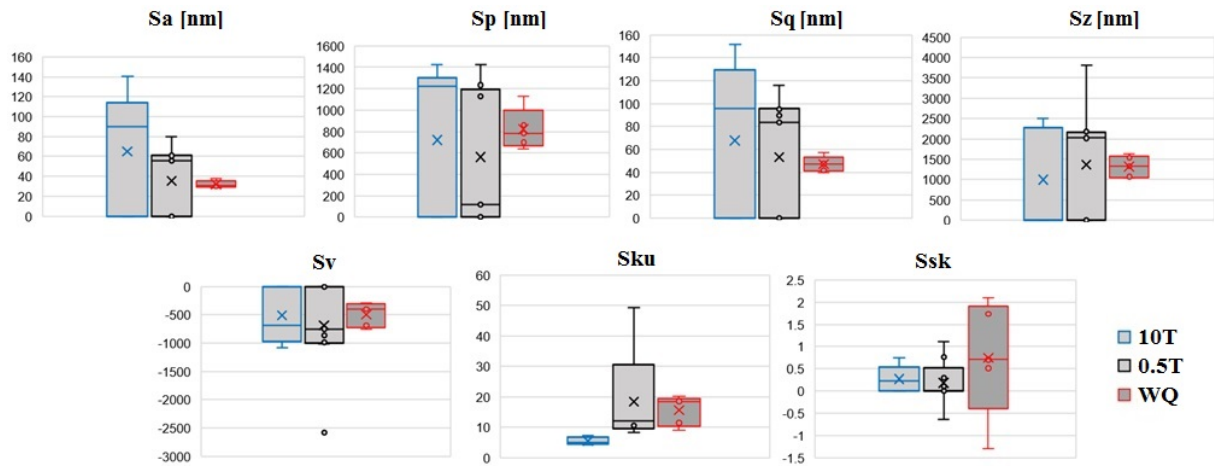


Figure 5.1.6: Box-plot charts of the 3D measured parameters

According to the ANOVA results, the parameters R_a , R_q , R_z , R_{ku} , S_a , and S_q have a significant difference between the three microstructures (p value > 0.05). For the cases of R_a , R_q , R_z , the sample 10T showed higher values, meaning that the surface relief is more evident, as already seen in the previous chapters. The values of R_{sk} (skewness) for all samples are positive, this signifies that the surface contains mainly peaks and sharpness, whereas a negative value of R_{sk} or S_{sk} indicates that the surface is composed of valleys. The S_{ku} parameter (Kurtosis) is always presented in combination with the Skewness to describe the shape of the topography height distribution. The S_{ku} value above 3 indicates acute peaks and below 3 designates smooth surfaces [240]. Despite the ANOVA did not indicate a significant difference between the S_{ku} parameter, the values are very discrepant. The 10T sample presents lower values, far from the other structures, this may be linked to the shape of extrusions found, where very few isolated extrusions have been identified in this microstructure.

5.1.3 Fatigue response

Figure 5.1.7 summarizes all the stress-curves response as a function of the number of cycles for the three microstructures, the fatigue data is present in the *Appendix B*). Different behaviors have been observed for each microstructure and we can see that the stress levels decrease as the time of the tempering heat treatment increases, and the initial stress hardening was present for both WQ and 10T samples which have the highest austenite content.

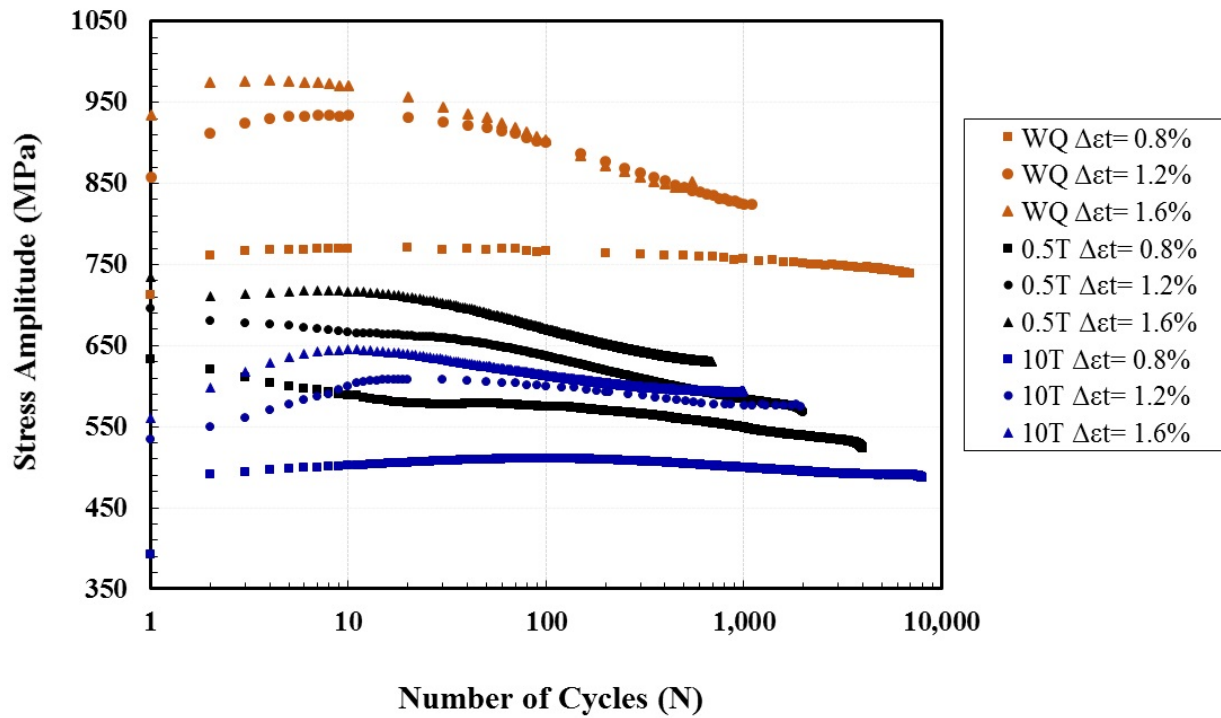


Figure 5.1.7: Evolution of the stress amplitude versus the number of cycles of the 9Ni steel submitted to different heat treatments

The Manson-Coffin relation displayed in Figure 5.1.8 shows that despite having higher stress levels, the WQ sample presents lower fatigue resistance and the bi-linear behavior. At this interval of applied strains, no bi-linear behavior was observed for the 10T and 0.5T microstructures.

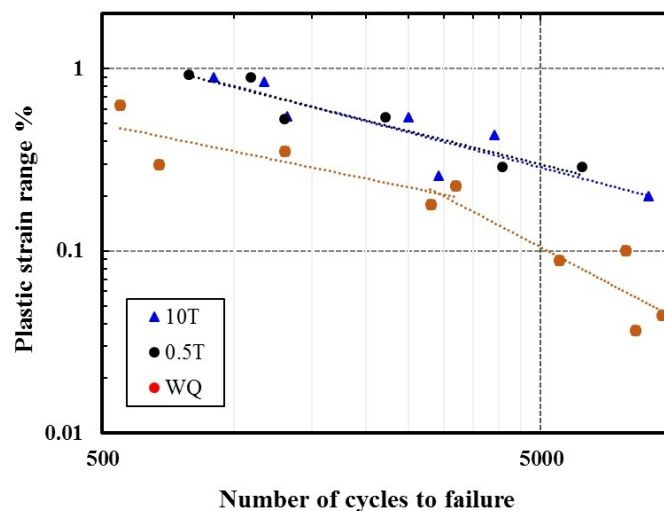


Figure 5.1.8: Manson-Coffin curves of 9Ni steel submitted to different heat treatments

The stabilized hysteresis curves at different strain levels for each microstructure were grouped to show the difference in shapes (Figure 5.1.9). The area covered by the

hysteresis loops represents the cyclic plastic work consumed in each cycle. As noticed by the measured plastic strain together with the amount of deformation in the surface, the hysteresis loops of the 0.5T and 10T microstructures are similar and a smaller plastic strain was observed for the WQ samples.

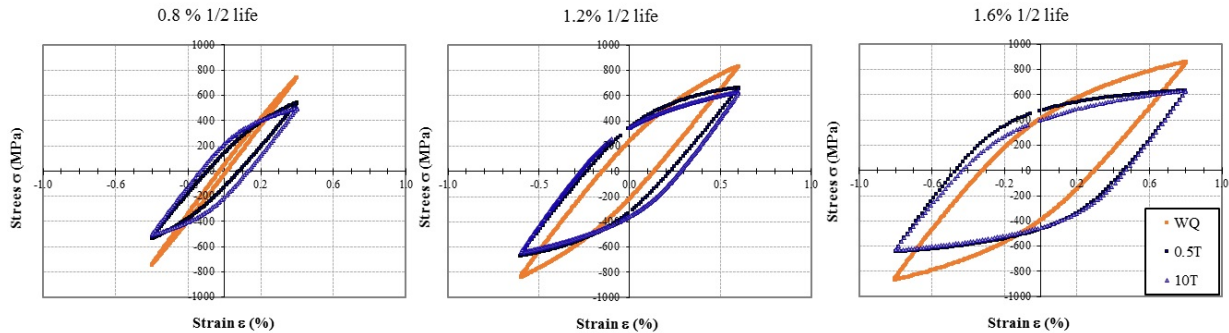


Figure 5.1.9: Hysteresis loops of the 9Ni steel submitted to different heat treatments

5.1.4 Answer to the question

Based on all aspects investigated in this research, the findings allowed a proper choice of the heat treatment that should be applied for situations that put this material into fatigue work.

The water quenched structure presented increased strength and hardness compared to the other samples submitted to tempering heat treatment. Despite showing higher stress levels during the LCF tests, the quenched microstructure presented the lowest fatigue resistance. This is justified by the fact that the microstructure is constrained by the dislocations inherited from the rapid cooling, making the material less resistant to cyclic solicitations.

In the point of view of the fatigue resistance, the longer tempering heat treatment aiming the highest amount of reversed austenite is not effectively necessary. The reversed austenite plays an important role in the cyclic accommodation facilitating the boundary sliding, however, only a small amount of stable austenite is already sufficient to improve the mechanical properties of the 9Ni steel regarding the fatigue behavior. So the material tempered for 30 minutes is the most proper microstructure combining gains in heat treatment times and fatigue performance, including stress and fatigue life.

5.2 From intrusion to microcrack

The transition point from an intrusion to microcrack is an interesting subject, not only for their classification but to comprehend what leads to the formation of an embryo crack. This is an intriguing point to be observed because there is no exact consensus on the differentiation between microcracks and intrusions, they are usually distinguished by length, but there are cases in which this can lead to an erroneous designation. It is known that a microcrack is governed by mechanical factors, like stress concentration in a sufficiently small area. An intrusion otherwise, is governed by diffusion (the movement of dislocations and vacancies). Here, an approach will be made on cross-sectional visualizations with the help of the EBSD analyses.

5.2.1 Water Quenched Microstructure

Cross-sectional cuts from samples deformed at the lowest ($\Delta\epsilon_t=0.8\%$) and highest level ($\Delta\epsilon_t=1.6\%$) of total applied strain were chosen based on the bi-linear behavior of Manson-Coffin curve of the WQ material and scanned by EBSD with a 30 nm step size. At lower levels, the sample was almost without cracks, by contrast, at higher levels the sample was full of cracks. The goal was to observe a transition point in length from intrusions to microcracks and their relation to the microstructure. Figure 5.2.1 shows one of the transverse cuts along the load axis of a deformed sample at 50% of fatigue life, the surface is fulfilled by extrusions and microcracks.

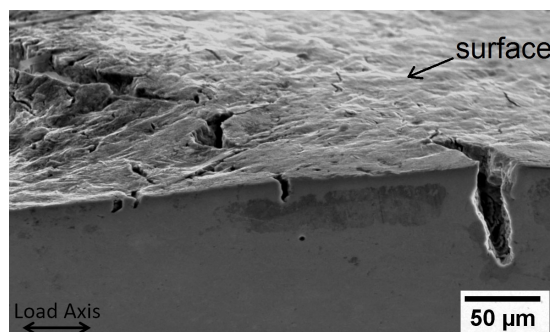


Figure 5.2.1: Cross-section view of a sample deformed at 50% of fatigue life ($\Delta\epsilon_t=1.6\%$)

Figure 5.2.2 represents some of the intrusions/microcracks found in the sample deformed at $\Delta\epsilon_t=0.8\%$. A very small number of intrusions and microcracks were found, the findings are in agreement with the topographic images obtained from direct observation done in the surface by SEM, and the FIB lamellae visualized by HRTEM, once the intrusions are localized in a short distance from the boundaries. Two intrusions with

very different dimensions were here chosen to represent observations done at this level of deformation. Subgrains were identified by the IPF maps along the load axis for both Figure 5.2.2-a and Figure 5.2.2-b, classified as slight orientation variation combined with a lower IQ, those subgrains are represented by a minor color change. LSM maps also highlight the LAB around the intrusions. Few nanograins were also present in Figure 5.2.2-a assigned in the IPF maps as an orientation changing in relation to the neighboring zone. Those nanograins were not identified in a smaller intrusion in Figure 5.2.2-b, suggesting that this could be a criterion to differentiate intrusions from microcracks. Regardless of different fatigue crack initiation modes, a parallel will be established here from the nanograins noticed in this material with the fine granular area (FGA) frequently seen in the very-high cycle fatigue regime (VHCF). The FGA is thought to be the most significant type of early fatigue damage in VHCF, consisting of fine grains in order of tens to hundreds of nanometers, high-density dislocations, and sub-grains with high angle grain boundaries. A large local strain triggers the formation of FGA [241, 242]. Despite being considered only for high and very high cycle fatigue damage, it sounds coherent to relate this definition to the evidence seen in this study, once the nanograins are present at the tip of the well-developed intrusions or their point of changing in direction.

KAM maps were used to evaluate the strain-related distribution and it has indicated a plastic zone around the intrusions. This is more evident in Figure 5.2.2-b, at the tip of the intrusion; the LSM map shows in that zones a LAB with a range of 2-5°, indicating a dislocation arrangement. Nanograins were only identified in supposed intrusions with dimensions superior to 3 μm , where HAB were evident in the LSM maps.

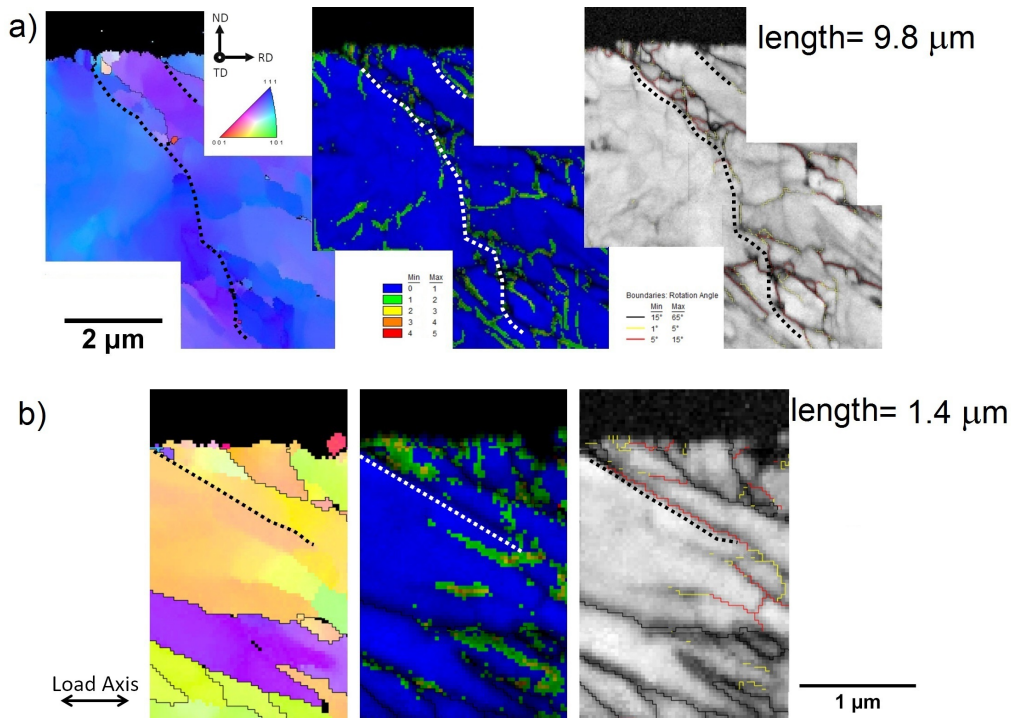


Figure 5.2.2: Cross-section view of a sample deformed until the end of fatigue life ($\Delta\epsilon_t=0.8\%$). The dashed lines indicate the intrusions location

At a higher level of total applied strain, the intrusions and microcracks were abundant, facilitating the data acquisition for a better comprehension of the transition point of an intrusion to a microcrack. Figure 5.2.3 shows three selected intrusions/microcracks from the numerous that have been collected with average length, leading to the two considered cases: with or without FGA. As seen at lower levels of total applied strain, the intrusions are localized from a certain distance from the boundaries. An interesting point is that the nanograins were identified in high quantity at the microcrack/intrusion tip, but as well as along its whole length, when they are longer than 2-3 μm. Those nanograins were even more concentrated when a change in direction was seen, as demonstrated in Figure 5.2.3-a. KAM maps again indicated a possible high plastic activity concentrated around the intrusions and at the surface, where the extrusions are present. The plasticity seems to be more concentrated in the corresponding zones with nanograins formation, indicating a mechanism to impede the intrusion/microcrack to grow. LSM maps confirm the subgrains to nanograins formation by the misorientations superior to 15°. Moreover, Figure 5.2.3-b also confirms results previously found by HRTEM, when an intrusion develops breaking the lath apart (IPF map shows the intrusion surrounded by zones with no orientation change), but after some cycling, it changed the path towards the boundary. Figure 5.2.3-c shows a sharp intrusion localized away from a boundary with no presence of nanograins around it, helping to reinforce the theory that the transition of an intrusion to microcrack has two evidences: the length and the FGA around it. This last intrusion has not yet

reached the critical size and does not present the FGA next to it.

The latest observation confirms that length is not the only marker of the intrusion/microcrack transition. Indeed, the existence of nanograins attests the changeover from an intrusion to a microcrack associated with a critical length/depth around $3\ \mu\text{m}$, below this size, nanograins were not found and only sharp intrusions surrounded by some subgrains were identified. So the continuous formation of fine grains with high angle grain boundaries is the indicator of the transition point from an intrusion to microcrack. It occurs in the place of dislocations cells. This transition involves both the intrusion length and the stress state. The latter results from the overall external loading and the local confined constraint caused by the metallurgical environment of the intrusion tip. An intrusion that has initiated in the middle of a lath, far from interfaces, would require a longer length to evolve into a microcrack than an intrusion close to an interface.

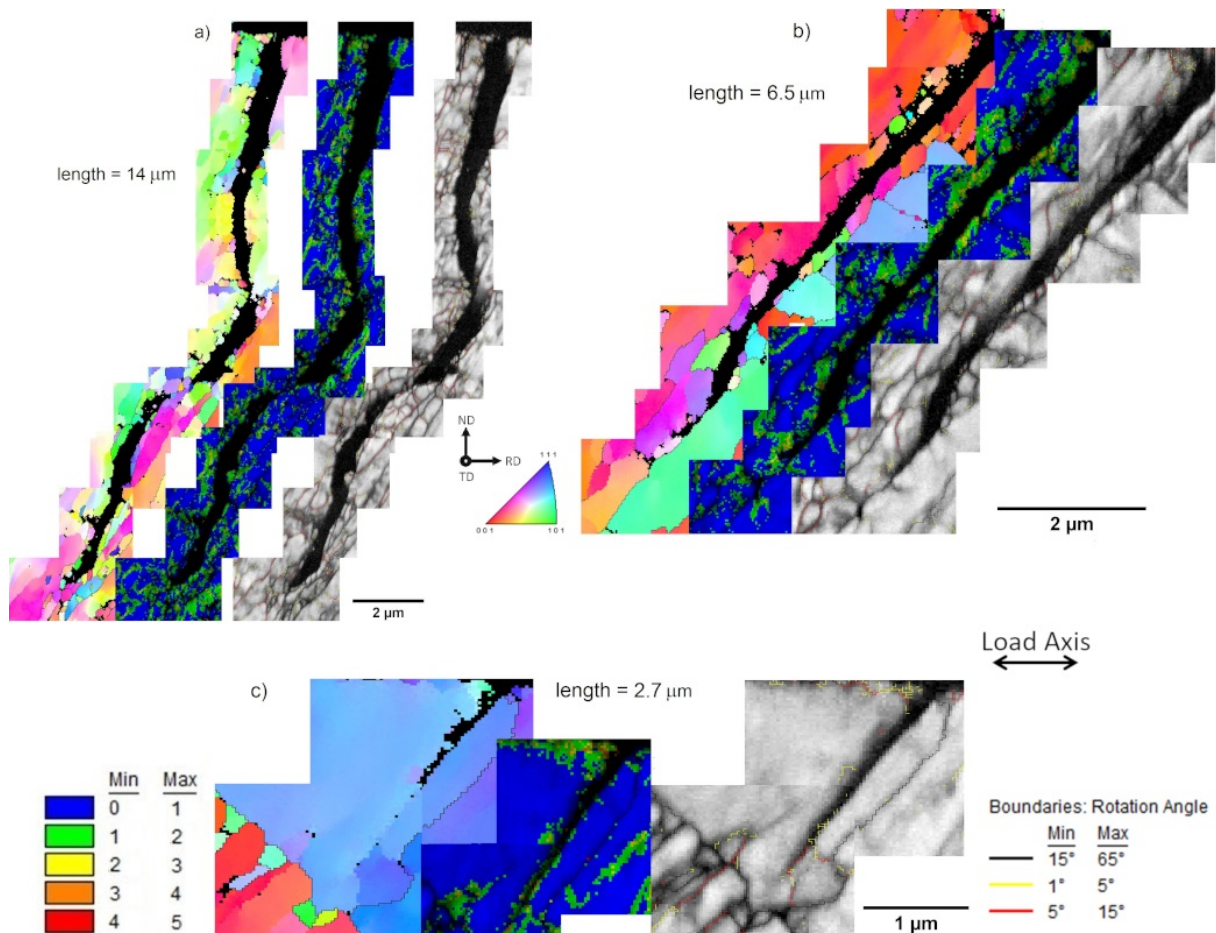


Figure 5.2.3: Cross-section view of a WQ sample deformed until the end of fatigue life ($\Delta\epsilon_t=1.6\%$)

5.2.2 10 Hours Tempered Microstructure

Figure 5.2.4 shows one of the transverse cuts along the load axis of a deformed sample at 100% of fatigue life, few extrusions, and one small intrusion are visible from this cut. The objective is to understand the transition state from intrusions to microcracks and establish a parallel with the WQ samples. For this observation, samples tested at $\Delta\varepsilon_t=0.8\%$ and $\Delta\varepsilon_t=1.6\%$ were chosen and analyzed by EBSD with a 30 nm step size.

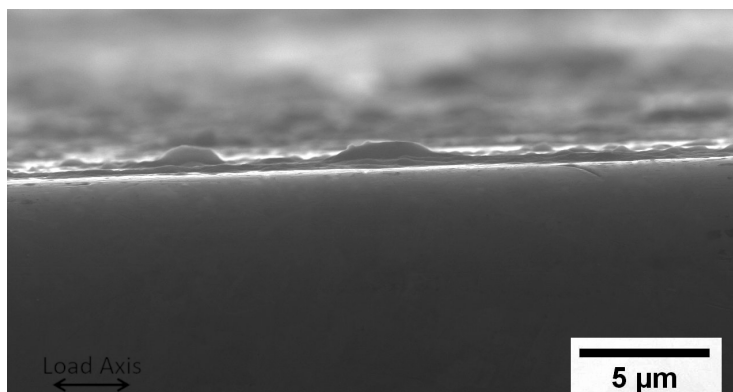


Figure 5.2.4: Cross-section view of a 10T sample deformed at the end of fatigue life ($\Delta\varepsilon_t=1.6\%$)

At lower levels of total applied strain, the sample was almost without cracks, in contrast, at higher levels the sample is filled by them.

Figure 5.2.5 shows one intrusion and an extrusion scanned from the sample with $\Delta\varepsilon_t=0.8\%$ at the end of fatigue life. Again, few thin intrusions were hardly found and no microcrack was identified at least in this sectioned zone.

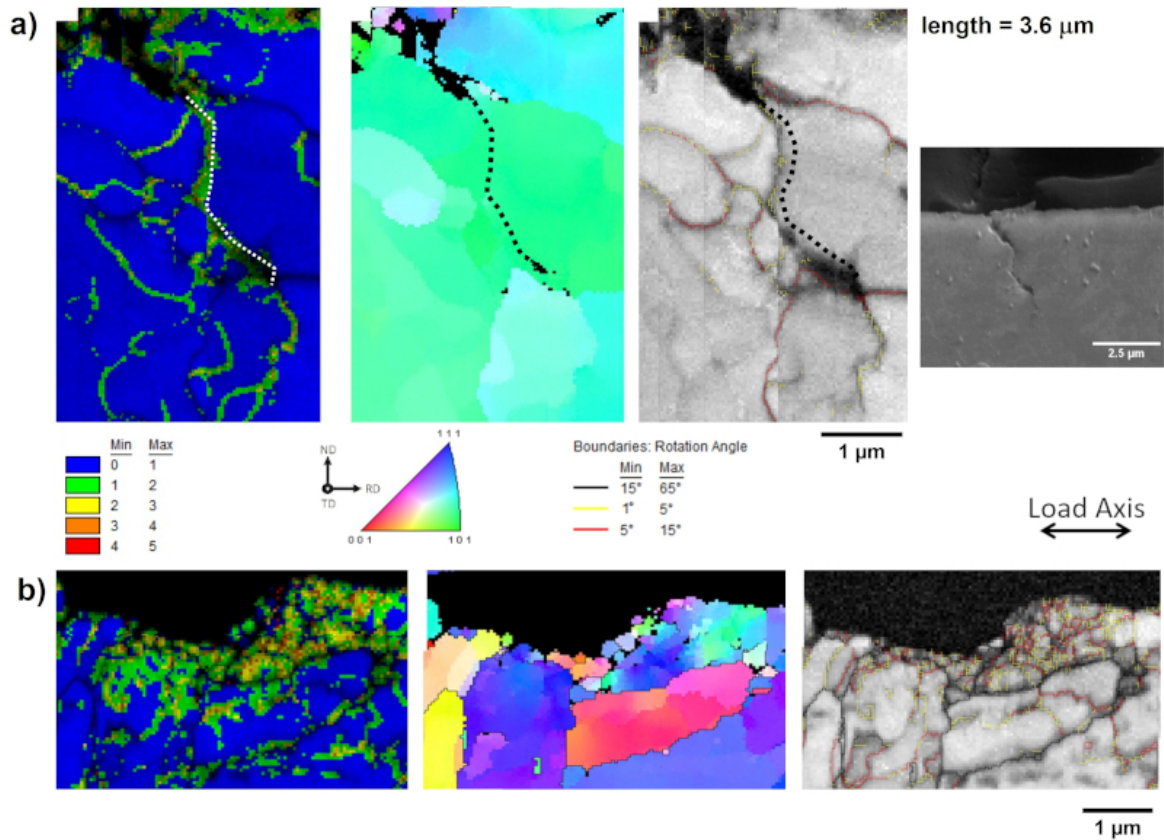


Figure 5.2.5: Cross-section view of the 10T sample deformed until the end of fatigue life ($\Delta\epsilon_t=0.8\%$). The dashed lines indicate the intrusions location

The scanned intrusion shown in Figure 5.2.5-a is located within a martensitic substructure (lath), identified as a light orientation changing by the IPF map. Few nanograins are visible at the level of the surface and very light misorientation is seen around the intrusion, being assigned as subgrains. The LSM map confirms this observation, showing LABs around the intrusion. The KAM maps point to a high strain localization close to the surface, where the extrusions are present, and along the intrusion. Figure 5.2.5-b shows an extrusion with a high dislocation activity, an intense plastic zone, with the presence of subgrains and nanograins at the level of the surface. No clear conclusion could be taken from the sample tested at $\Delta\epsilon_t=0.8\%$ in respect of differentiation between microcracks and intrusions due to an insufficient number of encountered intrusions. On the other hand, the sample tested at $\Delta\epsilon_t=1.6\%$ had a considerable amount of microcracks and intrusions that could help to obtain a proper interpretation. Figure 5.2.6 shows some intrusions/microcracks selected with distinct dimensions to illustrate the findings.

Figure 5.2.6-a shows a KAM map with intense plastic activity at the tip of the crack, IPF map indicates the presence of a FGA mostly at the tip of the microcrack and at the level of the surface. The LSM map points the dislocations and their substructures along the crack marked as LABs. Figure 5.2.6-b shows another small microcrack, the

presence of nanograins is also noticed. Plastic zones are present at the level of the surface and along the microcrack. One interesting point is the microcrack path, at the very first microns, it stays inside a martensitic unit, as indicated by the IPF map, changing its path towards a HAB. The same behavior was observed for the WQ microstructure. LSM map again highlights the LAB structures present along the microcrack. Finally, Figure 5.2.6-c shows an intrusion marked by the dotted lines. The FGA was not found around microcracks with less than 4 μm in length, the evidence is that the FGA together with a limited length of 4 μm are the keys to differentiate the intrusions from microcracks in the case of the 10T microstructure.

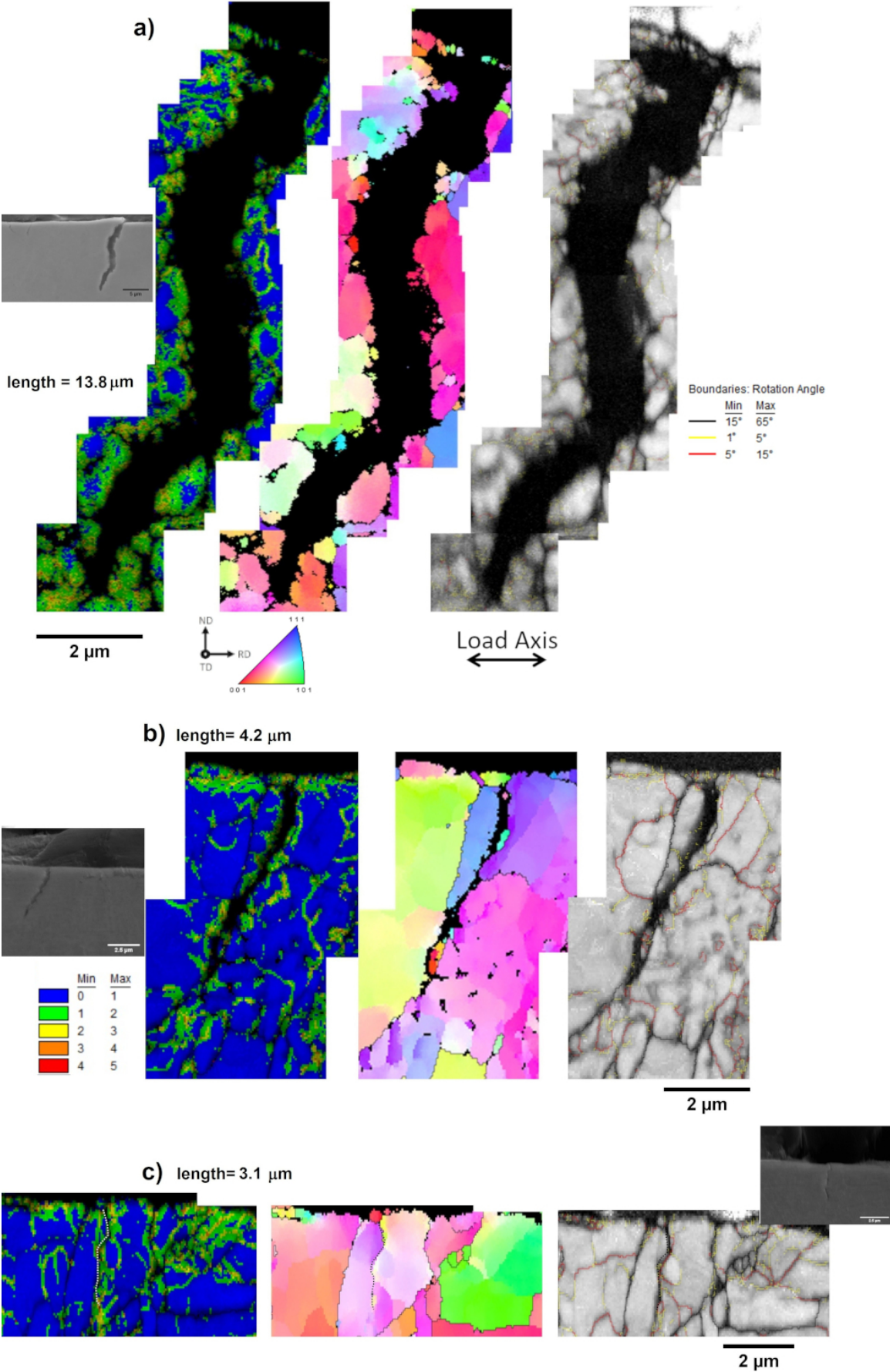


Figure 5.2.6: Cross-section view of the 10T sample deformed until the end of fatigue life ($\Delta\epsilon_t=1.6\%$). The dashed lines indicate the intrusions location

5.2.3 Remarks

As far as we know, only the length parameter was used to label and distinguish an intrusion from a microcrack. With these investigations done here with two complex but dissimilar microstructures, we could manage to do the identification of several microcracks and intrusions found during the intensive analysis. Progress has been made to understand the transition point of an intrusion to a microcrack. There is evidence to suggest that the length of the intrusion indeed gives us an idea of the changeover, but it needs to be combined with the presence of a fine granular area around it. Both microstructures showed a length threshold around 3-4 μm , below this value no high misoriented nanograins were seen.

This has gone some way towards enhancing our understanding of the mechanism of fatigue crack initiation. Our results are encouraging and should be validated by deeper investigations with similar complex structures.

5.3 Selection criteria for technical analysis of austenite identification

It was remarked a certain difficulty to assure the real amount of austenite combined to their precise location. Each technique has its limitation. For example, the XRD technique quantifies very well the amount of austenite, still, it does not provide tools to indicate the precise location of the films. The SEM-EDS technique solves this issue, based on the knowledge that the gammagenic elements are related to the austenitic phase, but it is limited to their thickness. Actually, the microscopy techniques, principally the EBSD technique, presented a difficulty to identify the austenitic phase in a reliable quantity and it was incapable to resolve the very thin austenitic films, even on a very well prepared flat surface. This issue becomes more problematic when the samples presented a considerable topography originated from the fatigue tests. The amount of relief impeded, even more, the identification of the austenite. Inducing the thought that both austenitic phases were meta-stable, not being well identified after deformation.

At first, the TEM microscopy technique offers enough resolution to resolve the austenitic films. But two main issues come from this technique. First of all, the sample must be destroyed to produce the thin foils. Secondly, it represents a very small area collected from the sample. After deformation, another drawback is imposed, mostly in the case of the meta-stable retained austenite. The FIB machining puts too much energy into a very small zone that will induce the transformation of the austenite into martensite. In

the case of the reversed austenite, due to the increased content in gamma-genic elements, it still remained intact even after the FIB machining.

One very interesting and non-destructive tool that allows the identification of the austenite and its location even after the LCF tests is the Magnetic Force Microscope. This technique represents a viable choice to complement the investigation and correlation between the austenite and the surface relief. More details on this tool will be given in the following section.

5.3.1 Magnetic force microscopy (MFM)

Magnetic force microscopy can be used in addition to basic AFM to quantify the magnetic interaction between the tip and magnetic domains of the sample surface, the tip is coated with a ferromagnetic film. In other words, the MFM technique is ideal for differentiating the ferromagnetic phase (ferrite) from the paramagnetic phase (austenite) at an adequate lateral resolution and provides complementary information when used in conjunction with other techniques.

Several studies have been reported on the nondestructive characterization of microstructure and stress-induced perturbations using magnetic techniques, which are sensitive to the ferromagnetic phase [243–248]. MFM is a two-pass semi-contact mode approach, the topography of the surface is acquired in the first pass using tapping mode scanning. The second pass traces the same path as the first mode, with a little small offset to detect the magnetic interaction from the tip and the surface. Figure 5.3.1 shows how the data is collected while a sample is scanned. MFM can be used in a variety of situations and requires minimal sample preparation. The resolution depends on the tip size, but typically a value around 50 to 100 nm can be reached. However, nanometric films can be detected due to the magnetic field effect, which exaggerates their dimensions. In the case of the 9Ni steel, which is composed mostly of a magnetic phase, the goal is to observe places that the magnetic domain stays unchanged and correlate their position to the very thin austenitic films. Although it is known that a MFM interpretation is not always simple, the findings thus need to be treated with caution, the combination with other techniques acts as a support for the observations done with this technique.

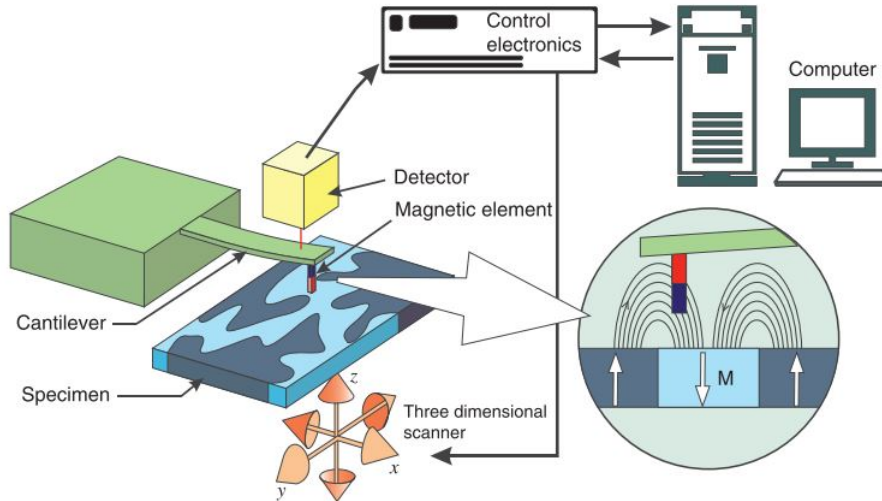


Figure 5.3.1: MFM principle of work [249]

Due to the maze (or labyrinth) type magnetic domains prevalent in the ferrite phase, MFM imaging clearly distinguishes the ferrite phase from the austenite phase [250]. An MFM scan from duplex stainless steel is illustrated in Figure 5.3.2.

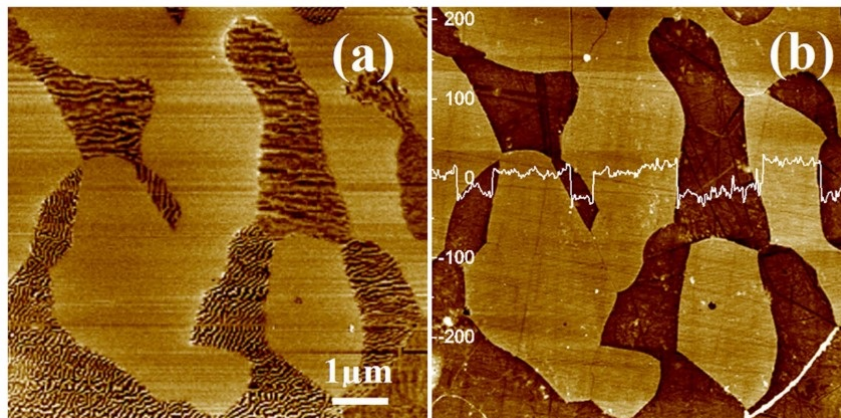


Figure 5.3.2: a) MFM image of the duplex stainless steel with austenite (uniform) and ferrite (labyrinth pattern) b) Corresponding AFM topography with austenite (lighter) and ferrite (darker) [251]

The MFM technique shows itself as a novel model for visualization of the very thin films of retained austenite, which is hardly observed by other techniques. The MFM measurements were done on a Bruker's Dimension Icon machine. The experiments were performed at Bordeaux University under the expertise of Dr. Jean-Marc Olive. Specimens of each WQ and 10T microstructures, before and after the LCF tests with $\Delta\epsilon_t=1.2\%$ were used for the investigation.

5.3.1.1 Interesting findings

Figure 5.3.3 presents two $50\ \mu\text{m} \times 50\ \mu\text{m}$ topographic and magnetic force images of a non-deformed specimen, a SEM micrograph taken from a Nital-etched specimen was put together to allow a comparison between the obtained images from the MFM analysis. The magnetic force image was taken at a lift height of 60 nm. The bright and dark regions in the magnetic force image correspond to repulsive and attractive forces, respectively. Zones with intense repulsive force are seen in a very fine scale, and may be correlated to the austenitic nanofilms that were only observed by the TEM technique, those thin films were present at the boundaries. If this supposition is done, the deformed specimens would still present zones with intense magnetic perturbation, once a very small fraction suffered strain-induced martensitic transformation. The MFM approach has been already used to visualize the retained austenite in TRIP steel, as demonstrated by Zens et al [248] and those literature findings support what is being observed in our investigation.

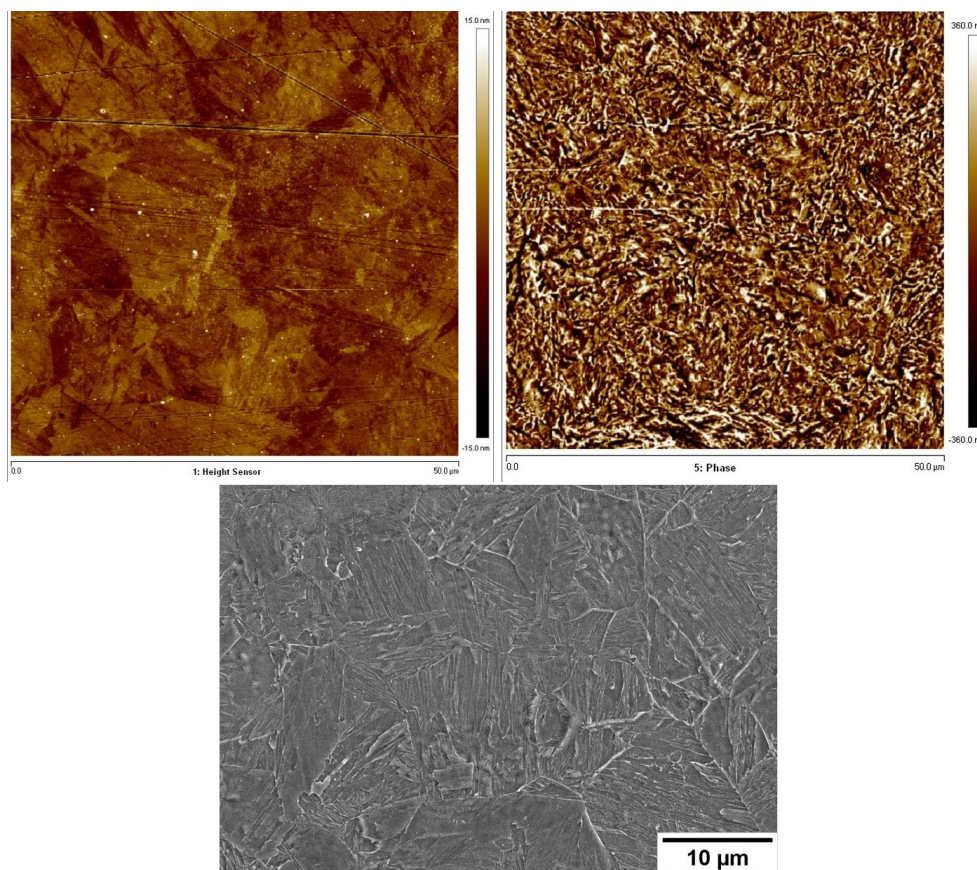


Figure 5.3.3: MFM topographical (left) and magnetic force (right) and corresponding SEM image (bottom) image of the WQ sample, without deformation

Going into a deeper examination in a $5\ \mu\text{m} \times 5\ \mu\text{m}$ scan (Figure 5.3.4), the observed diagonal bright-line pointed by the blue arrow can be attributed to a martensite lath indicated by a dashed line in the topographic image. With the observations done by

MFM in the WQ sample before LCF testing, our findings appear to present satisfactory agreement with the TEM results obtained for the same material in the same condition.

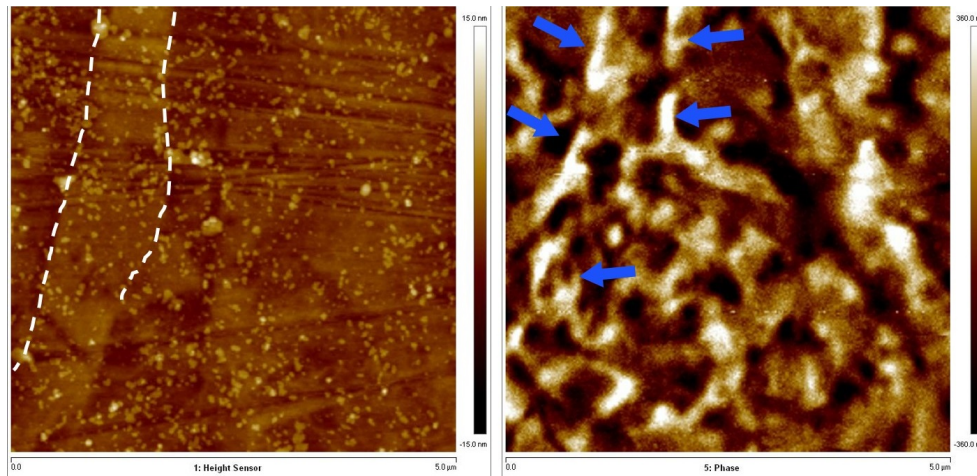


Figure 5.3.4: Closer view of a MFM topographical (left) and magnetic force (right) of the WQ sample, without deformation. The dashed lines in the topographical image indicates a lath boundary, the blue arrows in the corresponding magnetic force image points to the bright spots aligned in the same location of the indicated boundary

Figure 5.3.5 exhibits topographical and magnetic force images for a WQ specimen submitted to LCF test at $\Delta\epsilon_t=1.2\%$. The topography of the sample composed by the PSMs is clearly observed, where the bright zones correspond to a relief produced by the extrusions. The corresponding magnetic image indicates a very light repulsive force next to some of the extrusions observed. In this case, after the fatigue test, a proper height of 80 nm was chosen to assure that the influence of surface topography was eliminated and the cantilever was only affected by the magnetic forces.

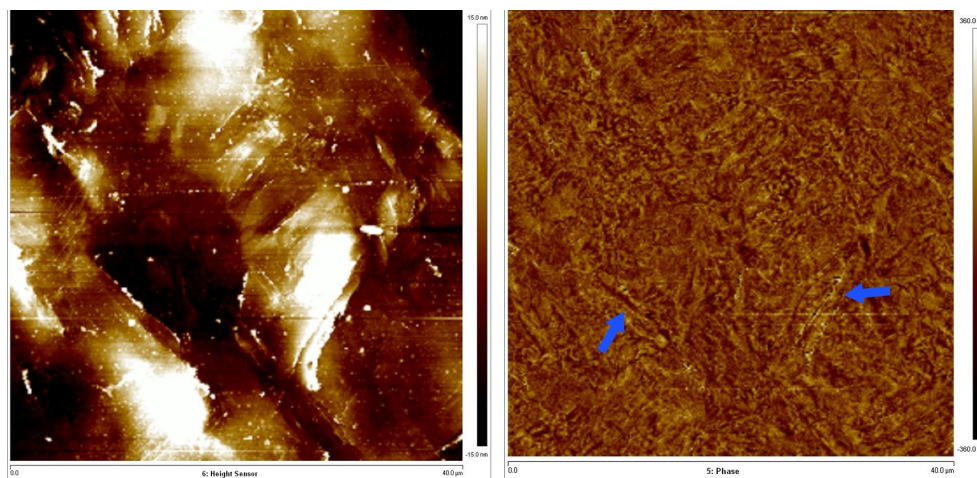


Figure 5.3.5: MFM topographical (left) and magnetic force (right) of the WQ sample, after LCF test ($\Delta\epsilon_t=1.2\%$).

A closer look into a zone with some extrusions gives us more details of the possible presence and influence of the austenitic films in the boundary sliding mechanism (Figure 5.3.6). By superposing the images we could observe that the same repulsive bright spots is present in the vicinity of some extrusions reinforcing, even more, our theory that the austenite adjacent to the boundaries acts as a greasy film allowing the displacement of martensite matter towards the surface.

In some identified extrusions, no perturbation was clearly observed, still, the cause of this lack of evidence of the austenitic phase can probably be attributed to a partial strain-induced transformation into martensite, which was supposed based on the XRD results.

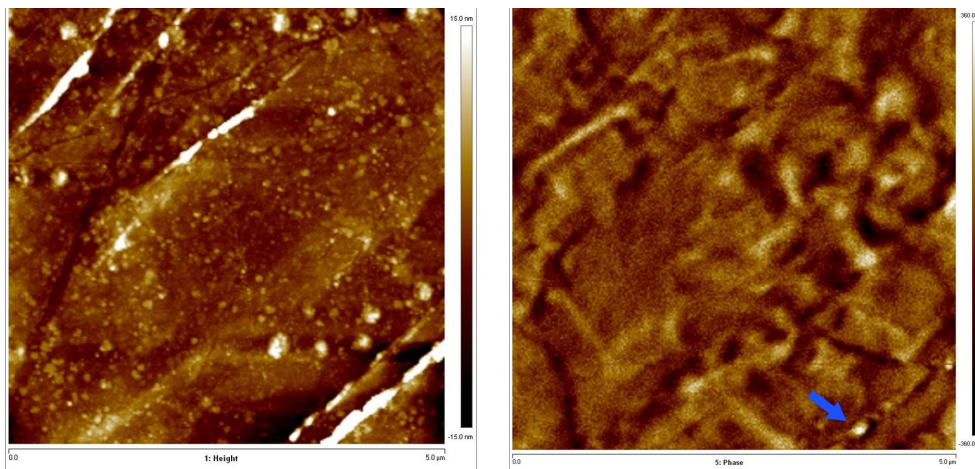


Figure 5.3.6: MFM topographical (left) and magnetic force (right) of the WQ sample after LCF test ($\Delta\epsilon_t=1.2\%$). The blue arrow points to the austenitic phase placed next to the extrusion.

The magnetic field may disturb up to a considerable extension, in that case, it is important to find a good height value that allows a clear magnetic visualization that is also unaffected by the topography. The 10T microstructure presented a considerable magnetic perturbation, being detected up to 80 nm from the surface. Figure 5.3.7 shows the different trials in order to achieve the better height lift for the MFM scan when the 10T sample was analyzed.

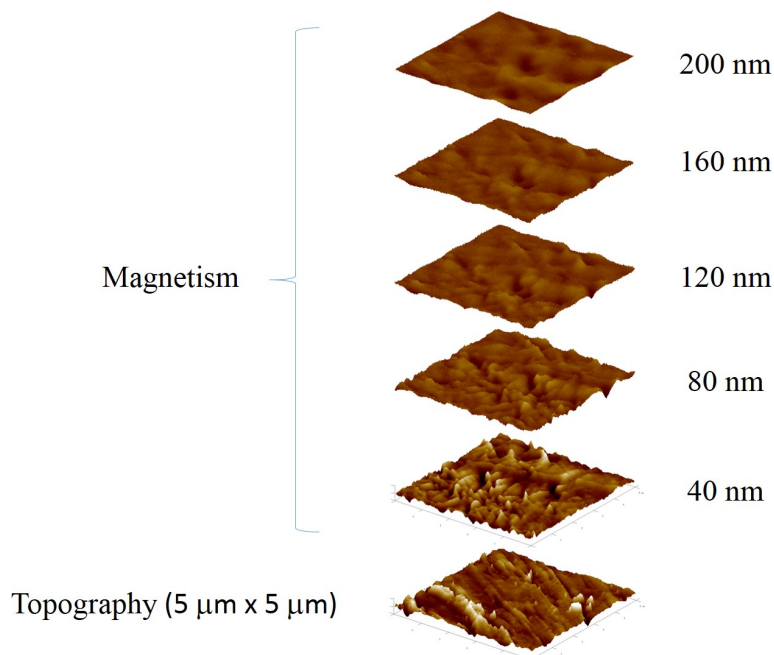


Figure 5.3.7: MFM topographical images as a function of the lift height

Two $20\ \mu\text{m} \times 20\ \mu\text{m}$ topographic and magnetic force images of a 10T non-deformed specimen is represented in Figure 5.3.8. The magnetic force image was taken at a lift height of 60 nm. Again, the bright and dark zones in the magnetic force image are related to repulsive and attractive forces, respectively. By comparing with the SEM micrograph of the same sample etched by Nital, we can conclude that the white spots in the magnetic force images correspond to the austenitic phase present at the interfaces. The austenitic phase noticeably exerts some perturbations on the magnetic force acquisition. In addition to the results found in TRIP steels [248], duplex stainless steels also display the austenitic phase as the light zones and the striped brown zones correspond to ferrite [252, 253].

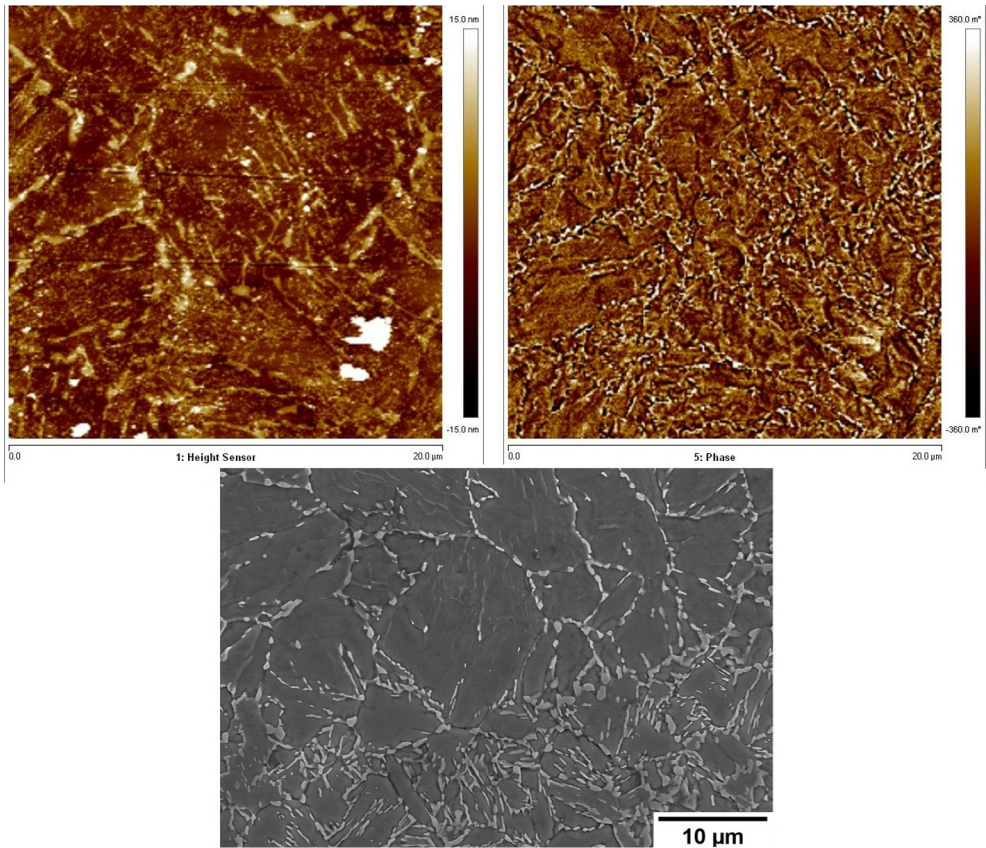


Figure 5.3.8: MFM topographical (left) a magnetic force (right) of the 10T sample, without deformation

A detailed scan in a $5 \mu\text{m} \times 5 \mu\text{m}$ reduced area validates the theory that the very light spots are linked to the reversed austenite islands present dispersed in the matrix boundaries (Figure 5.3.9).

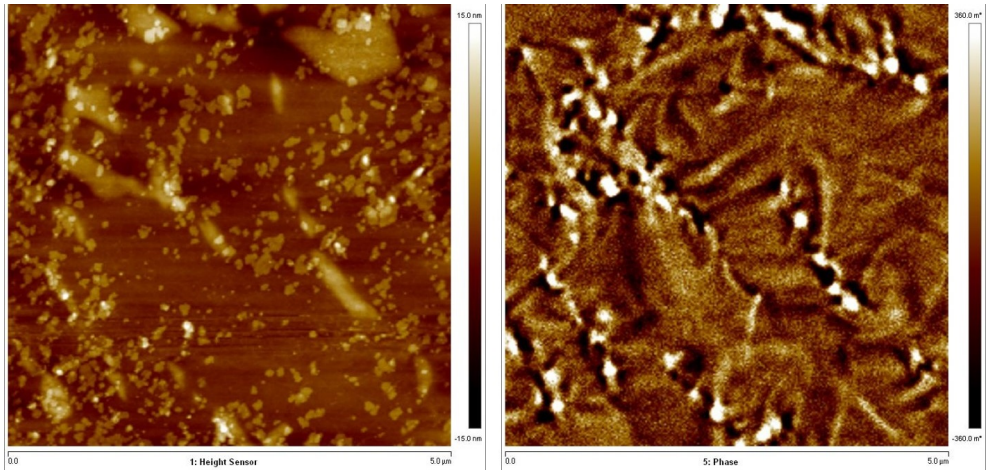


Figure 5.3.9: Closer MFM topographical (left) and magnetic force (right) of the 10T sample, without deformation

The SEM corresponding zone showing the deformed zones of the 10T sample with 1.2% of total applied strain is placed next to the $40\ \mu\text{m} \times 40\ \mu\text{m}$ zone scanned by the MFM technique (Figure 5.3.10). The magnetic force image was taken at a lift height of 60 nm.

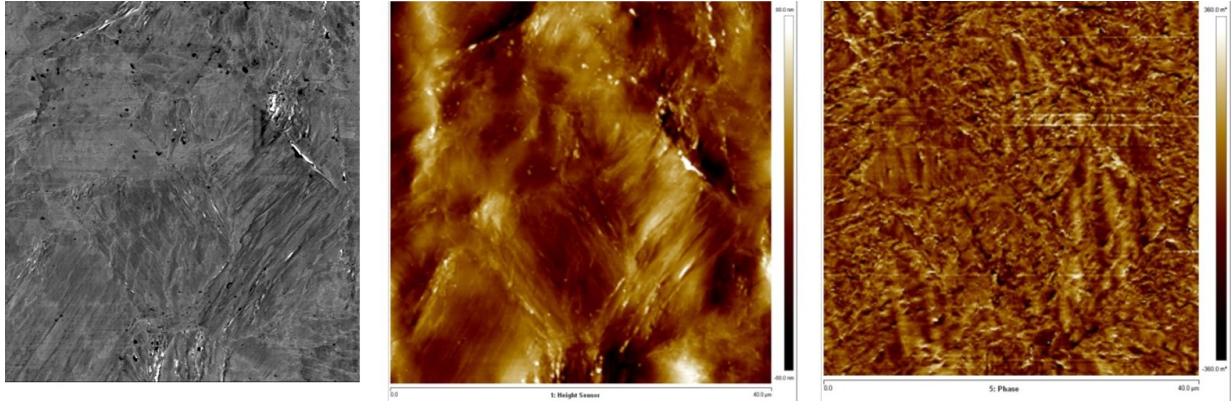


Figure 5.3.10: SEM image (left), MFM topographical (middle) and magnetic force (right) of the 10T sample after LCF test ($\Delta\epsilon_t=1.2\%$)

Figure 5.3.11 shows both topographic and magnetic $5\ \mu\text{m} \times 5\ \mu\text{m}$ images of a LCF deformed specimen at $\Delta\epsilon_t=1.2\%$. By superposing the images, very light zones exhibiting magnetic perturbation can be observed, and once again, they are in the vicinity of the extrusions, as indicated by the blue arrows. In addition, dashed lines were made to represent the PSMs, allowing a proper visualization of their location. These observations made here are consistent with those analyzed by TEM in the FIB lamellae and also by the *c*-ECCI technique, where the austenite films lied between the martensitic laths and were very close to the extrusions.

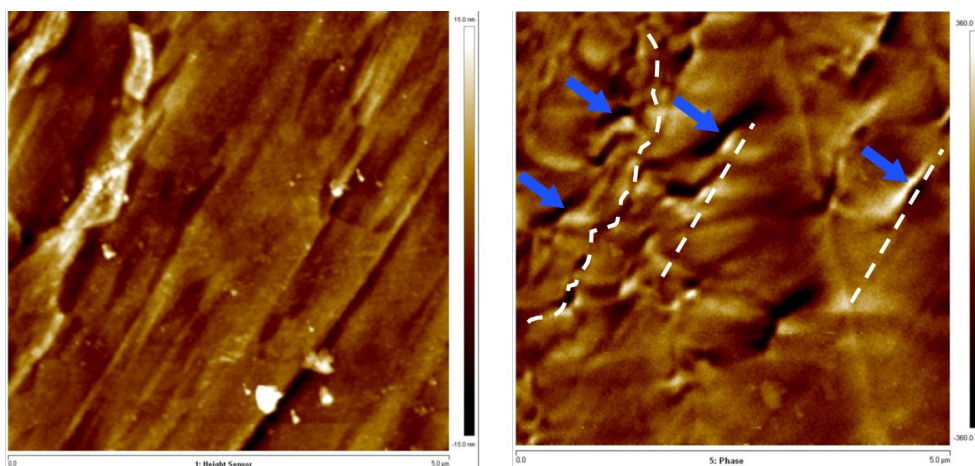


Figure 5.3.11: Detailed view of a MFM topographical (left) and magnetic force (right) of the 10T sample after LCF test ($\Delta\epsilon_t=1.2\%$)

The fraction of brighter zones was measured with the aid of the ImageJ software, and it was found an area fraction of about 10% for the 10T ample and 7.7% for the WQ sample, result very near to the austenite fraction identified by XRD technique.

It was provided here with further evidence that the austenitic films present at the interface behave as a lubricant. Taken together, these findings suggest that the austenitic films facilitate the sliding between the laths and consequently allowing the rise of an extruded volume due to the plastic activity along the cyclic deformation. The present findings have important implications on proposing the mechanism for complex hierarchical structures and the ones that would permit gentle interface modifications.

5.4 Fatigue crack initiation in martensitic steels: role of greasy interface

It would have been very tempting to draw a parallel between the behavior of the present multi-phased 9Ni steel and other multi-phased material such as TRIP steels or duplex steels, where there is a successive contribution of the phases according to the increasing yield stress. Here, the austenitic phase, independently of its yield stress, contributes to the cyclic plastic deformation in another way than by its own deformation and transformation.

The results obtained from this research converged into a single model for the mechanism of fatigue crack nucleation which depends on the presence or not of the interlath austenitic film. The mechanism is summarized in Figure 5.4.1.

First of all, this model covers two different situations. The presence of austenite will drastically change the distribution of stresses along the laths and their interfaces, this is illustrated in Stage 0. In the presence of the austenitic film, the sliding will be facilitated in this zone due to a local decrease in stress, the following steps will be detailed in the subsequent stages. However, in the case of the absence of austenitic films, a built-up of stress at the boundaries will take place. Together with that, a drop in stress levels in the adjacent zones will be noticed. The main important thing to highlight is that the location of the pair of extrusions-intrusions will be dislocated by some nanometers from the boundaries and it is linked to the facility of slip due to a local decrease in the stress levels. The point in common is that at the initial state, the dislocations are distributed homogeneously in the matrix, usually entangled. Depending on the heat treatment applied, the dislocations will be already organized as recovered cells.

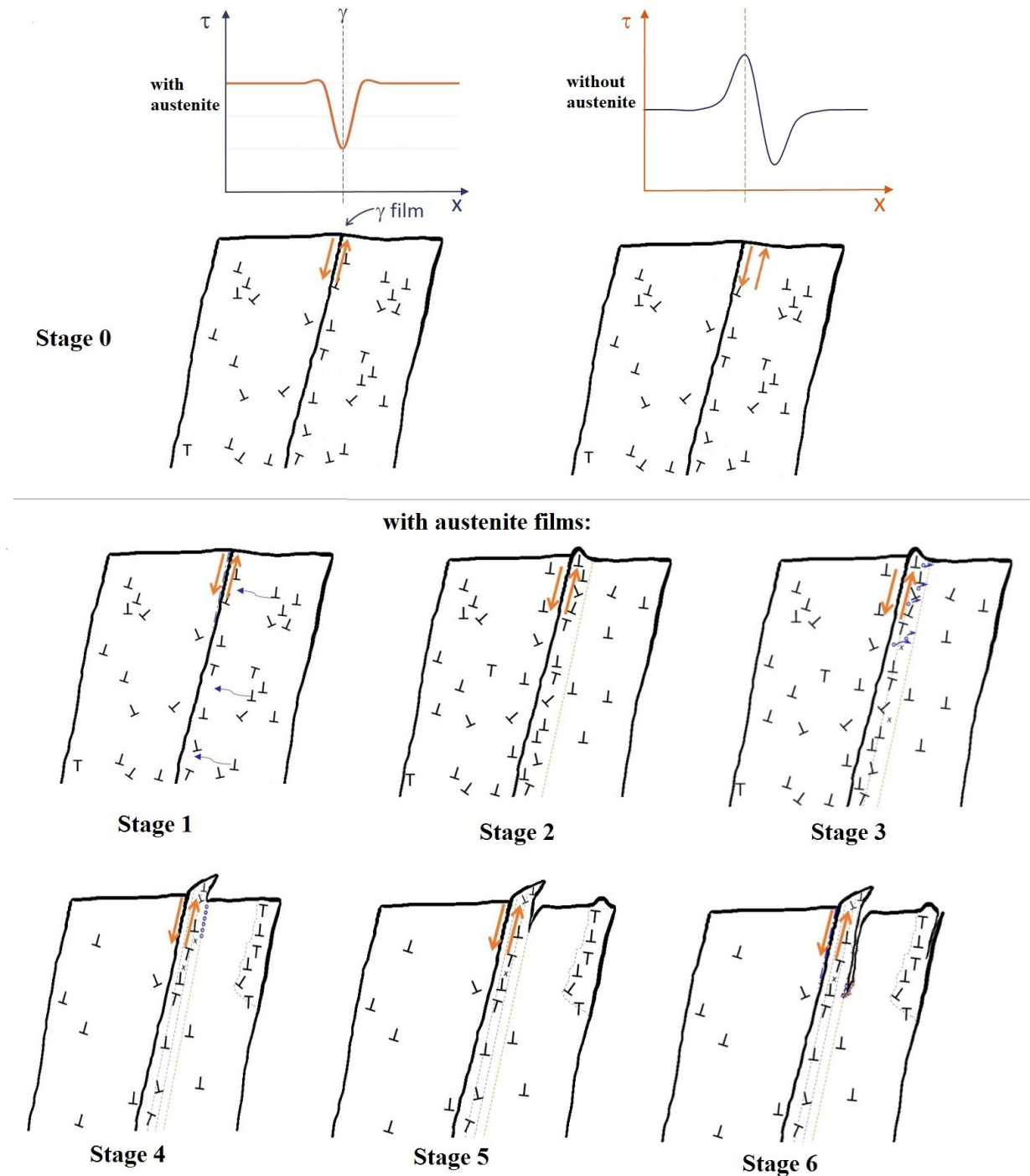


Figure 5.4.1: Proposed mechanism of fatigue crack initiation in martensitic steels

Stage 1: Owing to a small misorientation between each other and the presence of austenite films/islands, the laths have easy slip among them. During the cycling, the dislocations will start to glide, and some will be impeded by other dislocations arrangements. As the cycling continues, the dislocations will be released and will continue moving towards the boundaries.

Stage 2: The accumulated dislocations at the boundaries will tend to pile-up and arrange themselves, leading to a formation of a very thin Persistent Slip Band (PSB) right at the interface. In this case, the entire lath will not behave as a PSB itself, but only a small portion of it.

Stage 3: The combination of dislocation movement together with the facilitated cross slip, due to the several activated slip planes leads to their strong interaction causing their annihilation or production of point defects (interstitial). At the very early stage of fatigue life, compressive stress will build up in the zones with interstitial accumulation, originating the first slip steps (very early stage of the PSMs). The appearance of those slip steps corresponds to the beginning of the cycling softening. Due to the highest mobility, the vacancies will migrate and accumulate towards the virtual interface created between the zone with intense plastic activity and the quasi-elastic matrix.

Stage 4: As the cycling continues, more dislocations will be released and migrate toward the interfaces or will rearrange themselves into a more stable structure, such as cells walls. The austenite, acting as a greasy film facilitating the boundary sliding, will be partially transformed by the intense activity, producing strain-induced martensite. This partial transformation will originate stress compression fields that tend to repel the vacancies, they will rather prefer to move toward the virtual interface (between the PSB and the matrix). The zones with a stronger accumulation of vacancies will lead to a local decrease of the elastic modulus [254, 255]. As proposed by Polak [7], a rearrangement of matter will be originated by the ongoing migration and accumulation of vacancies at the interface of the PSB and a motion of atoms in the opposite direction (interior of the PSB). This rearrangement of matter will lead to a volume increase within the PSB. In a tentative of relaxing the internal compressive stress, the matter will be extruded transforming the slip steps into extrusions, which later will widen and heighten with subsequent cycling.

Stage 5: Later, tensile stresses will concentrate in the zones with vacancy accumulation. As soon as the peak stress reaches the higher yield stress of the matrix, the internal tensile stress will be also relaxed by cyclic creep, generating an intrusion in the virtual layer between the PSB and the matrix [7].

Stage 6: The sharp intrusions with a crack-shape will raise the stress in this zone and will develop in length along the PSB/matrix interface, deviating towards the lath interface. FGA will be generated around the intrusion as a tentative to blunt the intrusion development into a microcrack. However, if the radius of the tip of the intrusion and the amount of deformation imposed is high enough, the intrusion will transform into a microcrack. If the microcrack continues to grow as a stage I crack and suits the fracture criterion, it will then propagate and maybe transforming into a macrocrack.

5.5 Concluding remarks

The challenge of the PhD project aiming to understand the mechanism of fatigue crack in a material with a complex structure has finally been met. The 9Ni martensitic steel appeared as a very suitable material to investigate the role of any metallurgical item possible to be found in a material: interfaces, multiple phases and dislocation density. The right selection of heat treatments allowed investigating all these metallurgical items, and even more, such as the nature of austenite (retained or reversed).

This work has also pointed out the necessity of carefully choosing the investigation technique. Because of the hierarchical microstructure, the size of the investigated element becomes so small that it approaches to the resolution of the equipment. The difficulty lying on the detection of some features was also challenging, and this can deviate the conclusions towards another point. For example, the visualization of the retained austenitic film was difculted when the FIB machining was used, because of its strain-induced transformation property. It does not mean that the austenitic phase was not there, though.

Nevertheless, by taking into account all these considerations, a generalized concept of crack initiation in materials of the martensitic family has been proposed based on the previously explored in the literature for less complex microstructures, such as austenitic and ferritic steels or monocrystals. The obtained results also lead to the practical use of this material and a recommendation of the “best” heat treatment for fatigue resistance has been mentioned. The present results can be employed to other alloys with martensitic structure, like the 17-4PH steel (precipitation hardened stainless steel).

Finally, I would suggest to continue the present research by these three actions:

- Would a 9Ni steel free of austenite be much less fatigue resistant than a microstructure of this same alloy containing austenite? In other words, does the austenite bring a substantial advantage regarding fatigue resistance? This must not be confused with TRIP steel, where the austenite contributes to the mechanical strength by the transformation of austenite.
- Because 9Ni steel is planned to be used at low temperature, what is the fatigue behavior in liquid nitrogen? Is the austenite still stable and provides the greasy effect?
- Since we have identified a criterion for distinguishing intrusion from microcrack, the study at low temperature could confirm or not this hypothesis. Since the intrusion formation involves the diffusion process of vacancies, then their growth should be reduced at lower temperature ranges.

Bibliography

- [1] Pook, L., *Why Metal Fatigue Matters*. Springer, 2007.
- [2] Zhang, J., Li, H., Yang, F., Chi, Q., Ji, L., and Feng, Y., “Effect of heat treatment process on mechanical properties and microstructure of a 9% ni steel for large lng storage tanks”, *Journal of materials engineering and performance*, vol. 22, no. 12, pp. 3867–3871, 2013.
- [3] Zhao, X., PAN, T., Wang, Q., Su, H., Yang, C., Yang, Q., and Zhang, Y., “Effect of intercritical quenching on reversed austenite formation and cryogenic toughness in qlt-processed 9% ni steel”, *Journal of Iron and Steel Research, International*, vol. 14, no. 5, pp. 240–244, 2007.
- [4] Ahsan, Q., Haseeb, A., Hussein, N. S. B., and Chang, S., “9% nickel steels and their welding behavior”, 2014.
- [5] Kacem, H., “Influence des chargements cycliques sur les proprietes mecaniques des aciers a 9% de nickel et 316l dans des conditions cryogeniques”, Ph.D. dissertation, Lille 1, 2016.
- [6] Mughrabi, H., Herz, K., and Stark, X., “Cyclic deformation and fatigue behaviour of α -iron mono-and polycrystals”, *International Journal of fracture*, vol. 17, no. 2, pp. 193–220, 1981.
- [7] Polák, J. and Man, J., “Mechanisms of extrusion and intrusion formation in fatigued crystalline materials”, *Materials Science and Engineering: A*, vol. 596, pp. 15–24, 2014.
- [8] Sangid, M. D., “The physics of fatigue crack initiation”, *International journal of fatigue*, vol. 57, pp. 58–72, 2013.
- [9] Seidametova, G., “Formation of extrusion-intrusion in a martensitic steel studied by advanced microscopies”, Ph.D. dissertation, Lille 1, 2017.
- [10] Bain, E. C. and Dunkirk, N., “The nature of martensite”, *trans. AIME*, vol. 70, no. 1, pp. 25–47, 1924.
- [11] Liu, J. and Kaoumi, D., “Use of in-situ tem to characterize the deformation-induced martensitic transformation in 304 stainless steel at cryogenic temperature”, *Materials Characterization*, vol. 136, pp. 331–336, 2018.
- [12] Bhadeshia, H., “Martensite and bainite in steels: Transformation mechanism & mechanical properties”, *Le Journal de Physique IV*, vol. 7, no. C5, pp. C5–367, 1997.
- [13] Smallman, R. and Ngan, A., “Chapter 12 - steel transformations”, in *Modern Physical Metallurgy (Eighth Edition)*, R. Smallman and A. Ngan, Eds., Eighth Edition, Oxford: Butterworth-Heinemann, 2014, pp. 473–498, ISBN: 978-0-08-098204-5. DOI: <https://doi.org/10.1016/B978-0-08-098204-5.00012-2>. [Online]. Available: <https://www.sciencedirect.com/science/article/pii/B9780080982045000122>.

- [14] Krauss, G., *Steels: processing, structure, and performance*. Asm International, 2015.
- [15] Morito, S., Tanaka, H., Konishi, R., Furuhashi, T., Maki, and T., “The morphology and crystallography of lath martensite in Fe-C alloys”, *Acta Materialia*, vol. 51, no. 6, pp. 1789–1799, 2003.
- [16] Maki, T., “Morphology and substructure of martensite in steels”, in *Phase transformations in steels*, Elsevier, 2012, pp. 34–58.
- [17] Morsdorf, L., Jeannin, O., Barbier, D., Mitsuhashi, M., Raabe, D., and Tasan, C. C., *Acta Materialia*, vol. 121, pp. 202–214, 2016.
- [18] Krauss, G., “Martensite in steel: Strength and structure”, *Materials science and engineering: A*, vol. 273, pp. 40–57, 1999.
- [19] Kitahara, H., Ueki, R., Tsuji, N., and Minamino, Y., “Crystallographic features of lath martensite in low-carbon steel”, *Acta Materialia*, vol. 54, no. 5, pp. 1279–1288, 2006.
- [20] Jahrsengene, G., “Ebsd microstructure characterization of 9% nickel steel during in situ heat treatment”, M.S. thesis, NTNU, 2015.
- [21] Wu, H. B., Li, L., Zhang, K., and Tang, D., “Stability of reversed austenite in 9Ni steel”, in *Advanced Materials Research*, Trans Tech Publ, vol. 535, 2012, pp. 580–585.
- [22] Soeiro Junior, J. C. and Brandi, S. D., “Soldabilidade metalúrgica do aço ASTM A553 tipo I com 9% de níquel”, 2017.
- [23] Morsdorf, L., Tasan, C. C., Ponge, D., and Raabe, D., “3D structural and atomic-scale analysis of lath martensite: Effect of the transformation sequence”, *Acta Materialia*, vol. 95, pp. 366–377, 2015.
- [24] Ryou, K., Nambu, S., and Koseki, T., “Effect of carbon content on selection of slip system during uniaxial tensile deformation of lath martensite”, *Materials Science and Engineering: A*, vol. 777, p. 139 090, 2020.
- [25] Lee, S. H., Kang, J.-Y., Han, H. N., Oh, K. H., Lee, H.-C., Suh, D.-W., and KIM, S.-J., “Variant selection in mechanically-induced martensitic transformation of metastable austenitic steel”, *ISIJ international*, vol. 45, no. 8, pp. 1217–1219, 2005.
- [26] Morito, S., Yoshida, H., Maki, T., and Huang, X., “Effect of block size on the strength of lath martensite in low carbon steels”, *Materials Science and Engineering: A*, vol. 438, pp. 237–240, 2006.
- [27] Cayron, C., “Arpge: A computer program to automatically reconstruct the parent grains from electron backscatter diffraction data”, *Journal of applied crystallography*, vol. 40, no. 6, pp. 1183–1188, 2007.
- [28] Germain, L., Gey, N., Mercier, R., Blaineau, P., and Humbert, M., “An advanced approach to reconstructing parent orientation maps in the case of approximate orientation relations: Application to steels”, *Acta Materialia*, vol. 60, no. 11, pp. 4551–4562, 2012.
- [29] Nyssönen, T., Peura, P., and Kuokkala, V.-T., “Crystallography, morphology, and martensite transformation of prior austenite in intercritically annealed high-aluminum steel”, *Metallurgical and Materials Transactions A*, vol. 49, no. 12, pp. 6426–6441, 2018.

- [30] Du, C., Hoefnagels, J., Vaes, R., and Geers, M., “Plasticity of lath martensite by sliding of substructure boundaries”, *Scripta Materialia*, vol. 120, pp. 37–40, 2016.
- [31] Ohmura, T., Tsuzaki, K., and Matsuoka, S., “Evaluation of the matrix strength of fe-0.4 wt% c tempered martensite using nanoindentation techniques”, *Philosophical Magazine A*, vol. 82, no. 10, pp. 1903–1910, 2002.
- [32] Zhang, Z., Hu, Z., and Schmauder, S., “Fatigue behavior of 9–12% cr ferritic-martensitic steel”, in. Jan. 2018, pp. 1–46.
- [33] Milella, P. P., *Fatigue and corrosion in metals*. Springer Science & Business Media, 2012.
- [34] Mughrabi, H., “Specific features and mechanisms of fatigue in the ultrahigh-cycle regime”, *International journal of fatigue*, vol. 28, no. 11, pp. 1501–1508, 2006.
- [35] Pyttel, B., Schwerdt, D., and Berger, C., “Very high cycle fatigue—is there a fatigue limit?”, *International Journal of fatigue*, vol. 33, no. 1, pp. 49–58, 2011.
- [36] Cooper, C. and Fine, M., “Coffin-manson relation for fatigue crack initiation”, *TMS (The Metallurgical Society) Paper Selection;(USA)*, vol. 56, no. CONF-840909-, 1984.
- [37] Petrenec, M., Polák, J., Obrtlík, K., and Man, J., “Dislocation structures in cyclically strained x10cral24 ferritic steel”, *Acta materialia*, vol. 54, no. 13, pp. 3429–3443, 2006.
- [38] Marmy, P. and Kruml, T., “Low cycle fatigue of eurofer 97”, *Journal of Nuclear Materials*, vol. 377, no. 1, pp. 52–58, 2008.
- [39] Sauzay, M., Brilllet, H., Monnet, I., Mottot, M., Barcelo, F., Fournier, B., and Pineau, A., “Cyclically induced softening due to low-angle boundary annihilation in a martensitic steel”, *Materials Science and Engineering: A*, vol. 400, pp. 241–244, 2005.
- [40] Giordana, M. F., Alvarez-Armas, I., and Armas, A., “On the cyclic softening mechanisms of reduced activity ferritic/martensitic steels”, *steel research international*, vol. 83, no. 6, pp. 594–599, 2012.
- [41] Jing, H., Luo, Z., Xu, L., Zhao, L., and Han, Y., “Low cycle fatigue behavior and microstructure evolution of a novel 9cr–3w–3co tempered martensitic steel at 650° c”, *Materials Science and Engineering: A*, vol. 731, pp. 394–402, 2018.
- [42] Mughrabi, H., Wang, R., Differt, K., and Essmann, U., “Fatigue crack initiation by cyclic slip irreversibilities in high-cycle fatigue”, in *Fatigue mechanisms: advances in quantitative measurement of physical damage*, ASTM International, 1983.
- [43] Mughrabi, H., “Cyclic slip irreversibilities and the evolution of fatigue damage”, *Metallurgical and Materials Transactions B*, vol. 40, pp. 1257–1279, Aug. 2009.
- [44] Brechet, Y., *Euromat 99, Microstructures, Mechanical Properties and Processes: Computer Simulation and Modelling*. John Wiley & Sons, 2000, vol. 3.
- [45] Fournier, B., “Fatigue-fluage des aciers martensitiques a 9-12% cr: Comportement et endommagement”, Ph.D. dissertation, 2007.
- [46] Laird, C., Wang, Z., Ma, B.-T., and Chai, H.-F., “Low energy dislocation structures produced by cyclic softening”, *Materials Science and Engineering: A*, vol. 113, pp. 245–257, 1989.

- [47] Roven, H. and Nes, E., “Cyclic deformation of ferritic steel—i. stress-strain response and structure evolution”, *Acta metallurgica et materialia*, vol. 39, no. 8, pp. 1719–1733, 1991.
- [48] Lukaš, P. and Kunz, L., “Role of persistent slip bands in fatigue”, *Philosophical magazine*, vol. 84, no. 3-5, pp. 317–330, 2004.
- [49] Kruml, T. and Polák, J., “Fatigue softening of x10cral24 ferritic steel”, *Materials Science and Engineering: A*, vol. 319, pp. 564–568, 2001.
- [50] Davidson, D., Lankford, J., Yokobori, T., and Sato, K., “Fatigue crack tip plastic zones in low carbon steel”, *International Journal of Fracture*, vol. 12, no. 4, pp. 579–585, 1976.
- [51] Katagiri, K., Omura, A., Koyanagi, K., Awatani, J., Shiraishi, T., and Kaneshiro, H., “Early stage crack tip dislocation morphology in fatigued copper”, *Metallurgical Transactions A*, vol. 8, no. 11, pp. 1769–1773, 1977.
- [52] Ewing, J. A. and Humfrey, J., “Vi. the fracture of metals under repeated alternations of stress”, *Philosophical Transactions of the Royal Society of London. Series A, Containing Papers of a Mathematical or Physical Character*, vol. 200, no. 321-330, pp. 241–250, 1903.
- [53] Thompson, N., Wadsworth, N., and Louat, N., “Xi. the origin of fatigue fracture in copper”, *Philosophical Magazine*, vol. 1, no. 2, pp. 113–126, 1956.
- [54] Man, J., Klapetek, P., Man, O., Weidner, A., Obertlik, K., and Polák, J., “Extrusions and intrusions in fatigued metals. part 2. afm and ebsd study of the early growth of extrusions and intrusions in 316l steel fatigued at room temperature”, *Philosophical Magazine*, vol. 89, no. 16, pp. 1337–1372, 2009.
- [55] Polák, J., Obertlik, K., and Hajek, M., “Cyclic plasticity in type 316l austenitic stainless steel”, *Fatigue & Fracture of Engineering Materials & Structures*, vol. 17, no. 7, pp. 773–782, 1994.
- [56] Basinski, Z. and Basinski, S., “Fundamental aspects of low amplitude cyclic deformation in face-centred cubic crystals”, *Progress in Materials Science*, vol. 36, pp. 89–148, 1992.
- [57] Bayerlein, M. and Mughrabi, H., “The formation of wither tongue-or ribbon-like extrusions in fatigued copper polycrystals”, *Acta metallurgica et materialia*, vol. 39, no. 7, pp. 1645–1650, 1991.
- [58] Hull, D., “Surface structure of slip bands on copper fatigued at 293, 90, 20, and 4.2 k”, *J. Inst. Metals*, vol. 86, 1958.
- [59] Ahmed, J., Wilkinson, A., and Roberts, S., “Electron channelling contrast imaging characterization of dislocation structures associated with extrusion and intrusion systems and fatigue cracks in copper single crystals”, *Philosophical Magazine A*, vol. 81, no. 6, pp. 1473–1488, 2001.
- [60] Polák, J., Lepistö, T., and Kettunen, P., “Surface topography and crack initiation in emerging persistent slip bands in copper single crystals”, *Materials Science and Engineering*, vol. 74, no. 1, pp. 85–91, 1985.
- [61] Hunsche, A. and Neumann, P., “Quantitative measurement of persistent slip band profiles and crack initiation”, *Acta metallurgica*, vol. 34, no. 2, pp. 207–217, 1986.

- [62] Basinski, Z. and Basinski, S., “Copper single crystal psb morphology between 4.2 and 350 k”, *Acta Metallurgica*, vol. 37, no. 12, pp. 3263–3273, 1989.
- [63] Bao-Tong, M. and Laird, C., “Overview of fatigue behavior in copper single crystals—i. surface morphology and stage i crack initiation sites for tests at constant strain amplitude”, *Acta Metallurgica*, vol. 37, no. 2, pp. 325–336, 1989.
- [64] Schwab, A., Meissner, O., and Holste, C., “Atomic force microscopy of slip lines on the surface of a fatigued nickel single crystal”, *Philosophical magazine letters*, vol. 77, no. 1, pp. 23–31, 1998.
- [65] Forsyth, P. and Stubbington, C., “The slip-band extrusion effect observed in some aluminium alloys subjected to cyclic stresses”, *Journal of the Institute of Metals*, vol. 83, no. 8, pp. 395–399, 1955.
- [66] King, A. and Teer, D., “Crack initiation in polycrystalline aluminium fatigued at low strain”, *Metal Science Journal*, vol. 3, no. 1, pp. 121–126, 1969.
- [67] Mughrabi, H., Bayerlein, M., and Wang, R., “Direct measurement of the rate of extrusion growth in fatigue copper mono- and polycrystals”, *Strength of Metals and Alloys.*, vol. 2, pp. 879–886, 1991.
- [68] Laird, C., “Mechanisms of fatigue crack nucleation”, *Corros. Fatigue, NACE-2,(1972)*, 1972.
- [69] Essmann, U., Gosele, U., and Mughrabi, H., “A model of extrusions and intrusions in fatigued metals i. point-defect production and the growth of extrusions”, *Philosophical Magazine A*, vol. 44, no. 2, pp. 405–426, 1981.
- [70] Man, J., Petrevec, M., Obrtlík, K., and Polák, J., “Afm and tem study of cyclic slip localization in fatigued ferritic x10cral24 stainless steel”, *Acta materialia*, vol. 52, no. 19, pp. 5551–5561, 2004.
- [71] Man, J., Polák, J., Vičar, M., Obrtlík, K., Matějková, J., and Rek, A., “Afm study of slip localization and surface relief evolution in fatigued ferritic x10cral24 stainless steel”, *WIT Transactions on Engineering Sciences*, vol. 40, 2003.
- [72] Polák, J., Man, J., Vystavěl, T., and Petrevec, M., “The shape of extrusions and intrusions and initiation of stage i fatigue cracks”, *Materials Science and Engineering: A*, vol. 517, no. 1-2, pp. 204–211, 2009.
- [73] Motoyashiki, Y., Brueckner-Foit, A., and Sugeta, A., “Investigation of small crack behaviour under cyclic loading in a dual phase steel with an fib tomography technique”, *Fatigue & Fracture of Engineering Materials & Structures*, vol. 30, no. 6, pp. 556–564, 2007.
- [74] Serre, I., Salazar, D., and Vogt, J.-B., “Atomic force microscopy investigation of surface relief in individual phases of deformed duplex stainless steel”, *Materials Science and Engineering: A*, vol. 492, no. 1-2, pp. 428–433, 2008.
- [75] Balbi, M., Avalos, M., El Bartali, A., and Alvarez-Armas, I., “Microcrack growth and fatigue behavior of a duplex stainless steel”, *International journal of fatigue*, vol. 31, no. 11-12, pp. 2006–2013, 2009.
- [76] Marinelli, M. and Hereñú, S., “Short fatigue crack behavior in duplex stainless steels”

- [77] El Bartali, A., Aubin, V., and Degallaix, S., “Fatigue damage analysis in a duplex stainless steel by digital image correlation technique”, *Fatigue & Fracture of Engineering Materials & Structures*, vol. 31, no. 2, pp. 137–151, 2008.
- [78] Batista, M. N., Marinelli, M. C., and Alvarez-Armas, I., “Effect of initial microstructure on surface relief and fatigue crack initiation in aisi 410 ferritic-martensitic steel”, *Fatigue & Fracture of Engineering Materials & Structures*, vol. 42, no. 1, pp. 61–68, 2019.
- [79] Kruml, T. and Polák, J., “Fatigue cracks in eurofer 97 steel: Part i. nucleation and small crack growth kinetics”, *Journal of nuclear materials*, vol. 412, no. 1, pp. 2–6, 2011.
- [80] Salazar, D., “Etude du partage de la plasticite cyclique d’un acier duplex par microscopie a force atomique”, Ph.D. dissertation, Lille 1, 2008.
- [81] Godha, A., “Microstructural effects on fatigue damage evolution in advanced high strength sheet (ahss) steels”, Ph.D. dissertation, Georgia Institute of Technology, 2015.
- [82] Polák, J., Man, J., and Obrtlík, K., “Afm evidence of surface relief formation and models of fatigue crack nucleation”, *International Journal of Fatigue*, vol. 25, no. 9-11, pp. 1027–1036, 2003.
- [83] Yang, F. and Saxena, A., “Mechanisms of fatigue crack initiation in annealed, quenched and tempered 4340 steel”, *Proceedings of the Institution of Mechanical Engineers, Part C: Journal of Mechanical Engineering Science*, vol. 214, no. 9, pp. 1151–1161, 2000.
- [84] Polak, J., “Os05w0314 atomic force microscopy and high resolution scanning electron microscopy evidence concerning fatigue crack nucleation”, in *The Abstracts of ATEM: International Conference on Advanced Technology in Experimental Mechanics: Asian Conference on Experimental Mechanics 2003.2*, The Japan Society of Mechanical Engineers, 2003, _OS05W0314–_OS05W0314.
- [85] Wang, Y., Meletis, E., and Huang, H., “Quantitative study of surface roughness evolution during low-cycle fatigue of 316l stainless steel using scanning whitelight interferometric (swli) microscopy”, *International journal of fatigue*, vol. 48, pp. 280–288, 2013.
- [86] Ahmed, J., Wilkinson, A., and Roberts, S., “Study of dislocation structures near fatigue cracks using electron channelling contrast imaging technique (ecc-i)”, *Journal of microscopy*, vol. 195, no. 3, pp. 197–203, 1999.
- [87] Man, J., Vystavěl, T., Weidner, A., Kuběna, I., Petrevec, M., Kruml, T., and Polák, J., “Study of cyclic strain localization and fatigue crack initiation using fib technique”, *International Journal of Fatigue*, vol. 39, pp. 44–53, 2012.
- [88] Polák, J., Kuběna, I., and Man, J., “The shape of early persistent slip markings in fatigued 316l steel”, *Materials Science and Engineering: A*, vol. 564, pp. 8–12, 2013.
- [89] Kraft, O., Schwaiger, R., Zhang, G., and Volkert, C., “Crack nucleation and propagation during fatigue of thin metal films”,
- [90] Polák, J., Mazanova, V., Kuběna, I., Heczko, M., and Man, J., “Surface relief and internal structure in fatigued stainless sanicro 25 steel”, *Metallurgical and Materials Transactions A*, vol. 47, no. 5, pp. 1907–1911, 2016.

- [91] Polák, J., “On the role of point defects in fatigue crack initiation”, *Materials Science and Engineering*, vol. 92, pp. 71–80, 1987.
- [92] Höppel, H. W., Goik, P., Krechel, C., and Göken, M., “Ex and in situ investigations on the role of persistent slip bands and grain boundaries in fatigue crack initiation”, *Journal of Materials Research*, vol. 32, no. 23, pp. 4276–4286, 2017.
- [93] Mughrabi, H., “Damage mechanisms and fatigue lives: From the low to the very high cycle regime”, *Procedia Engineering*, vol. 55, pp. 636–644, 2013.
- [94] Okada, K., Shibata, A., Takeda, Y., and Tsuji, N., “Crystallographic analysis of fatigue fracture initiation in 8ni-0.1 c martensitic steel”, *International Journal of Fatigue*, vol. 143, p. 105921, 2021.
- [95] Avery, R. E. and Parsons, D., “Welding stainless and 9% nickel steel cryogenic vessels”, *Welding journal*, vol. 74, no. 11, 1995.
- [96] Yang, Y.-h., Cai, Q.-w., Tang, D., and Wu, H.-b., “Precipitation and stability of reversed austenite in 9ni steel”, *International Journal of Minerals, Metallurgy, and Materials*, vol. 17, no. 5, pp. 587–595, 2010.
- [97] Price, A. H., “Significant system parameters influencing haz properties in 9% ni steel”, *Science and technology of welding and joining*, vol. 6, no. 4, pp. 255–260, 2001.
- [98] Huibin, Y. Y. C. Q. W. and Hua, W., “Formation of reversed austenite and its effect on cryogenic toughness of 9ni steel during two-phase region heat treatment”, *Acta Metall Sin*, vol. 45, no. 3, pp. 270–274, 2009.
- [99] Strife, J. and Passoja, D., “The effect of heat treatment on microstructure and cryogenic fracture properties in 5ni and 9ni steel”, *Metallurgical Transactions A*, vol. 11, no. 8, p. 1341, 1980.
- [100] Wang, M., Liu, Z.-Y., and Li, C.-G., “Correlations of ni contents, formation of reversed austenite and toughness for ni-containing cryogenic steels”, *Acta Metallurgica Sinica (English Letters)*, vol. 30, no. 3, pp. 238–249, 2017.
- [101] Zhang, K., Di, T., and Wu, H.-b., “Effect of heating rate before tempering on reversed austenite in fe-9ni-c alloy”, *Journal of Iron and Steel Research, International*, vol. 19, no. 9, pp. 73–78, 2012.
- [102] Bhadeshia, H. and Honeycombe, R., *Steels: microstructure and properties*. Butterworth-Heinemann, 2017.
- [103] Kim, K. and Schwartz, L., “On the effects of intercritical tempering on the impact energy of fe9ni0.1c”, *Materials Science and Engineering*, vol. 33, no. 1, pp. 5–20, 1978.
- [104] Choi, H. and Schwartz, L., “Fatigue crack propagation in intercritically tempered fe-9ni-0.1 c and fe-4mn-0.15 c”, *Metallurgical Transactions A*, vol. 14, no. 6, p. 1089, 1983.
- [105] The International Nickel Company Inc, *Low temperature properties of nickel alloy steels*, 1975.
- [106] Syn, C. K., Morris, J., and Jin, S., “Cryogenic fracture toughness of 9ni steel enhanced through grain refinement”, *Metallurgical Transactions A*, vol. 7, no. 12, pp. 1827–1832, 1976.

- [107] Tavares, S., Rodrigues, C., Oliveira, C. de, Woyames, C., and Dille, J., “Influence of heat treatments on microstructure and toughness of 9% ni steel”, *Journal of Materials Engineering and Performance*, vol. 27, no. 4, pp. 1530–1536, 2018.
- [108] Zhang, J., Li, H., Yang, F., Chi, Q., Ji, L., and Feng, Y., “Effect of heat treatment process on mechanical properties and microstructure of a 9% ni steel for large lng storage tanks”, *Journal of materials engineering and performance*, vol. 22, no. 12, pp. 3867–3871, 2013.
- [109] Rodrigues, R., “Avaliação das transformações de fase do aço com 9% de níquel e das zonas termicamente afetadas simuladas in situ com difração de raios-x síncrotron”, *Universidade Federal Fluminense, RJ*, 2016.
- [110] Chen, Y., Liu, F., Yang, G., Liu, N., and Zhou, Y., “ δ/γ transformation in non-equilibrium solidified peritectic fe-ni alloy”, *Science in China Series G: Physics, Mechanics and Astronomy*, vol. 50, no. 4, pp. 421–431, 2007.
- [111] Toussaint, P., Pillot, S., and Chauvy, C., “Challenges, properties, and features of 9% nikel steel plates for lng storage and transport: Towards ultra-large designs”, *Poster PO-20*, pp. 1–9, 2000.
- [112] Maresca, F., Kouznetsova, V., and Geers, M., “On the role of interlath retained austenite in the deformation of lath martensite”, *Modelling and Simulation in Materials Science and Engineering*, vol. 22, no. 4, p. 045 011, 2014.
- [113] Morito, S., Oh-ishi, K., Hono, K., and Ohba, T., “Carbon enrichment in retained austenite films in low carbon lath martensite steel”, *ISIJ international*, vol. 51, no. 7, pp. 1200–1202, 2011.
- [114] Syn, C., Fultz, B., and Morris, J., “Mechanical stability of retained austenite in tempered 9ni steel”, *Metallurgical Transactions A*, vol. 9, no. 11, pp. 1635–1640, 1978.
- [115] Nakada, N., Syarif, J., Tsuchiyama, T., and Takaki, S., “Improvement of strength–ductility balance by copper addition in 9% ni steels”, *Materials Science and Engineering: A*, vol. 374, no. 1-2, pp. 137–144, 2004.
- [116] Petrov, R., Kestens, L., Wasilkowska, A., and Houbaert, Y., “Microstructure and texture of a lightly deformed trip-assisted steel characterized by means of the ebsd technique”, *Materials Science and Engineering: A*, vol. 447, no. 1-2, pp. 285–297, 2007.
- [117] Verlinden, B., Bocher, P., Girault, E., and Aernoudt, E., “Austenite texture and bainite/austenite orientation relationships in trip steel”, *Scripta materialia*, vol. 45, no. 8, pp. 909–916, 2001.
- [118] Lacroix, G., Pardoën, T., and Jacques, P. J., “The fracture toughness of trip-assisted multiphase steels”, *Acta Materialia*, vol. 56, no. 15, pp. 3900–3913, 2008.
- [119] Liu, Q., Tang, D., Jiang, H.-t., Liu, R.-d., and Tang, X.-y., “Research and development of 780 mpa cold rolling trip-aided steel”, *International Journal of Minerals, Metallurgy and Materials*, vol. 16, no. 4, pp. 399–406, 2009.
- [120] Zaefferer, S., Romano, P., and Friedel, F., “Ebsd as a tool to identify and quantify bainite and ferrite in low-alloyed al-trip steels”, *Journal of microscopy*, vol. 230, no. 3, pp. 499–508, 2008.

- [121] De Knijf, D., Petrov, R., Föjer, C., and Kestens, L. A., “Effect of fresh martensite on the stability of retained austenite in quenching and partitioning steel”, *Materials Science and Engineering: A*, vol. 615, pp. 107–115, 2014.
- [122] Brandl, D., Lukas, M., Stockinger, M., Ploberger, S., and Ressel, G., “Evidence of austenite memory in ph 15-5 and assessment of its formation mechanism”, *Materials & Design*, vol. 176, p. 107841, 2019.
- [123] Jiang, W., Zhao, K.-y., Ye, D., Li, J., Li, Z.-d., and Su, J., “Effect of heat treatment on reversed austenite in cr15 super martensitic stainless steel”, *Journal of Iron and Steel Research International*, vol. 20, no. 5, pp. 61–65, 2013.
- [124] Kim, J., Syn, C., and Morris, J., “Microstructural sources of toughness in qlt-treated 5.5 ni cryogenic steel”, *Metallurgical Transactions A*, vol. 14, no. 1, pp. 93–103, 1983.
- [125] De Moor, E., Matlock, D. K., Speer, J. G., and Merwin, M. J., “Austenite stabilization through manganese enrichment”, *Scripta Materialia*, vol. 64, no. 2, pp. 185–188, 2011.
- [126] Ming, L. *et al.*, “Formation of precipitated austenite in 9% ni steel and its function at cryogenic temperature”, *Acta Metall Sin*, vol. 25, no. 1, pp. 13–17, 1989.
- [127] Bojack, A., Zhao, L., Morris, P., and Sietsma, J., “Austenite formation from martensite in a 13cr6ni2mo supermartensitic stainless steel”, *Metallurgical and Materials Transactions A*, vol. 47, no. 5, pp. 1996–2009, 2016.
- [128] Park, E. S., Yoo, D. K., Sung, J. H., Kang, C. Y., Lee, J. H., and Sung, J. H., “Formation of reversed austenite during tempering of 14cr- 7ni- 0.3 nb- 0.7 mo- 0.03 c super martensitic stainless steel”, *Metals and Materials International*, vol. 10, no. 6, p. 521, 2004.
- [129] Santos, T. A. A. dos, “Estudo da reversão da austenita em aço inoxidável martensítico-ferrítico para aplicação no setor de óleo e gás”, 2014.
- [130] Fultz, B., Kim, J., Kim, Y., Kim, H., Fior, G., and Morris, J., “The stability of precipitated austenite and the toughness of 9ni steel”, *Metallurgical Transactions A*, vol. 16, no. 12, pp. 2237–2249, 1985.
- [131] Lei, M. and Guo, Y., “Formation of precipitated austenite in 9% ni steel and its performance at cryogenic temperature”, *Acta Metall. Sin.(Engl. Ed.) A*, vol. 2, no. 4, pp. 244–248, 1989.
- [132] Chen, S., Zhao, M., Li, X., and Rong, L., “Compression stability of reversed austenite in 9ni steel”, *Journal of Materials Science & Technology*, vol. 6, no. 28, pp. 558–561, 2012.
- [133] Brauser, S., Kromm, A., Kannengiesser, T., and Rethmeier, M., “In-situ synchrotron diffraction and digital image correlation technique for characterizations of retained austenite stability in low-alloyed transformation induced plasticity steel”, *Scripta Materialia*, vol. 63, no. 12, pp. 1149–1152, 2010.
- [134] Kotan, H., “Microstructural evolution of 316l stainless steels with yttrium addition after mechanical milling and heat treatment”, *Materials Science and Engineering: A*, vol. 647, pp. 136–143, 2015.
- [135] Shiratsuchi, T. and Osawa, N., “Fatigue life prediction for 9% ni steel butt welded joints”, *International Journal of Fatigue*, vol. 142, p. 105925, 2021.

- [136] Kim, Y.-K., Shim, K.-T., and Kim, J.-H., “Fatigue crack growth properties of the base metal and weld metal of a 9% ni steel for lng storage tank”, in *Second International Conference on Smart Materials and Nanotechnology in Engineering*, International Society for Optics and Photonics, vol. 7493, 2009, p. 74936D.
- [137] Mu, W., Li, Y., Cai, Y., Wang, M., and Hua, X., “The cryogenic low-cycle fatigue performance of 9% ni steel joint made by flux cored arc welding”, *Materials Characterization*, vol. 151, pp. 27–37, 2019.
- [138] Lee, J.-S., You, W.-H., Yoo, C.-H., Kim, K.-S., and Kim, Y., “An experimental study on fatigue performance of cryogenic metallic materials for imo type b tank”, *International Journal of Naval Architecture and Ocean Engineering*, vol. 5, no. 4, pp. 580–597, 2013.
- [139] A553M-17e1, A. A. /., *Standard specification for pressure vessel plates, alloy steel, quenched and tempered 7, 8, and 9% nickel, astm international, west conshohocken*, en, PA, 2017.
- [140] Yoo, C.-H., Kim, K.-S., Choung, J., Kim, S.-H., and You, W.-H., “An experimental study on behaviors of imo type b ccs materials at room and cryogenic temperatures”, in *International Conference on Offshore Mechanics and Arctic Engineering*, vol. 44359, 2011, pp. 241–250.
- [141] Park, J.-Y. and Kim, M.-H., “Fatigue crack propagation characteristics of 3.5 to 9 wt% nickel steels for low temperature applications”, in *International Conference on Offshore Mechanics and Arctic Engineering*, American Society of Mechanical Engineers, vol. 49958, 2016, V004T03A010.
- [142] Kozlovskaya, V., Potak, Y. M., and Orzhekhovskii, Y. F., “Increasing the ductility of martensitic steels by heat treatment”, *Metal Science and Heat Treatment*, vol. 11, no. 5, pp. 400–405, 1969.
- [143] Stan, C. V., Beavers, C. M., Kunz, M., and Tamura, N., “X-ray diffraction under extreme conditions at the advanced light source”, *Quantum Beam Science*, vol. 2, no. 1, p. 4, 2018.
- [144] Blondé, R., Jimenez-Melero, E., Zhao, L., Wright, J., Brück, E., Van der Zwaag, S., and Van Dijk, N., “High-energy x-ray diffraction study on the temperature-dependent mechanical stability of retained austenite in low-alloyed trip steels”, *Acta Materialia*, vol. 60, no. 2, pp. 565–577, 2012.
- [145] Cullity, B. D., *Elements of X-ray Diffraction*. Addison-Wesley Publishing, 1956.
- [146] Motoyashiki, Y., Brückner-Foit, A., and Sugeta, A., “Microstructural influence on small fatigue cracks in a ferritic–martensitic steel”, *Engineering Fracture Mechanics*, vol. 75, no. 3-4, pp. 768–778, 2008.
- [147] Holzappel, C., Schäf, W., Marx, M., Vehoff, H., and Mücklich, F., “Interaction of cracks with precipitates and grain boundaries: Understanding crack growth mechanisms through focused ion beam tomography”, *Scripta Materialia*, vol. 56, no. 8, pp. 697–700, 2007.
- [148] Zellmer, L., Tereschenko, S., Brueckner-Foit, A., and Lehmann, P., “Investigation of the three-dimensional shape of slip bands in fatigued dual phase steel”, in *Advanced Materials Research*, Trans Tech Publ, vol. 891, 2014, pp. 482–487.

- [149] Saraf, L., “Kernel average misorientation confidence index correlation from fib sliced ni-fe-cr alloy surface”, *Microscopy and Microanalysis*, vol. 17, no. S2, pp. 424–425, 2011.
- [150] Castaldo, V., “High resolution scanning ion microscopy”, 2011.
- [151] Forbes, R. G., “The theory of bright field electron and field ion emission sources”, *Nanofabrication Using Focused Ion and Electron Beams: Principles and Applications*, p. 45, 2012.
- [152] Yuan, H., “3d morphological and crystallographic analysis of materials with a focused ion beam (fib)”, Ph.D. dissertation, 2014.
- [153] Kiener, D., Motz, C., Rester, M., Jenko, M., and Dehm, G., “Fib damage of cu and possible consequences for miniaturized mechanical tests”, *Materials Science and Engineering: A*, vol. 459, no. 1-2, pp. 262–272, 2007.
- [154] Hofer, C., Bliznuk, V., Verdiere, A., Petrov, R., Winkelhofer, F., Clemens, H., and Primig, S., “Correlative microscopy of a carbide-free bainitic steel”, *Micron*, vol. 81, pp. 1–7, 2016.
- [155] Wen, J. G., “Transmission electron microscopy”, in *Practical Materials Characterization*, Springer, 2014, pp. 189–229.
- [156] Inkson, B., “Scanning electron microscopy (sem) and transmission electron microscopy (tem) for materials characterization”, in *Materials characterization using nondestructive evaluation (NDE) methods*, Elsevier, 2016, pp. 17–43.
- [157] Pennycook, S. J., David, B., Williams, C. B., *et al.*, “Transmission electron microscopy: A textbook for materials science”, *Microscopy and Microanalysis*, vol. 16, no. 1, p. 111, 2010.
- [158] Williams, D. B. and Carter, C. B., *Transmission electron microscopy: A textbook for materials science. 2009.*
- [159] Buseck, P., Cowley, J., and Eyring, L., *High-Resolution Transmission Electron Microscopy: And Associated Techniques*. Oxford University Press, 1989.
- [160] Spence, J. C., *High-resolution electron microscopy*. OUP Oxford, 2013.
- [161] Wu, Y., Huang, H., and Zou, J., “A focused review on nanoscratching-induced deformation of monocrystalline silicon”, *International Journal of Surface Science and Engineering*, vol. 7, no. 1, pp. 51–80, 2013.
- [162] Zaefferer, S., Elhami, N.-N., and Konijnenberg, P., “Electron backscatter diffraction (ebbsd) techniques for studying phase transformations in steels”, in *Phase Transformations in Steels*, Elsevier, 2012, pp. 557–587.
- [163] Michael, J. R., “Introduction to ebbsd and applications in materials science.”, 2018.
- [164] Oxford. (2020). “Symmetry s2 brochure”, [Online]. Available: <https://nano.oxinst.com/symmetry2> (visited on 02/20/2021).
- [165] Thomsen, K., Schmidt, N., Bewick, A., Larsen, K., and Goulden, J., “Improving the accuracy of orientation measurements using ebbsd”, *Microscopy and Microanalysis*, vol. 19, no. S2, pp. 724–725, 2013.
- [166] Goulden, J. and Bewick, A., “The application of the aztec ebbsd system to the study of strain in the sem”, *Microscopy and Microanalysis*, vol. 22, no. S3, pp. 18–19, 2016.

- [167] Field, D., Merriman, C., Allain-Bonasso, N., and Wagner, F., “Quantification of dislocation structure heterogeneity in deformed polycrystals by ebsd”, *Modelling and Simulation in Materials Science and Engineering*, vol. 20, no. 2, p. 024 007, 2012.
- [168] Chen, Y., Hjelen, J., Gireesh, S., and Roven, H. J., “Optimization of ebsd parameters for ultra-fast characterization”, *Journal of microscopy*, vol. 245, no. 2, pp. 111–118, 2012.
- [169] Kamaya, M., “Characterization of microstructural damage due to low-cycle fatigue by ebsd observation”, *Materials Characterization*, vol. 60, no. 12, pp. 1454–1462, 2009.
- [170] Schayes, C., “Low cycle fatigue of the fe-3si steel: Damage mechanisms and strain localisation by ebsd”, Ph.D. dissertation, Lille 1, 2016.
- [171] Marinelli, M., Balbi, M., and Krupp, U., “Influence of plastic deformation in fatigue crack behavior in bainitic steel”, *International Journal of Fatigue*, vol. 143, p. 106 014, 2021.
- [172] Schwartz, A. J., Kumar, M., Adams, B. L., and Field, D. P., *Electron backscatter diffraction in materials science*. Springer, 2009, vol. 2.
- [173] Zaefferer, S. and Romano, P., “Attempt to identify and quantify microstructural constituents in low-alloyed trip steels by simultaneous ebsd and eds measurements”, *Microscopy and Microanalysis*, vol. 13, no. S02, p. 944, 2007.
- [174] Wasilkowska, A., Petrov, R., Kestens, L., EA, W., Kremaszky, C., Traint, S., and Pichler, A., “Microstructure and texture changes in a low-alloyed trip-aided steel induced by small plastic deformation”, *ISIJ international*, vol. 46, no. 2, pp. 302–309, 2006.
- [175] Bouquerel, J., “Modelling and characterisation of multiphase trip steel under static and dynamic loading”, Ph.D. dissertation, Ghent University, 2008.
- [176] Ruggles, T., Rampton, T., Khosravani, A., and Fullwood, D., “The effect of length scale on the determination of geometrically necessary dislocations via ebsd continuum dislocation microscopy”, *Ultramicroscopy*, vol. 164, pp. 1–10, 2016.
- [177] Wright, S. I., Nowell, M. M., and Field, D. P., “A review of strain analysis using electron backscatter diffraction”, *Microscopy and microanalysis*, vol. 17, no. 3, p. 316, 2011.
- [178] Wilkinson, A. J. and Hirsch, P. B., “Electron diffraction based techniques in scanning electron microscopy of bulk materials”, *Micron*, vol. 28, no. 4, pp. 279–308, 1997.
- [179] Humphreys, F., “Review grain and subgrain characterisation by electron backscatter diffraction”, *Journal of materials science*, vol. 36, no. 16, pp. 3833–3854, 2001.
- [180] Jedrychowski, M., Tarasiuk, J., Bacroix, B., and Wronski, S., “Electron backscatter diffraction investigation of local misorientations and orientation gradients in connection with evolution of grain boundary structures in deformed and annealed zirconium. a new approach in grain boundary analysis”, *Journal of Applied Crystallography*, vol. 46, no. 2, pp. 483–492, 2013.

- [181] Calcagnotto, M., Ponge, D., Demir, E., and Raabe, D., “Orientation gradients and geometrically necessary dislocations in ultrafine grained dual-phase steels studied by 2d and 3d ebsd”, *Materials Science and Engineering: A*, vol. 527, no. 10-11, pp. 2738–2746, 2010.
- [182] Schayes, C., Bouquerel, J., Vogt, J.-B., Palleschi, F., and Zaefferer, S., “A comparison of ebsd based strain indicators for the study of fe-3si steel subjected to cyclic loading”, *Materials Characterization*, vol. 115, pp. 61–70, 2016.
- [183] Li, H., Hsu, E., Szpunar, J., Utsunomiya, H., and Sakai, T., “Deformation mechanism and texture and microstructure evolution during high-speed rolling of az31b mg sheets”, *Journal of materials science*, vol. 43, no. 22, pp. 7148–7156, 2008.
- [184] Kamaya, M., Fonseca, J. Q. da, Li, L., and Preuss, M., “Local plastic strain measurement by ebsd”, in *Applied Mechanics and Materials*, Trans Tech Publ, vol. 7, 2007, pp. 173–179.
- [185] Harte, A., Atkinson, M., Preuss, M., and Da Fonseca, J. Q., “A statistical study of the relationship between plastic strain and lattice misorientation on the surface of a deformed ni-based superalloy”, *Acta Materialia*, vol. 195, pp. 555–570, 2020.
- [186] Paul, S. K., Stanford, N., Taylor, A., and Hilditch, T., “The effect of low cycle fatigue, ratcheting and mean stress relaxation on stress–strain response and microstructural development in a dual phase steel”, *International Journal of Fatigue*, vol. 80, pp. 341–348, 2015.
- [187] Vogt, J. B., Bouquerel, J., Leaux, F., and Palleschi, F., “Fatigue damage assessment of alternator fans by ebsd”, *Procedia Engineering*, vol. 66, pp. 608–614, 2013.
- [188] Buque, C., Bretschneider, J., Schwab, A., and Holste, C., “Dislocation structures in cyclically deformed nickel polycrystals”, *Materials Science and Engineering: A*, vol. 300, no. 1-2, pp. 254–262, 2001.
- [189] Zhang, Y., Lai, P., Jia, H., Ju, X., and Cui, G., “Investigation of test parameters on ebsd analysis of retained austenite in trip and pipeline steels”, *Metals*, vol. 9, no. 1, p. 94, 2019.
- [190] Keller, R. R. and Geiss, R. H., “Transmission ebsd from 10 nm domains in a scanning electron microscope”, *Journal of Microscopy*, vol. 245, no. 3, pp. 245–251, 2012.
- [191] Coates, D., “Kikuchi-like reflection patterns obtained with the scanning electron microscope”, *The Philosophical Magazine: A Journal of Theoretical Experimental and Applied Physics*, vol. 16, no. 144, pp. 1179–1184, 1967.
- [192] Kaneko, Y., Ishikawa, M., and Hashimoto, S., “Dislocation structures around crack tips of fatigued polycrystalline copper”, *Materials Science and Engineering: A*, vol. 400, pp. 418–421, 2005.
- [193] Weidner, A. and Biermann, H., “Case studies on the application of high-resolution electron channelling contrast imaging–investigation of defects and defect arrangements in metallic materials”, *Philosophical Magazine*, vol. 95, no. 7, pp. 759–793, 2015.
- [194] Zaefferer, S. and Elhami, N.-N., “Theory and application of electron channelling contrast imaging under controlled diffraction conditions”, *Acta Materialia*, vol. 75, pp. 20–50, 2014.

- [195] Lloyd, G. E., “Atomic number and crystallographic contrast images with the sem: A review of backscattered electron techniques”, *Mineralogical Magazine*, vol. 51, no. 359, pp. 3–19, 1987.
- [196] Vincent, R. and Midgley, P., “Double conical beam-rocking system for measurement of integrated electron diffraction intensities”, *Ultramicroscopy*, vol. 53, no. 3, pp. 271–282, 1994.
- [197] Joy, D. C., Newbury, D. E., and Davidson, D. L., “Electron channeling patterns in the scanning electron microscope”, *Journal of Applied Physics*, vol. 53, no. 8, R81–R122, 1982.
- [198] Guyon, J., Mansour, H., Gey, N., Crimp, M., Chalal, S., and Maloufi, N., “Sub-micron resolution selected area electron channeling patterns”, *Ultramicroscopy*, vol. 149, pp. 34–44, 2015.
- [199] Mansour, H., “Caractérisation des défauts cristallins au meb par canalisation d’électrons assistée par diagrammes pseudo-kikuchi haute résolution: Application à l’acier if, uo2 et tial”, Ph.D. dissertation, Université de Lorraine, 2016.
- [200] Morin, P., Pitaval, M., Besnard, D., and Fontaine, G., “Electron–channelling imaging in scanning electron microscopy”, *Philosophical Magazine A*, vol. 40, no. 4, pp. 511–524, 1979.
- [201] L’hôte, G., Lafond, C., Steyer, P., Deschanel, S., Douillard, T., Langlois, C., and Cazottes, S., “Rotational-electron channeling contrast imaging analysis of dislocation structure in fatigued copper single crystal”, *Scripta Materialia*, vol. 162, pp. 103–107, 2019.
- [202] Gutierrez-Urrutia, I., Zaefferer, S., and Raabe, D., “Electron channeling contrast imaging of twins and dislocations in twinning-induced plasticity steels under controlled diffraction conditions in a scanning electron microscope”, *Scripta Materialia*, vol. 61, no. 7, pp. 737–740, 2009.
- [203] ———, “Coupling of electron channeling with ebsd: Toward the quantitative characterization of deformation structures in the sem”, *Jom*, vol. 65, no. 9, pp. 1229–1236, 2013.
- [204] Dong, W., Sullivan, P., and Stout, K., “Comprehensive study of parameters for characterising three-dimensional surface topography: Iii: Parameters for characterising amplitude and some functional properties”, *Wear*, vol. 178, no. 1-2, pp. 29–43, 1994.
- [205] Biasin, R. N., “Caracterização da qualidade superficial em diferentes etapas do processo de polimento por rodas flap e buffing”, 2016.
- [206] Olympus. (2008). “Surface roughness measurement”, [Online]. Available: <https://www.olympus-ims.com/en/metrology/surface-roughness-measurement-portal/parameters> (visited on 09/20/2019).
- [207] Whitehouse, D. J., *Surfaces and their Measurement*. Elsevier, 2004.
- [208] Schindelin, J., Arganda-Carreras, I., Frise, E., Kaynig, V., Longair, M., Pietzsch, T., Preibisch, S., and Rueden, C., “714 saalfeld s, schmid b, tinevez jy, white dj, hartenstein v, eliceiri k, tomancak p, cardona a. 2012. 715 fiji: An open-source platform for biological-image analysis”, *Nat Methods*, vol. 9, pp. 676–682,

- [209] Miyamoto, G., Iwata, N., Takayama, N., and Furuhashi, T., “Mapping the parent austenite orientation reconstructed from the orientation of martensite by ebsd and its application to ausformed martensite”, *Acta Materialia*, vol. 58, no. 19, pp. 6393–6403, 2010.
- [210] Pinto, L., Escobar, D. P., Santos, O., Lopes, N., Carneiro, J., and Ribeiro-Andrade, R., “Influence of surface preparation method on retained austenite quantification”, *Materials Today Communications*, vol. 24, p. 101 226, 2020.
- [211] Gutierrez-Urrutia, I. and Raabe, D., “Dislocation and twin substructure evolution during strain hardening of an fe–22 wt.% mn–0.6 wt.% c twip steel observed by electron channeling contrast imaging”, *Acta Materialia*, vol. 59, no. 16, pp. 6449–6462, 2011.
- [212] Kwon, H., Barlat, F., Lee, M., Chung, Y., and Uhm, S., “Influence of tempering temperature on low cycle fatigue of high strength steel”, *ISIJ international*, vol. 54, no. 4, pp. 979–984, 2014.
- [213] Zhang, F., Long, X., Kang, J., Cao, D., and Lv, B., “Cyclic deformation behaviors of a high strength carbide-free bainitic steel”, *Materials & Design*, vol. 94, pp. 1–8, 2016.
- [214] Vogt, J.-B., DeCallaix, G., and Focet, J., “Cyclic mechanical behavior and microstructure of a 12cr-mo-v martensitic stainless steel”, *Fatigue & Fracture of Engineering Materials & Structures*, vol. 11, no. 6, pp. 435–446, 1988.
- [215] Vogt, J.-B., Bigeon, C., Stein, G., and Focet, J., “Low cycle fatigue of nitrogen alloyed martensitic stainless steels”, in *Low Cycle Fatigue and Elasto-Plastic Behaviour of Materials—3*, Springer, 1992, pp. 70–75.
- [216] Cruzado, A., Lucarini, S., LLorca, J., and Segurado, J., “Microstructure-based fatigue life model of metallic alloys with bilinear coffin-manson behavior”, *International Journal of Fatigue*, vol. 107, pp. 40–48, 2018.
- [217] Zhang, X.-C., Li, H.-C., Zeng, X., Tu, S.-T., Zhang, C.-C., and Wang, Q.-Q., “Fatigue behavior and bilinear coffin-manson plots of ni-based gh4169 alloy with different volume fractions of δ phase”, *Materials Science and Engineering: A*, vol. 682, pp. 12–22, 2017.
- [218] Sanders, T., Frishmuth, R., and Embley, G., “Temperature dependent deformation mechanisms of alloy 718 in low cycle fatigue”, in *Fatigue*, Springer, 1983, pp. 163–182.
- [219] Prasad, N. E., Paradkar, A., Malakondaiah, G., and Kutumbarao, V., “An analysis based on plastic strain energy for bilinearity in coffin-manson plots in an al-li alloy”, *Scripta Metallurgica et Materialia;(United States)*, vol. 30, no. 12, 1994.
- [220] Archie, F., Li, X., and Zaefferer, S., “Micro-damage initiation in ferrite-martensite dp microstructures: A statistical characterization of crystallographic and chemical parameters”, *Materials Science and Engineering: A*, vol. 701, pp. 302–313, 2017.
- [221] Noh, H.-S., Kang, J.-H., Kim, K.-M., and Kim, S.-J., “The effect of carbon on hydrogen embrittlement in stable cr-ni-mn-n austenitic stainless steels”, *Corrosion Science*, vol. 124, pp. 63–70, 2017.

- [222] Wan, D., Alvaro, A., Olden, V., and Barnoush, A., “Hydrogen-enhanced fatigue crack growth behaviors in a ferritic fe-3wt% si steel studied by fractography and dislocation structure analysis”, *International Journal of Hydrogen Energy*, vol. 44, no. 10, pp. 5030–5042, 2019.
- [223] Luo, Z. and Huang, M., “The role of interstitial carbon atoms on the strain-hardening rate of twinning-induced plasticity steels”, *Scripta Materialia*, vol. 178, pp. 264–268, 2020.
- [224] Lee, Y.-K., “Microstructural evolution during plastic deformation of twinning-induced plasticity steels”, *Scripta Materialia*, vol. 66, no. 12, pp. 1002–1006, 2012.
- [225] Chen, S., Rana, R., Haldar, A., and Ray, R. K., “Current state of fe-mn-al-c low density steels”, *Progress in Materials Science*, vol. 89, pp. 345–391, 2017.
- [226] Astafurova, E. G., Moskvina, V. A., Maier, G. G., Gordienko, A. I., Burlachenko, A. G., Smirnov, A. I., Bataev, V. A., Galchenko, N. K., and Astafurov, S. V., “Low-temperature tensile ductility by v-alloying of high-nitrogen crmn and crnimn steels: Characterization of deformation microstructure and fracture micromechanisms”, *Materials Science and Engineering: A*, vol. 745, pp. 265–278, 2019.
- [227] Hansen, N. and Jensen, D., “Philosophical transactions of the royal society of london. series a”, *Mathematical Physic Eng Sci*, vol. 357, pp. 1447–1469, 1999.
- [228] Wright, S. I. and Nowell, M. M., “A review of in situ ebsd studies”, *Electron Backscatter Diffraction in Materials Science*, pp. 329–337, 2009.
- [229] Michiuchi, M., Nambu, S., Ishimoto, Y., Inoue, J., and Koseki, T., “Relationship between local deformation behavior and crystallographic features of as-quenched lath martensite during uniaxial tensile deformation”, *Acta materialia*, vol. 57, no. 18, pp. 5283–5291, 2009.
- [230] Cretegnny, L. and Saxena, A., “Evolution of surface deformation during fatigue of ph 13-8 mo stainless steel using atomic force microscopy”, *Fatigue & Fracture of Engineering Materials & Structures*, vol. 25, no. 3, pp. 305–314, 2002.
- [231] Polák, J. and Sauzay, M., “Growth of extrusions in localized cyclic plastic straining”, *Materials Science and Engineering: A*, vol. 500, no. 1-2, pp. 122–129, 2009.
- [232] Batista, M. N., Marinelli, M. C., Hereñu, S., and Alvarez-Armas, I., “The role of microstructure in fatigue crack initiation of 9–12% cr reduced activation ferritic–martensitic steel”, *International Journal of Fatigue*, vol. 72, pp. 75–79, 2015.
- [233] Verma, P., Basu, J., Srinivas, N. S., and Singh, V., “Deformation behavior of modified 9cr–1mo steel under low cycle fatigue at 600° c”, *Materials Characterization*, vol. 131, pp. 244–252, 2017.
- [234] Zhang, Z., Hu, Z., Schmauder, S., Zhang, B., and Wang, Z., “Low cycle fatigue properties and microstructure of p92 ferritic-martensitic steel at room temperature and 873 k”, *Materials Characterization*, vol. 157, p. 109 923, 2019.
- [235] Jürgens, M., Olbricht, J., Fedelich, B., and Skrotzki, B., “Low cycle fatigue and relaxation performance of ferritic–martensitic grade p92 steel”, *Metals*, vol. 9, no. 1, p. 99, 2019.
- [236] Junak, G. and Cieśła, M., “Low-cycle fatigue of p91 and p92 steels used in the power engineering industry”, in *International Conference “Achievements in Mechanical and Materials Engineering”*, *Archives of Materials Science and Engineering*, vol. 48, 2011, pp. 19–24.

- [237] Vogt, J.-B., Serre, I., and Verleene, A., “Fatigue behaviour of a 9cr1monbv martensitic steel in a liquid metal”, *Materials Testing*, vol. 51, no. 11-12, pp. 810–813, 2009.
- [238] Vogt, J.-B., “Fatigue properties of high nitrogen steels”, *Journal of materials processing technology*, vol. 117, no. 3, pp. 364–369, 2001.
- [239] Jacques, P., Furnémont, Q., Lani, F., Pardoën, T., and Delannay, F., “Multiscale mechanics of trip-assisted multiphase steels: I. characterization and mechanical testing”, *Acta Materialia*, vol. 55, no. 11, pp. 3681–3693, 2007.
- [240] Leach, R., *Optical measurement of surface topography*. Springer, 2011, vol. 8.
- [241] Zhang, H., Yu, F., Li, S., and He, E., “Fine granular area formation induced by localized shear strain accumulation under very high cycle fatigue”, 2021.
- [242] Morales-Rivas, L., Ram, F., Spriestersbach, D., Sippel, J., De Graef, M., and Kerscher, E., “Fine granular area linked to very high cycle fatigue in martensitic and bainitic steels: Characterization by means of ebsd-dictionary indexing”, *Scripta Materialia*, vol. 194, p. 113 644, 2021.
- [243] Tavares, S., Pedrosa, P., Teodósio, J., Da Silva, M., Neto, J., and Pairis, S., “Magnetic properties of the uns s39205 duplex stainless steel”, *Journal of alloys and compounds*, vol. 351, no. 1-2, pp. 283–288, 2003.
- [244] Normando, P. G., Moura, E. P., Souza, J. A., Tavares, S. S., and Padovese, L. R., “Ultrasound, eddy current and magnetic barkhausen noise as tools for sigma phase detection on a uns s31803 duplex stainless steel”, *Materials Science and Engineering: A*, vol. 527, no. 12, pp. 2886–2891, 2010.
- [245] Mészáros, I. and Szabo, P., “Complex magnetic and microstructural investigation of duplex stainless steel”, *NDT & E International*, vol. 38, no. 7, pp. 517–521, 2005.
- [246] Camerini, C., Sacramento, R., Areiza, M., Rocha, A., Santos, R., Rebello, J., and Pereira, G., “Eddy current techniques for super duplex stainless steel characterization”, *Journal of Magnetism and Magnetic Materials*, vol. 388, pp. 96–100, 2015.
- [247] Costa, O. A. and Maria, I., “Relations entre la microstructure, les propriétés mécaniques et électromagnétiques de fils d’acier au carbone traités thermomécaniquement”, Ph.D. dissertation, Lille 1, 2020.
- [248] Zens, A. S., Appel, T., Broekaert, J. A., and Friedel, F., “Determination of retained austenite in multiphase steels by magnetic force microscopy”, *International journal of materials research*, vol. 97, no. 8, pp. 1158–1162, 2006.
- [249] Abelmann, L., “Magnetic force microscopy”, in *Encyclopedia of Spectroscopy and Spectrometry (Third Edition)*, J. C. Lindon, G. E. Tranter, and D. W. Koppenaal, Eds., Third Edition, Oxford: Academic Press, 2017, pp. 675–684, ISBN: 978-0-12-803224-4. DOI: <https://doi.org/10.1016/B978-0-12-803224-4.00029-7>.
- [250] Dias, A. and Andrade, M. S., “Atomic force and magnetic force microscopies applied to duplex stainless steels”, *Applied surface science*, vol. 161, no. 1-2, pp. 109–114, 2000.
- [251] Guo, L., Hua, G., Yang, B., Lu, H., Qiao, L., Yan, X., and Li, D., “Electron work functions of ferrite and austenite phases in a duplex stainless steel and their adhesive forces with afm silicon probe”, *Scientific reports*, vol. 6, no. 1, pp. 1–7, 2016.

- [252] Ramírez-Salgado, J., Domínguez-Aguilar, M., Castro-Domínguez, B., Hernández-Hernández, P., and Newman, R., “Detection of secondary phases in duplex stainless steel by magnetic force microscopy and scanning kelvin probe force microscopy”, *Materials characterization*, vol. 86, pp. 250–262, 2013.
- [253] Gheno, S., Santos, F., and Kuri, S., “Probing the duplex stainless steel phases via magnetic force microscopy”, *Journal of Applied Physics*, vol. 103, no. 5, p. 053 906, 2008.
- [254] Konchakov, R. and Khonik, V., “Effect of vacancies and interstitials in the dumbbell configuration on the shear modulus and vibrational density of states of copper”, *Physics of the Solid State*, vol. 56, no. 7, pp. 1368–1373, 2014.
- [255] Xi, J., Zhang, P., He, C., Zang, H., Guo, D., and Li, T., “The role of point defects in the swelling and elastic modulus of irradiated cubic silicon carbide”, *Nuclear Instruments and Methods in Physics Research Section B: Beam Interactions with Materials and Atoms*, vol. 356, pp. 62–68, 2015.



Appendix A

ANOVA - Roughness from SWLI

Anova: Single Factor

SUMMARY		Ra					
Groups	Count	Sum	Average	Variance			
10T	5	0.226	0.0452	0.0000177			
0.5T	5	0.138	0.0276	5.33E-05			
WQ	5	0.069	0.0138	0.0000027			
ANALYSE DE VARIANCE							
Source of variation	SS	df	MS	F	P-value	F Crit	
Between Groups	0.002476933	2	0.001238467	50.41248304	1.44763E-06	3.885293835	
Within Groups	0.0002948	12	2.45667E-05		P-value<0.05?		YES
Total	0.002771733	14					

SUMMARY		Rq					
Groups	Count	Sum	Average	Variance			
10T	5	0.326	0.0652	0.0000387			
0.5T	5	0.229	0.0458	0.0001597			
WQ	5	0.108	0.0216	0.0000128			
ANALYSE DE VARIANCE							
Source of variation	SS	df	MS	F	P-value	F Crit	
Between Groups	0.0047716	2	0.0023858	33.88920455	1.15818E-05	3.885293835	
Within Groups	0.0008448	12	0.0000704		P-value<0.05?		YES
Total	0.0056164	14					

SUMMARY		Rz					
Groups	Count	Sum	Average	Variance			
10T	5	1.296	0.2592	0.0039062			
0.5T	5	0.744	0.1488	0.0018637			
WQ	5	0.455	0.091	0.000216			
ANALYSE DE VARIANCE							
Source of variation	SS	df	MS	F	P-value	F Crit	
Between Groups	0.073033733	2	0.036516867	18.30144172	0.000226525	3.885293835	
Within Groups	0.0239436	12	0.0019953		P-value<0.05?		YES
Total	0.096977333	14					

APPENDIX A. ANOVA - ROUGHNESS FROM SWLI

SUMMARY		Rku		
Groups	Count	Sum	Average	Variance
10T	5	36.844	7.3688	3.0082512
0.5T	5	46.358	9.2716	1.0299003
WQ	5	53.103	10.6206	4.1352218

ANALYSE DE VARIANCE						
Source of variation	SS	df	MS	F	P-value	F Crit
Between Groups	26.6910868	2	13.3455434	4.89842183	0.027843628	3.885293835
Within Groups	32.6934932	12	2.724457767		P-value<0.05? YES	
Total	59.38458	14				

SUMMARY		Rsk		
Groups	Count	Sum	Average	Variance
10T	5	2.896	0.5792	0.1521387
0.5T	5	1.504	0.3008	0.0094177
WQ	5	4.039	0.8078	0.1908507

ANALYSE DE VARIANCE						
Source of variation	SS	df	MS	F	P-value	F Crit
Between Groups	0.6446892	2	0.3223446	2.74408149	0.104381209	3.885293835
Within Groups	1.4096284	12	0.117469033		P-value<0.05? NO	
Total	2.0543176	14				

SUMMARY		Sa		
Groups	Count	Sum	Average	Variance
10T	5	530.236	106.0472	608.3025077
0.5T	5	318.165	63.633	83.8535635
WQ	5	159.649	31.9298	12.5471892

ANALYSE DE VARIANCE						
Source of variation	SS	df	MS	F	P-value	F Crit
Between Groups	13829.07706	2	6914.538529	29.43595802	2.35636E-05	3.885293835
Within Groups	2818.813042	12	234.9010868		P- value<0.05? YES	
Total	16647.8901	14				

APPENDIX A. ANOVA - ROUGHNESS FROM SWLI

SUMMARY		Sq		
Groups	Count	Sum	Average	Variance
10T	5	608.705	121.741	573.902434
0.5T	5	480.347	96.0694	147.1808443
WQ	5	235.108	47.0216	47.7137153

ANALYSE DE VARIANCE						
Source of variation	SS	df	MS	F	P-value	F Crit
Between Groups	14412.84411	2	7206.422056	28.12090363	2.95654E-05	3.885293835
Within Groups	3075.187974	12	256.2656645		P-value<0.05? YES	
Total	17488.03209	14				

SUMMARY		Sp		
Groups	Count	Sum	Average	Variance
10T	5	6488.38	1297.6762	8080.088693
0.5T	5	5058.18	1011.6352	265194.8499
WQ	5	4113.22	822.644	36386.32724

ANALYSE DE VARIANCE						
Source of variation	SS	df	MS	F	P-value	F Crit
Between Groups	571987.864	2	285993.932	2.770710743	0.102494078	3.885293835
Within Groups	1238645.063	12	103220.4219		P-value<0.05? NO	
Total	1810632.927	14				

SUMMARY		Sv		
Groups	Count	Sum	Average	Variance
10T	5	-4552.02	-910.4048	24573.09581
0.5T	5	-6192.89	-1238.5788	577000.2073
WQ	5	-2461.52	-492.303	45846.90553

ANALYSE DE VARIANCE						
Source of variation	SS	df	MS	F	P-value	F Crit
Between Groups	1399058.099	2	699529.0493	3.241460677	0.07489689	3.885293835
Within Groups	2589680.835	12	215806.7362		P-value<0.05? NO	
Total	3988738.933	14				

APPENDIX A. ANOVA - ROUGHNESS FROM SWLI

SUMMARY					Sz	
Groups	Count	Sum	Average	Variance		
10T	5	8971.48	1794.295	1050422.666		
0.5T	5	12281.1	2456.214	583925.4692		
WQ	5	6574.74	1314.947	69851.73579		
ANALYSE DE VARIANCE						
Source of variation	SS	df	MS	F	P-value	F Crit
Between Groups	3284002.722	2	1642001.361	2.890508423	0.094481747	3.885293835
Within Groups	6816799.485	12	568066.6237		P-value<0.05?	
Total	10100802.21	14			NO	

SUMMARY					Ssk	
Groups	Count	Sum	Average	Variance		
10T	5	2.41	0.482	0.0528295		
0.5T	5	1.625	0.325	0.4441975		
WQ	5	3.745	0.749	1.749131		
ANALYSE DE VARIANCE						
Source of variation	SS	df	MS	F	P-value	F Crit
Between Groups	0.459523333	2	0.229761667	0.306872891	0.741349557	3.885293835
Within Groups	8.984632	12	0.748719333		P-value<0.05?	
Total	9.444155333	14			NO	

SUMMARY					Sku	
Groups	Count	Sum	Average	Variance		
10T	5	27.693	5.5386	1.4782188		
0.5T	5	92.306	18.4612	298.9388207		
WQ	5	78.258	15.6516	25.1367063		
ANALYSE DE VARIANCE						
Source of variation	SS	df	MS	F	P-value	F Crit
Between Groups	461.9336865	2	230.9668433	2.128375234	0.161765178	3.885293835
Within Groups	1302.214983	12	108.5179153		P-value<0.05?	
Total	1764.14867	14			NO	



Appendix B

Fatigue data

<i>Sample</i>	% $\Delta\varepsilon_t$	Sample n	$\Delta\varepsilon_p$ 50% life	$\Sigma\Delta\varepsilon_p$	N_f
<i>WQ - 8% retained austenite</i>	0.8	1	0.09	773	8000
		2	0.10	998	9469
	0.9	1	0.21	1150	5596
		2	0.23	1750	7800
	1	1	0.18	484	2800
		2	0.23	713	3200
	1.2	1	0.35	231	650
		2	0.35	440	1300
	1.6	1	0.69	406	599
		2	0.67	435.5	650
<i>0.5T - 4.5% reversed austenite</i>	0.8	1	0.23	1014.8	4563
		2	0.32	2055.8	6221
	1.2	1	0.55	698.1	1300
		2	0.53	695.4	1342
	1.6	1	0.98	722.7	750
		2	0.96	1046	1089
<i>10T - 11% reversed austenite</i>	0.8	1	0.37	1077	2923
		2	0.26	2357	8868
	1.2	1	0.56	1418	2600
		2	0.72	1414	1960
	1.6	1	0.90	1032	1150
		2	0.92	787	850

INTERRUPTED TESTS

<i>Sample</i>	% $\Delta\varepsilon_t$	$\Delta\varepsilon_p$ 50% life	$\Sigma\Delta\varepsilon_p$	N 50% life
<i>WQ - 8% retained austenite</i>	0.9	0.21	675.5	3261
	1.2	0.38	237	620
<i>0.5T - 4.5% reversed austenite</i>	1.2	0.7	440	630
<i>10T - 11% reversed austenite</i>	1.2	0.72	1414	1960

Summary

<u>WATER QUENCHED (WQ)</u>	➔	<u>30 MINUTES (0.5T)</u>	➔	<u>10 HOURS (10T)</u>
<ul style="list-style-type: none"> • Few Reversed austenite + Tempered Martensite; 		<ul style="list-style-type: none"> • Retained austenite + Martensite; 		<ul style="list-style-type: none"> • Reversed austenite + Bainite + Tempered Martensite
<ul style="list-style-type: none"> • KAM - intermediate between WQ and 10h; 		<ul style="list-style-type: none"> • KAM - highly disoriented zones at initial state; 		<ul style="list-style-type: none"> • KAM - less disoriented zones at initial state;
<ul style="list-style-type: none"> • 50% isolated PSM's and 50% of Protrusions; 		<ul style="list-style-type: none"> • Majority of isolated PSM's; 		<ul style="list-style-type: none"> • Majority of Protrusions;
<p>Extrusions emerges at boundaries, intrusions in the middle; Extrusions in the middle of wider laths, when no austenite is found;</p>				
<ul style="list-style-type: none"> • PSMs present at LAB (laths/blocks); Sometimes HAB (packets) 		<ul style="list-style-type: none"> • PSMs present at GB for higher $\Delta\epsilon_t$; And at LAB for lower $\Delta\epsilon_t$ 		<ul style="list-style-type: none"> • PSMs present at LAB (laths/lath interfaces) or within blocks

Abstract

The very complex hierarchical structure of the 9Ni martensitic steel was used in this study as a tentative of proposing a mechanism of fatigue crack initiation. The PhD work took into consideration the impact of the interface nature and the matrix morphology. These metallurgical parameters have been successfully managed with controlled heat treatments. Thus, the austenite content as well in the retained form as in the reversed one and the change from martensitic to bainitic matrix were considered as relevant to answer the primary objective of the thesis. In addition, the goal of this work was also to suggest heat treatments leading to the best fatigue performance. Low cycle fatigue (LCF) tests were carried out at room temperature under several constant strain ranges ($\Delta\varepsilon_t$) from 0.8% to 1.6%. The microstructure and dislocations structures were deeply characterized by advanced microscopy techniques (SEM, c-ECCI, EBSD, TEM, HRTEM, and MFM). The stress response to strain cycling was microstructural dependent. The quenched martensitic steel with 8% of retained austenite was more prone to cyclic softening and presented less fatigue resistance than the tempered bainite-martensitic one with 10% of reversed austenite. The latter had a more deformed surface fulfilled by small cracks for all strain levels. The investigations allowed concluding that in all cases, the austenite films play an important role in the accommodation of plastic deformation, acting as a lubricant and promoting matter displacement along the thin martensitic laths. This resulted in extrusion development at interface boundaries and intrusion nucleation in the laths, differently than what was observed before with a 12Cr martensitic steel without any interface modification.

Keywords LCF, Martensite, Austenite, Plastic Deformation, Persistent Slip Marks, 9Ni steel, Microcrack initiation, SEM-EBSD.

Résumé

La structure hiérarchisée très complexe de l'acier martensitique 9Ni a été utilisée dans cette étude afin de proposer un mécanisme d'amorçage des fissures de fatigue. Le travail de thèse a pris en considération l'impact de la nature de l'interface et de la morphologie de la matrice de l'acier. Ces paramètres métallurgiques ont été gérés avec succès par les traitements thermiques contrôlés. Ainsi, la teneur en austénite aussi bien sous forme retenue que sous forme de réversion et le passage d'une matrice martensitique à une matrice bainito-martensitique sont apparus pertinents pour répondre à l'objectif premier de la thèse. De plus, le but de ce travail était également de proposer des traitements thermiques conduisant aux meilleures performances en fatigue. Des essais de fatigue oligocyclique (LCF) ont été réalisés à température ambiante sous plusieurs variations de déformations ($\Delta\varepsilon_t$) de 0,8% à 1,6%. La microstructure et les structures de dislocations ont été soigneusement analysées par microscopies de pointe (MEB, c-ECCI, EBSD, MET, HRMET et MFM). L'évolution des contraintes au cours du cyclage était dépendante de la microstructure. L'acier martensitique trempé avec 8% d'austénite retenue était plus sensible à l'adoucissement cyclique et moins résistant à la fatigue que l'acier bainito-martensitique revenu avec 10% d'austénite de réversion. Ce dernier avait une surface plus déformée couverte de micro-fissures pour tous les niveaux de déformation. Les investigations ont permis de conclure que, dans tous les cas, les films d'austénite jouent un rôle important sur l'accommodation de la déformation plastique, agissant comme un lubrifiant favorisant l'écoulement de la matière le long des très fines lattes martensitiques. Cela a conduit au développement d'extrusions au niveau des interfaces et une germination d'intrusions (embryon de fissure) dans les lattes, ce qui diffère des observations préalablement menées avec un acier martensitique 12Cr sans aucune modification d'interface.

Mots clés: LCF, Martensite, Austénite, Déformation plastique, Bandes persistantes, Acier 9Ni, Amorçage de fissures, MEB-EBSD.